Boundary Layer Transition on Airfoils and Wings in Unsteady Low-Reynolds Number Flows

by

Connor Toppings

A thesis
presented to the University of Waterloo
in fulfillment of the
thesis requirement for the degree of
Doctor of Philosophy
in
Mechanical and Mechatronics Engineering

Waterloo, Ontario, Canada, 2025

© Connor Toppings 2025

Examining Committee Membership

The following served on the Examining Committee for this thesis. The decision of the Examining Committee is by majority vote.

External Examiner	Dr. P. Lavoie Professor Institute for Aerospace Studies University of Toronto
Supervisor	Dr. S. Yarusevych Professor Dept. of Mechanical and Mechatronics Engineering University of Waterloo
Internal Members	Dr. S. Peterson Professor Dept. of Mechanical and Mechatronics Engineering University of Waterloo
	Dr. K. Daun Professor Dept. of Mechanical and Mechatronics Engineering University of Waterloo
Internal-External Member	Dr. B. Zemskova Assistant Professor Dept. of Applied Mathematics University of Waterloo

Author's Declarations

This thesis consists of material all of which I authored or co-authored: see Statement of Contributions included in the thesis. This is a true copy of the thesis, including any required final revisions, as accepted by my examiners.

I understand that this document may be made electronically available to the public.

Statement of Contributions

Connor Toppings is the sole author of Chapters 1–3 and Chapter 8. This thesis contains portions of three co-authored publications and one co-authored manuscript under review for publication. Exceptions to sole authorship are as follows:

Chapter 4 is adapted from [1] and is co-authored by Dr. Serhiy Yarusevych.

Chapter 5 is adapted from [2] and is co-authored by Dr. Serhiy Yarusevych.

Chapter 6 is adapted from [3] and is co-authored by Dr. Serhiy Yarusevych.

Chapter 7 is under review for publication in the Journal of Fluid Mechanics and is co-authored by Dr. Serhiy Yarusevych.

Abstract

Laminar separation bubbles (LSBs) often form on wings and turbine blades that operate at aerodynamically low chord Reynolds numbers. Changes in the oncoming velocity magnitude, direction, and disturbance amplitudes may cause bursting of the LSB and a severe reduction in wing or blade performance. The objective of this thesis is to understand the transient dynamics of LSBs in unsteady conditions that are relevant to practical applications of low chord Reynolds number wings and turbine blades. To this end, a series of wind tunnel experiments were performed on a set of NACA 0018 airfoil and wing models at chord Reynolds numbers ranging from 4×10^4 to 1×10^5. The influence of isolated ramp changes in Reynolds number, isolated ramp changes in angle of attack, and large-scale high-intensity free-stream turbulence on the LSB development and aerodynamic loading were investigated. Three-dimensional end effects on LSB development, which are present for all real wings and turbine blades, were also studied in unsteady operating conditions. Two-component particle image velocimetry measurements were performed to investigate the suction surface boundary layer development on the wing and airfoil models. Direct force measurements were employed to quantify the effects of unsteadiness on the lift coefficient.

Transient changes in free-stream velocity and angle of attack leading to LSB formation or bursting were found to produce lift coefficient hysteresis. Stronger hysteresis effects were observed for more rapid changes in operating conditions, and for two-dimensional airfoils relative to finite wings. Although the dynamics of boundary layer transition affect the conditions at which LSB bursting or formation initiates, the temporal evolution of the aerodynamic forces after the onset of LSB bursting or formation were similar across widely varying flow conditions. When undergoing an increase in angle of attack that leads to bursting, the LSB initially contracted. In contrast, the LSB continuously expanded prior to bursting during a decrease in Reynolds number. However, LSB formation was followed by a contraction of the LSB during both decreases in angle of attack and increases in Reynolds number. The frequencies of unstable disturbances that lead to transition in the separated shear layer varied continuously during the LSB formation and bursting transients. The duration of the LSB bursting and formation transients was on the order of 10 global convective timescales. On a finite span wing, end effects caused spanwise expansion of the separated flow region during bursting. Conversely, the separated flow region contracted in the spanwise direction during LSB formation on a finite wing. The gradual spanwise progression of bursting on a finite wing in unsteady conditions caused changes in aerodynamic loads that were more gradual than those experienced by a two-dimensional airfoil. In large-scale, high-intensity free-stream turbulence, fluctuations in the instantaneous effective oncoming velocity direction may lead to large variations in transition location and intermittent boundary layer separation. These findings elucidate the physical mechanisms responsible for the performance characteristics of wings and turbine blades in unsteady low chord Reynolds number flows.

Acknowledgements

- Thank you to God for giving me the opportunity to be a scholar.
- Funding was provided by the Natural Sciences and Engineering Research Council of Canada and the Ontario Graduate Scholarship Program.
- Thank you to Professor Yarusevych for supervising this work.
- Thank you to my committee members for the time they spent reading my thesis and giving me feedback for improvement.
- Thank you to Florian Kähler for designing and building the active turbulence grid, and thereby enabling me to complete my experiments within the PhD program time limits.
- Thank you to Supun, Yash, Nikhilesh, Kaycee, Deep, Nianhua, Hicham, Johan, and Shreenivas for helping me in the lab.
- Thank you to Jason Benninger and Karl Janzen for their technical support.
- The scientific colour map vik [4] is used in this work to prevent visual distortion of the data and exclusion of readers with colour-vision deficiencies [5].

Table of Contents

List of Figures x

List of Tables xv

List of Abbreviations xvi

List of Symbols xvii

1 Introduction 1
- 1.1 Motivation . . . 2
- 1.2 Objectives . . . 4

2 Background 5
- 2.1 Conservation Laws and Kinematics of Fluid Flow . . . 6
- 2.2 Aerodynamics of Lifting Surfaces . . . 6
  - 2.2.1 Unsteady Aerodynamics of Lifting Surfaces . . . 10
- 2.3 Boundary Layer Transition at Aerodynamically Low Reynolds Numbers . . . 13
  - 2.3.1 Transition in Unsteady Operating Conditions . . . 18
  - 2.3.2 Effect of Finite Span on Laminar Separation Bubbles . . . 21

3 Methodology 24
- 3.1 Experimental Setup . . . 25
  - 3.1.1 Facility and Lifting Surface Models . . . 25
- 3.2 Lifting Surface Models . . . 26
- 3.3 Measurement Techniques . . . 28
  - 3.3.1 Particle Image Velocimetry . . . 28
  - 3.3.2 Aerodynamic Forces . . . 30
- 3.4 Analysis Methods . . . 31
  - 3.4.1 Frequency-Domain Analysis . . . 31
  - 3.4.2 Continuous Wavelet Transform . . . 32
  - 3.4.3 Proper Orthogonal Decomposition . . . 33
- 3.5 Uncertainty Estimation . . . 34

4 Transient LSB Development During a Change in Reynolds Number 37
4.1 Introduction . . . 38
4.2 Description of Experiments . . . 39
4.2.1 Measurement Techniques . . . 39
4.3 Results . . . 42
4.3.1 Limiting flow states . . . 42
4.3.2 Transient flow development . . . 44
4.4 Concluding Remarks . . . 53

5 Spanwise Flow Development and Transient Loading During LSB Formation and Bursting 55
5.1 Introduction . . . 56
5.2 Description of Experiments . . . 56
5.2.1 Measurement Techniques . . . 58
5.2.2 Data Processing Techniques . . . 61
5.3 Results . . . 62
5.3.1 Flow Field Development . . . 66
5.4 Discussion . . . 86
5.5 Concluding Remarks . . . 91

6 Comparison of Transient LSB Development During Changes in Angle of Attack and Reynolds Number 93
6.1 Introduction . . . 94
6.2 Description of Experiments . . . 94
6.2.1 Measurement Techniques . . . 96
6.2.2 Data processing techniques . . . 98
6.3 Results and Discussion . . . 102
6.3.1 Limiting flow states . . . 102
6.3.2 Transient Flow Development . . . 104
6.3.3 Spanwise Flow Development . . . 114
6.3.4 Influence of limiting flow conditions . . . 118
6.3.5 Influence of pitch rate . . . 120
6.4 Concluding Remarks . . . 123

7 Boundary Layer Transition on an Airfoil in Large-Scale Free-Stream Turbulence 125
7.1 Introduction . . . 126

7.2 Description of Experiments . . . 127
7.2.1 Flow Measurements . . . 127
7.2.2 Free-stream Turbulence Generation . . . 130
7.2.3 Data Processing Techniques . . . 133
7.3 Results . . . 135
7.3.1 Aerodynamic Forces . . . 135
7.3.2 Overview of Boundary Layer Transition . . . 136
7.3.3 Mean Flow Development . . . 137
7.3.4 Transition Dynamics . . . 144
7.3.5 Correlation of Oncoming Disturbances to Boundary Layer Development 157
7.4 Concluding Remarks . . . 162

8 Conclusions & Recommendations 165

Letter(s) of Copyright Permission 173

References 174

Appendices 192

A Uncertainty Estimation 193
A.1 Experimental Conditions . . . 194
A.1.1 Free-stream Velocity . . . 194
A.1.2 Turbulence Intensity . . . 195
A.1.3 Integral Length Scale . . . 195
A.1.4 Angle of Attack . . . 195
A.2 Particle Image Velocimetry . . . 196
A.2.1 Reynolds Stress . . . 197
A.2.2 Integral Boundary Layer Parameters . . . 198
A.2.3 POD Modes . . . 198
A.3 Power Spectral Density . . . 199
A.4 Surface Pressure . . . 199
A.5 Lift and Drag Forces . . . 200

List of Figures

2.1 Sectional forces acting on an airfoil. 7
2.2 Wing-tip vortex formation in the wake of a finite wing. 8
2.3 Effect of pressure gradient on curvature of streamwise velocity profile. . . . 9
2.4 Streamlines and streamwise velocity profiles in the vicinity of boundary layer separation. 10
2.5 Boundary layer separation from an airfoil and its effect on the pressure distribution. 10
2.6 Qualitative schematic of attached and separated boundary layer transition. 14
2.7 Sectional lift and drag coefficients versus angle of attack for the Lissaman 7769 airfoil. 16
2.8 Schematic of bypass transition. 20
2.9 Horseshoe vortex and corner separation at a wing-root body junction. . . . 22

3.1 University of Waterloo recirculating wind tunnel. 25
3.2 Active turbulence grid. 27
3.3 NACA 0018 airfoil models for low-FSTI experiments. 28
3.4 PIV laser set-up and particle images. 29
3.5 Example of an Airy wavelet scaled with a peak frequency of 1 Hz. 32

4.1 Controlled free-stream velocity ramp change. 40
4.2 Fields of view for low-speed and high-speed PIV configurations and coordinate system definitions. 42
4.3 Surface pressure distributions of limiting flow states at steady chord Reynolds number. 43
4.4 Mean streamwise velocity, streamwise RMS velocity fluctuations, and wall-normal RMS velocity fluctuations of limiting flow states at steady chord Reynolds number. 44
4.5 Frequency and wavenumber spectra of wall-normal velocity fluctuations in the limiting flow states. 45
4.6 Instantaneous spanwise vorticity contours during bubble formation, and bubble bursting. 46
4.7 Ensemble and temporal window averaged spanwise vorticity contours during bubble formation, and bubble bursting. 47
4.8 Transient change of the ensemble averaged dividing streamline during increasing Re_c and decreasing Re_c. 48

4.9 Locations of separation, transition, and reattachment during increasing Re_c and decreasing Re_c. 49
4.10 Reynolds shear stress and displacement thickness during increasing Re_c, and decreasing Re_c. 50
4.11 Frequency and wavenumber of integrated wall-normal velocity fluctuations during ramp changes in Re_c. 51
4.12 Temporal acceleration and separated shear layer angle. 53

5.1 Coordinate system definitions and PIV measurement plane orientations. . . 57
5.2 Ramp change in free-stream velocity for $\alpha = 3°$, $\alpha = 5°$ and $6°$, and $\alpha = 9°$. 58
5.3 Ensemble-averaged lift coefficient versus convective time. 63
5.4 Ensemble-averaged lift coefficient versus Reynolds number. 65
5.5 Methodology for calculating transient period and ensemble-averaged transient periods. 66
5.6 Mean streamwise velocity fields of the limiting flow states from top-view PIV. 68
5.7 Mean streamwise velocity fields of the limiting flow states from side-view PIV. 70
5.8 Reynolds shear stress fields of limiting flow states from side-view PIV. . . . 71
5.9 Instantaneous snapshots of streamwise velocity during ramp up of free-stream velocity. 72
5.10 Instantaneous snapshots of streamwise velocity during ramp up of free-stream velocity. 73
5.11 Contours of minimum ensemble-averaged streamwise velocity during ramp up and ramp down in free-stream velocity. 75
5.12 Contours of minimum streamwise velocity, lift coefficient, and Reynolds number for ramp up and ramp down for the wing. 76
5.13 Instantaneous snapshots of spanwise vorticity during ramp up in free-stream velocity. 77
5.14 Instantaneous snapshots of spanwise vorticity during ramp down in free-stream velocity. 78
5.15 Transient movement of separation, transition, and reattachment locations for airfoil at $\alpha = 5°$ and finite wing at $\alpha = 6°$. 80
5.16 Ensemble-averaged wavelet amplitude scalograms of integrated wall-normal velocity fluctuations during ramp up in free-stream velocity. 83
5.17 Ensemble-averaged wavelet amplitude scalograms of integrated wall-normal velocity fluctuations during ramp down in free-stream velocity. 84
5.18 Gaster [7] bursting criterion during ramp changes in free-stream velocity. . 87

6.1 Model setup and coordinate system definition. 95
6.2 Controlled angle of attack and Reynolds number changes leading to LSB bursting and formation. 96

6.3 Unfiltered and filtered lift coefficients for the airfoil undergoing a pitch up manoeuvre at $\dot{\alpha}c/(2u_\infty) = 5 \times 10^3$. 99
6.4 Definition of reaction and step times for pitching motion. 100
6.5 Definition of reaction and step times for Re_c change. 100
6.6 Mean streamwise velocity contours in steady conditions measured by side-view PIV configuration. 102
6.7 Quasi-steady and transient lift coefficients for pitching airfoil and wing at $\mathrm{Re}_c = 1 \times 10^5$. 103
6.8 Quasi-steady and ensemble-averaged transient lift coefficients for airfoil and wing for changes in Re_c. 104
6.9 Lift coefficients from individual runs of the pitching motion with rate $\dot{\alpha}c/(2u_\infty) = 3 \times 10^{-5}$ and Reynolds number decrease. 105
6.10 Lift coefficients from 20 individual runs of the pitching motion with rate $\dot{\alpha}c/(2u_\infty) = -3 \times 10^{-5}$ and Reynolds number increase. 105
6.11 Ensemble-averaged lift coefficient, angle of attack, streamwise velocity, and instantaneous spanwise vorticity contours for $\dot{\alpha}c/(2u_\infty) = 3 \times 10^{-4}$. 107
6.12 Ensemble-averaged lift coefficient, Reynolds number, streamwise velocity, and instantaneous spanwise vorticity contours for Reynolds number decrease. 107
6.13 Ensemble-averaged lift coefficient, angle of attack, streamwise velocity, and instantaneous spanwise vorticity contours for $\dot{\alpha}c/(2u_\infty) = -3 \times 10^{-4}$. 109
6.14 Ensemble-averaged lift coefficient, Reynolds number, streamwise velocity, and instantaneous spanwise vorticity contours for Reynolds number increase. 109
6.15 Transient locations of separation, transition, and reattachment during LSB bursting and formation on airfoil. 110
6.16 Contours of ensemble-averaged Reynolds shear stress during LSB bursting and formation on airfoil. 112
6.17 Contours of ensemble-averaged wavelet amplitude during LSB bursting and formation on airfoil. 113
6.18 Streamwise velocity contours in steady conditions measured by top-view PIV configuration. 115
6.19 Contours of minimum ensemble-averaged streamwise velocity during LSB bursting. 116
6.20 Contours of minimum ensemble-averaged streamwise velocity during LSB formation. 117
6.21 Comparison of transient lift coefficients of individual runs for pitching motions over narrow and wide angle ranges. 119
6.22 Comparison of pitching transients leading to stall with data from Kiefer *et al.* (2022). 119
6.23 Ensemble averaged lift coefficient time-history during pitching motion for airfoil and wing. 120

6.24 Reaction delay versus pitch rate for pitching between 10° and 13°. 122
6.25 Step time versus pitch rate for pitching between 10° and 13°. 123

7.1 Experimental setup. 128
7.2 PIV measurement plane configurations and coordinate system definitions. The z axis is in the out-of-plane direction in the sense of a right-handed coordinate system. 129
7.3 Free-stream turbulence spectra. 132
7.4 Lift and drag coefficients. 136
7.5 Instantaneous snapshots of spanwise vorticity. 138
7.6 Mean streamwise velocity, streamwise RMS velocity fluctuations, and wall-normal RMS velocity fluctuations for $\alpha = 5°$. 139
7.7 Mean streamwise velocity, streamwise RMS velocity fluctuations, and wall-normal RMS velocity fluctuations for $\alpha = 12°$. 140
7.8 Reynolds shear stress at $y = \delta^*$, shape factor, and global entropy from P-POD at $\alpha = 5°$ and $\alpha = 12°$. 141
7.9 Locations of maximum shape factor and mean transition location for $\alpha = 5°$, $\Lambda_{ux}/c = 1$. 144
7.10 Instantaneous spanwise vorticity. 145
7.11 Relative energy of POD modes from F-POD. 146
7.12 Streamwise component of POD spatial modes for $\alpha = 5°$ and $\Lambda_{ux}/c = 1$. . 148
7.13 Streamwise component of POD spatial modes for $\alpha = 12°$. 149
7.14 Frequency-wavenumber power spectral density of wall-normal velocity fluctuations at $y = \delta^*$ for clean flow and elevated FSTI with $\Lambda_{ux}/c = 1$. 151
7.15 Contours of spatial entropy from P-POD and histograms of x_t at $\alpha = 5°$. . 152
7.16 Contours of spatial entropy from P-POD and histograms of x_t at $\alpha = 12°$. 153
7.17 Intermittency factor for clean flow and elevated FSTI with $\Lambda_{ux}/c = 1$. . . . 155
7.18 Power spectral density of spatial entropy fluctuations from P-POD averaged over $0.4 < x/c < 0.5$ for $\alpha = 5°$. 156
7.19 Instantaneous streamwise velocity measurements for relatively high and low $E_{s,F}$. 157
7.20 Correlation coefficient between upstream hot-wire anemometer velocity and spatially averaged velocity magnitude from PIV and transition location from P-POD. 158
7.21 Estimated mean surface pressure distributions at $\alpha = 5°$. Shaded areas denote uncertainty (95% confidence). Dotted lines: inviscid surface pressure distributions from XFOIL [192]. 160

7.22 Estimated conditional surface pressure distributions at $\alpha = 5°$. Dashed lines: conditional average of $\Theta_2 < \overline{\Theta_2} - S_{\Theta_2}$, dash-dotted lines: conditional average of $\Theta_2 > \overline{\Theta_2} + S_{\Theta_2}$, dotted lines: inviscid surface pressure distributions from XFOIL [192]. 161

7.23 Correlation between the temporal coefficient of the second mode Θ_2 and spatial entropy $E_{s,P}$ from F-POD. 162

A.1 Example of mean streamwise and wall-normal velocity fields, and corresponding uncertainty due to random displacement errors. 197

List of Tables

4.1 PIV measurement parameters 41

5.1 Reynolds number ranges for free-stream velocity ramp changes. 58
5.2 Ensemble sizes of transient lift force and PIV measurements. 59
5.3 PIV parameters. 61
5.4 Comparison of stall and reattachment durations from selected previous studies. 89

6.1 PIV parameters. 98

7.1 PIV measurement parameters 130
7.2 PIV fields of view and sampling times for time resolved measurements. . . 130
7.3 PIV fields of view and sampling times for non-time resolved measurements. 130
7.4 Free-stream turbulence conditions and active grid parameters. 132

A.1 Maximum uncertainties of measured and derived quantities at a confidence level of 95%. 200
A.1 Maximum uncertainties of measured and derived quantities at a confidence level of 95%. 201

List of Abbreviations

AC	Alternating Current
DSV	Dynamic Stall Vortex
FOV	Field Of View
FSTI	Free-Stream Turbulence Intensity
LSB	Laminar Separation Bubble
NACA	National Advisory Committee for Aeronautics
PIV	Particle Image Velocimetry
POD	Proper Orthogonal Decomposition
F-POD	Proper Orthogonal Decomposition of velocity Field
P-POD	Proper Orthogonal Decomposition of velocity Profile
RMS	Root Mean Square
TS	Tollmein Schlichting
TKE	Turbulent Kinetic Energy

List of Symbols

Accents and Subscripts

Example	Description
$\overline{a}$	time-averaged quantity
$\hat{a}$	Fourier transform of a
$\widetilde{a}$	Phase-average of a
a'	fluctuating quantity; $a - \overline{a}$
a^*	complex conjugate of a
$\dot{a}$	time derivative of a
$\mathbf{a}$	vector or tensor quantity
a_e	value of a at the boundary layer edge
a_i	imaginary part of a
a_r	real part of a
a_∞	mean value of a in the free-stream

Dimensionless Quantities

Symbol	Description	Definition
$\mathfrak{C}$	number of vector components	
C_cont	contraction coefficient	$\frac{2\Delta P}{\rho u_\infty^2}$
C_L	lift coefficient	$\frac{L}{\frac{1}{2}\rho u_\infty^2 cs}$
C_l	sectional lift coefficient	$\frac{l}{\frac{1}{2}\rho u_\infty^2 c}$
C_D	drag coefficient	$\frac{D}{\frac{1}{2}\rho u_\infty^2 cs}$
C_d	sectional drag coefficient	$\frac{d}{\frac{1}{2}\rho u_\infty^2 c}$
C_f	wall friction coefficient	$\rho\nu \left.\frac{\partial u}{\partial y}\right\vert_{y=0} \frac{2}{\rho u_e^2}$
C_p	pressure coefficient	$\frac{p-p_\infty}{\frac{1}{2}\rho u_\infty^2}$
C_sf	suction force coefficient	$-\frac{1}{c}\int C_p dx$
$\mathcal{D}$	convective time	$\frac{1}{c}\int_0^t u_\infty dt$

E_g	global entropy	
$E_\mathrm{s,F}$	spatial entropy of F-POD	
$E_\mathrm{s,P}$	spatial entropy of P-POD	
H	shape factor	δ^*/θ
I	intermittency factor	
K	number of segments of signal	
M	number of velocity measurement locations	
N	number of samples	
P_D	Diwan *et al.* [6] pressure gradient parameter	$\frac{h^2}{\nu}\frac{\Delta u_e}{\Delta x}$
P_G	Gaster [7] pressure gradient parameter	$\frac{\theta_\mathrm{s}^2}{\nu}\frac{\Delta u_e}{\Delta x}$
R_{aa}	autocorrelation coefficient of a	$\int_{-\infty}^{\infty}\frac{(a(t)-\overline{a})(a(t-\Delta t)-\overline{a})}{s_a^2}dt$
R_{ab}	cross-correlation coefficient of a and b	$\int_{-\infty}^{\infty}\frac{(a(t)-\overline{a})\left(b(t-\Delta t)-\overline{b}\right)}{s_a s_b}dt$
Re_a	Reynolds number; length scale a	$u_\infty a/\nu$
Tu	Turbulence intensity	$\frac{\sqrt{\frac{1}{3}\left(\overline{u'^2}+\overline{v'^2}+\overline{w'^2}\right)}}{u_\infty}$

Roman Symbols

Symbol	Description	Units
A	area	m^2
$\mathcal{A}$	disturbance amplitude	arbitrary units
c	chord	m
D	drag	N
f	frequency	Hz
f_s	sampling frequency	Hz
g	gravitational acceleration	$\mathrm{m\,s^{-1}}$
k	wavenumber	$\mathrm{rad\,m^{-1}}$
L	lift	N
$\mathcal{L}$	wavelength	m

$\mathcal{P}_{aa}$	power spectral density of a	(units of a)^{2}s^{-1}
p	pressure	Pa
$\mathbf{q}'$	$[\mathbf{u}', p']$	$[\mathrm{m\,s^{-1}}, \mathrm{Pa}]$
S_a	sample standard deviation	units of a
s	wing span	m
t	time	s
T	period	s
U_a	uncertainty of a	units of a
u	velocity vector	$\mathrm{m\,s^{-1}}$
u	wall-tangent/streamwise velocity component	$\mathrm{m\,s^{-1}}$
v	wall-normal velocity component	$\mathrm{m\,s^{-1}}$
w	spatial correlation weighting factor	$\mathrm{m^2\,s^{-2}}$
X	chordwise coordinate	m
x	wall-tangent/streamwise coordinate	m
x_{nl}	location of onset of non-linear disturbance growth	m
x_{s}	x location of separation	m
x_{t}	x location of transition	m
x_{r}	x location of reattachment	m
y	wall-normal coordinate	m
z	spanwise coordinate	m

Greek Symbols

Symbol	**Description**	**Units**
α	angle of attack	rad, unless specified in degrees
Δa	difference in quantity a	units of a
δ	boundary layer thickness	m

δ^*	displacement thickness $\int_0^\delta (1 - u/u_e)\, dy$	m
Γ	circulation	$\mathrm{m^2\,s^{-1}}$
γ	separation angle	rad
ζ	arc length	m
$\boldsymbol{\Theta}$	POD temporal coefficient matrix	-
Θ_i	POD temporal coefficient i	-
θ	momentum thickness $\int_0^\delta (u/u_\mathrm{e}\,(1 - u/u_\mathrm{e}))\, dy$	m
Λ_{ux}	streamwise integral length scale $\int_0^\infty R_{uu} dx$	m
$\boldsymbol{\lambda}$	POD eigenvalue matrix	$\mathrm{m\,s^{-1}}$
λ_i	eigenvalue i of snapshot matrix	$\mathrm{m\,s^{-1}}$
ν	kinematic viscosity	$\mathrm{m\,s^{-2}}$
ρ	density	$\mathrm{kg\,m^{-3}}$
ς	wavelet scale	s
τ_N	critical value of Student's t-distribution with N degrees of freedom	-
$\boldsymbol{\Phi}$	POD spatial mode matrix	-
$\boldsymbol{\Phi}_i$	POD spatial mode i	-
$\Phi_{i,u}$, $\Phi_{i,v}$, $\Phi_{i,w}$	u, v, w components of POD spatial mode i	-
φ	angular frequency	$\mathrm{rad\,s^{-1}}$
χ^2_N	critical value of the chi-squared probability distribution with N degrees of freedom	
Ψ_a	continuous wavelet transform of a	units of a
ψ	wavelet function	-
ω	vorticity	$\mathrm{s^{-1}}$

ω_z	spanwise vorticity	s^{-1}

Chapter 1

Introduction

The relevance of unsteady operating conditions to the aerodynamics of airfoils and wings at aerodynamically low Reynolds numbers is highlighted. Open questions are identified that guide the formulation of research objectives.

1.1 Motivation

The efficiency of a lifting surface, such as a wing or turbo-machinery blade, is fundamentally affected by the state of the boundary layers on its surfaces [8, 9]. Boundary layers may be broadly classified as laminar or turbulent [10]. The tendency of a fluid flow to assume a turbulent state is related to the Reynolds number, which quantifies the ratio of inertial forces to viscous forces. For lifting surfaces, the Reynolds number is usually expressed as $\mathrm{Re}_c = u_\infty c/\nu$, where u_∞ is the free-stream velocity, c is the chord length, and ν is the kinematic viscosity [11]. Usually, the higher the Reynolds number, the less stable the laminar flow state becomes, and the more likely a flow is to transition from laminar to turbulent states [10]. The range of chord Reynolds numbers common in everyday life span several orders of magnitude, from the laminar flow over insect wings at $\mathrm{Re}_c \sim 10^3$, to the almost entirely turbulent flow over commercial aircraft wings at $\mathrm{Re}_c \sim 10^8$ [8, 11]. In the range of aerodynamically low chord Reynolds numbers ($7 \times 10^4 \leq Re_c \leq 5 \times 10^5$), the spatial extent of both laminar and turbulent regions of the boundary layers may be comparable [8, 11]. This is the range in which small unmanned air vehicles [12], small wind turbines [13], and low pressure turbines of aircraft engines [14] operate.

Laminar boundary layers are prone to separation under an adverse pressure gradient, leading to a loss in lift and increase in drag, whereas turbulent boundary layers have a greater tendency to remain attached [10]. For this reason, the highest performance lifting surfaces, measured in terms of the lift to drag ratio, typically operate at very high chord Reynolds numbers ($\mathrm{Re}_c \geq 1.0 \times 10^7$) where the boundary layers are predominantly turbulent [8]. This regime has been studied extensively, due to its relevance to applications including commercial aircraft wings and utility scale wind turbines [11]. At lower Reynolds numbers ($5.0 \times 10^4 \leq Re_c \leq 5.0 \times 10^5$), boundary layer transition is delayed, and laminar flow often persists into the region of adverse pressure gradient [11]. As a consequence, laminar boundary layer separation is a common phenomenon at low Reynolds numbers [11]. However, transition to turbulence is accelerated in the separated laminar shear layer [15], and reattachment of a turbulent boundary layer is possible if the adverse pressure gradient is not too severe [7]. If the separated shear layer transitions to turbulence and reattaches to the lifting surface, a thin region of recirculating flow known as a laminar separation bubble (LSB) is formed [16]. The formation of an LSB substantially improves performance relative to the case of laminar separation without reattachment, but the drag is still higher than that of the fully attached flow condition possible at higher Reynolds numbers [8]. This reduction in lifting surface performance at low Reynolds numbers presents a challenge to the design of efficient lifting surfaces that operate at aerodynamically low chord Reynolds numbers.

The increase in lifting surface performance at low chord Reynolds numbers caused by boundary layer transition and reattachment has motivated numerous investigations of the transition dynamics in LSBs. However, most studies of boundary layer transition phenomena in low-Reynolds number flows have been undertaken on two-dimensional geometries in steady conditions, with uniform free-stream velocity magnitude and direction, [e.g., 15–25]. This leaves a significant gap between the current state of knowledge and applications, since

for virtually all practical applications of low-Reynolds number lifting surfaces, especially those that operate in the atmospheric boundary layer, unsteadiness prevails over a wide range of time and length scales [26, 27], and three-dimensional end effects are present. The type of high-intensity large-scale turbulence that is common in the atmosphere is a particularly relevant form of unsteadiness for unmanned air vehicles and small wind turbines [26, 28]. Although analytical theories of unsteady lift production have seen success at higher Reynolds numbers where the boundary layers remain attached, small regions of separation such as LSBs can render these theories inaccurate for use at low Reynolds numbers [26].

The types of unsteadiness that are most detrimental to the performance of lifting surfaces at low Reynolds numbers are those types of unsteadiness that delay or prevent reattachment of the separated shear layer. Such an expansion of an LSB, leading to a sudden loss of lift and increase in drag, is termed bubble bursting, and may be triggered by a change in free-stream velocity, angle of attack, or the amplitudes of environmental disturbances [7, 29]. Therefore, a detailed understanding of the influence of unsteady operating conditions on transition and reattachment in LSBs is required to predict the aerodynamic forces on low-Reynolds number lifting surfaces that operate in unsteady conditions.

Because of the performance penalty of bubble bursting, early studies of LSBs focused on describing and predicting the conditions necessary to trigger bursting [7, 30]. Subsequent developments in experimental and numerical capabilities have elucidated the instability mechanisms and coherent structures that characterise the transition process in LSBs and lead to flow reattachment [e.g., 6, 18, 24, 31]. In an effort to mitigate the adverse effects of laminar boundary layer separation at low chord Reynolds numbers, active and passive flow control methods for increasing the extent of attached boundary layers have also been investigated [32–38].

However, previous efforts towards understanding, predicting, and controlling the flows over lifting surfaces at low chord Reynolds numbers have occurred primarily in the context of quasi-steady, two-dimensional, statistically stationary flows. The dynamics of the transition process during LSB formation and bursting transients remain largely unexplored. Considering this knowledge gap, the following research questions have been formulated to guide this thesis:

1. How does aerodynamic loading, LSB structure, and transition dynamics evolve during a transient change in free-stream velocity magnitude or direction?

2. How does the type of change in free-stream velocity magnitude or direction affect the transient loading and LSB development?

3. How do three-dimensional end effects affect aerodynamic loads and LSB development during a transient change in free-stream velocity magnitude or direction?

This thesis aims to address these open questions through an experimental investigation of the transient flow development of LSBs on two- and three-dimensional lifting surface geometries in unsteady operating conditions. This work is focused on those changes in operating conditions that lead to LSB formation and bursting, because such changes are expected to produce the most severe changes in aerodynamic loads in practice.

1.2 Objectives

Motivated by the identified knowledge gap between steady, two-dimensional flows in the LSB literature and the unsteady, three-dimensional flows relevant to low-Reynolds number devices, the following research objectives are established for this thesis:

1. Characterise LSB structure and shear layer transition dynamics during LSB formation and bursting transients on a lifting surface during a change in free-stream velocity magnitude or angle of attack.

2. Quantify the influence of three-dimensional end effects on the aerodynamic forces produced during LSB formation and bursting, and relate these forces to the LSB flow field development.

3. Quantify the influence of the time and length scale of an imposed change in operating conditions on boundary layer transition dynamics.

4. Correlate oncoming free-stream disturbances in turbulent free-stream environments to variations in boundary layer development and the resulting aerodynamic forces.

The foregoing research objectives guide an incremental approach towards the overall goal of relating the forces produced by low-Reynolds number lifting surfaces to the flow field development in unsteady conditions. Objective 1 was achieved through experiments performed on airfoil and wing models subjected to an isolated large-scale change in free-stream velocity magnitude in Chapters 4 and 5, and subjected to isolated ramp changes in angle of attack in Chapter 6. Objective 2 was achieved through a comparison of the flow development over a two-dimensional airfoil and finite wing in Chapters 5 and 6. Objective 3 was achieved through varying the speed of the angle of attack change in Chapter 6, and through subjecting an airfoil model to large scale turbulence that contained a wide range of time and length scales in Chapter 7. Objective 4 was achieved through simultaneous measurements of the boundary layer development and oncoming flow velocity in large-scale high-intensity free-stream turbulence in Chapter 7.

Chapter 2

Background

A review of the literature pertaining to unsteady aerodynamics and boundary layer transition is presented, with a focus on flows at aerodynamically low Reynolds numbers.

2.1 Conservation Laws and Kinematics of Fluid Flow

The conservation of momentum and mass in a continuous incompressible Newtonian fluid is governed by the Navier-Stokes and continuity equations [39]:

$$\frac{\partial \mathbf{u}}{\partial t} + \mathbf{u} \cdot \boldsymbol{\nabla} \mathbf{u} = -\frac{1}{\rho} \boldsymbol{\nabla} p + \nu \boldsymbol{\nabla}^2 \mathbf{u} + \mathbf{g} \tag{2.1}$$

$$\boldsymbol{\nabla} \cdot \mathbf{u} = 0 \tag{2.2}$$

where $\mathbf{u}$ is the fluid velocity, p is the pressure, ρ is the fluid density, ν is the kinematic viscosity, and $\mathbf{g}$ is the gravitational acceleration. As an alternative to the velocity field, the motion of a fluid may also be described by its vorticity field. Vorticity ($\boldsymbol{\omega}$) is defined as the curl of the velocity:

$$\boldsymbol{\omega} = \boldsymbol{\nabla} \times \mathbf{u} \tag{2.3}$$

Vorticity quantifies the rate of rotation of an infinitesimal fluid element at a given location [39]. The vorticity field is often used to describe flows that contain vortices and other rotational motions, such as those that develop in engineering applications. Vortices are regions of a fluid with non-zero vorticity and circular rotation. Although vortices are intuitive to identify, there is no precise mathematical definition of a vortex [40], because shearing but non-rotating regions of a flow also posses non-zero vorticity [39].

Vortex lines are integral curves that are everywhere parallel to the vorticity field [41]. Inviscid flows containing simple arrangements of fixed vortex lines are relatively simple to describe mathematically [e.g., 39]. In flows around streamlined bodies, the regions of the flow where viscous stresses lead to the production and dissipation of vorticity are relatively localised. This enables the flows around streamlined bodies to be approximated as inviscid flows containing an analytically tractable arrangement of vortex lines. Consequently, the foundations of aerodynamic theory were historically formulated in terms of vorticity and vortices [41].

2.2 Aerodynamics of Lifting Surfaces

A lifting surface is a device designed to generate a component of force in the direction perpendicular to the velocity of an oncoming fluid flow [42]. This component of force is called lift (L), whereas the component of force generated parallel to the velocity of the oncoming flow is called drag (D) [43]. In practical applications, it is usually desired to maximise the ratio L/D [e.g., 44]. The wings and stabilisers of aircraft [42], sails of watercraft [45], and blades of turbo-machines [46], are all examples of lifting surfaces.

The two-dimensional shape of the cross-section of a lifting surface in a plane parallel to the velocity of the oncoming fluid is called an airfoil [43]. Because airfoils are two-dimensional shapes, their performance is quantified in terms of the sectional lift (l) and sectional drag (d) (i.e. lift and drag forces per unit span). Airfoils are often designed with a streamlined, tear-drop-like shape to minimize sectional drag [8], as illustrated in Fig. 2.1.

The optimal shape of an airfoil depends on its operating conditions [8]. An important geometric parameter of an airfoil is its chord length (c), defined as the line connecting the leading and trailing edges [43]. The angle between the chord line and the free-stream velocity vector ($\mathbf{u}_\infty$) is called the angle of attack (α) [43]. When positioned at an angle of attack to the free-stream, the pressure on the leeward surface of the airfoil is reduced, thus the leeward surface is also known as the suction surface [41]. Conversely, the windward surface experiences an increase in pressure near the forward stagnation point. Thus, the windward surface is also known as the pressure surface [41]. The lift and drag forces acting on a lifting surface are usually presented using the lift (C_L) and drag (C_D) coefficients, respectively [43]:

$$C_L = \frac{L}{\frac{1}{2}\rho u_\infty^2 cs} \tag{2.4}$$

$$C_D = \frac{D}{\frac{1}{2}\rho u_\infty^2 cs} \tag{2.5}$$

where s is the span. When an airfoil moves through a fluid, the lift per unit span produced by the airfoil depends on the circulation around the airfoil (Γ) as expressed by the Kutta-Joukowski theorem [43]:

$$\frac{L}{s} = \rho u_\infty \Gamma \tag{2.6}$$

where ρ is the density of the fluid and Γ is the line integral of the velocity ($\mathbf{u}$) over a closed contour containing the airfoil:

$$\Gamma = \oint \mathbf{u} \cdot d\boldsymbol{\xi} \tag{2.7}$$

In this thesis, ρ is assumed to be constant. This assumption is justified when the speed of the fluid flow is much less than the speed of sound in the fluid [43]. Such is the case for small aircraft flying at relatively low speeds in Earth's atmosphere [12].

Real lifting surfaces always have a finite span. This introduces end effects that render the real flow different from that developing around a two-dimensional airfoil of infinite span. End effects occur due to the presence of end-walls or free tips [47]. A lifting surface of finite

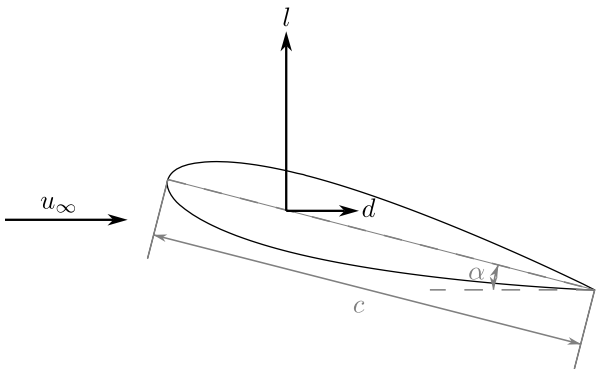


Figure 2.1: Sectional forces acting on an airfoil.

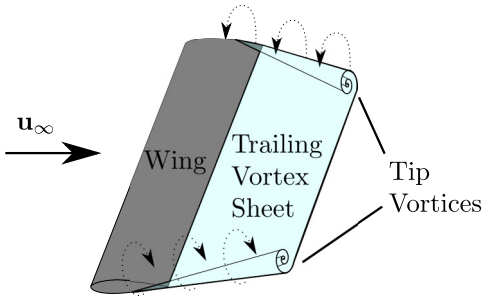


Figure 2.2: Wing-tip vortex formation in the wake of a finite wing. Adapted from [49]

span is called a wing [48]. The requirement for continuity of the velocity and pressure fields around a wing leads to a reduction in sectional lift near a wing-tip relative to the sectional lift of an airfoil at the same geometric angle of attack [42]. This means that the circulation around a wing is not constant with respect to spanwise position. Continuity of the velocity field requires that the spanwise change in circulation be accompanied by the shedding of streamwise vorticity continuously along the span, producing a trailing vortex sheet [42], as illustrated in Fig. 2.2. Roll-up of the trailing vortex sheet in the wing's wake leads to the formation of wing-tip vortices [43]. The trailing vortex sheet and the wing-tip vortices induce a downwash velocity that reduces the effective angle of attack of the wing relative to an airfoil at the same geometric angle of attack [42].

Whereas lift production can be described using inviscid flow theory, drag is a consequence of viscous forces [50]. In continuous viscous flows such as those commonly encountered in air or water at standard temperatures and pressures, the no-slip condition requires that the fluid velocity at a solid boundary be equal to the velocity of the solid boundary [39]. The resulting velocity gradient between the surface of a moving lifting surface and the outer free-stream flow leads to the development of shear forces that contribute primarily to drag.

When the Reynolds number is large ($\mathrm{Re}_c \to \infty$), viscous shearing forces are confined to a thin region of fluid near the surface, called a boundary layer [10]. Under the assumption of large Reynolds number, the Navier-Stokes equation (Eq. 2.1) within a two-dimensional boundary layer may be simplified to [10]:

$$\frac{\partial u}{\partial t} + u\frac{\partial u}{\partial x} + v\frac{\partial u}{\partial y} = -\frac{1}{\rho}\frac{\partial p}{\partial x} + \nu\frac{\partial^2 u}{\partial y^2} \tag{2.8}$$

$$\frac{\partial p}{\partial y} = 0 \tag{2.9}$$

where x is the coordinate tangent to the surface, y is the coordinate normal to the surface, u is the velocity component tangent to the surface, and v is the velocity component normal to the surface. A consequence of Eq. 2.9 is that the pressure within the boundary layer is determined only by the flow outside of the boundary layer. At the solid surface, application of the no-slip condition to Eq. 2.8 leads to a relationship between the streamwise pressure

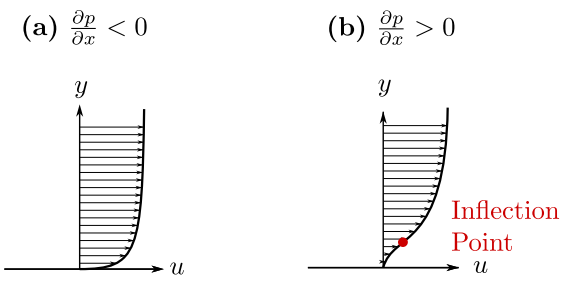


Figure 2.3: Effect of pressure gradient on curvature of streamwise velocity profile.

gradient and the second derivative of the streamwise velocity [10]:

$$\frac{\partial p}{\partial x} = \rho\nu \left.\frac{\partial^2 u}{\partial y^2}\right|_{y=0} \tag{2.10}$$

Thus, the curvature of the streamwise velocity profile at the surface depends on the streamwise pressure gradient. In a favourable pressure gradient ($\partial p/\partial x < 0$) the curvature of the streamwise velocity profile is negative everywhere, since u must smoothly match the velocity of the external flow [10] (Fig. 2.3a). In an adverse pressure gradient, the requirement for $\partial^2 u/\partial y^2 > 0$ at the surface and $\partial^2 u/\partial y^2 < 0$ at the boundary layer edge results in an inflection point in the streamwise velocity profile (Fig. 2.3b) [10]. The presence of the inflection point has important consequences for the stability of the boundary layer that will be reviewed in Section 2.3.

A boundary layer subject to an adverse pressure gradient may eventually reach a point where the curvature of the streamwise velocity profile at the surface is sufficiently positive such that the velocity gradient at the surface vanishes [50]. That is:

$$\left.\frac{\partial u}{\partial y}\right|_{y=0} = 0 \tag{2.11}$$

In a two-dimensional flow, such a point is called a separation point, because this point lies on a streamline that breaks away from the surface [50] (Fig. 2.4). It follows from Eq. 2.10 that a separation point can only occur in a region of adverse pressure gradient. The simplifying assumptions used to obtain the boundary layer equations are no longer valid downstream of the separation point, because the region of flow where viscous effects are substantial is no longer thin, and the wall-normal velocity component is comparable in magnitude to the streamwise velocity component [10].

Boundary layer separation from an immersed body such as a lifting surface causes a severe drag penalty [11]. This is because the separated flow alters the trajectory of the flow outside of the boundary layer, reducing the pressure rise on the leeward side of the body below that necessary to offset the pressure increase on the windward side [10] (Fig. 2.5). Because large regions of separated flow substantially alter the flow outside of the boundary layer, massive separation also leads to a loss of lift [50].

The circulation around an airfoil and the adverse pressure gradient on the suction

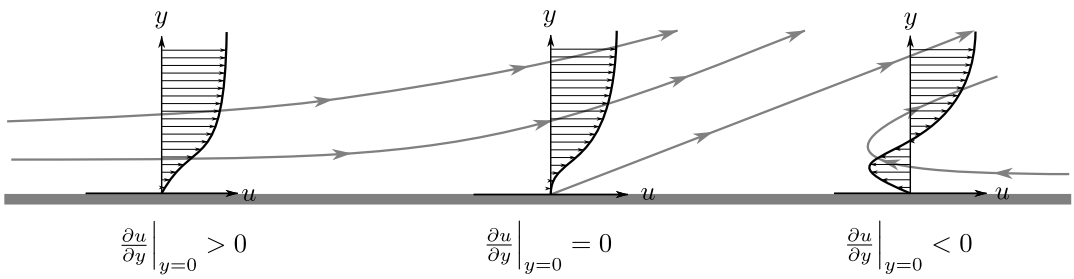


Figure 2.4: Streamlines and streamwise velocity profiles in the vicinity of boundary layer separation.

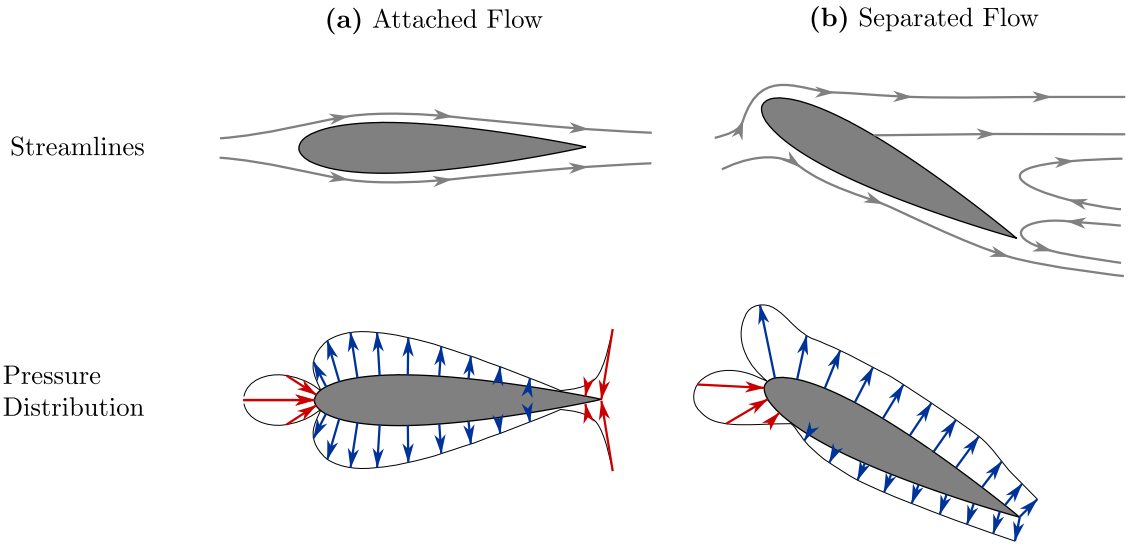


Figure 2.5: Boundary layer separation from an airfoil and its effect on the pressure distribution. Attached flow at a low angle of attack (a), separated flow at a high angle of attack (b). Red arrows: $p > p_\infty$, blue arrows: $p < p_\infty$.

surface become stronger as the angle of attack is increased up to the stall angle [43]. When the angle of attack is increased beyond the stall angle, the adverse pressure gradient on the suction surface is sufficient to cause massive separation, leading to a loss of lift and increase in drag [43, 51]. For this reason, lifting surfaces are usually designed to operate at angles of attack below the stall angle. However, unsteady environmental conditions may lead to excursions in angle of attack beyond the stall angle [26].

2.2.1 Unsteady Aerodynamics of Lifting Surfaces

The effects of unsteady operating conditions on lifting surfaces can be grouped into two categories: time-lag effects resulting from the finite convection speeds of boundary layer and wake structures, and boundary layer improvement effects resulting from changes in the fluid velocity at the boundary layer edge and changes in the airfoil surface velocity [52].

One type of time lag effect is circulation lag [52]. Kelvin's circulation theorem requires

that any change in the circulation around an airfoil be accompanied by the shedding of a vortex with equal circulation and opposite sign into the wake. Since the shed vortex is of opposite sign to the change in circulation around the airfoil, the induced velocity field of the shed vortex reduces the rate of change of effective angle of attack experienced by the airfoil [53]. For example, an airfoil undergoing an increase in angle of attack sheds a vortex from its trailing edge that induces a decrease in effective angle of attack. Von Kármán & Sears [54] derived analytical expressions for the influence of circulation lag on the lift produced by an airfoil using inviscid thin airfoil theory.

Another type of time-lag effect is boundary layer convection lag, which has the greatest influence on airfoil performance when turbulent separation occurs near the trailing edge [52]. Boundary layer convection lag is a consequence of the finite convection speed of pressure fluctuations in a turbulent boundary layer, which leads to a time delay between changes in angle of attack and changes in local turbulent boundary layer development [52].

Boundary layer improvement effects are those effects that reduce the susceptibility of a boundary layer to separation during increases in effective angle of attack or free-stream velocity. In this category of unsteady effects, Ericsson & Reding [52] place accelerated flow effects and moving wall effects. Conversely, these effects promote boundary layer separation during decreases in effective angle of attack or free-stream velocity.

The accelerated flow effect is a result of unsteady changes to the boundary layer edge velocity, which affect the streamwise pressure gradient [52]. Applying the unsteady Bernoulli equation to the potential flow at the edge of the boundary layer [52], the following equation is obtained:

$$\frac{\partial u_e}{\partial t} + u_e \frac{\partial u_e}{\partial x} = -\frac{1}{\rho}\frac{\partial p}{\partial x} \tag{2.12}$$

where u_e is the velocity at the edge of the boundary layer. Noting that the streamwise pressure gradient in a steady flow is equal to $-\rho u_e \frac{\partial u_e}{\partial x}$, Eq. 2.12 can be rewritten as:

$$\frac{dp}{dx} = \left(\frac{\partial p}{\partial x}\right)_{steady} - \rho \frac{\partial u_e}{\partial t} \tag{2.13}$$

Therefore, the difference in streamwise surface pressure gradient between steady and unsteady flows is proportional to the time rate of change of the boundary layer edge velocity. The boundary layer edge velocity is proportional to the free-stream velocity, and the boundary layer edge velocity on the suction surface increases with angle of attack. This means that on an airfoil experiencing an increase in angle of attack or free-stream velocity, the adverse pressure gradient downstream of the suction peak is reduced relative to the pressure gradient on the same airfoil at an equivalent angle of attack in steady conditions. Conversely, a reduction in angle of attack or free-stream velocity causes a stronger adverse pressure gradient downstream of the suction peak relative to the pressure gradient in steady conditions.

Another boundary layer improvement effect is the moving-wall effect [52]. The moving wall effect can be explained by considering an airfoil undergoing a rotation about a point along its chord. During such a motion, the surface of the airfoil has a component of velocity

that is tangential to the boundary layer flow, which leads to a reduction in boundary layer thickness on the suction surface when the angle of attack is increasing, and an increase in boundary layer thickness on the suction surface when the angle of attack is decreasing.

Because time-lag and boundary layer improvement effects influence the possibility of boundary layer separation, unsteadiness can substantially affect the loading on lifting surfaces. The loads in unsteady conditions may exceed those possible in quasi-steady conditions [1] [52, 55]. Due to its relevance to rotorcraft, the case of an airfoil undergoing harmonic oscillations in angle of attack beyond the static stall angle has received much attention [e.g., 55–58]. With this type of motion, time-lag and boundary layer improvement effects enable the suction surface boundary layer to remain attached at angles of attack exceeding the static stall angle, causing an overshoot of the lift force [52]. However, the increasingly adverse pressure gradient during the upward pitching motion eventually leads to separation of the suction surface boundary layer, triggering a process called dynamic stall [55]. The onset of dynamic stall is delayed to higher angles of attack at faster pitch rates [59]. In the wake mode of dynamic stall, the separated shear layer rolls-up into a dynamic stall vortex (DSV) that grows locally until being shed downstream [57]. In the shear layer mode of dynamic stall, multiple vortices form from the convective growth of disturbances in the separated shear layer [57]. The vortices produced by the separated shear layer reduce the pressure on the suction surface, contributing to the lift force overshoot [55]. The time delay between passing of the static stall angle and roll-up of the separated shear layer is on the order of $10c/u_\infty$ [57]. When the vortices formed from the leading edge shear layer are shed downstream, the lift decreases rapidly as the vortices convect past the trailing edge [55]. The phenomenon of vortex shedding from the leading edge shear layer observed during harmonic pitching is similar to that observed during other types of airfoil motions that lead to dynamic stall, such as harmonic plunging [60] and ramp changes in angle of attack [61–63].

Analogous to the overshoot in lift that occurs during dynamic stall, an undershoot in lift occurs during dynamic recovery from stall due to the delay of reattachment below the static stall angle [57, 64, 65]. Dynamic reattachment occurs first near the leading edge and propagates towards the trailing edge [64]. The speed of the downstream movement of the separation location is on the order of $0.1u_\infty$, and increases as the pitch rate becomes more negative [64]. The delay in boundary layer separation and reattachment relative to quasi-steady conditions during dynamic stall and reattachment, respectively, causes hysteresis of the aerodynamic loading with respect to angle of attack in unsteady conditions [55].

[1] In this work, a system is said to undergo a quasi-steady change in a given parameter when the system would remain in a statistically stationary state if the change in said parameter was stopped at any time during the change.

2.3 Boundary Layer Transition at Aerodynamically Low Reynolds Numbers

The shear forces exerted by a boundary layer, as well as the possibility for boundary layer separation, are strongly dependent on whether the boundary layer is laminar or turbulent [10]. The boundary layers forming on lifting surfaces in low-disturbance environments are laminar near the leading edge [66], but typically transition to turbulence if the chord Reynolds number is of order 10^4 or greater [11]. The transition process begins in the laminar boundary layer with the receptivity process, whereby perturbations in the environment, such as free-stream turbulence, acoustic waves, or surface roughness, produce wave-like disturbances within the boundary layer [67]. The resulting boundary layer disturbances then undergo decay or growth, depending on the stability characteristics of the boundary layer. The stability of a flow may be categorised as either convective or absolute [10]. In a convectively unstable flow, a disturbance introduced at a given location will grow as it convects away from its source, i.e., the amplitude of the disturbance increases in a reference frame moving with the disturbance, but the amplitude measured at its initial location in a fixed frame will not increase. In an absolutely unstable flow, a disturbance introduced at a fixed location will increase in amplitude in a reference frame fixed at that location. The nature of the instability of attached boundary layers is that of convective instability [10].

The stability of a boundary layer depends on the local Reynolds number, often expressed as the displacement thickness Reynolds number ($\mathrm{Re}_{\delta^*} = u_e\delta^*/\nu$, where $\delta^* = \int_0^\delta (1 - u/u_e))dy$ is the boundary layer displacement thickness and δ is the boundary layer thickness.). There is a certain value of Re_{δ^*} called the indifference Reynolds number, below which all disturbances decay, and above which disturbances within a certain frequency range are amplified [10].

The unstable wave-like disturbances that precede boundary layer transition in attached boundary layers in low disturbance environments are called Tollmien-Schlichting (TS) waves [10]. A schematic illustration of attached boundary layer transition is presented in Fig. 2.6a. Initially, small-amplitude TS waves undergo exponential amplitude growth that can be well-modelled using linear stability theory [66]. Once the amplitudes of the TS waves are on the order of 1% of the free-stream velocity, non-linear three-dimensional effects begin to significantly deform the initially two-dimensional TS waves, reorienting vorticity into the streamwise direction [68]. This leads to the formation of hairpin-shaped Λ-vortices, which break-down into turbulent spots [68]. The transition to turbulence in the boundary layer is completed by the streamwise and spanwise growth of the turbulent spots as they convect downstream [10]. This transition scenario is typical of unswept lifting surfaces at relatively high chord Reynolds numbers, where the indifference Reynolds number is reached and transition is completed upstream of the adverse pressure gradient on the aft portion of the lifting surface [69].

At low chord Reynolds numbers, TS waves may not attain sufficient amplitudes to trigger transition before reaching the region of adverse pressure gradient on a lifting surface. The laminar boundary layer that persists into the region of adverse pressure gradient is

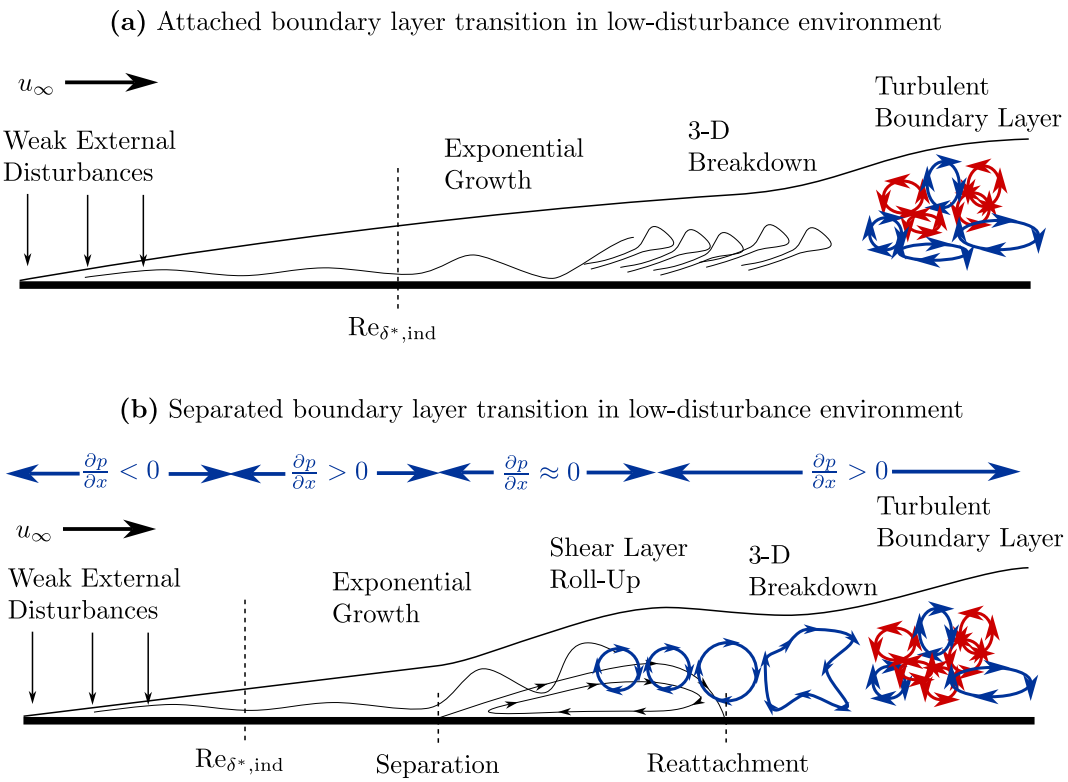


Figure 2.6: Qualitative schematic of attached (a), and separated (b) boundary layer transition in a low-disturbance environment, after [66] and [20].

prone to separation due to its low rate of wall-normal momentum transfer relative to a turbulent boundary layer [10]. Transition in the case of a separating laminar boundary layer is illustrated schematically in Fig. 2.6b.

Even when laminar boundary layer separation occurs prior to transition, exponential growth of boundary layer disturbances may begin in the attached laminar boundary layer if the Reynolds number is sufficiently high [15]. In the region of adverse pressure gradient, an inflection point develops in the velocity profile (cf. Section 2.2). The presence of an inflection point substantially increases the growth rates of boundary layer disturbances through the Kelvin-Helmholtz instability mechanism [70], which leads to a rapid increase in the amplitudes of disturbances in the separated shear layer. When the shear layer disturbances reach sufficiently high amplitude, non-linear effects cause the shear layer to roll-up into spanwise vortices [e.g., 71] (Fig. 2.6). When the free-stream turbulence is relatively low, the roll-up vortices are highly coherent in the spanwise direction [71, 72]. If the adverse pressure gradient is not too severe, the increased wall-normal momentum transfer induced by the roll-up vortices may cause the shear layer to reattach in a time-average sense [16]. However, the flow near the reattachment point is highly unsteady due to the periodic shedding of the shear layer roll-up vortices [20]. The relatively thin region of recirculating flow between the separated shear layer and the lifting surface is called a laminar separation bubble (LSB) [16]. Three-dimensional deformations of the roll-up vortices eventually lead

to a fully turbulent boundary layer downstream of the LSB [73]. The vortex deformations may be caused by the superposition of waves with non-zero spanwise wavenumber [18], or by global [24] or secondary [21] instabilities.

Due to the coupling between boundary layer separation and the outer flow development, the streamwise pressure gradient along the separated shear layer is substantially reduced upstream of the location of maximum LSB height, and the flow in the forward part of the LSB, termed the dead-air region, is nearly stagnant [20]. In the aft part of the LSB, the roll-up vortices produce substantially stronger reverse flow, and a rapid streamwise pressure increase occurs [20].

The size, location, and transition dynamics of an LSB on a lifting surface depend on the angle of attack, chord Reynolds number, and the disturbance environment [72, 74]. Increasing the angle of attack reduces the pressure near the leading edge on the suction surface, producing a stronger adverse pressure gradient downstream of the location of minimum pressure. Because a stronger adverse pressure gradient leads to earlier separation, a suction surface LSB moves upstream if the angle of attack is increased in a quasi-steady manner [74]. Because of the the higher boundary layer edge velocity near the leading edge, the vortex shedding frequency of the LSB also increases with angle of attack [74]. Increasing the chord Reynolds number causes higher disturbance growth rates in the boundary layer and separated shear layer, leading to earlier transition. Thus, the transition and reattachment locations move upstream and the LSB shortens and thins when subject to a quasi-steady increase in Reynolds number [74]. The length and thickness of an LSB is also reduced because of accelerated transition when the initial amplitudes of disturbances in the boundary layer are increased. The initial disturbance amplitudes may increase due to elevated free-stream turbulence [72], for example. Thinning of the LSB due to an increase in Reynolds number or free-stream turbulence also increases the boundary layer edge velocity, which increases the shear-layer vortex shedding frequency [72, 75].

The effect of an LSB on the global pressure distribution may be used to classify an LSB as short or long. Short LSBs cause relatively limited local changes in the pressure distribution on a lifting surface relative to fully attached flow, whereas long LSBs cause a substantial loss of leading edge suction, leading to a relatively large decrease in lift and increase in drag [16]. In a process called bursting, a short LSB may become a long one, or reattachment may cease entirely [7]. Bursting can occur due to a sufficient reduction in chord Reynolds number, increase in angle of attack, or reduction in the amplitudes of external disturbances that the boundary layer is receptive to [7, 29]. All three of these types of changes in operating conditions inhibit the ability of the separated shear layer to reattach, causing the lifting surface to stall [16]. Due to the sensitivity of the transition process to these factors, relatively small changes in operating conditions may lead to large changes in aerodynamic loads [7, 76].

Bursting of an LSB is also accompanied by notable changes in the stability characteristics of the separated shear layer. The reduction in boundary layer edge velocity associated with bursting typically leads to a decrease in the velocity gradient across the separated shear layer, which decreases disturbance growth rates and the most amplified frequency [19, 77]. However, this increase in stability is moderated by the increased distance between the

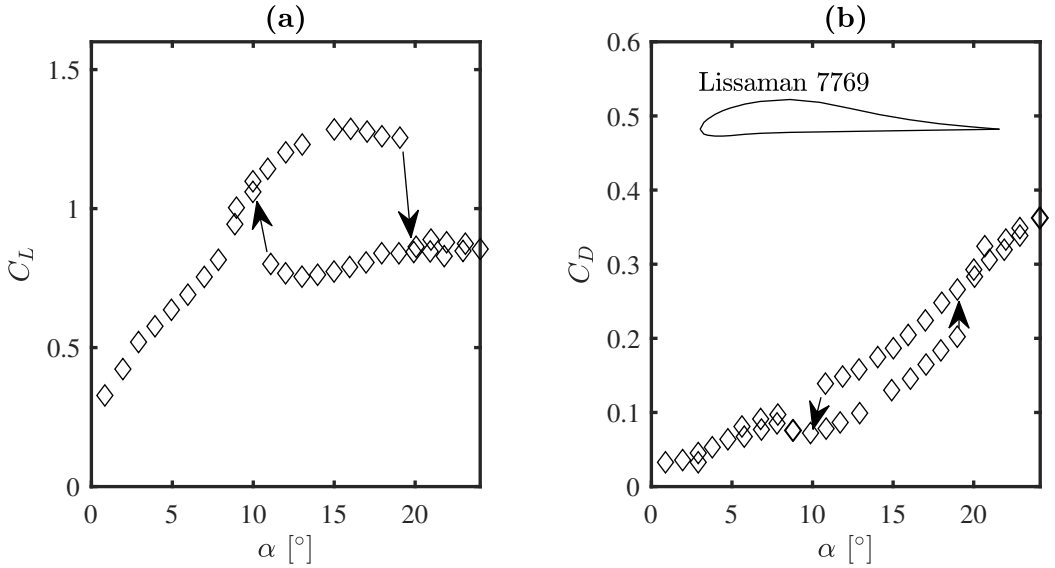


Figure 2.7: Sectional lift (a), and drag (b) coefficients versus angle of attack for the Lissaman 7769 airfoil at $\mathrm{Re}_c = 1.5 \times 10^5$ from [79]. Arrows indicate the direction of hysteresis loops.

separated shear layer and the wall, which has a destabilising effect [17]. The characteristics of coherent structures formed in the transition process are also affected by bursting. In numerical simulaions, Marxen & Henningson [29] found that bursting was associated with a reduction in the spanwise coherence of the shear layer roll-up vortices. Furthermore, they reported that the relatively smaller vortical structures formed in the transition process in long LSBs were less spanwise coherent than those in short LSBs. This implies that the relatively large and two-dimensional spanwise roll-up vortices formed in short LSBs are more effective for transferring momentum across the shear layer than the smaller three-dimensional structures present in long LSBs and massively separated flows. Furthermore, the rate of turbulent kinetic energy production is greater in short LSBs than in long LSBs [78].

The difference in stability characteristics and transition dynamics between massively separated and reattaching boundary layers often leads to hysteresis in the stall angle of a lifting surface at low chord Reynolds numbers [79]. An example of stall hysteresis typical of airfoils that have suction surface LSBs at low angles of attack is provided in Fig. 2.7 for the Lissaman 7769 airfoil at $\mathrm{Re}_c = 1.5 \times 10^5$ from measurements performed by Mueller [79]. The stall angle for this airfoil during an increase in angle of attack is approximately 19°, at which there is a relatively sudden loss of lift and increase in drag due to a failure of the separated shear layer to reattach. However, due to the reduction in disturbance growth rates that occurs after stall, reattachment of the separated shear layer during a decrease in angle of attack does not occur until approximately 10°, as evidenced by the lift recovery and drag reduction that occur at this angle.

Due to the severe effect of bursting on the performance of lifting surfaces, several authors have proposed criteria for determining whether a short or long LSB will form under a given

set of operating conditions. Gaster [7] developed a two-parameter bursting criterion involving the momentum thickness Reynolds number at the separation point ($\mathrm{Re}_{\theta_\mathrm{s}} = \theta_\mathrm{s} u_{\mathrm{e,s}}/\nu$), and a non-dimensional pressure gradient parameter ($P_\mathrm{G} = (\theta_\mathrm{s}^2/\nu)\,(\Delta u_e/\Delta x)$, where $\Delta u_e/\Delta x$ is the mean edge velocity gradient over the length of the LSB in a hypothetical fully attached flow). The momentum thickness is defined as $\int_0^\delta (u/u_\mathrm{e}\,(1-u/u_\mathrm{e}))\,dy$. The two parameters used in the bursting criterion developed by Gaster [7] have a straightforward physical interpretation. Since the Reynolds number is related to the tendency of a flow to become turbulent [80], higher $\mathrm{Re}_{\theta_\mathrm{s}}$ is indicative of greater instability and more rapid transition to turbulence. The pressure gradient parameter P_G is analogous to the non-dimensional pressure gradient parameter $(\theta^2/\nu)\,(\partial u_e/\partial x)$ used by Thwaites [81] to predict the separation of laminar boundary layers. Thwaites' pressure gradient parameter and the momentum thickness Reynolds number are related through the momentum-integral equation. The momentum-integral equation may be obtained by integrating Eq. 2.8 across the boundary layer [10], and can be written in terms of Re_θ and $(\theta^2/\nu)\,(\partial u_e/\partial x)$:

$$\frac{\theta^2}{\nu}\frac{\partial u_e}{\partial x} = \mathrm{Re}_\theta \frac{C_\mathrm{f} - \frac{1}{2}\frac{\partial \theta}{\partial x}}{4+2H} \tag{2.14}$$

where C_f is the skin friction coefficient and $H = \theta/\delta^*$ is the shape factor. Thus, the strength of the adverse pressure gradient that an attached laminar boundary layer is capable of overcoming is proportional to the momentum thickness Reynolds number. The definitions of $\mathrm{Re}_{\theta_\mathrm{s}}$ and P_G used by Gaster [7] facilitate an analogous description of the flow development in LSBs. The two parameters in the bursting criterion of Gaster [7] involve the momentum thickness at the separation point because this quantity does not change substantially downstream of separation in the laminar flow up to the location of transition [30].

During a quasi-steady reduction in free-stream velocity for a short LSB approaching bursting, both $\mathrm{Re}_{\theta_\mathrm{s}}$ and P_G vary with the free-stream velocity [7]. Gaster [7] used experimental measurements of an LSB forming on a flat plate to determine the strength of the adverse pressure gradient required for bursting as a function of $\mathrm{Re}_{\theta_\mathrm{s}}$. However, the criterion of Gaster [7] is not universal because it predicts that long LSBs should form in some cases where short LSBs have been reported [6, 82].

Other researchers have attempted to develop LSB bursting criteria that overcome deficiencies in the method of Gaster [7]. Horton [30] developed a semi-empirical bursting criterion using the momentum and energy conservation equations to estimate the pressure rise that a transitioning shear layer would be capable of overcoming for a given $\mathrm{Re}_{\theta_\mathrm{s}}$. Later, Diwan *et al.* [6] developed a single parameter bursting criterion using a reformulation of the non-dimensional pressure gradient as $P_D = (h^2/\nu)\,(\Delta u_e/\Delta x)$, where h is the maximum height of the separation streamline and the velocity gradient is the actual mean edge velocity gradient over the length of the LSB. The threshold for bursting is $P_D \leq -28$ [6]. Although formulated from data taken in steady conditions, this single parameter criterion was demonstrated to give a reasonable prediction of bursting for an airfoil undergoing a dynamic change in angle of attack [83].

2.3.1 Transition in Unsteady Operating Conditions

Unsteady variations in operating conditions can cause changes in LSB structure directly through modulation of the streamwise pressure gradient, or indirectly through the instability mechanisms that lead to transition. The former are typically caused by variations in the oncoming flow with characteristic length scales much larger than the chord, such as spatially coherent gusts [e.g., 84, 85]. The latter are typically caused by variations in the oncoming flow with characteristic length scales on the order of the boundary layer thickness, such as those occurring in free-stream turbulence [86].

Spatially coherent changes in the oncoming flow impose unsteady changes in angle of attack or free-stream velocity. Unsteady increases in angle of attack or free-stream velocity cause delayed separation and transition relative to quasi-steady increases due to the reduction in adverse pressure gradient required for temporal acceleration of the flow [84, 85, 87, 88]. This is the accelerated flow effect described by Eq. 2.13. Conversely, expedited separation and transition relative to quasi-steady decreases in angle of attack or free-stream velocity occur during unsteady decreases due to the increase in adverse pressure gradient required for temporal deceleration of the flow [84, 85, 87, 88]. Since reattachment is a consequence of transition in the separated shear layer, the relationship between the reattachment location and unsteady changes in angle of attack and free-stream velocity is similar to that of the transition location [85, 88].

Variations in free-stream velocity magnitude of sufficient amplitude can lead to complete elimination of separation or bursting of an LSB. In the direct numerical simulation of Wissink & Rodi [89] of an LSB on a flat plate with periodic variations in free-stream velocity of 20% of the mean free-stream velocity, the entire LSB was eliminated when the free-stream velocity was increasing due to the delay in separation caused by the more favourable pressure gradient. In the experiments of Greenblatt *et al.* [85], the flow over a NACA0018 airfoil at an angle of attack of $\alpha = 0°$ was studied during periodic variations in free-stream velocity of 50% of the mean free-stream velocity. The more favourable pressure gradient during the increase in free-stream velocity lead to LSB bursting because of a delay in transition and reattachment. The different responses of the LSBs to high-amplitude free-stream accelerations in the studies of [89] and [85] are likely due to the different flow geometries employed.

A change of angle of attack can also precipitate LSB formation or bursting. The LSB bursting process on a NACA0012 airfoil undergoing a pitch-up manoeuvre from an initial angle of attack of $\alpha = 10.55°$ to a final angle of attack of $\alpha = 10.8°$ was studied in large eddy simulations by Alferez *et al.* [83] at a Reynolds number of $\mathrm{Re}_c = 1 \times 10^5$. They reported that bursting initiated with a slow linear increase in LSB length as the height of the LSB remained relatively constant. In this stage of the bursting process, the LSB was short according to the bursting criterion of Diwan *et al.* [6]. The initial stage of relatively slow LSB lengthening was followed by a rapid downstream movement of the reattachment point and thickening of the LSB, becoming a long LSB according to the criterion of Diwan *et al.* [6]. After the cessation of reattachment on the suction surface of the airfoil, Alferez *et al.* [83] reported an overshoot in drag and shear layer separation angle. The increase

in shear layer separation angle coincided with an upstream shift in transition [83]. The precise time-histories of the lift and drag coefficients during bursting were highly sensitive to the initial conditions of the boundary layer, indicating that the bursting process is non-deterministic. The overall duration of the bursting transient in the simulations of Alferez *et al.* [83] was approximately $20c/u_\infty$ [83].

Although several researchers have investigated LSB bursting due to changes in oncoming velocity magnitude or direction [e.g., 6, 7, 78, 82, 83], the process of LSB formation on a stalled lifting surface has received little attention. However, a limited number of studies have considered from a global perspective the process of dynamic reattachment at relatively high Reynolds numbers [e.g., 64, 65, 90]. In the dynamic reattachment process during a pitch-down motion, low-momentum fluid within the wake must first be convected downstream before boundary layer reattachment can occur [64]. The time required for the low-momentum fluid within the wake to be convected away from the lifting surface scales with the free-stream velocity [64, 90]. Thus, reattachment during a pitch-down motion is delayed to lower angles of attack for faster pitch rates [64]. Once the wake becomes sufficiently thin, the boundary layer separation point moves downstream along the suction surface [64, 90]. The lift coefficient begins to increase as the wake fluid is convected away from the lifting surface, and continues to increase as the boundary layer continues to evolve after attached flow is re-established [90]. Rezapour & Mulleners [90] reported that the dynamic reattachment process occurs over a time period on the order of $10c/u_\infty$ after the passing of the static reattachment angle.

In contrast to large-scale changes in free-stream velocity magnitude or direction which affect the global operating conditions of a lifting surface, disturbances with spatial scales on the order of the boundary layer thickness primarily affect the transition process, leading indirectly to changes in aerodynamic loads [91]. For example, the relatively small-scale disturbances present in the free-stream at elevated levels of free-stream turbulence intensity (FSTI) lead to higher initial amplitudes of disturbances in the boundary layer, causing accelerated shear layer roll-up and transition [72]. Two important parameters used to describe free-stream turbulence are the turbulence intensity (Tu), and streamwise integral length scale (Λ_{ux}). The turbulence intensity is defined as [28]:

$$Tu = \frac{\sqrt{\overline{u'^2}}}{u_\infty} \tag{2.15}$$

and measures the strength of the turbulent velocity fluctuations relative to the mean free-stream velocity. The streamwise integral length scale is a measure of the size of the largest energy containing vortices in a turbulent flow, and is defined as [92]:

$$\Lambda_{ux} = \int_0^\infty R_{uu} dx \tag{2.16}$$

where R_{uu} is the correlation coefficient of the streamwise velocity. The turbulence occurring at low altitudes in Earth's atmosphere can often be on the order of 10%, and is of particular significance to the operation of small aircraft with relatively low flight speeds [28]. The size

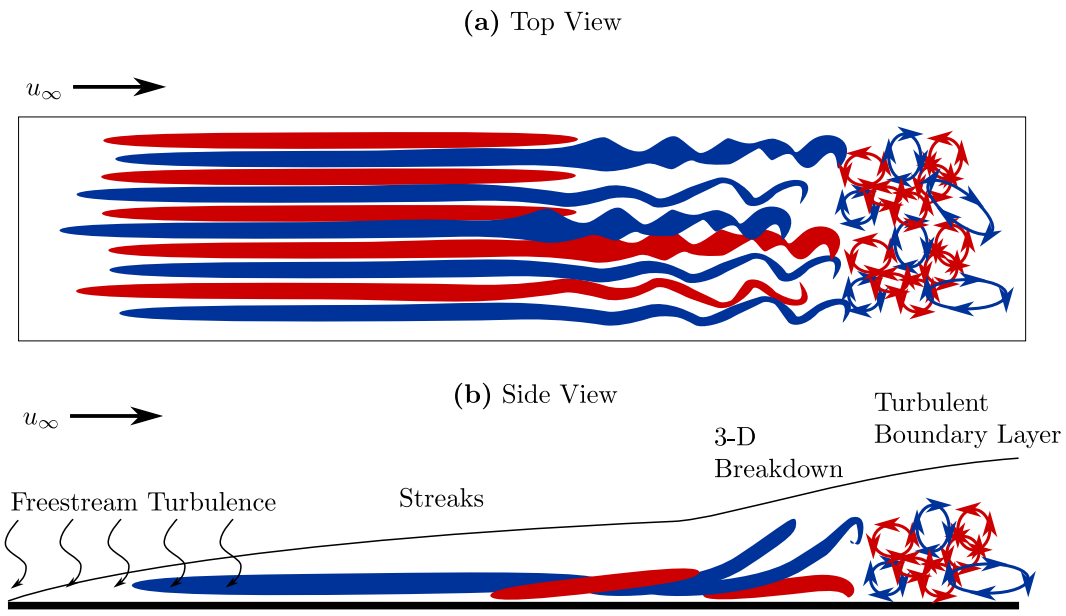


Figure 2.8: Schematic of bypass transition, with low-speed (blue), and high-speed (red) streaks.

of the energy containing vortices in the atmosphere ranges from centimetres to kilometres, but the most detrimental length scales of free-stream turbulence for the safe and controlled operation of aircraft are expected to be those on the order of the airfoil chord or wingspan [28]. The low pressure turbines of aircraft engines also operate at low Reynolds numbers in cruise conditions and are subject to relatively high free-stream turbulence intensities ($Tu \sim 5\%$) due to the periodic passage of wakes from upstream blades [14, 93].

When $Tu \gtrapprox 1\%$, transition may proceed more rapidly than would otherwise occur through the TS or Kelvin-Helmholtz instability mechanisms [73, 94]. This type of transition is called bypass transition [95], and is illustrated schematically in Fig. 2.8.

As a consequence of the no-slip condition, the leading edge causes vortices present in the turbulent free-stream to be tilted into the streamwise direction [96]. This streamwise vorticity leads to the formation of elongated high- and low-speed streaks in the boundary layer through the lift-up effect [97, 98]. Low-speed streaks form when the relatively low-velocity fluid near the wall is lifted up away from the wall, and high-speed streaks are formed when relatively high-velocity fluid is brought from the edge of the boundary layer towards the wall [99]. There is a consensus that the streak-formation process depends on the receptivity of the leading-edge region [e.g., 96, 100, 101]. The leading-edge receptivity acts as a low-pass filter, enabling low-frequency disturbances to penetrate into the boundary layer while attenuating high-frequency content from the outer flow [86, 102]. The shear layers between high- and low-speed streaks are inflectionally unstable, and roll-up into vortices [94]. The vortices formed in these shear layers then lead to three-dimensional deformations of the streaks and breakdown into turbulent spots [94]. For a given level of turbulence intensity, there is a specific ratio of the integral length scale (Λ_{ux}) to the boundary layer thickness (δ) at the location of transition that optimally promotes transition

[99]. Mamidala *et al.* [97] reported that this ratio is between 10 and 15. At very high turbulence intensities ($\sim 20\%$) and large length scales ($\Lambda_{ux} > 1000\nu/u_\infty$), turbulent spots may form without streaks as precursors [96, 100].

At low levels of FSTI ($0.5\% \lessapprox Tu \lessapprox 1\%$), streaks may interact with the primary inflectional instability of an LSB, reducing the spanwise coherence of the vortices formed from the roll-up of the separated shear layer. At $Tu = 1.5\%$, Burgmann *et al.* [103] and Burgmann & Schröder [104] observed the formation of disconnected c-shaped vortices rather than the largely spanwise uniform vortices observed at lower FSTIs. If the FSTI is sufficiently high, transition may occur rapidly enough that the boundary layer becomes turbulent before the region of adverse pressure gradient, eliminating laminar separation entirely [105].

The reduction in the extent of separated flow caused by elevated FSTI generally improves lifting surface performance at low Reynolds numbers by increasing the stall angle and maximum lift coefficient [72, 106, 107]. The increase in initial amplitudes of boundary layer disturbances at elevated FSTI also decreases stall hysteresis, and makes the decrease in lift associated with stall more gradual [79, 106]. However, increasing FSTI at low chord Reynolds numbers increases drag, due to the greater extent of turbulent boundary layers [106]. This drag increase is because turbulent boundary layers have higher wall shear stress than laminar boundary layers [50]. Despite this increase in drag, the lift-to-drag ratio of lifting surfaces at low chord Reynolds numbers often improves when the FSTI is increased above $Tu \approx 1\%$ [e.g., 108, 109].

Although lifting surface performance can be broadly expected to improve with increasing FSTI, the relationship between the integral length scale of the free-stream turbulence and aerodynamic loads is more nuanced [105]. This is because there is a specific ratio between Λ_{ux} and the boundary layer thickness (δ) at the transition location that is most optimal for promoting transition [97]. An increase in lift slope, maximum lift coefficient, and a decrease in stall angle occur when Λ_{ux}/δ deviates from the optimal ratio [106, 110]. At very large integral length scales ($\Lambda_{ux} \gg c$) and high turbulence intensities ($Tu \geq 10\%$), fluctuations in effective angle of attack caused by oncoming vortices may be large enough to cause intermittent LSB bursting [111, 112].

2.3.2 Effect of Finite Span on Laminar Separation Bubbles

All real lifting surfaces have a finite span. Therefore, end effects are present in all applications of low Reynolds number lifting surfaces, usually resulting in a decrease in lift to drag ratio and increase in stall angle [112, 113]. Due to the reduction in effective angle of attack caused by the tip vortices (Fig. 2.2), the locations of separation, transition, and reattachment on the suction surface of a finite wing with an LSB are shifted downstream relative to a two dimensional airfoil at the same geometric angle of attack [e.g., 112, 114, 115]. Within approximately $0.5c$ of the tip of a rectangular wing, downwash from the tip vortex has been observed to cause a substantial delay in transition [114, 116]. In close proximity to the tip, the downwash may be sufficient to prevent laminar boundary layer separation entirely [116]. The spanwise pressure gradient near the wing tip leads to spanwise flow within the

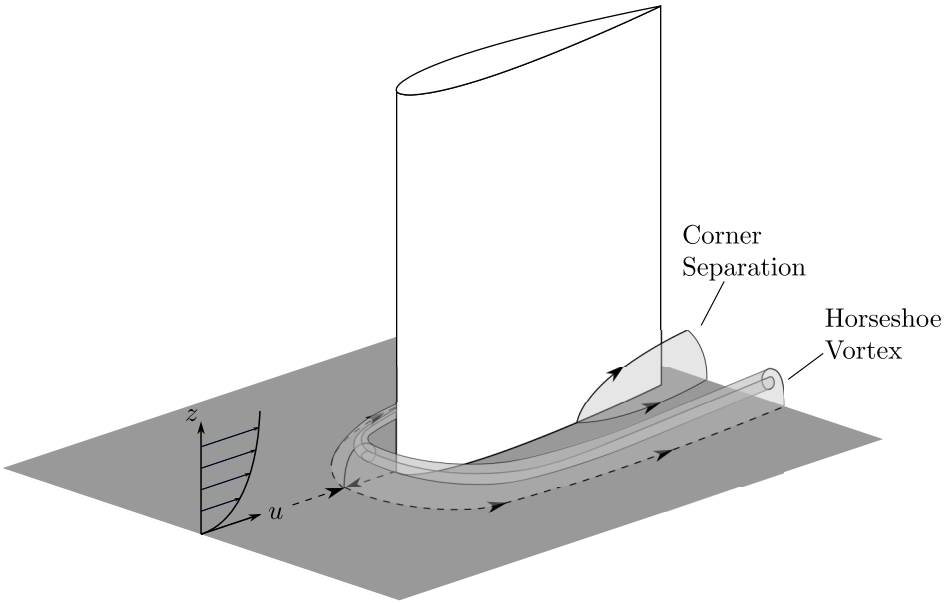


Figure 2.9: Horseshoe vortex and corner separation at a wing-root body junction, after [120].

recirculation region of the LSB, directed from the wing tip toward the midspan [47, 116, 117]. Outside of the portion of the span where tip effects are dominant, the LSB on a finite wing is largely spanwise uniform, analogous to an LSB formed on a two-dimensional airfoil at an equivalent effective angle of attack [e.g., 115, 118, 119]. Despite the spanwise flow and reduction in LSB height that occur near a wing tip [116], the dynamics of the transition process in LSBs on finite wings at low free-stream turbulence intensities is similar to that in LSBs on two-dimensional airfoils, being dominated by the shedding of spanwise uniform shear layer vortices near the location of maximum bubble height [115].

In a similar manner to the formation of a wing tip vortex, trailing streamwise vorticity is also produced at the junction between a wing root and a side-wall or aircraft fuselage. This is a result of interaction between the wing and the oncoming side-wall or fuselage boundary layer, which causes a decrease in circulation and sectional lift for the portion of the wing within the oncoming boundary layer [e.g., 121, 122]. However, the spanwise extent of the sectional lift reduction near a wing root can extend well beyond the thickness of the oncoming boundary layer, with Delafin *et al.* [122] observing a sectional lift reduction persisting $0.26c$ away from a wing root in their numerical simulations.

Reorientation of the vorticity of the oncoming boundary layer into the streamwise direction leads to the formation of a horseshoe vortex [120], illustrated in Fig. 2.9. The horseshoe vortex legs on the suction and pressure sides of the wing rotate in opposite senses when viewed from the streamwise direction. Similar to the effect of the tip vortex, downwash produced by the horseshoe vortex system suppresses laminar boundary layer separation in the vicinity of the wing root [47]. This downwash also leads to increased drag [123], and a spanwise pressure gradient that causes spanwise flow from the root region towards the midspan [47]. Within the LSB, the spanwise flow from the wing root may

persist up to $0.5c$ along the span [124]. At moderate Reynolds numbers, the horseshoe vortex system is unsteady [120], leading to increased levels of velocity fluctuations near the wing root [125]. Corner separations may also form at a wing root because of interaction between the wing and oncoming boundary layers [126, 127] (Fig. 2.9). If the oncoming boundary layer is turbulent, transition in the boundary layer on the wing surface in the vicinity of the wing root can be accelerated by earlier shear layer roll-up vortex breakdown [124]. Consequently, the location of reattachment also shifts upstream near the wing root when the oncoming boundary layer is turbulent [124]. In the vicinity of the wing root and tip, localised LSB thickening may occur due to the spanwise flow of fluid into the LSB [124]. However, the spanwise extent of wing root effects on LSBs is less than that of wing tip effects because the effective angle of attack is substantially reduced over a larger portion of the span near at wing tip than near a wing root. [42, 124].

In addition to altering the mean flow development in steady conditions, finite span effects also influence the dynamics of stall and reattachment transients. The reduction in effective angle of attack due to root and tip effects leads to an increase in the static and dynamic stall angles, and this increase is greater for smaller aspect ratios [128]. On wings undergoing dynamic stall due to an increase in angle of attack, the LSB widens in the spanwise direction as the angle of attack increases [129]. Usually, stall is expected to progress from the wing root towards the wing tip when the effective angle of attack of the wing tip is lower than that of the wing root, such as for an untwisted rectangular wing [42, 128]. The DSV formed during dynamic stall of a finite wing becomes highly three-dimensional because it remains anchored to the leading edge corners of the wing tip and root before it is shed [130]. At low aspect ratios ($\lesssim 4$), a single arch vortex may form from the DSV, but at higher aspect ratios ($\gtrsim 4$), multiple arch vortices may form along the span [131]. The three-dimensional flow development and aerodynamic loading on finite wings during dynamic reattachment are also sensitive to aspect ratio and end conditions. This is because stronger three-dimensional deformations of the trailing edge vortex occur for lower aspect ratio wings and in the presence of a gap between the wing and end-wall [130].

Chapter 3

Methodology

The facilities and measurement techniques employed in experiments are described. Mathematical details of specialised data processing methods are also presented.

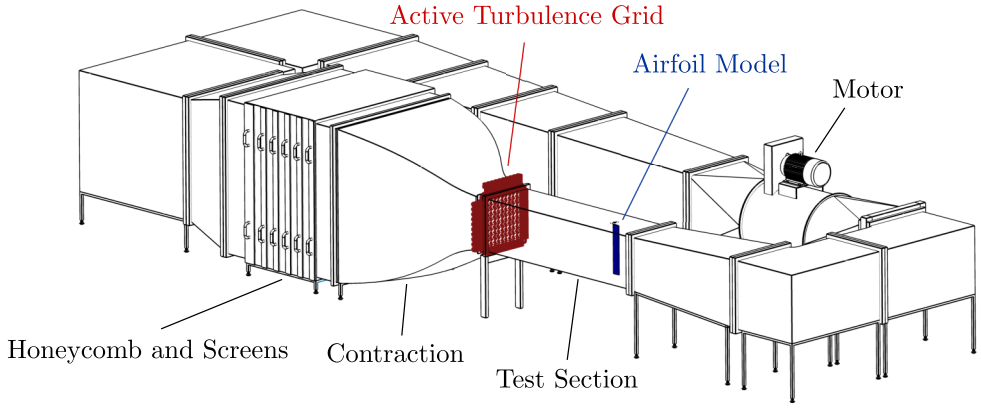


Figure 3.1: University of Waterloo recirculating wind tunnel. Adapted from [49, 133]

3.1 Experimental Setup

3.1.1 Facility and Lifting Surface Models

All experiments were performed in the recirculating wind tunnel at the University of Waterloo, illustrated in Fig. 3.1. This wind tunnel is powered by a variable frequency alternating current motor driving a six-bladed fan, and capable of producing test section velocities of up to $30\,\mathrm{m\,s^{-1}}$. The test section is square, with a width and height of 0.61 m and a length of 2.44 m. Upstream of the test section are a $9:1$ contraction and a set of flow conditioning elements composed of a honeycomb and 5 wire screens, designed to reduce the turbulence intensity in the test section. The turbulence intensity in the test section can optionally be increased with a removable active turbulence grid situated at the upstream end of the test section. The FSTI without the active turbulence grid, measured using a single normal hot-wire anemometer with the signal low-pass filtered at 10 kHz, was less than 0.24% across all free-stream velocities tested. The minimum FSTI for this wind tunnel, which is less than 0.1%, occurs at $u_\infty \approx 10\,\mathrm{m\,s^{-1}}$ [49]. The spatial variation of the streamwise velocity in the test section at a fixed downstream location is within 0.5% of the mean free-stream velocity [132]. During experiments, the mean free-stream velocity in the test section was set according to an empirical relationship between the measured pressure drop across the contraction and the free-stream velocity in the test section.

Active Turbulence Grid

To create a turbulent free-stream representative of the conditions experienced by devices operating in the atmosphere, a method to precisely increase the free-stream turbulence intensity while controlling the integral length scale was required. Historically, fixed grids or meshes have been placed in the flow upstream of the test section for this purpose [134]. Passive grids can be used to generate large-scale high-intensity turbulence when large bar widths and spacings are employed [e.g., 111, 135]. However, as the width and spacing of

the bars increases, the turbulence statistics may become unacceptably inhomogeneous in relatively small wind tunnels where there is limited streamwise distance available downstream of the grid for the turbulence to develop [136]. The active turbulence grid conceived by Makita [137] enables the production of large-scale high-intensity turbulence with a high degree of homogeneity in relatively small wind tunnels [138].

An active grid inspired by the original design of Makita [137] was employed in the recirculating wind tunnel at the University of Waterloo to generate turbulence intensities of up to $Tu = 16\%$ and integral length scales up to $\Lambda_{ux} = 0.2\,\mathrm{m}$. The active grid, as illustrated in Fig. 3.2, consisted of 10 vertical and 10 horizontal shafts with a mesh spacing of 61 mm. The horizontal and vertical shafts were offset in the streamwise direction by 12 mm. Attached to each shaft were 9 square aluminium wings with a diagonal of 60 mm and thickness of 2 mm. Adjacent to the walls of the test section, triangular half wings were attached to the shafts. Each shaft was independently controlled by an Applied Motion STM23IP-3EN stepper motor, connected to a personal computer via an ethernet network.

Two different modes of active grid operation were used to produce free-stream turbulence with specific characteristics. In the first mode of operation, the grid was operated such that the shafts oscillated about a mean angle of attack of zero, relative to the incoming flow velocity. The amplitude and frequency of the shafts' oscillation were varied depending on the desired turbulence intensity and integral length scale, respectively. The frequency of oscillation of each shaft was varied according to a uniform probability distribution to create broadband turbulent velocity fluctuations. To mitigate the creation of peaks in the energy spectrum of the free-stream velocity fluctuations at the oscillation frequencies of the active grid, the oscillation frequency of each shaft was continually re-sampled from the uniform distribution. The flapping mode was used to generate free-stream turbulence intensities of $Tu \leq 7\%$. In the second mode of operation, higher free-stream turbulence intensities of $13\% < Tu < 16\%$ were achieved by commanding the stepper motors to perform complete rotations at random rotational velocities for random intervals of time [e.g., 138]. The rotational velocities and time intervals were both varied according to uniform distributions.

A minimum streamwise distance of approximately $20 - 40$ grid mesh spacings is usually recommended for grid generated turbulence to become homogeneous and approximately isotropic [139–142]. For the experiments with the active turbulence grid in present work, the airfoil model was positioned 30 grid mesh spacings ($18c$) downstream of the active grid. The dimensions of the test section also limit the size of the largest turbulent vortices generated by the active grid, and thus isotropy of the grid generated turbulence is only theoretically possible when Λ_{ux} is less than the width of the test section.

3.2 Lifting Surface Models

Low-FSTI experiments in the recirculating wind tunnel (Chapters 4–6) were performed using two different airfoil models, both having a NACA 0018 profile and a chord of $c = 0.2\,\mathrm{m}$. The first airfoil model, illustrated in Fig. 3.3a and used for experiments in Chapter 4, was constructed from a machined aluminium frame covered by a aluminium sheet skin and

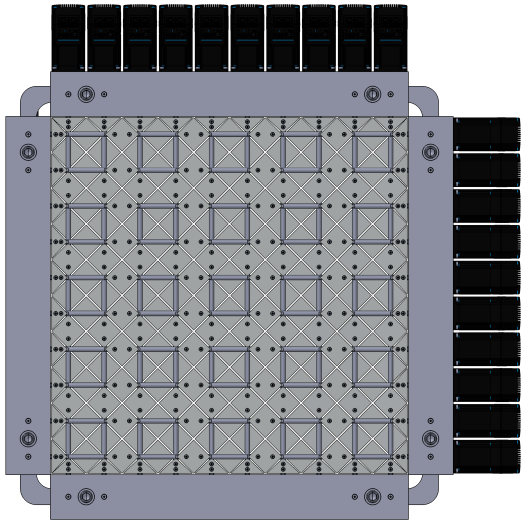


Figure 3.2: Active turbulence grid viewed in the streamwise direction with wings in fully closed position.

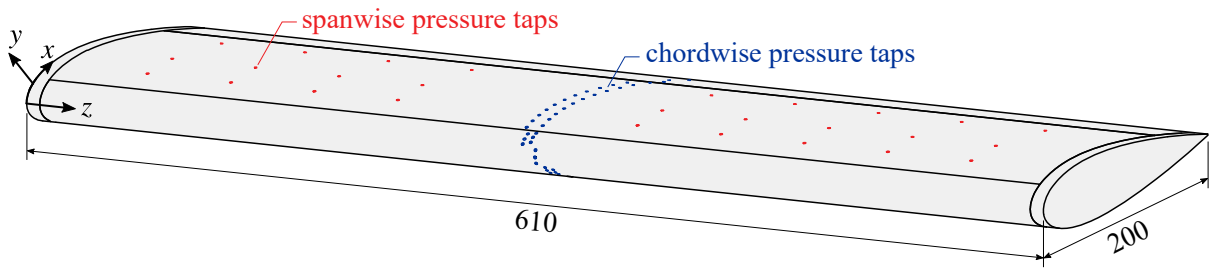
anodised black [143]. This airfoil model was used in several previous studies of laminar separation bubbles [e.g., 31, 74, 144–146], and is equipped with 95 surface pressure taps, 65 of which are situated in a staggered chordwise array at the midspan, while the remaining surface pressure taps are arranged in three spanwise rows on the suction surface.

A second airfoil model machined from acrylic glass was used for experiments that involved measurements of aerodynamic forces in Chapters 5–6 (Fig. 3.3b). The acrylic airfoil model did not contain pressure taps or associated tubing so that all reaction forces supporting the model would be entirely transmitted through the load cell used for direct force measurements as described in Section 3.3.2. The surface of the acrylic airfoil model was sanded by hand to 1500 grit, and finished with a finer polishing paste. A NACA 0018 profile with a chord of $c = 0.2\,\mathrm{m}$ was also used for this model, but the span was approximately 10 mm shorter than the width of the test section to structurally isolate the model from the test section walls. The acrylic airfoil model was segmented into two sections, one of 500 mm span and one of 100 mm span. The 100 mm section could be removed so that the remaining 500 mm section functioned as a finite wing with an aspect ratio of $s/c = 2.5$.

Experiments performed on the aluminium and acrylic airfoil models with chord lengths of 0.2 m were performed at Reynolds numbers in the range $4 \times 10^4 \leq \mathrm{Re}_c \leq 1 \times 10^5$, corresponding to free-stream velocities in the range $3.0\,\mathrm{m\,s^{-1}} \leq u_\infty \leq 7.7\,\mathrm{m\,s^{-1}}$.

To attain Λ_{ux} on the same order as the airfoil chord length without excessive inhomogeneity of freestream turbulence, an airfoil model with a smaller chord length was used for the experiments with the active turbulence grid in Chapter 7. This airfoil model was similar in design to the larger acrylic airfoil model with a NACA 0018 profile and removable segment, except that it was made of solid aluminium with a chord of $c = 0.1\,\mathrm{m}$. The two sections of this model were also of span 500 mm and 100 mm. The surface of this model was hand polished up to 1000 grit and anodised black to minimise light reflections. Experiments

(a) Aluminium Airfoil Model



(b) Acrylic Airfoil Model

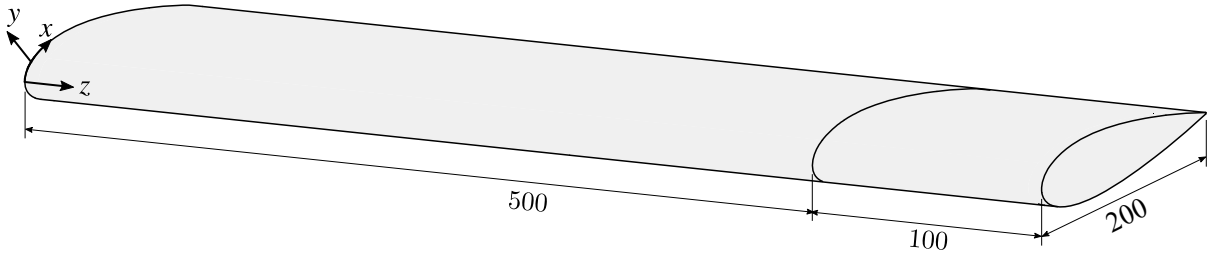


Figure 3.3: NACA 0018 airfoil models for low-FSTI experiments. Dimensions in mm. Adapted from [133].

with this airfoil model were performed at a Reynolds number of 7.0×10^4, corresponding to a free-stream velocity of $10.7\,\mathrm{m\,s^{-1}}$.

3.3 Measurement Techniques

Several quantitative measurement techniques were employed throughout the experiments documented in this thesis. The majority of quantitative flow-field and aerodynamic loading data come from particle image velocimetry (PIV) and direct force measurements, respectively. Therefore, an introduction to PIV and direct force measurements is provided in this section. Details of the implementation of these and other measurement techniques for specific experimental set-ups are provided in Chapters 4–7

3.3.1 Particle Image Velocimetry

Particle image velocimetry (PIV) is a quantitative flow visualisation technique that facilitates measurement of the velocity field in a region of space by measuring the displacements of tracer particles in the flow [147]. The use of optical methods for measuring these displacements renders this technique relatively non-intrusive, since physical probes do not need to be placed in the flow.

To faithfully follow pathlines in the flow, the tracer particles employed for PIV should be sufficiently small and have a density that is similar to the fluid flow of interest [147].

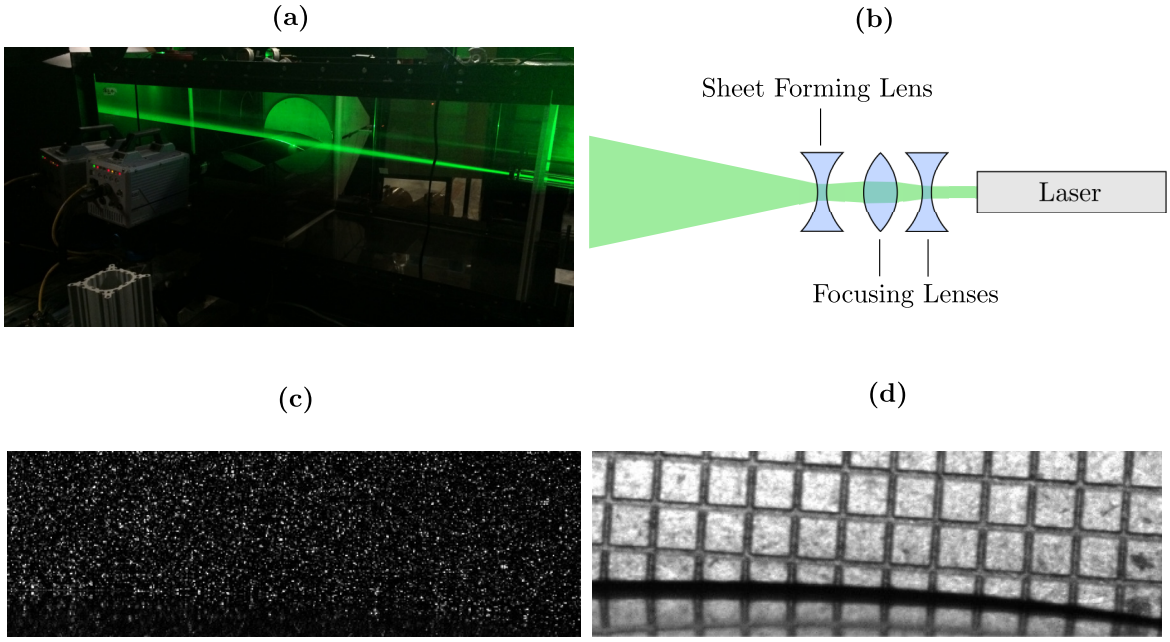


Figure 3.4: (a) Illumination of tracer particles with laser light. (b) The laser light is focused into a sheet using lenses. (c) Typical particle image from the flow over the suction surface of an airfoil. (d) Corresponding image of calibration target.

However, practical considerations often dictate the use of particles with significantly different density to that of the flowing fluid, especially in air [147]. When particles with a different density are used, it is important that the particle diameter is as small as practical, since the characteristic response time of a tracer particle is proportional to the square of particle diameter [147]. In this work, fog particles made from a mixture of water and glycol with a diameter on the order of 1 µm were used due to their low cost, small size, and non-toxicity.

To render the tracer particles visible for imaging, a light source is required. Typically, the illumination is provided using a pulsed laser [147]. In planar PIV (used exclusively in this work) the laser light is formed into a thin sheet using lenses, as illustrated in Fig. 3.4. This enables the tracer particles in the plane of the laser sheet to be imaged for the determination of the velocity field in that plane.

Imaging of the illuminated particles is performed by one or more cameras. An example of a particle image from the flow over the suction surface of an airfoil is shown in Fig. 3.4c. In the most basic form of PIV, one or more cameras are positioned to image independent regions of illuminated particles. This form of PIV is called 2-component PIV (2C-PIV) because the two velocity components in the plane of the light sheet can be measured [147]. Calibration of the PIV cameras must be performed to obtain a mapping between image coordinates and physical space [147]. This is done by imaging a planar target onto which is printed a grid with known pitch (Fig. 3.4d). Using the calibration images, a least-squares fit is performed on the known grid point locations to obtain the parameters of a mapping function.

Precise synchronisation of the cameras and laser is required for accurate velocity

measurements. In this work, a field-programmable-gate-array controlled the camera shutters and laser pulses in what is known as frame straddling mode [147]. Frame straddling mode was used in this work because it enables independent control of particle displacements and sampling period. In frame straddling mode, two camera exposures are acquired, the second exposure immediately after the first. During the fist exposure, a short ($\approx 500\,\text{ns}$) laser pulse is triggered near the end of the exposure, and during the second exposure, a short laser pulse is triggered near the beginning of the exposure. Adjusting the time between the two laser pluses changes the displacements of the particles appearing in the two exposures. Typically, particle displacements of approximately 10 pixels are recommended as a balance between the relative uncertainty in particle displacements, which decreases as the displacement increases, and the number of outliers, which increases as the displacement increases [147]. In the present work, the time interval between laser pulses was on the order of $10\,\mu\text{s}$ for all measurements. After the second exposure is complete, the process is repeated with another set of two exposures with two corresponding laser pulses. The time period for one repetition of this process is the sampling period.

After particle images are acquired, pre-processing of the images is typically performed to remove spurious light reflections and background artefacts [147]. In the present work, pre-processing involved subtracting the minimum intensity value of each pixel computed over a sliding temporal window. Velocity vector fields were then computed from each set of paired exposures using an iterative cross-correlation method [148]. The spatial resolution of the resulting velocity vector fields depends on the size of the spatial window used for cross-correlation. The window size must be chosen according to the seeding density and magnification factor such that a sufficient number of distinct particles are present in each window to minimise uncertainty in the location of the peak of the cross-correlation function [147]. In the present work, the final correlation window sizes ranged from $16\text{px} \times 16\text{px}$ to $24\text{px} \times 24\text{px}$, depending on the PIV configuration. Random errors in velocity vector calculation were estimated using the correlation statistics method, which evaluates the asymmetric contributions of the correlations between individual pixels to the overall cross-correlation peak [149]. After velocity vector calculation, post processing of the velocity vector fields was performed using the universal outlier detection method [150].

3.3.2 Aerodynamic Forces

Aerodynamic forces acting on the lifting surface models were measured using a JR3 30E12A4 6-axis load cell. The full scale range of the chordwise and chord-normal forces that can be measured by this load cell is 40 N. The load cell contains strain gauges whose electrical resistance is proportional to strain. The resistance of the strain gauges was converted into an electrical voltage signal ranging from $-10\,\text{V}$ to $10\,\text{V}$ using a bridge circuit and amplifier. The voltage output of the amplifier was digitized using a National Instruments PCI-4472 data acquisition device. The digitised voltage signals were converted into forces using a calibration provided by the load cell manufacturer. The models used for force measurements were simply supported by the load cell and were structurally isolated from all other components of the wind tunnel. Because the fundamental structural resonant periods

of the lifting surfaces were close to the periods of the flow transients, filtering was performed on the raw force signals. Details of the filtering procedures are given in Chapters 5 and 6. The lift coefficients presented in this thesis were not corrected for wind-tunnel blockage. The model solid blockage in all experiments was less than 10%, with the majority of detailed investigations conducted with model solid blockages less than 7%.

3.4 Analysis Methods

Several specialised data analysis methods are used throughout this thesis, details of which are provided in this section.

3.4.1 Frequency-Domain Analysis

Although not specialised to the field of fluid mechanics, frequency-domain analysis was employed extensively in this thesis to analyse the frequency content of measured signals. Furthermore, the underlying Fourier transform is foundational to the continuous wavelet transform discussed later.

The Fourier transform $\hat{u}(f,T)$ of a finite length signal $u(t)$ measured on the interval $[-T/2, T/2]$ is [151]:

$$\hat{u}(f,T) = \int_{-\frac{T}{2}}^{\frac{T}{2}} u(t) e^{-i2\pi ft} dt \tag{3.1}$$

It should be noted that the Fourier transform can be performed over a spatial dimension instead of time, in which case $\hat{u}$ becomes a function of wavenumber instead of frequency. If u is stationary ergodic process, the power spectral density (PSD) of u can be obtained from [151]:

$$\mathcal{P}_{uu}(f) = \lim_{T\to\infty} \frac{1}{T} \left|\hat{u}(f,T)\right|^2 \tag{3.2}$$

In practice, the discrete analogue of Eq. 3.2 is used to compute an approximation of $\mathcal{P}_{uu}$ from a set of N discrete measurements of u obtained at a sampling frequency f_s over a finite sampling period T.[1] $\mathcal{P}_{uu}$ represents the squared magnitudes of the coefficients of the Fourier series of u, which describe the sinusoidal components that are contained in u. If u has dimensions of velocity, then $\mathcal{P}_{uu}(f)$ has dimensions of energy per unit mass times time. When u is discretely sampled for a finite measurement period T, $\mathcal{P}_{uu}(f)$ can only be determined uniquely for $0 \leq f \leq f_s\,(1/2 - 1/N)$, and the frequency resolution is limited to f_s/N. The upper frequency limit is a consequence of the Nyquist-Shannon theorem [152]. Therefore, only frequencies less than one-half of the sampling frequency can be resolved in experimental data.

When computing $\mathcal{P}_{uu}$ from experimental data containing noise, Welch's method [153] was used to reduce the uncertainty in $\mathcal{P}_{uu}$. However, this reduction in uncertainty comes at the cost of decreased frequency resolution. A thorough explanation of Welch's method is

[1] The MATLAB (v24.2) function `fft` was used to compute the discrete Fourier transform.

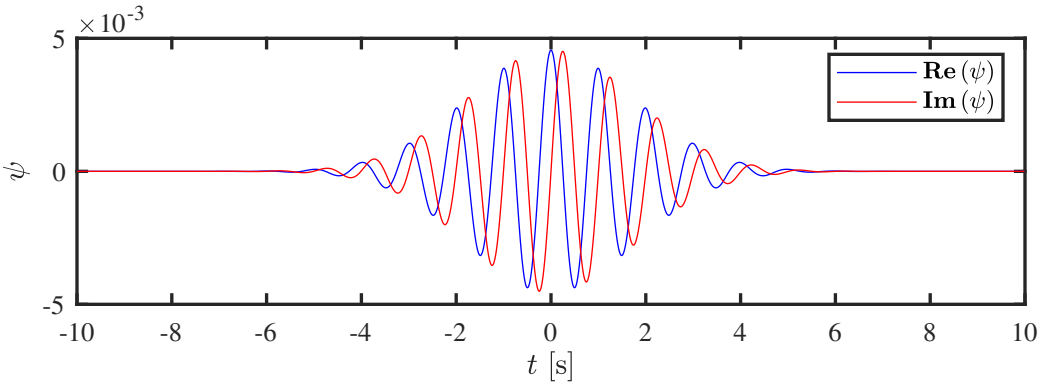


Figure 3.5: Example of an Airy wavelet scaled with a peak frequency of 1 Hz.

provided in [154]. Briefly, in Welch's method the PSD is computed for multiple overlapping segments of the data that are each shorter than the total sampling period.[2] Then, $\mathcal{P}_{uu}$ is taken as the average PSD over all of the segments. Usually, a weighting function is applied to the segments when computing the Fourier transform in Welch's method to reduce spectral leakage [154]. The averaging operation reduces random errors in the final PSD estimate.

3.4.2 Continuous Wavelet Transform

Although frequency-domain analysis using the Fourier transform provides information about the frequency content of a signal, it does not provide information about how the frequency components of a signal change in time. When dealing with non-stationary signals, such as those obtained from transient fluid flows, the continuous wavelet transform can provide valuable information about both the frequencies of oscillatory components contained in a signal and their localisation in time [155]. The continuous wavelet transform is similar to the Fourier transform in that it is also an integral transform that expresses a signal in terms of a set of predefined basis functions. In the Fourier transform, the basis functions are complex exponentials, whereas in the continuous wavelet transform the basis functions (wavelets) are complex oscillatory functions that vanish in the limit as $t \to \pm\infty$. In the present work, the Airy wavelet [156] was exclusively used. An example of an Airy wavelet is shown in Fig. 3.5. The continuous wavelet transform (Ψ) of a signal $u(t)$ with respect to the wavelet ψ is [157]:[3]

$$\Psi(t, \varsigma) = \frac{1}{\varsigma} \int_{-\infty}^{\infty} \psi^* \left(\frac{\tau - t}{\varsigma} \right) u(\tau)\, d\tau \tag{3.3}$$

where ς is the wavelet scale and $*$ denotes complex conjugation. This is a convolution between the signal u and shifted and dilated copies of the wavelet ψ. The scale is related to the inverse of the frequency of oscillation of the wavelet. Because wavelets are not pure

[2]The MATLAB (v24.2) function `pwelch` was used to compute Welch's power spectral density estimate.
[3]The MATLAB (v24.2) function `wt` was used to compute the continuous wavelet transform.

sinusoids, the frequency of a wavelet is often characterised by the peak frequency of its Fourier transform [158]. The relationship between scale and peak frequency for the Airy wavelet is given by Lilly [157]. Since the continuous wavelet transform is a function of time and scale, it provides information about the amplitude and frequency of oscillatory components of the signal u as a function of time. Like the Fourier transform, the continuous wavelet transform can also be applied over a spatial dimension instead of time.

3.4.3 Proper Orthogonal Decomposition

In the basic form of the Fourier and continuous wavelet transforms presented above, the signal being analysed is a scalar function of time. However, there are numerous situations in which it is desired to identify patterns in higher-dimensional functions, such as in a two-dimensional image, or in the velocity field of a fluid flow. Proper orthogonal decomposition (POD) is a modal decomposition technique for this purpose that is commonly applied to the analysis of fluid flows [159]. Unlike in the Fourier and continuous wavelet transforms, where the basis functions were pre-defined, in POD the basis functions (modes) are extracted from the signal itself. POD aims to decompose a signal $\mathbf{u}(\mathbf{x}, t)$ into a set of temporal coefficients ($\Theta_i(t)$), modal energies (λ_i^2), and spatial modes ($\mathbf{\Phi}_i(\mathbf{x})$):

$$\mathbf{u}(\mathbf{x}, t) = \sum_{i=1}^{N} \Theta_i(t)\lambda_i \mathbf{\Phi}_i(\mathbf{x}) \tag{3.4}$$

The modes obtained from POD are optimal in the sense that no other representation of the signal with a given number of modes can account for a greater portion of the variance of the signal [160]. A useful property of the POD temporal coefficients is that they are orthogonal, and thus uncorrelated [160]. In this work, the snapshot method [161] is used to compute the POD. To obtain the POD of the discrete velocity data $\mathbf{u}(\mathbf{x}, t)$ obtained at M spatial locations at N instants in time, the data is first arranged into a snapshot matrix $\mathbf{S}$ [162]:

$$\mathbf{S} = \begin{bmatrix} \mathbf{u}(\mathbf{x}_1, t_1) & \mathbf{u}(\mathbf{x}_1, t_2) & \dots & \mathbf{u}(\mathbf{x}_1, t_N) \\ \mathbf{u}(\mathbf{x}_2, t_1) & \mathbf{u}(\mathbf{x}_2, t_2) & \dots & \mathbf{u}(\mathbf{x}_2, t_N) \\ \vdots & \vdots & \ddots & \vdots \\ \mathbf{u}(\mathbf{x}_M, t_1) & \mathbf{u}(\mathbf{x}_M, t_2) & \dots & \mathbf{u}(\mathbf{x}_M, t_N) \end{bmatrix} \tag{3.5}$$

Note that in Eq. 3.5 $\mathbf{u}$ is a column vector with $\mathfrak{C}$ velocity components, and thus $\mathbf{S}$ has $M\mathfrak{C}$ rows and N columns. Next, the temporal coefficients, modal energies, and mode shapes can be obtained by performing a singular value decomposition on the snapshot matrix [159]:[4]

$$\mathbf{S} = \mathbf{\Phi}\boldsymbol{\lambda}\mathbf{\Theta}^T \tag{3.6}$$

Where $\mathbf{\Phi}$ is a rectangular matrix with $M\mathfrak{C}$ rows and N columns, $\boldsymbol{\lambda}$ is a square $N \times N$ diagonal matrix, and $\mathbf{\Theta}$ is a square $N \times N$ matrix. $\mathbf{\Phi}_i(\mathbf{x})$ can be obtained from the columns

[4]The MATLAB (v24.2) function `svd` was used to compute the singular value decomposition.

of the matrix $\mathbf{\Phi}$, the diagonal elements of $\boldsymbol{\lambda}$ are λ_i, and $\Theta_i(t)$ can be obtained from the columns of the matrix $\mathbf{\Theta}$:

$$\mathbf{\Phi} = \begin{bmatrix} \mathbf{\Phi}_1(\mathbf{x}_1) & \mathbf{\Phi}_2(\mathbf{x}_1) & \dots & \mathbf{\Phi}_N(\mathbf{x}_1) \\ \mathbf{\Phi}_1(\mathbf{x}_2) & \mathbf{\Phi}_2(\mathbf{x}_2) & \dots & \mathbf{\Phi}_N(\mathbf{x}_2) \\ \vdots & \vdots & \ddots & \vdots \\ \mathbf{\Phi}_1(\mathbf{x}_M) & \mathbf{\Phi}_2(\mathbf{x}_M) & \dots & \mathbf{\Phi}_N(\mathbf{x}_M) \end{bmatrix} \tag{3.7}$$

$$\boldsymbol{\lambda} = \begin{bmatrix} \lambda_1 & 0 & \dots & 0 \\ 0 & \lambda_2 & \dots & 0 \\ \vdots & \vdots & \ddots & \vdots \\ 0 & 0 & \dots & \lambda_N \end{bmatrix} \tag{3.8}$$

$$\mathbf{\Theta} = \begin{bmatrix} \Theta_1(t_1) & \Theta_2(t_1) & \dots & \Theta_N(t_1) \\ \Theta_1(t_2) & \Theta_2(t_2) & \dots & \Theta_N(t_2) \\ \vdots & \vdots & \ddots & \vdots \\ \Theta_1(t_N) & \Theta_2(t_N) & \dots & \Theta_N(t_N) \end{bmatrix} \tag{3.9}$$

The POD modes are ranked in terms of their modal energies (λ_i^2), with the first mode containing the greatest energy. The most energetic spatially coherent structures are found in the highest-ranking spatial modes. The temporal coefficients describe the temporal evolution of the spatial modes. In flows with periodic vortex shedding, spatial modes are obtained that contain information about the size, strength, trajectory, and wavenumber of the vortices [163]. When the vortex shedding is strongly coherent in space, a pair of POD modes will be obtained with similar modal energy and a similar spatial structure that is phase shifted by $\pi/2$ in space [163].

3.5 Uncertainty Estimation

Meaningful interpretation of experimental data requires quantification of the uncertainties in measured and derived quantities. The uncertainty of a quantity is the range of values within which the error in the quantity will fall with a certain probability [164]. Errors may be classified as bias errors or random errors [151]. Bias errors are those that remain constant over repeated measurements, whereas random errors lead to unpredictable changes in repeated measurements [151]. The uncertainty due to random errors can be quantified using repeated measurements. The uncertainty due to random errors in the mean of quantity F obtained from N independent measurements can be estimated from [165]:

$$U_{\overline{F}} = \tau_{N-1} \frac{S_F}{\sqrt{N}} \tag{3.10}$$

Where S_F is the sample standard deviation of F, and τ_{N-1} is the critical value of Student's t-distribution with $N-1$ degrees of freedom at the prescribed confidence level. For 95%

confidence, which is used throughout this thesis, $\lim_{N\to\infty} \tau_{N-1} \approx 1.96$.

Bias errors are relatively more difficult to quantify, since they can only be estimated when comparing measurements from two different measurement systems. Numerous sources of bias and random errors may be combined in a measurement. The overall uncertainty in a quantity F subject to N sources of error is given by [151]:

$$U_F = \sqrt{\sum_{l=1}^{N} U_{F,l}^2} \tag{3.11}$$

where $U_{F,l}$ is the uncertainty in F due to error source l assuming no other sources of error, and each source of error is assumed independent. Usually it is impossible to account for all sources of error in a measurement. However, since the overall uncertainty is the Euclidean norm of the contributions from each error source, only the dominant sources of uncertainty require inclusion for the order of magnitude of the overall uncertainty to be estimated.

Often, quantities are measured using instruments with discrete measurement scales, such as the graduations on a liquid thermometer or the numerical display on a digital protractor. When measurements are made with such instruments, a resolution uncertainty is introduced. The resolution uncertainty in the measured quantity is assumed to be one-half of the smallest increment on the scale [166].

The uncertainty in a derived quantity can be estimated from the uncertainties in the quantities it is derived from. Assuming that the errors are small, or that the derived quantity is a linear function of measured quantities, one may apply the linearised error propagation formula to estimate the overall uncertainty (U_F) in a derived quantity $F = f(a_1, a_2, \ldots, a_N)$ that is itself a function of uncertain measurements a_l [167]:

$$U_F = \sqrt{\sum_{l=1}^{N}\sum_{m=1}^{N} \frac{\partial F}{\partial a_l}\frac{\partial F}{\partial a_m} R_{a_l,a_m} U_{a_l} U_{a_m}} \tag{3.12}$$

where U_{a_l} and U_{a_m} are the uncertainties in a_l and a_m and R_{a_l,a_m} is the correlation coefficient between the errors in a_l and a_m. If the errors in each a_l are independent, as is often assumed, $R_{a_l,a_m} = 0$ for $l \neq m$ and Eq. 3.12 can be simplified [167].

Application of the linear error propagation formula requires that the sensitivities ($\frac{\partial F}{\partial a_l}$) be known. Commonly, quantities are computed using algorithms for which it is impractical to obtain the sensitivities. In such a case, the method of sequential perturbation [168] is used. The method of sequential perturbation for estimating the uncertainty in quantity $F = f(a_1, a_2, \ldots, a_N)$ is as follows:

1. Obtain F from $F = f(a_1, a_2, \ldots, a_N)$
2. For $l = 1, \ldots, N$

   Increase the value of a_l by U_{a_l} and recompute F, recording this value as F_l^+

   Decrease the value of a_l by U_{a_l} and recompute F, recording this value as F_l^-

The uncertainty in F due to a_l is $U_{F,l} = \left|F_l^+ - F_l^-\right|/2$

3. Compute the overall uncertainty in F using Eq. 3.11

Derived quantities presented in this thesis are presented with uncertainty estimates obtained using the linear error propagation formula (Eq. 3.12) or the method of sequential perturbation where appropriate. Details of the uncertainty estimation process for specific quantities are provided in Appendix A

Chapter 4

Transient LSB Development During a Change in Reynolds Number

The unsteady dynamics of laminar separation bubble formation and bursting are studied using quasi-steady ramp changes in free-stream velocity. The experiments are performed on a model set-up that approximates a two-dimensional airfoil. The limiting flow conditions before and after the ramp changes in free-stream velocity correspond to conditions where a short LSB forms on the suction surface of the airfoil and where the airfoil is stalled. The results show that LSB formation involves a relatively rapid upstream movement of the location of reattachment after initial formation of the LSB during the increase in free-stream velocity. Conversely, LSB bursting involves a relatively more gradual downstream movement of the location of reattachment prior to complete cessation of reattachment. The time required for the flow field to reach a statistically steady state is found to be longer after LSB bursting than after LSB formation. Because the imposed change in free-stream velocity is quasi-steady, the unsteady response of the flow is primarily a consequence of bifurcation between the two limiting flow configurations.

This chapter has been adapted from

Toppings, C. E. & Yarusevych, S. March 2023 Transient dynamics of laminar separation bubble formation and bursting. *Experiments in Fluids* **64** (3), 57. DOI.

4.1 Introduction

At low chord Reynolds numbers ($Re_c < 5.0 \times 10^5$ [11]), a stall often occurs due to a sudden increase in length (or bursting) of a short laminar separation bubble (LSB) on the suction side of a lifting surface [16]. Several authors have attempted to develop criteria for predicting whether a short LSB will burst, using information about the adverse pressure gradient and the state of the upstream boundary layer obtained from experiments in steady operating conditions [e.g., 6, 7, 30]. Although these bursting criteria attempt to predict the complex process of LSB bursting using a few parameters, bursting is a complex transient change between two different quasi-steady flow states that depends on the time-history of the flow [83]. This is evidenced by the hysteresis observed in LSB formation and bursting, such that the angle of attack or chord Reynolds number required for LSB re-formation are lower than or higher than the bursting angle and bursting chord Reynolds number, respectively [79]. The disturbance environment also plays a role in LSB bursting. An increase in incoming disturbance amplitudes can decrease the size of an LSB, whereas cessation or reduction in amplitude of disturbances can lead to LSB bursting [25, 29]. Therefore, knowledge of the temporal flow development and the process of disturbance amplification in an LSB during bursting is essential for a complete understanding of stall at low chord Reynolds numbers.

The evolution of the flow field during bursting is sensitive to the initial conditions of the LSB, making the bursting process non-deterministic [83]. However, similar characteristic events in the bursting process have been reported in controlled experiments [25] and numerical simulations [29, 83]. Bursting begins with a relatively slow increase in LSB length, followed by a rapid lengthening [83] and overshoot of the size of the recirculating flow region [25, 83], before the recirculation region contracts slightly to its final quasi-steady state. Yarusevych & Kotsonis [25] observed that the transient period associated with LSB bursting after the cessation of forced disturbances lasts for approximately five global convective time units, and is longer than the transient period associated with LSB contraction when forced disturbances are introduced.

In short bubbles, velocity fluctuations in the separated shear layer are largely periodic and the transition process is dominated by the shedding of spanwise vortices from the separated shear layer [7, 29]. However, in long bubbles, large amplitude velocity fluctuations in the separated shear layer are intermittent [7] and the spanwise coherence of shed vortices is substantially reduced due to rapid three-dimensional deformations [29]. This implies that the characteristics of the vortical structures produced during the transition process influence the rate of momentum transfer through the shear layer and thus its ability to reattach [29]. LSB bursting also weakens the feedback loop between pressure fluctuations generated by vortex shedding and the receptivity of the upstream boundary layer, leading to changes in the initial amplitudes of disturbances [17, 25].

Because LSB bursting and formation both result in significant and sudden changes in lift and drag, understanding the transient process of LSB bursting and formation is a prerequisite for the design of efficient lifting surfaces and controls for low chord Reynolds number applications. Thus, the objective of this experiment is to elucidate the spatio-

temporal evolution of a laminar separation bubble between short bubble and fully separated states due to changes in free-stream conditions. To this end, wind tunnel tests were conducted on a NACA 0018 airfoil model subjected to a controlled decrease or increase in free-stream velocity that caused an LSB on the suction surface to burst or re-form on the suction surface, respectively. Surface pressure and particle image velocimetry (PIV) measurements were performed to provide a quantitative description of the transient development of the flow field during LSB bursting and formation.

4.2 Description of Experiments

Experiments were performed on an aluminium NACA 0018 airfoil model with a chord length of 0.2 m in the recirculating wind tunnel at the University of Waterloo. The airfoil model spanned the entire 0.61 m width of the square test section, and was set to an angle of attack of 6°. The turbulence intensity at the centre of the empty test section over the range of free-stream velocities considered in this study was $0.13 \pm 0.01\%$, with velocity signals low-pass filtered at 10 kHz.

At the selected angle of attack, LSB bursting and formation occurs on the suction side between $\mathrm{Re}_c = 4.0 \times 10^4$ and 6.0×10^4, with these Reynolds numbers corresponding to quasi-steady stalled and short LSB states, respectively. To investigate the flow dynamics associated with the changes between these flow regimes, the free-stream velocity in the test section was varied in a controlled manner using a variable frequency alternating-current motor drive to control the wind tunnel fan speed. The ramp changes in free-stream velocity were performed in a continuous periodic cycle between $\mathrm{Re}_c = 4.0 \times 10^4$ and $\mathrm{Re}_c = 6.0 \times 10^4$, with an approximately 1 min ($1000c/u_\infty$) delay between each ramp change. This mitigated any possible hysteresis effects and allowed the flow to reach quasi-steady conditions between ramp changes. Figure 4.1 plots the ensemble of hotwire free-stream velocity measurements for 13 runs each for increasing and decreasing velocity between $3.0\,\mathrm{m\,s^{-1}}$ and $4.5\,\mathrm{m\,s^{-1}}$, corresponding to chord Reynolds numbers between 4.0×10^4 and 6.0×10^4. Because the free-stream velocity changed during the experiment, the non-dimensional time that the data is plotted against is defined as $\mathcal{D} = (1/c)\int_0^t u_\infty dt$, equivalent to the number of chord lengths that the free-stream has travelled at time t. The time corresponding to $\mathcal{D} = 0$ is defined as the time when the variable frequency motor drive was commanded to start the ramp change. The maximum acceleration in terms of the free-stream velocity and airfoil chord was approximately $\pm 0.015 u_\infty^2/c$. The high degree of overlap between the plots of the individual runs indicates low run-to-run variability in the prescribed free-stream velocity change.

4.2.1 Measurement Techniques

The free-stream velocity was measured using a single normal hotwire probe located at the inlet of the test section, calibrated against a Pitot tube. The hotwire probe was connected to a Dantec Dynamics constant temperature anemometry bridge, and the Pitot tube was

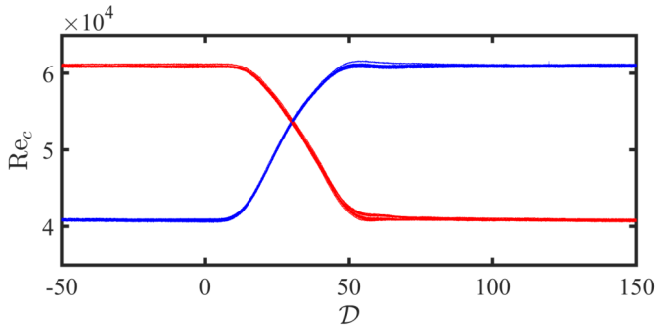


Figure 4.1: Controlled free-stream velocity ramp change. Red lines: decreasing Re_c, blue lines: increasing Re_c.

connected to a Setra Model 239 pressure transducer. The hotwire bridge and the pressure transducer were sampled using a National Instruments USB-6259 data acquisition system. Free-stream velocity measurements were taken from the hotwire at a sampling frequency of 20 kHz. Controlled changes in free-stream velocity were highly repeatable as shown in Fig. 4.1, and ensemble averaging was performed for random error reduction. Run-to-run variability of the free-stream velocity during repeated ramps was within 2% of the ensemble mean.

Mean surface pressure measurements in steady free-stream conditions were performed using an array of 67 pressure taps near the midspan of the airfoil model, arranged in a staggered pattern with an offset of $0.05c$ in the spanwise direction. The pressure taps were connected through two mechanical Scanivalve multiplexers to two Setra model 239 pressure transducers with input ranges of ±250 Pa which were sampled using the USB-6259 data acquisition system. The uncertainty in the mean surface pressure coefficients is estimated to be less than 0.4 (with 95% confidence limits), largely attributed to the relatively low free-stream dynamic pressures at the chord Reynolds numbers considered in this work.

For quantitative measurements of the separated flow on the suction surface of the airfoil model, two-component PIV was performed in a plane at the midspan of the model, as illustrated in Fig. 4.2. The flow was seeded with water-glycol fog particles with a diameter on the order of 1 µm, which were illuminated by a Photonics DM20-527 Nd:YLF pulsed laser. Particle images were recorded in double frame mode using two different camera configurations for low- and high-speed recordings, with essential PIV parameters presented in Table 4.1. In the low-speed configuration, particle images were acquired using two LaVision Imager sCMOS 5.5 megapixel cameras at a sampling frequency of 52.35 Hz and a laser pulse separation of 50 µs. Images from both low-speed cameras were cropped to 2560×1024 pixels, yielding a combined field of view of $0.70c \times 0.12c$. In the high-speed configuration, a single Photron FastCam SA4 1 megapixel camera imaged the area near location of transition in the separated shear layer at a sampling frequency of 750 Hz and a laser pulse separation of 70 µs. The uncropped sensor size of the highspeed camera was 1024×1024 pixels, and the resulting field of view was $0.25c \times 0.10c$. All cameras were equipped with Nikon 200 mm focal length lenses at an aperture setting of $f/4$. Particle

Table 4.1: PIV measurement parameters

Parameter	Low-speed	High-speed
Cameras	2× LaVision Imager sCMOS	Photron FastCam SA4
Cropped Sensor Size	2560px × 1024 px	1024px × 1024 px
Field of View	$0.70c \times 0.12c$	$0.25c \times 0.10c$
Lens Focal Length	200 mm	
Sampling Frequency	52.35 Hz	750 Hz
Sampling Time	20 s	3.64 s
Laser Pulse Separation	50 µs	70 µs
Maximum Particle Image Displacement	12 px	13 px
Initial Interrogation Window	24 px × 24 px	
Final Interrogation Window	16 px × 16 px	
Final Interrogation Window Overlap	75%	
Vector Pitch	$0.0006c$	$0.0009c$
Aperture	$f/4$	
Magnification Factor	0.23	0.47
Light Source	Photonics DM20-527 Nd:YLF Pulsed Laser	
Particles	Water-Glycol Fog	

images were pre-processed using sliding minimum subtraction, and velocity estimation was performed using the iterative multi-pass cross-correlation algorithm in the DaVis 10 software. The initial and final interrogation window sizes were 24×24 pixels and 16×16 pixels, respectively. A uniform initial window displacement of 10 pixels in the streamwise direction was employed to enable a small initial window size relative to the maximum particle displacement. Using the correlation statistics method [149], the random errors in the instantaneous PIV measurements in the vicinity of the separated shear layer for both PIV configurations are estimated to be less than 10% of the free-stream velocity with 95% confidence.

The PIV system was synchronised with the trigger signal for the periodic ramp change in free-stream velocity, and an ensemble of 13 runs was obtained with the low-speed PIV configuration for each of the increasing and decreasing free-stream velocity cases. For each run, 1047 images were acquired starting 10.00 s before the free-stream velocity change was initiated and ending 10.00 s after the initiation of the free-stream velocity change. In addition, two runs were recorded with the high-speed PIV configuration for each of increasing and decreasing free-stream velocity cases. For each run, the high-speed PIV acquisition of 2728 images began simultaneously with the initiation of the free-stream velocity change and ended 3.64 s later.

For data presentation, the PIV measurements were transformed into the $x - y$ surface attached coordinate system defined in Fig. 4.2. In this system, whose origin is at the leading edge, the x coordinate is the arc length along the surface of the airfoil and the y coordinate is the distance normal to the surface. The streamwise (u) and wall-normal (v) velocity components are parallel to the x and y axes, respectively. Mean surface pressure measurements are presented using a chord based coordinate axis X that is parallel to the airfoil chord and whose origin is also at the airfoil leading edge. Quantities that are

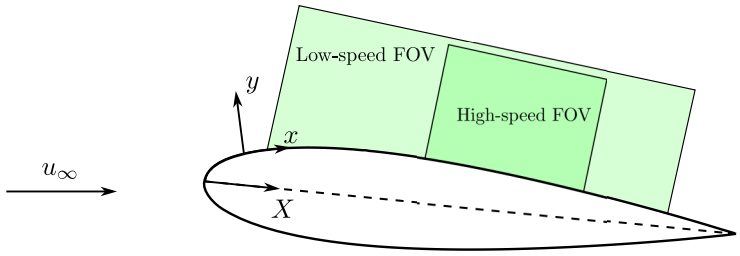


Figure 4.2: Fields of view for low-speed and high-speed PIV configurations and coordinate system definitions.

time-averaged over the entire data acquisition period are denoted by an overbar, and ensemble averaged quantities are denoted with a tilde. Fluctuations of quantities about an average are denoted by an apostrophe. Statistical quantities were computed using a sliding temporal window of length $4c/\overline{u_\infty}$, and then averaged over the ensemble of 13 runs. The selection of the temporal window length used for calculating statistics is a compromise between temporal resolution and statistical convergence. The overall trends in time-dependent statistics were found to be largely unaffected by window length for window lengths between $2c/\overline{u_\infty}$ and $8c/\overline{u_\infty}$.

4.3 Results

4.3.1 Limiting flow states

At an angle of attack of 6°, flow development over the suction side of the airfoil changes between stalled conditions at $\mathrm{Re}_c = 4.0 \times 10^4$ and a short LSB present at $\mathrm{Re}_c = 6.0 \times 10^4$. This is reflected in the mean suction surface pressure coefficient ($\overline{C_p} = (\overline{p} - p_\infty)/(1/2\rho u_\infty^2)$) distributions plotted in Fig. 4.3. In both the stalled and short LSB states, a pressure plateau begins near $x/c = 0.20$, indicating boundary layer separation near this location. In the stalled state ($\mathrm{Re}_c = 4.0 \times 10^4$), the suction peak is significantly reduced and the pressure plateau extends to the trailing edge. However, at $\mathrm{Re}_c = 6.0 \times 10^4$, the suction peak is stronger and a rapid pressure recovery occurs over $0.45 < x/c < 0.55$, indicating transition and reattachment of the separated shear layer [e.g., 20], which lead to the formation of the LSB.

Time-averaged streamwise velocity, streamwise RMS velocity fluctuations, and wall-normal RMS velocity fluctuations from PIV measurements on the suction surface of the airfoil model for the stalled state at $\mathrm{Re}_c = 4.0 \times 10^4$ and the short LSB state at $\mathrm{Re}_c = 6.0 \times 10^4$ are presented in Fig. 4.4. In the stalled state (Fig. 4.4a), the separated shear layer departs from the airfoil surface and a large reverse flow region forms. In the short LSB state (Fig. 4.4b), the separated shear layer curves back towards the surface, enclosing a thin region of relatively slower reverse flow. The plots of RMS velocity fluctuations reveal that maximum amplitudes of velocity fluctuations are reached farther upstream in the short LSB state compared to the stalled state, indicating earlier transition in the short LSB. Also,

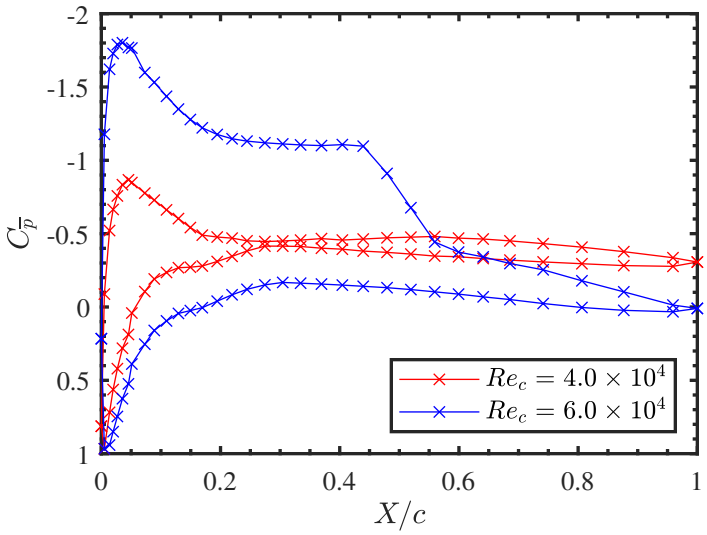


Figure 4.3: Surface pressure distributions of limiting flow states at steady chord Reynolds number.

higher maximum wall-normal velocity fluctuations occur as a result of shear layer vortex shedding in the short LSB, which are responsible for the increase in the rate of wall-normal momentum transfer that leads to reattachment [e.g., 21, 88]. Previous studies on LSBs have defined the transition point as the location of maximum displacement thickness (δ^*) [e.g., 88], maximum shape factor [e.g., 132], or the end of the pressure plateau [e.g., 169]. However, these locations are ill-defined for the stalled state. Therefore, a transition location criterion based on the one used by Hain *et al.* [170] and Ol *et al.* [171], defined as the x location where the Reynolds shear stress ($-\widetilde{u'v'}$) along the displacement thickness ($y = \delta^*$) exceeds a threshold of $0.001u_e^2$, where u_e is the local edge velocity, is used here, indicated by the dashed lines in Fig. 4.4. It can be seen that, relative to the short LSB state, transition is delayed in the stalled state.

The unstable frequencies and wavenumbers of wall-normal velocity fluctuations in the separated shear layer are explored in Fig. 4.5 for the two limiting states. Figure 4.5a presents frequency power spectra obtained from high-speed PIV measurements at the transition location averaged over the wall-normal extent of the field of view. The power spectral density was calculated using Welch's method [153] with a window length of $4c/\overline{u_\infty}$, and 50% overlap between windows. The resulting frequency resolution is $0.126\overline{u_\infty}/c$. Figure 4.5b presents wavenumber power spectra obtained by averaging the spatial Fourier transform of wall-normal velocity fluctuations along the line $y = \overline{\delta^*}$ from all low-speed PIV snapshots. The resulting wavenumber resolution is $5.5c^{-1}$.

The most amplified frequencies of disturbances that lead to vortex shedding in each limiting state can be inferred from the spectral peaks [19] denoted by dashed lines in Fig. 4.5a, which occur at $fc/u_\infty = 12.5$ and 5.1 for the short LSB and stalled states, respectively. These frequencies are in agreement with those expected for the investigated conditions based on the results of Boutilier & Yarusevych [74]. The stalled state exhibits substantially stronger velocity fluctuations than the short LSB state at low frequencies

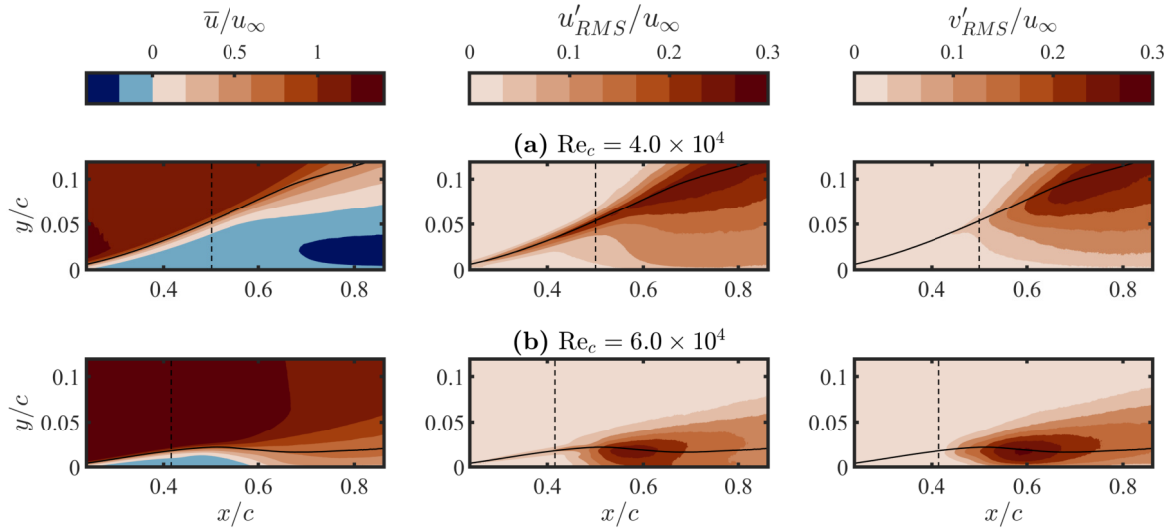


Figure 4.4: Mean streamwise velocity, streamwise RMS velocity fluctuations, and wall-normal RMS velocity fluctuations of limiting flow states at steady chord Reynolds number. Transition location - - - , displacement thickness — .

($fc/u_\infty \leq 11$), consistent with previous studies of unsteadiness over stalled airfoils [e.g., 172]. The wavenumber power spectra in Fig. 4.5b reveal multiple peaks for both limiting states. The peaks denoted by dashed lines at $kc = 38.4$ and $kc = 98.7$ are attributed to the fundamental vortex shedding frequency in the stalled and short LSB states respectively, because the resulting phase speeds of the fundamental disturbances are $2\pi f/k \approx 0.8u_\infty$, which is within the range of vortex convection speeds measured in LSBs on airfoils at comparable Reynolds numbers [e.g., 19, 75, 104]. The presence of the sub-harmonic peak at $kc = 49.4$ in the short LSB spectrum is attributed to aperiodic vortex merging [173].

The stalled and short LSB states at $\mathrm{Re}_c = 4.0 \times 10^4$ and $\mathrm{Re}_c = 6.0 \times 10^4$, respectively, are verified to be quasi-steady states for which state changes do not occur due to natural variation in free-stream disturbance environment. Thus, controlled ramp changes in chord Reynolds number between these two limiting states are used to study the transient LSB formation and bursting processes in the next section.

4.3.2 Transient flow development

The evolution of the instantaneous spanwise vorticity fields (ω_z) during LSB formation (Figs. 4.6a–4.6e) and bursting (Figs. 4.6f–4.6j) due to a ramp change in the chord Reynolds number (Fig. 4.6k) between $\mathrm{Re}_c = 4.0 \times 10^4$ and $\mathrm{Re}_c = 6.0 \times 10^4$ is presented in Fig. 4.6. The vertical lines in Fig. 4.6k associate the presented vorticity snapshots with the corresponding instances in the ramp-up/ramp-down cycle.

In both the stalled and short LSB states, vortex shedding from the separated shear layer is observed. This is followed by vortex breakdown and turbulent flow development,

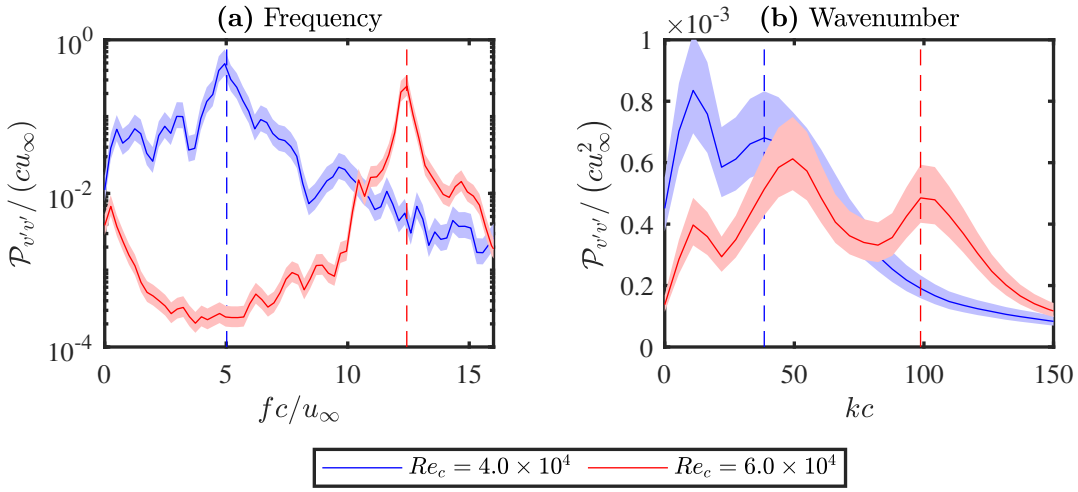


Figure 4.5: Frequency and wavenumber spectra of wall-normal velocity fluctuations in the limiting flow states. Dashed lines indicated fundamental frequency and wavenumber.

signifying that the shear layer undergoes laminar-to-turbulent transition at all flow conditions considered. During LSB formation, the initially massively separated flow (Figs. 4.6a–4.6c) approaches the reattached state between $\mathrm{Re}_c = 5.2 \times 10^4$ and $\mathrm{Re}_c = 5.8 \times 10^4$, bringing the separated shear layer closer to the airfoil surface. Between $\mathrm{Re}_c = 5.8 \times 10^4$ and $\mathrm{Re}_c = 6.0 \times 10^4$, there is a further minor reduction in the distance of the separated shear layer and the surface as the chord Reynolds number reaches its final steady-state value. The LSB bursting process begins with a progressive increase of the distance between the separated shear layer core and the wall between $\mathrm{Re}_c = 6.0 \times 10^4$ and $\mathrm{Re}_c = 5.3 \times 10^4$ (Figs. 4.6f–4.6h). The observed shear layer trajectory suggests that reattachment fails to occur between $\mathrm{Re}_c = 5.1 \times 10^4$ and $\mathrm{Re}_c = 4.3 \times 10^4$ (Figs. 4.6h–4.6i). After an initial overshoot in the angle of the separated shear layer (Fig. 4.6i), the separation angle reduces slightly at $\mathrm{Re}_c = 4.1 \times 10^4$ (Fig. 4.6j). The difference in the vorticity fields at $\mathrm{Re}_c = 5.2 \times 10^4$ between the LSB formation (Fig. 4.6c) and bursting (Fig. 4.6h) sequences points to a substantial hysteresis. In agreement with previous studies under steady incoming flow conditions, the chord Reynolds number at which the LSB forms is higher than the chord Reynolds number at which the LSB bursts [e.g., 79, 114, 118].

To illustrate deterministic features of the observed flow regime changes, ensemble-averaged streamwise velocity fields during LSB formation and bursting are shown in Fig. 4.7. For better statistical convergence, the ensemble-averaged velocity fields were averaged over a temporal window of length $4c/\overline{u_\infty}$. The results in Figs. 4.7a–4.7e show that LSB formation begins with a gradual contraction of the reverse flow region, before a relatively abrupt reduction in reverse flow extent and negative velocity magnitude occur as the separated shear layer reattaches. After LSB formation, the reverse flow region continues to contract as the chord Reynolds number reaches its final steady state.

The LSB bursting sequence (Figs. 4.7f–4.7j) shows that the initial reduction of the free-stream velocity brings about an increase in relative reverse flow magnitude within the LSB, accompanied by a gradual increase in bubble height. This is followed by bubble bursting,

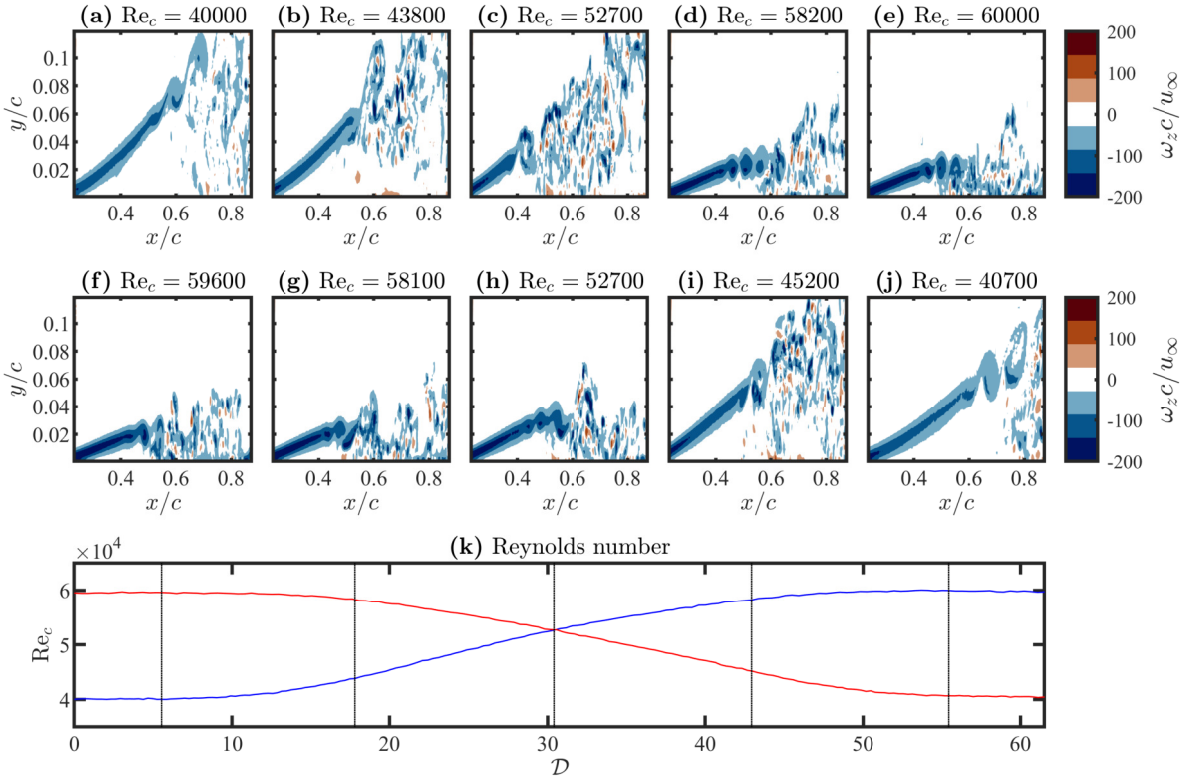


Figure 4.6: Instantaneous spanwise vorticity contours during bubble formation (a-e), and bubble bursting (f-j). (k) Ensemble averaged Reynolds number during increasing Re$_c$ (blue) and decreasing Re$_c$ (red). Vertical lines correspond to the times of the contours above.

leading to an initial overshoot of the extent of reverse flow region and its subsequent gradual contraction towards quasi-steady state conditions, similar to the trend observed in instantaneous vorticity sequences (Figs. 4.6f–4.6j). The observed trends in the ensemble statistics point to deterministic flow features of the LSB formation and bursting transients.

The development of the recirculating flow region during ramp changes in free-stream velocity can be described using the zero-net-streamwise mass flux line [20]. In quasi-steady flows, the zero-net-streamwise mass flux line is coincident with the streamline dividing the recirculation region from the surrounding flow. In unsteady conditions, such as those of the present study, the zero-net-streamwise mass flux line is not necessarily a streamline, however it is a robust integral parameter employed here to provide a comparison of the transient LSB development with the quasi-steady initial and final states. Figure 4.8 plots snapshots of the zero-net-streamwise mass flux line as a function of time from the initiation of the chord Reynolds number ramp up (Fig. 4.8a) and ramp down (Fig. 4.8b). The relatively wide spacing between the lines in the downstream part of Fig. 4.8a and clustering of the results around the limiting states indicate that the flow switches relatively rapidly from the stalled condition to the short LSB condition. In contrast, during the LSB bursting process (Fig. 4.8b), closer line spacing is seen near the initial short LSB state, indicating a

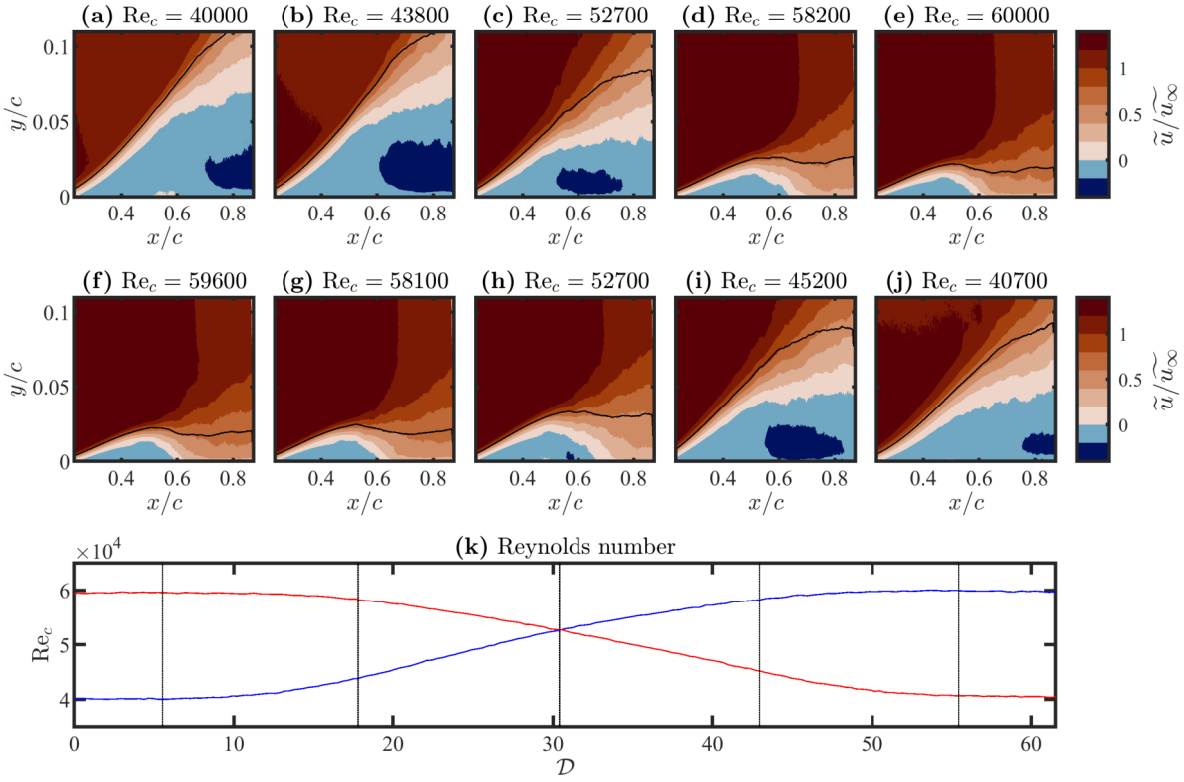


Figure 4.7: Ensemble and temporal window averaged spanwise vorticity contours during bubble formation (a-e), and bubble bursting (f-j). Displacement thickness —— . (k) Ensemble averaged Reynolds number during increasing Re$_c$ (blue) and decreasing Re$_c$ (red). Vertical lines correspond to the time instants of the contours above.

slower initial expansion of the LSB. After bursting, the contours show that the distance of the shear layer from the surface overshoots and then undershoots as the flow settles to the quasi-steady stalled state. Thus, the motion of the shear layer during the bursting transient bears similarity to the step response of a classical second-order under-damped system [174].

The movement of the ensemble-averaged separation, transition, and reattachment locations during ramp changes in free-stream velocity is examined in Fig. 4.9. The separation and reattachment locations were estimated by extrapolating the ensemble-averaged zero-net-streamwise mass flux line to the airfoil surface, and thus correspond to estimates of the locations where the wall shear stress changes sign.

The results in Fig. 4.9a show that LSB formation is initiated with a progressive upstream movement of the location of transition as the Reynolds number begins to increase during the ramp-up, which is consistent with the expected higher disturbance growth rates at higher Reynolds numbers [e.g., 17, 175, 176]. As the turbulent shear layer reattaches at $\mathcal{D} \approx 35$, there is a relatively rapid downstream movement in the location of transition. The transition and reattachment points then move upstream again as the reverse flow region contracts to the final quasi-steady short LSB state. The process of LSB formation is also

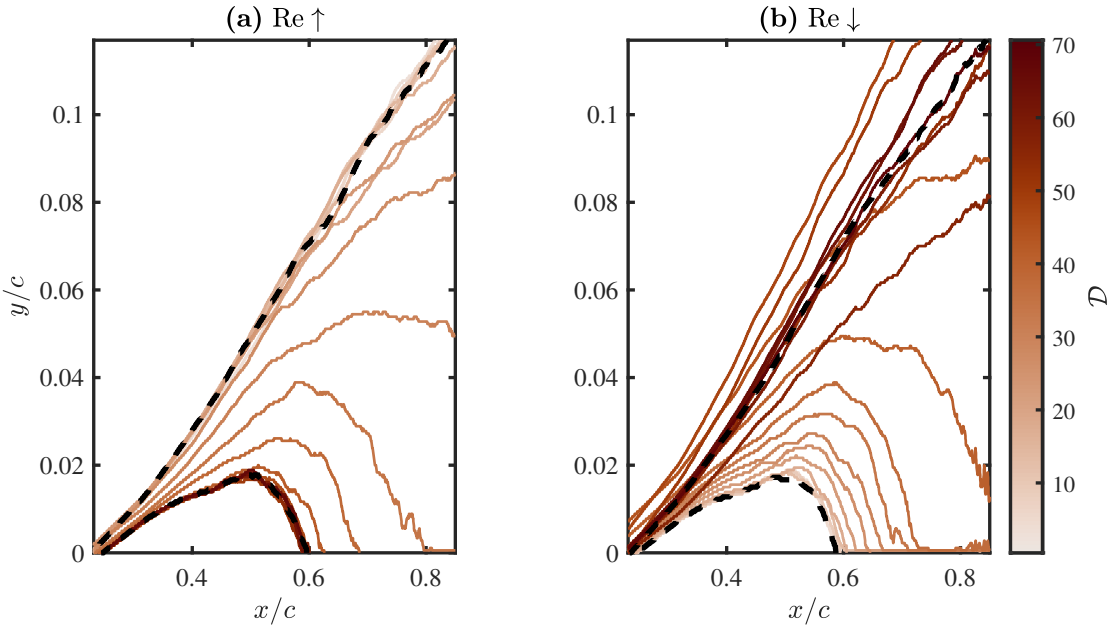


Figure 4.8: Transient change of the ensemble averaged dividing streamline during (a) increasing Re_c, and (b) decreasing Re_c. Black dashed lines are the limiting states.

accompanied by a minor downstream movement of the separation point.

During the LSB bursting transient (Fig. 4.9b), the locations of transition and reattachment begin to shift downstream, consistent with the expected reduction in disturbance growth rates and subsequent lengthening of the separated flow region with decreasing Reynolds number [e.g., 17, 175, 176]. When reattachment ceases at $\mathcal{D} \approx 39$, there is an upstream movement in both the separation and transition locations, which suggests a transient increase in the adverse pressure gradient [e.g., 87] and a reduction in shear layer stability [17] as the shear layer moves rapidly away from the airfoil surface. After cessation of reattachment, the separation and transition locations move downstream again until the quasi-steady stalled state is reached.

To explore the relationship between the wall-normal movement of the separated shear layer and the streamwise location of transition, the ensemble averaged displacement thickness ($\widetilde{\delta^*}$) and Reynolds shear stress ($-\widetilde{u'v'}$) at $y = \widetilde{\delta^*}$ for the LSB formation and bursting transients are plotted against time and streamwise location in Fig. 4.10. The limiting stalled state ($\mathcal{D} = 0$ in Figs. 4.10a and 4.10c, $\mathcal{D} = 100$ in Figs. 4.10b and 4.10d) is characterised by a monontonic increase in displacement thickness with increasing downstream distance, delayed growth of Reynolds shear stress, and a reduced peak Reynolds shear stress magnitude near $x/c \approx 0.7$. The limiting short LSB state ($\mathcal{D} = 0$ in Figs. 4.10a and 4.10c, $\mathcal{D} = 100$ in Figs. 4.10b and 4.10d) is characterised by a local maximum in displacement thickness near the location of maximum bubble height ($x/c \approxeq 0.5$), earlier growth of Reynolds shear stress, and an increased peak Reynolds shear stress magnitude near $x/c \approx 0.6$.

During the initial stages of LSB formation, the height of the separated shear layer remains

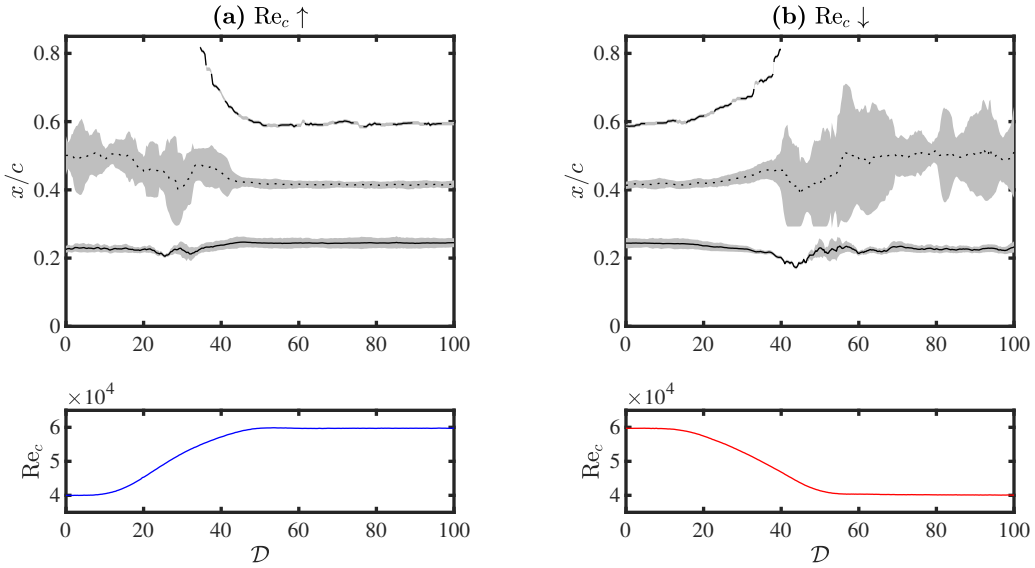


Figure 4.9: Locations of separation —, transition ..., and reattachment - - - during (a) increasing Re_c and (b) decreasing Re_c.

largely constant for $0 \lessapprox \mathcal{D} \lessapprox 35$ as Re_c begins to increase (Fig. 4.10c). Simultaneously, Fig. 4.10a shows a gradual upstream movement in the contours of Reynolds shear stress, consistent with the expected increase in disturbance growth rates with increasing Re_c. At $\mathcal{D} \approx 37$, Fig. 4.10c shows a rapid decrease in displacement thickness coincident with the initiation of reattachment (Fig. 4.9a), indicating a swift movement of the separated shear layer towards the airfoil surface. This event corresponds to a transient downstream shift in the transition point (Fig. 4.10c) and delayed Reynolds shear stress growth, which is attributed to the reduction in disturbance growth rates due to the closer proximity of the separated shear layer to the wall [17, 25]. However, due to the continued increase in chord Reynolds number and local increase in boundary layer edge velocity (Fig. 4.7), this delay in transition is not sustainable in light of the increase in Re_c, and there is a subsequent upstream movement of transition and an increase in the peak Reynolds shear stress magnitude for $37 \lessapprox \mathcal{D} \lessapprox 50$ as the flow settles to the limiting short LSB state at $t\overline{u_\infty}/c \approx 60$.

During the initial stages of the LSB bursting transient, the height of the separated shear layer slowly increases for $0 \lessapprox \mathcal{D} \lessapprox 30$ as Re_c begins to decrease (Fig. 4.10d). Simultaneously, Fig. 4.10d shows a gradual downstream movement in the contours of Reynolds shear stress, consistent with the expected decrease in disturbance growth rates with decreasing Re_c. At $\mathcal{D} \approx 40$, Fig. 4.10d shows a rapid increase in displacement thickness coincident with the cessation of reattachment (Fig. 4.9b), indicating a sudden movement of the separated shear layer away from the airfoil surface, and overshoot of the limiting stalled state. This event corresponds to a transient upstream shift in the transition point (Fig. 4.10d) and earlier Reynolds shear stress growth, which is attributed to the increase in disturbance growth rates due to the larger distance between the separated shear layer and the wall [17, 25]. However, due to the continued decrease in chord Reynolds number and local decrease in

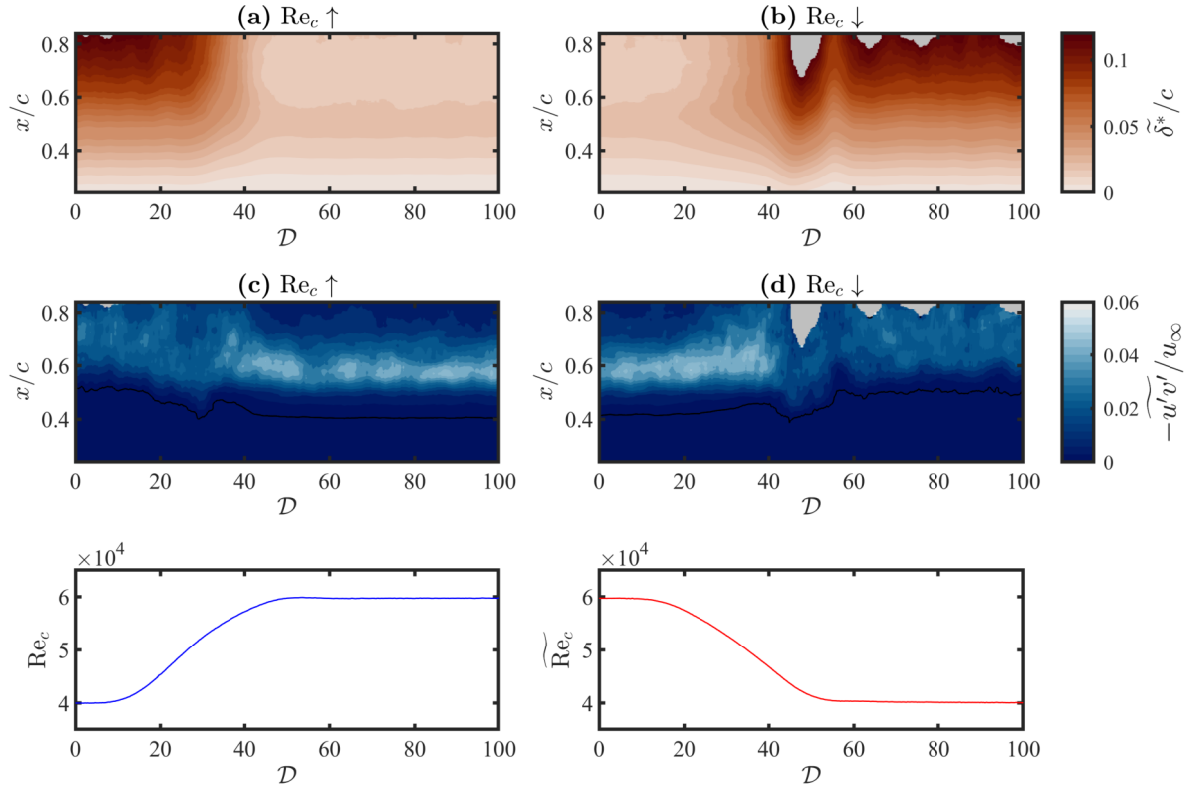


Figure 4.10: Reynolds shear stress (c,d), and displacement thickness (a,b), during (a,c) increasing Re$_c$, and (b,d) decreasing Re$_c$. Black line indicates transition point. Grey areas indicate where the displacement thickness is greater than the height of the PIV field of view.

boundary layer edge velocity (Fig. 4.7), this upstream movement of the transition point and overshoot in displacement thickness is not sustainable, and there is a subsequent downstream movement of transition and undershoot in displacement thickness before the flow settles to the limiting short LSB state at $\mathcal{D} \approx 60$.

To investigate the relationship between shear layer movement and changes in vortex shedding frequency during the ramp changes in Re$_c$, a short-time Fourier transform using a window length of $4c/\overline{u_\infty}$ and 75% overlap was performed on the wall-normal velocity fluctuations measured in the high-speed PIV configuration at the transition point. The frequency power spectra were averaged over the wall-normal extent of the field of view and over the two high-speed PIV runs. The results are presented in Figs. 4.11a and 4.11b for increasing and decreasing Re$_c$, respectively. Vortex shedding wavenumber (k) spectra were also calculated by performing a spatial Fourier transform on the wall-normal velocity measurements along the displacement thickness at each time instant of the low-speed PIV data. The wavenumber power spectra averaged over the ensemble of 13 low-speed PIV runs are plotted in Figs. 4.11c and 4.11d for increasing and decreasing Re$_c$, respectively.

During LSB formation (Fig. 4.11a), the strongest wall-normal velocity fluctuations start

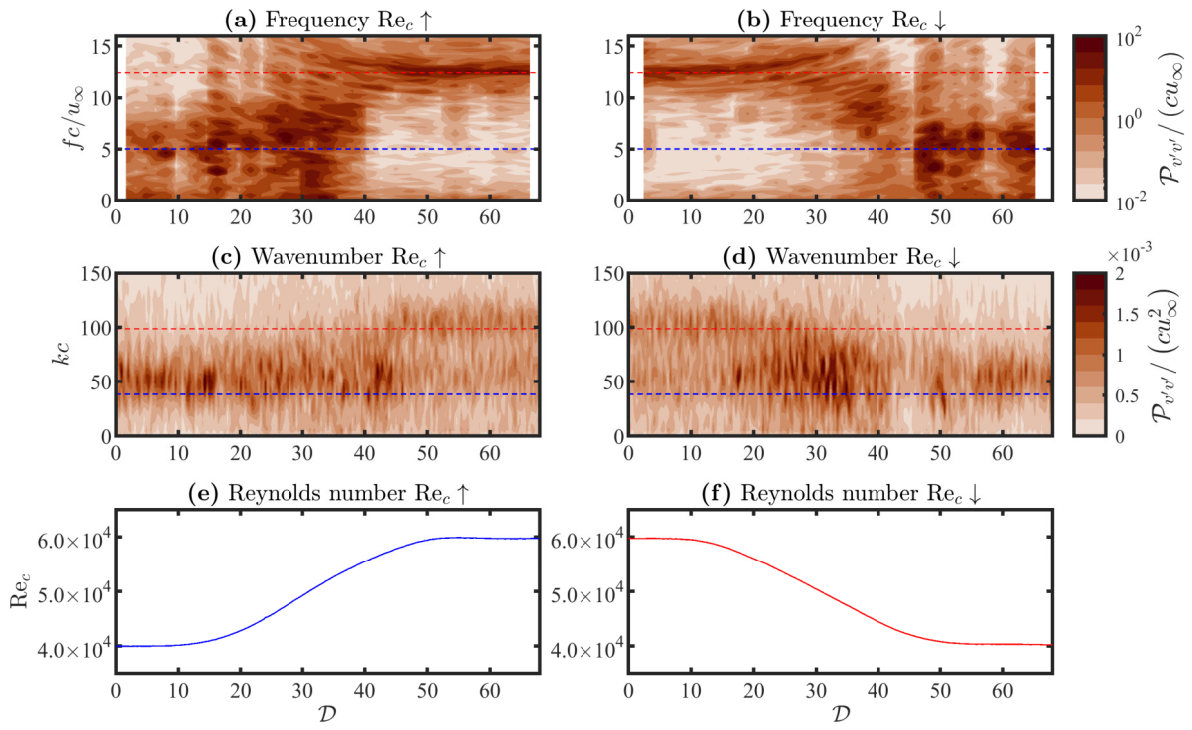


Figure 4.11: Frequency (a,b), and wavenumber (c,d), of integrated wall-normal velocity fluctuations during ramp changes in Re$_c$.

near the most amplified frequency of the limiting stalled state ($fc/\overline{u_\infty} = 5.1$, blue dashed line) until quasi-periodic vortex shedding is gradually established within a higher frequency band closely matching that observed in the limiting short LSB ($fc/\overline{u_\infty} = 12.5$, Fig. 4.5a, red dashed line). The wavenumber power spectrum (Fig. 4.11c) shows a progressive change between the relatively long wavelength disturbances amplified in the stalled state ($kc = 38.4$, blue dashed line) and the short wavelength disturbances ($kc = 98.7$, red dashed line) and their subharmonic ($kc = 49.4$) that are amplified in the short LSB state.

During LSB bursting, the most amplified frequency gradually decreases for $20 \lessapprox \mathcal{D} \lessapprox 40$ as the distance of the separated shear layer from the surface increases. Similar to the wavenumber spectrum for LSB formation, a progressive change in the wavelengths of amplified disturbances is also seen in the wavenumber power spectrum during LSB bursting (Fig. 4.11d). The overshoot in the distance of the separated shear layer from the surface at $\mathcal{D} \approx 50$ is accompanied by a widening of the band of unstable frequencies for $45 \lessapprox \mathcal{D} \lessapprox 55$. This transient change in frequency content is in agreement with linear stability theory, which predicts an increase in the most amplified frequency and broadening of the unstable frequency band with increasing distance of the separated shear layer from the surface [17]. Overall, the changes to the band of amplified frequencies and wavenumbers during LSB formation and bursting transients are consistent with the trends seen in quasi-steady LSBs, with higher frequencies and wavenumbers more amplified at higher Reynolds numbers [e.g., 74, 104].

Despite the relatively low acceleration employed in the present study, the processes of LSB formation and bursting display substantial hysteresis, as explored in the discussion of Figs. 4.7–4.10. Notably, after LSB bursting, transient-response-type low-frequency oscillations are observed in shear layer parameters (e.g., displacement thickness, Fig. 4.10). Variations in the location and angle of laminar separation from the airfoil surface are expected to be linked to variations in the streamwise surface pressure gradient [e.g., 176, 177]. Here, a simplified formulation of the governing equations is used to explore the relative significance of temporal and convective accelerations on the streamwise surface pressure gradient and the angle between the separated shear layer and the airfoil surface.

In the upstream portion of the separated shear layer, the flow is nearly wall-parallel and viscous effects are confined to a relatively thin region near the airfoil surface. Neglecting viscous effects at the edge of the boundary layer and the wall-normal pressure gradient within the boundary layer, the unsteady Bernoulli equation can be manipulated into an expression for the streamwise pressure coefficient gradient in terms of the edge velocity:

$$\frac{\partial C_p}{\partial (x/c)} = \frac{-2c}{u_\infty^2} \left(\frac{\partial u_e}{\partial t} + u_e \frac{\partial u_e}{\partial x} \right) \tag{4.1}$$

During quasi-steady free-stream velocity changes, the convective acceleration is expected to dominate the right hand side of Eq. 4.1. In the forward laminar part of the separated flow region, the shear layer rises at a nearly constant angle (γ) from the airfoil surface in the surface attached coordinate system (Figs. 4.4, 4.6, and 4.7), and the boundary layer edge velocity is approximately constant [e.g., 177]. Figure 4.12a presents the temporal and convective acceleration terms at the boundary layer edge, spatially averaged over the upstream laminar portion of the LSB ($0.24 \leq x/c \leq 0.34$) during the ramp up and ramp down. Also plotted is the temporal acceleration of the free-stream velocity ($\partial \widetilde{u_\infty}/\partial t$). The acceleration terms have been normalised by the time-dependent ensemble averaged free-stream velocity, which skews the peak non-dimensional free-stream accelerations to times when the free-stream velocity is lower. The figure confirms the quasi-steady nature of the imposed ramp changes in free-stream velocity, revealing that the convective acceleration term dominates the temporal acceleration term in the upstream laminar portion of the LSB. Figure 4.12b presents the ensemble-averaged separated shear layer angle in radians ($\widetilde{\gamma}$) during LSB formation and bursting transients, which qualitatively follows similar trends to the convective acceleration term in Fig. 4.12a. These results suggest that the observed LSB formation and bursting transients are primarily a consequence of a bifurcation from one limiting flow state to another, with the imposed acceleration playing a comparatively minor role in the flow development under the investigated conditions. On the other hand, the quantitative development of the observed transient may change at relatively high free-stream accelerations due to the increased influence of the temporal acceleration term on the streamwise pressure gradient in Eq. 4.1.

The results presented in Figs. 4.6–4.10 demonstrate that both formation and bursting transients last an order of magnitude longer than the global convective timescale ($\mathcal{D}$) and that quasi-steady conditions are reached sooner after LSB formation than after LSB

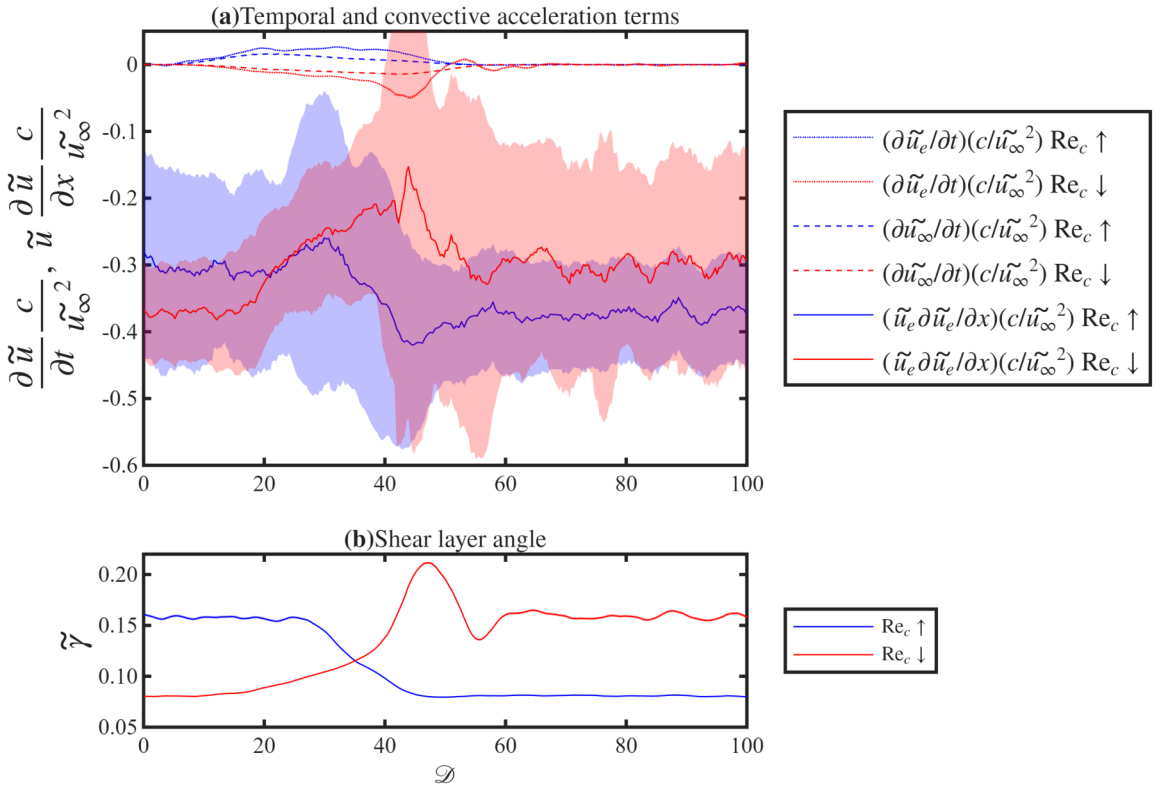


Figure 4.12: (a) Temporal acceleration of free-stream velocity - - - and boundary layer edge velocity ... and convective acceleration at boundary layer edge —. (b) Ensemble averaged separated shear layer angle. Shaded areas represent uncertainty (95% confidence).

bursting. The durations of the LSB formation and bursting transients can be quantified by the $90\% - 10\%$ and $10\% - 90\%$ transition durations of the shear layer angle, respectively [e.g., 178]. These transition durations are $14c/u_\infty$, and $22c/u_\infty$ for LSB formation and bursting, respectively. In the present study, the ratio of the LSB bursting period to the LSB formation period is approximately 1.5. Similar to the present results, previous studies involving the use of active flow control methods to suppress boundary layer separation on airfoils have reported that the transient associated with the deactivation of flow control leading to stall is longer than that associated with activation of flow control to promote reattachment [e.g., 25, 179, 180].

4.4 Concluding Remarks

An experimental study was performed on a NACA 0018 airfoil undergoing ramp changes in chord Reynolds number between $\mathrm{Re}_c = 4.0 \times 10^4$ and 6.0×10^4 at an angle of attack of 6°. At a steady state chord Reynolds number of 4.0×10^4, transition is delayed, the airfoil is stalled, and laminar separation without reattachment occurs. At a steady state chord

Reynolds number of 6.0×10^4, the separated laminar shear layer transitions to turbulence more quickly and reattaches, forming a short LSB. Surface pressure and PIV measurements were performed to study the transient dynamics of LSB formation and bursting on the suction surface of the airfoil during the ramp changes in free-stream velocity.

During the ramp-up in free-stream velocity, the flow switches from the stalled state to the short LSB state. LSB formation is preceded by a gradual upstream movement of transition as the chord Reynolds number increases. Although the ramp change in Re_c occurs over the time period $0 \leq \mathcal{D} \leq 60$, the LSB formation process is characterised by a largely constant separated shear layer trajectory followed by relatively abrupt decrease in the distance of the separated shear layer from the surface between $30 \leq \mathcal{D} \leq 50$. This coincides with the initiation of reattachment and a sudden downstream shift of the transition point due to the increase in stability of the separated shear layer with greater proximity to the surface. After reattachment, the transition point moves gradually upstream again until the flow converges to the limiting short LSB state.

During the ramp-down in free-stream velocity, the flow switches from the short LSB state to the stalled state. The LSB bursting transient is initiated by a gradual enlargement of the recirculating flow region and downstream movement of the transition point. When reattachment ceases and the separated shear layer moves rapidly away from the airfoil surface, the transition point moves suddenly upstream due to the reduced stability of the separated flow. After cessation of reattachment, the transition point gradually moves downstream again as the limiting stalled state is approached. The cessation of reattachment is also followed by significant oscillations of the distance of the separated shear layer from the airfoil surface that resemble the step response of a second-order under-damped system. The persistence of these oscillations causes the bursting transient to be longer than the LSB formation transient, with the final stalled state reached at $\mathcal{D} \approx 60$.

The results show that both LSB formation and bursting transients occur over a time period that is substantially longer than the time scales of unstable disturbances in the separated shear layer. Consequently, the most amplified frequencies and wavenumbers of the separated flow show a gradual increase or decrease with increasing or decreasing chord Reynolds number, respectively, following the trends expected for quasi-steady changes in Reynolds number between the limiting flow states.

The movement of the separated shear layer was linked to transient changes in the streamwise surface pressure gradient. A comparison of temporal and convective acceleration terms revealed that changes in the pressure gradient were balanced primarily by convective acceleration, whereas the temporal acceleration term was substantially smaller in magnitude, pointing to the quasi-steady nature of the imposed ramp changes in free-stream velocity. This suggests that, at relatively low free-stream acceleration magnitudes, the dynamics of the observed LSB formation and bursting transients are primarily a consequence of bifurcation between the limiting flow states.

Chapter 5

Spanwise Flow Development and Transient Loading During LSB Formation and Bursting

The transient streamwise and spanwise LSB development during a quasi-steady change in free-stream velocity is compared between airfoil and finite wing models at equivalent effective angles of attack. Transient lift forces are also characterised during LSB formation and bursting. The results show that LSB formation involves a spanwise contraction of the reverse flow region, whereas LSB bursting involves a spanwise expansion of the reverse flow region. The transient changes in the spanwise extent of reverse flow are more gradual on the wing than on the airfoil because of the spanwise variation in effective angle of attack of the wing. Likewise, the change in lift during LSB formation or bursting for the wing is more gradual than for the airfoil. During bursting, it is found that reattachment ceases first at the spanwise location of maximum LSB thickness. The LSB forming on the wing is classified as a short LSB near the root and tip of the wing, and as a long LSB near the midspan. This demonstrates that bursting of an LSB at a single spanwise location is not sufficient to cause bursting of the entire LSB, and that three-dimensional effects on LSB development must be accounted for when applying bursting criteria to finite wings.

This chapter has been adapted from

Toppings, C. E. & Yarusevych, S. May 2024 Laminar separation bubble formation and bursting on a finite wing. *Journal of Fluid Mechanics* **986**, A26. DOI.

5.1 Introduction

Due to the deleterious effects of LSB bursting on the performance of wings and airfoils, the description and prediction of the conditions under which bursting occurs has been the focus of multiple investigations [6, 7, 30, 78, 82, 181]. Although much effort has been focused on determining whether a short or long LSB will form under a given set of steady operating conditions, the evolution of an LSB between short LSB, long LSB, and fully separated states is an inherently unsteady process that has received significantly less attention. Previous studies of LSBs in unsteady flows have found differences in LSB structure and dynamics from those observed during quasi-steady changes in operating conditions [84, 87, 88].

Due to the abrupt changes in aerodynamic loads, bursting presents a challenge to the design of safe and efficient aircraft and turbo-machines that operate at low Reynolds numbers. In these applications, three-dimensional end effects are also present. Wing tip and root effects on LSBs have been documented in steady flows, but little is known about the effect of finite aspect ratio on the unsteady processes of LSB formation and bursting. The objectives of this chapter are to compare the dynamics of LSB formation and bursting on a nominally two-dimensional airfoil and a finite wing, to quantify the unsteady aerodynamic forces produced during LSB formation and bursting, and to relate the aerodynamic forces to the flow field development. To achieve these objectives, wind tunnel experiments were performed on a two-dimensional airfoil model and a finite wing model. The models were subjected to ramp changes in free-stream velocity which triggered LSB formation and bursting due to the corresponding change in Reynolds number. Synchronised direct-force and particle image velocimetry (PIV) measurements were performed to elucidate the physical mechanisms responsible for the transient aerodynamic forces produced during the changes in free-stream velocity.

5.2 Description of Experiments

Wind tunnel tests were undertaken on two-dimensional airfoil and finite wing models in the closed-loop wind tunnel at the University of Waterloo. Over the range of Reynolds numbers considered, the turbulence intensity was measured to be less than 0.16%. The free-stream velocity in the test section was monitored by a single normal hot-wire anemometer located at the exit of the tunnel's 9:1 contraction.

The NACA 0018 wing model had a chord length of $c = 0.2\,\mathrm{m}$ and a span of $0.5\,\mathrm{m}$, corresponding to an aspect ratio of 2.5. To convert the wing model into a nominally two-dimensional airfoil, an extension was added to the end of the wing so that the model spanned the entire test section, as illustrated in Fig. 5.1. Both the wing model and the extension were machined from a single block of acrylic and hand polished. Data are presented in a surface attached coordinate system with the origin located at the wing root leading edge, the positive x-axis tangent to the suction surface, the positive y-axis normal to the suction surface, and the positive z-axis parallel to the span. Data from the surface-tangent top-view

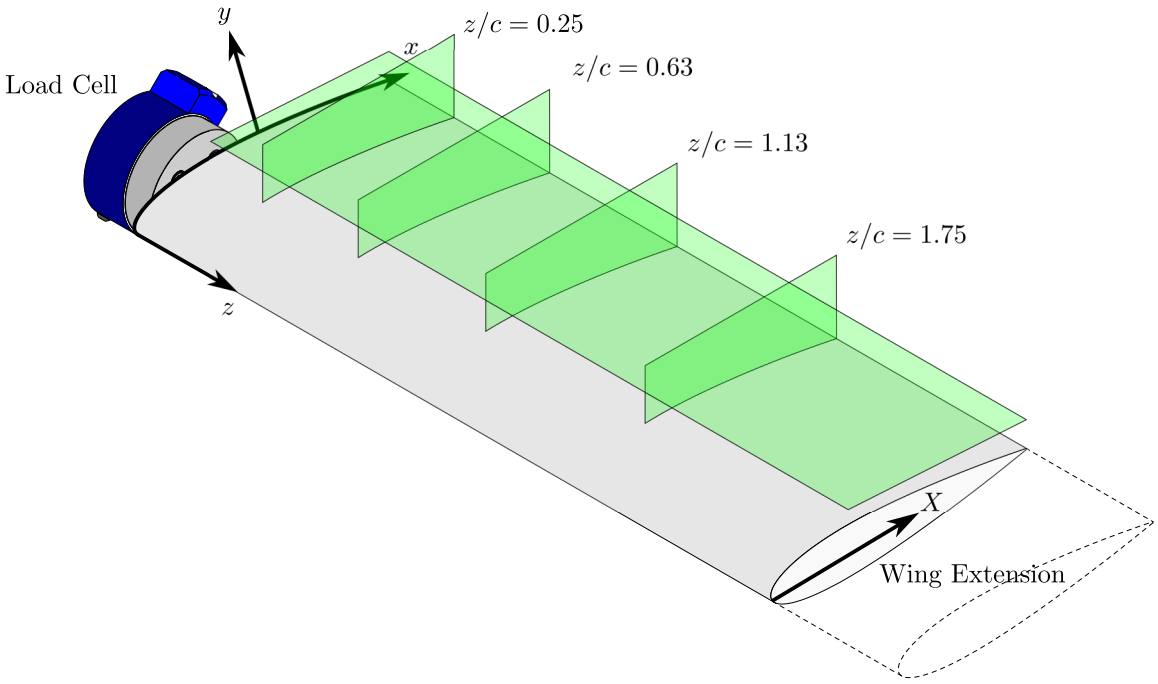


Figure 5.1: Coordinate system definitions and PIV measurement plane orientations.

PIV configuration is presented in a chord-based coordinate system, where the X-axis is parallel to the model chord.

Ramp changes in Reynolds number were produced by varying the wind tunnel's fan speed. Figure 5.2 presents ensemble-averaged hotwire measurements of the ramp changes in free-stream velocity used to cause LSB formation and bursting on the wing model due to the change in Reynolds number. Because the free-stream velocity changed during the experiment, the non-dimensional time that the data is plotted against is defined as $\mathcal{D} = (1/c)\int_0^t u_\infty dt$, equivalent to the number of chord lengths that the free-stream has travelled at time t. Because the LSB bursting Reynolds number depends on the angle of attack (α), three different sets of free-stream ramp changes were performed, as summarised in Table 5.1. For all angles of attack, the initial and final Reynolds numbers were separated by approximately 2×10^4, so that spontaneous LSB formation or bursting did not occur at the limiting Reynolds numbers, and were chosen such that LSB formation or bursting on the two-dimensional model occurred approximately halfway between the limiting Reynolds numbers during quasi-steady changes in free-stream velocity. The same limiting Reynolds numbers were used for all measurements at $\alpha = 5°$ and $6°$ to facilitate comparisons between the two-dimensional airfoil and wing models at similar geometric and effective angles of attack.

The duration of the ramps down was limited by the time required for the wind tunnel fan to coast down from the higher limiting free-stream velocity to the lower limiting free-stream velocity. The duration of the ramp up at each angle of attack was set to match the duration of the ramp down at the same angle of attack. Because the duration of the ramp changes was limited by the inertia of the fan, the ramp changes occurred over a greater number of

Table 5.1: Reynolds number ranges for free-stream velocity ramp changes.

Angle of attack	Reynolds number range	Non-dimensional Acceleration
$\alpha = 3°$	$4.8 \times 10^4 \leq Re_c \leq 7.0 \times 10^4$	$\lvert ac/u_\infty^2 \rvert \leq 0.011$
$\alpha = 5°$	$5.4 \times 10^4 \leq Re_c \leq 7.4 \times 10^4$	$\lvert ac/u_\infty^2 \rvert \leq 0.009$
$\alpha = 6°$	$5.4 \times 10^4 \leq Re_c \leq 7.4 \times 10^4$	$\lvert ac/u_\infty^2 \rvert \leq 0.009$
$\alpha = 9°$	$6.5 \times 10^4 \leq Re_c \leq 8.6 \times 10^4$	$\lvert ac/u_\infty^2 \rvert \leq 0.008$

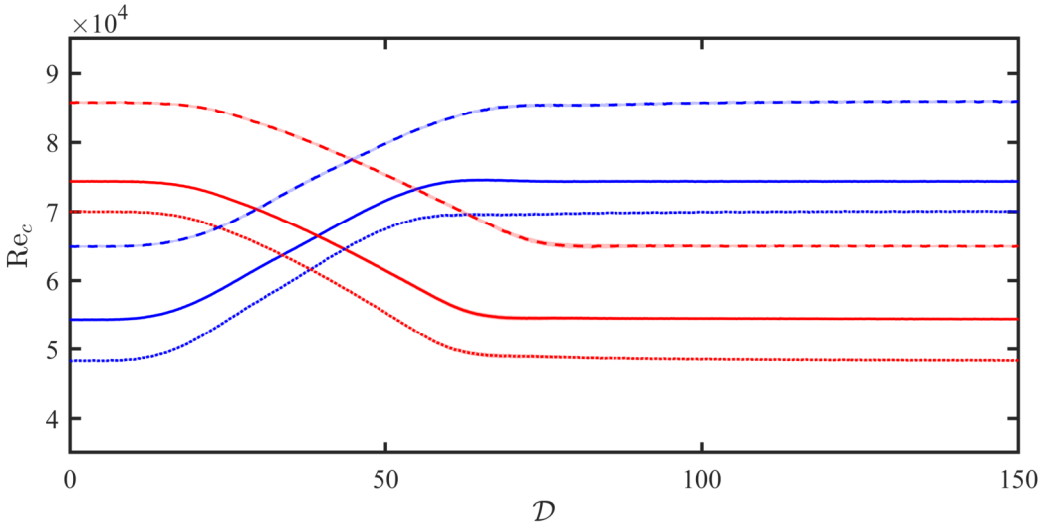


Figure 5.2: Ramp change in free-stream velocity for $\alpha = 3°$ ..... , $\alpha = 5°$ and $6°$ —— , and $\alpha = 9°$ - - - - . Note, the ensemble standard deviation is on the order of the line thicknesses.

convective time scales for the higher angles of attack where the Reynolds number was higher, as shown in Fig. 5.2. Thus, the non-dimensional accelerations (ac/u_∞^2, Table 5.1) were also lower for higher angles of attack. The largest non-dimensional acceleration, occurring at an angle of attack of $\alpha = 6°$, was less than 0.011. Therefore, the change in streamwise pressure gradient due to the acceleration of the free-stream during the ramp changes is assumed to be insignificant, and transient changes in the flow field are ascribed primarily to the effects of LSB formation or bursting [1].

5.2.1 Measurement Techniques

The principal results of this chapter are based on lift force and PIV measurements which are described in this section. Due to the differing data storage requirements for lift force and PIV measurements, the number of runs used to compute ensemble statistics varied depending on the flow conditions and measurement technique. For the PIV measurements, an ensemble of 20 runs was recorded for each type of transient change in operating conditions. For the finite wing, lift force measurements at an angle of attack of 6° were taken over

Table 5.2: Ensemble sizes of transient lift force and PIV measurements.

Model	α	Lift force	PIV
Airfoil	3°	40	-
Airfoil	5°	40	20
Airfoil	6°	40	20
Airfoil	9°	40	-
Wing	3°	40	-
Wing	6°	160	20
Wing	9°	40	-

an ensemble of 160 increasing and decreasing ramp changes in free-stream velocity. For all other angles of attack and model conditions, lift force measurements were taken over an ensemble of 40 increasing and decreasing ramp changes in free-stream velocity. The ensemble sizes for each model configuration and measurement technique are summarised in Table 5.2.

Lift Force

The finite wing and two-dimensional airfoil models were mounted on a 6-axis JR3 30E12A4 load cell for direct-force lift measurements. The resolution in lift force was 0.005 N, and the absolute accuracy was within 0.1 N. Due to the relatively small magnitudes and large uncertainties of drag force measurements under the conditions investigated, only lift measurements are considered in the present work. In addition to the lift force measurements obtained during ramp changes in free-stream velocity, quasi-steady lift force measurements were performed over the Reynolds number range of each ramp change in Reynolds number increments of approximately 700. For each quasi-steady lift measurement, the flow was allowed to stabilise for 20 s before the lift force was recorded for a period of 60 s. To investigate lift hysteresis, quasi-steady lift measurements were performed for both increasing and decreasing Reynolds numbers. All lift measurements were taken at a sampling frequency of 10 000 Hz and low-pass filtered at 10 Hz using a Chebyshev type II filter [182] to attenuate structural vibrations.

Particle Image Velocimetry

Particle image velocimetry measurements were performed on the finite wing at an angle of attack of 6° and two-dimensional airfoil at angles of attack of 6° and 5° during the imposed ramp changes in free-stream velocity. The angles of attack for PIV measurements on the two-dimensional airfoil were chosen to match the geometric angle of attack and the effective angle of the wing root region, respectively, on the finite wing. All PIV measurement planes (Fig. 5.1) were surveyed separately. PIV measurements were also taken in steady free-stream conditions at $\mathrm{Re}_c = 5.4 \times 10^4$ and $\mathrm{Re}_c = 7.4 \times 10^4$. To improve the statistical convergence of ensemble-averaged quantities obtained from transient side-view PIV measurements,

temporal averaging with a window length of $5c/\overline{u_\infty}$ was applied. The overall trends in time-dependent statistics were found to be largely unaffected for window lengths between $2c/\overline{u_\infty}$ and $8c/\overline{u_\infty}$.

For all PIV measurements, the flow was seeded with water-glycol fog particles with a diameter of approximately 1 µm that were illuminated with a Photonics DM20-527 Nd:YLF pulsed laser. The laser sheet thickness was approximately 2 mm. Particle image preprocessing was performed using sliding temporal minimum subtraction and local intensity normalisation. The correlation statistics method [149] was used to estimate the uncertainty in the resulting vector fields due to random errors. Vector fields were calculated using multi-pass cross-correlation algorithm with window deformation in the LaVision DaVis 10 software [148]. During transient ramp changes in free-stream velocity, PIV measurements were triggered to start 0.5 s before the wind tunnel fan was commanded to start changing speed. At each measurement plane for the side-view and top-view PIV configurations, an ensemble of 20 recordings were obtained for both increasing and decreasing ramp changes in free-stream velocity.

In the side-view PIV configuration, measurements were taken in z-normal planes at $z/c = 0.250$, 0.625, 1.125, and 1.750 for the finite wing, and at $z/c = 1.125$ and 1.750 on the two-dimensional airfoil, as illustrated in Fig. 5.1. The side-view PIV measurements employed two LaVision Imager sCMOS 5.5 megapixel cameras in a side-by-side arrangement with 200 mm focal length lenses and aperture settings of $f/2$. The camera sensors were cropped to a resolution of 2560 px $\times$ 1024 px, and their combined field of view spanned $0.28 \leq x/c \leq 0.98$ and $0 \leq y/c \leq 0.11$. Particle images were taken in double-frame mode with a frame separation of 50 µs at a sampling rate of 52.33 Hz. For measurements of the limiting flow states under steady free-stream conditions, 1500 samples were acquired at each measurement plane for a total sampling time of 28.66 s. During transient ramp changes in free-stream velocity, recordings of 523 samples at each measurement plane were obtained for a total sampling time of 9.99 s. For velocity vector calculation, the initial and final interrogation window sizes were 24px $\times$ 24px and 16px $\times$ 16px, respectively. With 75% window overlap, the resulting velocity fields have a vector pitch of 0.12 mm. The uncertainty in instantaneous velocity measurements from the side-view PIV measurements along the core of the separated shear layer is estimated to be 5% and 6% of the free-stream velocity for the streamwise (u) and wall-normal (v) velocity components, respectively, at a confidence level of 95%.

In the top-view PIV configuration, measurements were taken in a single plane tangent to but offset from the suction surface of the finite wing and two-dimensional airfoil (Fig. 5.1). The minimum distance between the top-view measurement plane and the model surface was approximately 8 mm. The top-view PIV measurements employed three LaVision Imager sCMOS 5.5 megapixel cameras in a side-by side arrangement with 50 mm focal length lenses and aperture settings of $f/2$. The combined field of view spanned $0.27 \leq x/c \leq 1$ and $0 \leq z/c \leq 2.50$. Particle images were taken in double-frame mode with a frame separation of 100 µs at a sampling rate of 25.03 Hz. For measurements of the limiting flow states under steady free-stream conditions, 1500 samples were acquired for a total sampling time of 28.66 s. During each ramp change in free-stream velocity, 250 samples were obtained

Table 5.3: PIV parameters.

Parameter	Side-view	Top-View
Cameras	2× LaVision Imager sCMOS	
Cropped sensor size	2560px × 1024px	2560px × 2560px
Combined field of view	$0.69c \times 0.11c$	$0.73c \times 2.50c$
Lens focal length	200 mm	50 mm
Aperture	$f/2$	
Magnification factor	0.22	0.10
Sampling frequency	52.33 Hz	25.03 Hz
Number of samples in transient conditions	523	250
Number of samples in limiting conditions	1500	
Laser pulse separation	50 µs	100 µs
Maximum particle image displacement	13px	8px
Initial interrogation window size	24px × 24px	64px × 64px
Final interrogation window size	16px × 16px	24px × 24px
Vector pitch	0.12 mm	0.40 mm
Light source	Photonics DM20-527 Nd:YLF pulsed laser	
Light sheet thickness	2 mm	
Particles	1 µm diameter water-glycol fog	

for a total sampling time of 9.99 s. For velocity vector calculation, the initial and final interrogation window sizes were 64px × 64px and 24px × 24px, respectively. With 75% window overlap, the resulting velocity fields have a vector pitch of 0.40 mm. The uncertainty due to random errors in instantaneous measurements of the streamwise (u) and spanwise (w) velocity components in the vicinity of the separated shear layer was estimated to be less than 6% and 5% of the free-stream velocity, respectively, at a confidence level of 95%.

Note that although the field of view of top-view PIV measurements on the two-dimensional airfoil is restricted to $z/c < 2.5$, the two-dimensional airfoil model extends across the entire width of the test section up to $z/c = 3.0$. Thus, the midspan of the airfoil model is located at $z/c = 1.5$.

5.2.2 Data Processing Techniques

To investigate the dynamics of the transition process, a continuous wavelet transform (Eq. 3.3) was applied to the wall-normal velocity fluctuations from side view PIV measurements, quantifying the wavenumbers of disturbances that lead to vortex shedding from the separated shear layer. The wall-normal velocity fluctuations (v') were extracted at the y location corresponding to the boundary layer displacement thickness. In this chapter, the Airy wavelet with a duration of $\sqrt{15}$ is used as the mother wavelet [e.g., 156]. The ensemble-averaged wavelet amplitude ($\widetilde{|\psi|}$) plotted in the scalograms in Figs. 5.16 and 5.17 was computed by averaging the absolute value of the wavelet transform magnitude over the

ensemble of 20 PIV recordings of ramp changes in free-stream velocity and over a sliding temporal window of length $5c/\overline{u_\infty}$.

5.3 Results

Transient ensemble-averaged lift coefficients ($\widetilde{C_L}$) are plotted in Fig. 5.3 for the first 100 convective timescales after initiation of the ramp changes in free-stream velocity for each model configuration and angle of attack. The ensemble size is 40 for all model configurations and angles of attack except for the wing at 6°, for which the ensemble size is 160. At a geometric angle of attack of $\alpha = 6°$, the effective angle of attack at the wing root is reduced to approximately 5° as shown by Toppings *et al.* [115]. To provide a comparison between the wing and the airfoil models at similar effective angles of attack, the lift coefficients from the wing at $\alpha = 6°$ (solid lines) and the airfoil at $\alpha = 5°$ (dashed lines) are both presented in Fig. 5.3e.

At each angle of attack, the lift coefficient of the wing is expectedly lower than that of the airfoil for both limiting flow states, and changes in lift coefficient during the ramp changes in free-stream velocity are more gradual for the wing. As the angle of attack is increased from $\alpha = 3°$ to 9°, the difference in lift coefficient between the limiting flow states increases, a trend which is observed for both the airfoil and wing. During the ramp up in free-stream velocity at a given angle of attack, a period of rapidly increasing lift coefficient occurs at similar times for the airfoil and wing models. However, the time at which the most rapid decrease in lift coefficient occurs during the ramp down is shifted to earlier times for the wing relative to the airfoil. For the airfoil and wing at $\alpha = 6°$ and 9° (Figs. 5.3b, 5.3c, 5.3e, and 5.3f), the most rapid changes in the ensemble-average lift coefficient occur simultaneously with a notable change in the level of ensemble root-mean-square (RMS) lift coefficient fluctuations (shaded regions). The change in RMS lift coefficient fluctuations suggests that these changes in ensemble-average lift coefficient are indicative of boundary layer reattachment or stall during the ramp up or ramp down cases, respectively [e.g., 183].

The asymmetry between the time-histories of the lift coefficients for the ramps up and ramps down is evidence of hysteresis in the reattachment and stall processes, which is most notable for the airfoil. For all cases, the lift coefficient takes longer to settle to the stalled limiting state during the ramp down in free-stream velocity than it does to settle to the reattached limiting state during the ramp up in free-stream velocity. For the airfoil at $\alpha = 9°$, the limiting stalled state was not reached within the data acquisition period after the ramp down. Although the imposed ramp changes in free-stream velocity are virtually monotonic, non-monotonic changes in lift coefficient are observed during the ramp down in free-stream velocity for the airfoil at $\alpha = 6°$ and 5° (Figs. 5.3b and 5.3e) within $50 \leq \mathcal{D} \leq 75$, where local maxima of the lift coefficient occur. A local maximum also occurs for the wing at $\alpha = 6°$ (Fig. 5.3e) near $\mathcal{D} = 50$. A similar local maximum in the lift coefficient time-history was observed by Kiefer *et al.* [63] for an airfoil during the dynamic stall process after a transient increase in angle of attack at significantly higher Reynolds numbers. The initial reduction in lift during dynamic stall is associated with the shedding

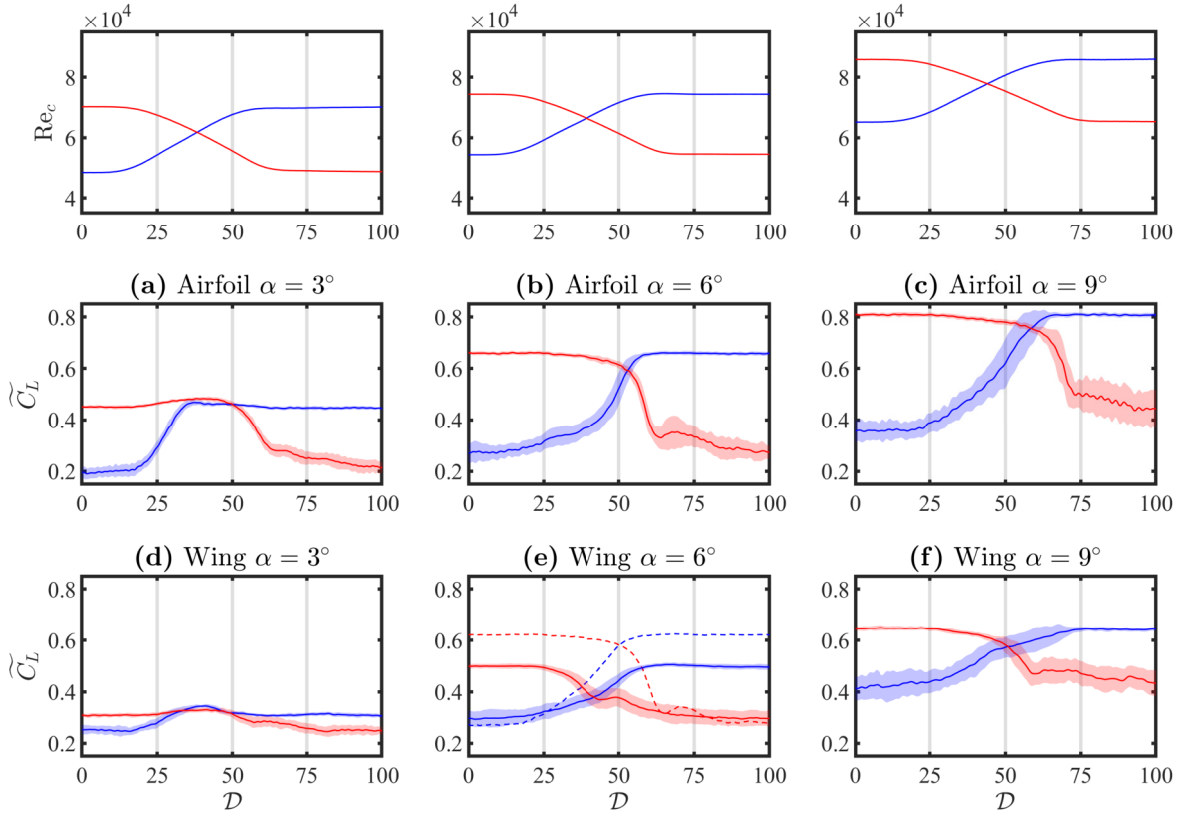


Figure 5.3: Ensemble-averaged lift coefficient versus convective time. Blue lines: ramp up, red lines: ramp down. Shaded areas represent ensemble RMS lift coefficient fluctuations. Dashed lines in e are from airfoil at $\alpha = 5°$.

of a dynamic stall vortex (DSV) from the leading edge shear layer [e.g., 57]. After the DSV is shed, a second weaker leading edge vortex forms [184]. The formation and shedding of the second vortex is associated with a transient increase and decrease in lift, respectively [184], and this mechanism is likely responsible for the local maximum in lift observed during the ramp down. This phenomenon is present to some extent for all cases considered here. Examination of individual runs for the airfoil at $\alpha = 9°$ revealed significant local maxima after the initial decrease in lift coefficient, and the absence of a local maximum in the ensemble-averaged lift coefficient during the ramp down for the airfoil $\alpha = 9°$ is the result of higher variability between runs at this angle of attack. Although not presented here for conciseness, non-monotonicity was also observed in the transient drag coefficients, with a local maximum in drag coefficient occurring at the same time as the initial decrease in lift coefficient, similar to that observed during dynamic stall at higher Reynolds numbers [63].

To compare the transient lift coefficients to those measured in quasi-steady flow, the ensemble-averaged lift coefficients during the ramp changes in free-stream velocity as well as lift coefficients measured in a steady free-stream are plotted versus Reynolds number in Fig. 5.4. The ensemble size is 40 for all model configurations and angles of attack except for the wing at 6°, for which the ensemble size is 160.

Similar to the results of Zaman & McKinzie [185], no significant hysteresis is observed in the quasi-steady lift measurements (black markers) for either the finite wing or two-dimensional airfoil. An increase in the quasi-steady lift coefficient (black markers) and decrease in root-mean-square (RMS) lift coefficient fluctuations (shaded grey region) with increasing Reynolds number is indicative of separated shear layer reattachment [16, 82]. This occurs at approximately $\mathrm{Re}_c = 6.2 \times 10^4$, 6.6×10^4, 6.7×10^4, and 7.6×10^4 for the airfoil at $\alpha = 3°$, $5°$, $6°$, and $9°$, respectively. The observed increase in Reynolds number required for reattachment with increasing angle of attack is consistent with the results of previous two-dimensional airfoil studies at low Reynolds numbers where reattachment is linked to the formation of an LSB [74, 186]. On the wing (Figs. 5.4d–5.4f), the increase of lift with increasing Reynolds number is noticeably more gradual (Figs. 5.4e and 5.4f), and no clear indication of sudden reattachment is observed at $\alpha = 3°$. For the wing at $\alpha = 6°$ and $9°$ (figs. 5e and 5f), reattachment and LSB formation can be inferred from the reduction in lift fluctuations that occurs near $\mathrm{Re}_c = 7.7 \times 10^4$ and $\mathrm{Re}_c = 8.1 \times 10^4$, respectively. This will be confirmed for the wing at $\alpha = 6°$ using PIV measurements in Section 5.3.1. The increase in the stall Reynolds number for the wing relative to the airfoil at the same geometric angles of attack for $\alpha = 6°$ and $9°$ is opposite of the change expected from the decrease of the effective angle of attack on the wing, and the underlying flow development will be explored in Section 5.3.1.

The transient lift coefficients during ramp changes in free-stream velocity (coloured lines) deviate substantially from the quasi-steady lift coefficients for the airfoil at all angles of attack (Figs. 5.4a–5.4c). For angles of attack of $\alpha = 5°$, $6°$, and $9°$ (Fig. 5.4e, Figs. 5.4b–5.4c) the transient lift coefficients of the airfoil exhibit similar hysteresis, lagging their quasi-steady values in counter-clockwise hysteresis loops. Although a counter-clockwise hysteresis loop is also observed in the transient lift coefficient of the airfoil at $\alpha = 3°$ (Fig. 5.4a), a different relationship between the transient and quasi-steady lift coefficients is observed. At this relatively low angle of attack, the transient lift coefficient during the ramp up is greater than the quasi-steady lift for $5.7 \times 10^4 \leq Re_c \leq 6.2 \times 10^4$. At low angles of attack, the adverse pressure gradient on the suction surface is expected to be weaker, and it is speculated that the increase in transient lift during the ramp up at the lowest angle of attack may be due to delayed separation resulting from the more favourable pressure gradient during free-stream acceleration. On the finite wing, both the quasi-steady and transient lift forces display a more gradual change with Reynolds number, and the differences between the two are largely within the experimental uncertainty.

The foregoing results pertain to a change in free-stream velocity that occurs over a time period on the order of 100 convective timescales at relatively low accelerations. Although the imposed changes in operating conditions are essentially quasi-steady, the lift coefficients display deviations from those in a steady free-stream. To quantify the duration of the lift coefficient transients, the time period of the largest amplitude excursion from the quasi-steady lift coefficient was computed using the methodology illustrated in Fig. 5.5a. Quasi-steady lift coefficients for the ramp up and ramp down were computed by linearly interpolating the quasi-steady lift coefficients at the instantaneous Reynolds number during the ramp change in free-stream velocity. The transient period ($\Delta\mathcal{D}_{\mathrm{transient}}$) is defined as the

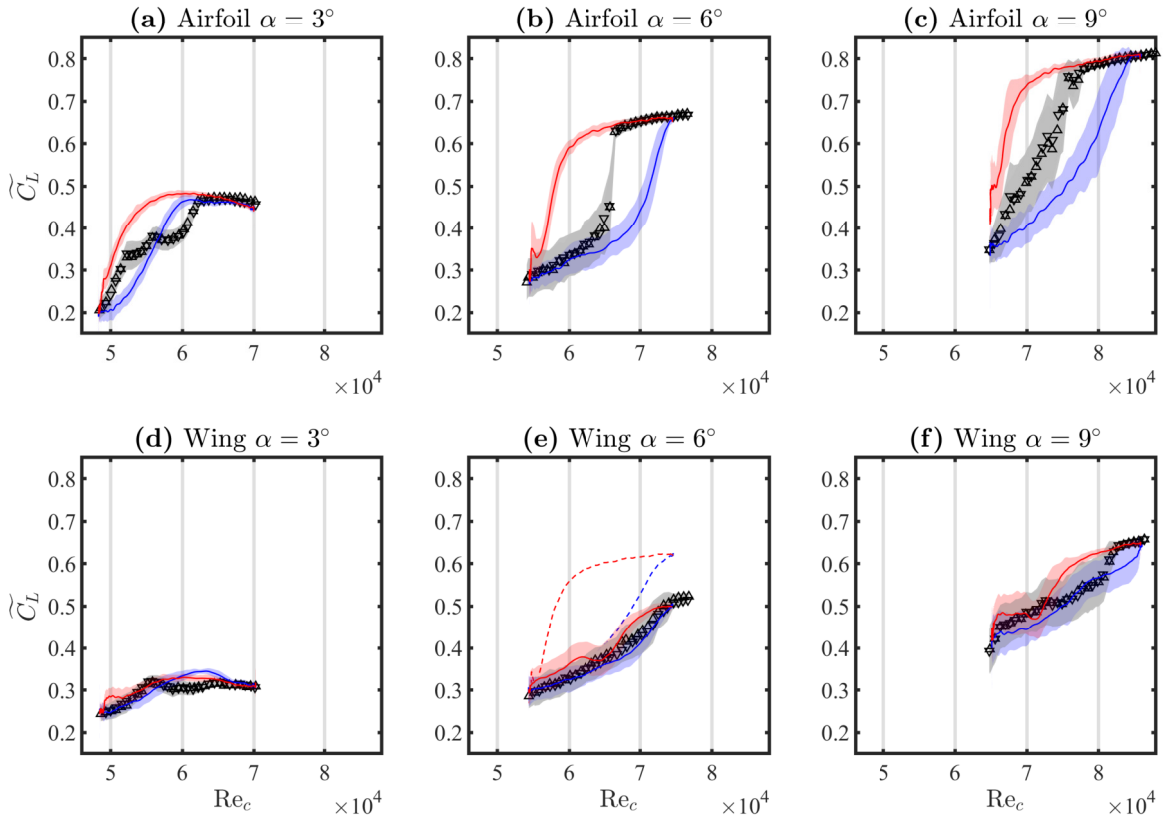


Figure 5.4: Ensemble-averaged lift coefficient versus Reynolds number. Blue lines: ramp up, red lines: ramp down, △: quasi-steady for increasing Re_c, ▽: quasi-steady for decreasing Re_c. Shaded areas represent ensemble RMS lift coefficient fluctuations. Dashed lines in e are from airfoil at $\alpha = 5°$.

time interval over which the lift coefficient in the unsteady flow continually deviates from the quasi-steady lift by more than twice the standard deviation of the quasi-steady lift estimates (shaded region in Fig. 5.5a) within the same time window. The ensemble-averaged transient periods are plotted in Fig. 5.5b. The ensemble size is 40 for all model configurations and angles of attack except for the wing at 6°, for which the ensemble size is 160.

For $\alpha > 3°$, the ensemble-averaged transient periods for the airfoil, which span $18 \leq \widetilde{\Delta\mathcal{D}}_{\text{transient}} \leq 26$, are substantially longer than those of the wing. These values are comparable to the mean stall delay period of $30c/u_\infty$ measured by Le Fouest *et al.* [187] for an airfoil undergoing a quasi-steady increase in angle of attack. At moderate angles of attack ($\alpha = 5°$ and 6°) the difference in transient times for the ramp up and ramp down are comparable. However, at $\alpha = 3°$ and 9°, there is a tendency for the stall transient to last longer than the reattachment transient. The relatively longer duration of the stall transient is consistent with previous studies that have observed longer stall transients than reattachment transients [e.g., 1, 25, 179, 180]. The significant decrease in estimated transient period for the airfoil during the ramp up at $\alpha = 3°$ is attributed to the crossing of the quasi-steady and unsteady lift coefficients in the $\mathrm{Re}_c - C_L$ plane

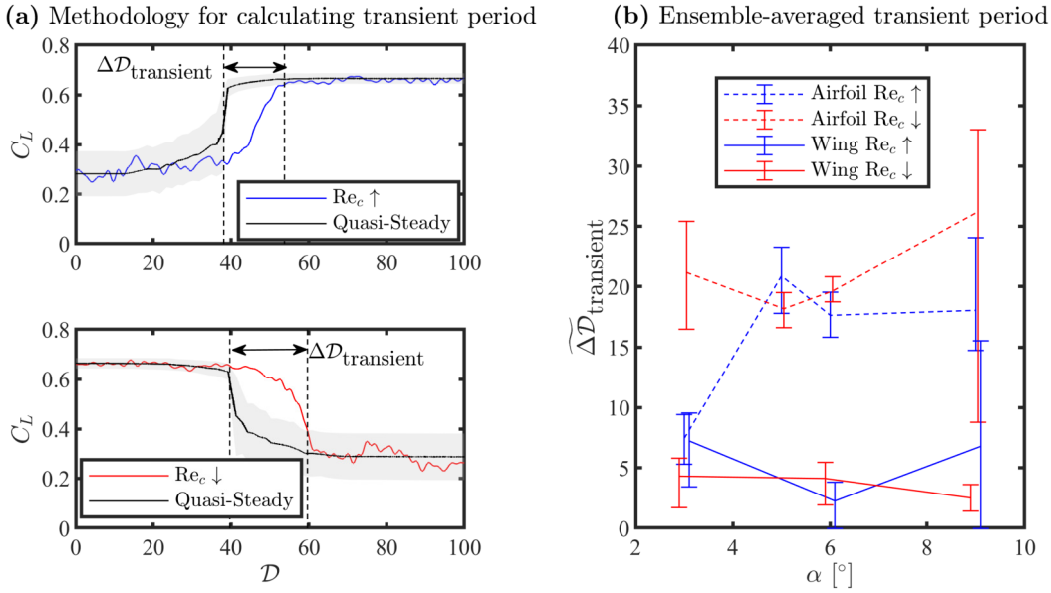


Figure 5.5: (a) Methodology for calculating transient period for a single ramp up (blue) and ramp down (red) for the airfoil at $\alpha = 6°$. Shaded areas indicated 2 standard deviations of the quasi-steady lift coefficients. (b) Ensemble-averaged transient period for all investigated conditions. Error bars denote quartiles. Horizontal axis shifted for clarity.

(Fig. 5.4a). For the wing, the ensemble-averaged transient periods span $2 \leq \widetilde{\Delta\mathcal{D}}_{\text{transient}} \leq 7$. The shorter transient periods for the wing are consistent with the relatively small differences between the ensemble-averaged transient and quasi-steady lift coefficients seen for the wing in Fig. 5.4, and no significant differences between stalling and reattachment transients are observed. Thus, the presence of the wing tip mitigates transient deviations of the unsteady lift coefficient from a quasi-steady response, which will be shown in Section 5.3.1 to stem from a more gradual progression of LSB formation and bursting across the span of the wing.

5.3.1 Flow Field Development

Limiting Flow States

Flow field development over the airfoil at angles of attack of $\alpha = 5°$ and $6°$ and over the wing at $\alpha = 6°$ was studied in detail using PIV measurements during the ramp changes in free-stream velocity and in steady free-stream conditions at the limiting Reynolds numbers of $\text{Re}_c = 5.4 \times 10^4$ and 7.4×10^4.

The mean streamwise velocity field from top-view PIV measurements on the two-dimensional airfoil in a steady free-stream at $\text{Re}_c = 5.4 \times 10^4$ and $\alpha = 6°$ is presented in Fig. 5.6a. Outside of the regions influenced by end effects, the top-view measurement plane intersects the core of the separated laminar shear layer at $x/c \approx 0.33$. Between $x/c \approx 0.40$ and 0.90, the top-view measurement plane is within the reverse flow region over the stalled

airfoil, and negative u velocities are measured. As the distance of the top-view measurement plane from the airfoil surface increases near the trailing edge, positive u velocities are again observed for $x/c \gtrapprox 0.90$. The plotted streamlines show relatively two-dimensional flow at the locations of both side-view measurement planes ($z/c = 1.13$ and 1.75), with larger three-dimensional effects present closer to the walls of the test section located at $z/c = 0$ and $z/c = 3$. The mean streamwise flowfield for the airfoil at $\mathrm{Re}_c = 5.4 \times 10^4$ and $\alpha = 6°$ is qualitatively similar to that at $\alpha = 5°$ (Fig. 5.6c), but a decrease in the boundary-layer separation angle reduces the measured extent of reverse flow.

In a steady free-stream at $\mathrm{Re}_c = 7.4 \times 10^4$, no reverse flow is present in the top-view PIV measurements outside of the regions influenced by end effects for the airfoil at $\alpha = 6°$ and 5° (Figs. 5.6b and 5.6d), but a corner separation [e.g., 126] persists at the end-wall junction at $z/c = 0$. The absence of reverse flow over most of the span is due to the relatively small maximum distance of the separated shear layer from the airfoil surface when an LSB forms.

For the wing at $\mathrm{Re}_c = 5.4 \times 10^4$ and an angle of attack of 6° (Fig. 5.6e) substantial tip effects are seen in the mean streamwise flow field for $z/c > 2.0$. No reverse flow is measured for $z/c > 2.0$, which suggests a reduction in the distance of the separated shear layer from the wing surface near the wing tip. The implied mean structure of the separated flow region, being thickest near the midspan and exhibiting spanwise flow towards the wing root and tip, is qualitatively similar to that previously reported for stalled cantilevered rectangular wings of aspect ratios between 1 and 4 [188]. At $\mathrm{Re}_c = 7.4 \times 10^4$, the flow development on the wing is notably different from that on the airfoil. On the wing, a region of reduced streamwise velocity occurs near $z/c = 1.13$ (Fig. 5.6f), implying an increase in the thickness of the LSB forming on the wing near the midspan, which will be confirmed later in this section using side-view PIV measurements. Excluding the difference in end conditions between the root and tip of the wing, the top-view PIV measurements over the midspan region of the wing are largely symmetric about the location $z/c = 1.13$ for both limiting Reynolds numbers. Noting that the true midspan of the wing is at $z/c = 1.25$, the shift of the symmetry location towards the wing root is consistent with the greater spanwise influence of the wing tip relative to the wing root on the separated flow [e.g., 188].

Using the side-view PIV configuration, LSB development on the wing and airfoil in steady free-stream conditions is illustrated in Fig. 5.7, which presents contours of mean streamwise velocity. The zero-net-streamwise mass flux line [20] is plotted to denote the wall-normal extent of recirculating flow. The locations of separation and reattachment were estimated by extrapolating the zero-net-streamwise mass flux line to the model surface. Because spanwise variations between the two side-view measurement planes on the airfoil are relatively minor compared to the wing, only the plane at $z/c = 1.75$ is presented for the airfoil. At $\mathrm{Re}_c = 5.4 \times 10^4$, the boundary layer separates upstream of the field of view and does not reattach on the airfoil or on the wing for $z/c \geq 0.63$ (Figs. 5.7b, 5.7d, 5.7e, 5.7h, and 5.7j). For the wing at $z/c = 0.25$, the influence of the wing root reduces the extent of separation due to spanwise flow [124], evidenced by the spanwise component of the streamlines in Fig. 5.6e.

At $\mathrm{Re}_c = 7.4 \times 10^4$ (Figs. 5.7b, 5.7d, 5.7f, 5.7h, 5.7j, and 5.7l), the separated shear layer reattaches to the airfoil and wing surfaces, forming an LSB. On the airfoil, as the angle of

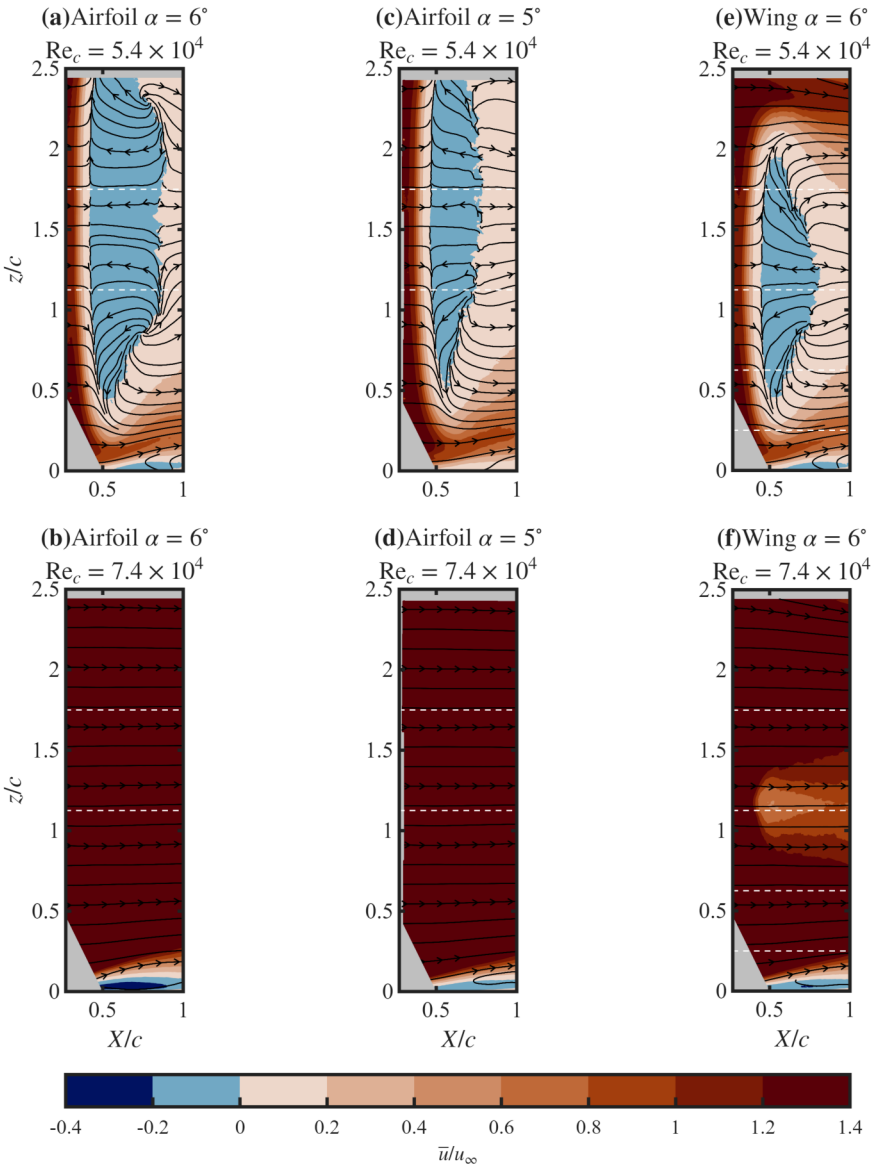


Figure 5.6: Mean streamwise velocity fields of the limiting flow states from top-view PIV. Dashed white lines indicate side-view measurement planes.

attack is reduced from $\alpha = 6^\circ$ to $\alpha = 5^\circ$ (Fig. 5.7b and Fig. 5.7d), there is a downstream shift in the locations of transition and reattachment, consistent with the established trend for LSBs on airfoils [e.g., 16]. For the same geometric angle of attack of $\alpha = 6^\circ$, reattachment on the airfoil (Fig. 5.7b) occurs farther upstream compared to that on the wing in the region outside of direct root effects ($z/c \geq 0.63$, Figs. 5.7f, 5.7h, and 5.7j). The differences in the separation and reattachment locations on the airfoil for $\alpha = 5^\circ$ and wing at $z/c = 0.63$ for $\alpha = 6^\circ$ are within the variations expected for a two-dimensional LSB [189]. Thus, the effective angle of attack at this location on the wing is approximately 5°, in agreement with

lifting line results for the same geometry [115]. Despite the expected monotonic decrease in effective angle of attack on the wing with increasing z, changes in the LSB thickness and the locations of separation and reattachment on the wing are non-monotonic for $0.63 \leq z/c \leq 1.75$. At $z/c = 1.13$ (Fig. 5.7h) there is a substantial increase in the distance of the separated shear layer from the wing surface, and the locations of separation and reattachment shift upstream and downstream, respectively. The presence of two separate regions of reverse flow below the separated shear layer in the PIV measurements suggests that spanwise flow not captured by the planar PIV measurements substantially alters the structure of the LSB at this location. Despite a further reduction in effective angle of attack at $z/c = 1.75$ (Fig. 5.7f), the streamwise velocity contours of the LSB at this location largely resemble those seen at $z/c = 0.63$, aside from a relatively small downstream shift in separation and reattachment locations. The decrease in LSB thickness near the wing root and tip relative to the midspan is consistent with the suppression of LSB formation due to tip effects observed at a higher Reynolds number [$\mathrm{Re}_c = 1.25 \times 10^5$, 124].

The momentum transfer across the shear layer due to velocity fluctuations as a result of transition is explored in Fig. 5.8, which presents contours of Reynolds shear stress ($\overline{u'v'}$). The point of transition is indicated by the white markers, defined as the streamwise location where the Reynolds shear stress at $y = \delta_x^*$ first exceeds the threshold of $0.001u_e^2$, where u_e is the local boundary layer edge velocity and δ_x^* is the displacement thickness of the u velocity profile. Although this transition criterion based on the one used by Ol *et al.* [171] and Hain *et al.* [170] depends on the threshold chosen, it is preferred in the present analysis because it is well defined for both reattaching and fully separated flow states. Other transition criteria used for LSBs that do not depend on an arbitrary threshold, such as the location of maximum displacement thickness [e.g., 169] or maximum boundary layer shape factor [e.g., 36], are not generally applicable when reattachment does not occur.

For both the airfoil and the wing, substantially higher maximum values of Reynolds shear stress occur at $\mathrm{Re}_c = 7.4 \times 10^4$ than at $\mathrm{Re}_c = 5.4 \times 10^4$ for $z/c > 0.25$, enabling reattachment at the higher Reynolds number. In all cases, the transition point shifts upstream as the Reynolds number is increased. The largest upstream shift in transition location occurs on the wing at $z/c = 1.13$, where there is notably earlier growth of Reynolds shear stress at $\mathrm{Re}_c = 7.4 \times 10^4$. The relatively large distance between transition and reattachment compared to the distance between separation and transition on the wing at $z/c = 1.13$ is a typical feature of long LSBs [29]. In contrast to the other spanwise locations on the wing, a reduction in the maximum Reynolds shear stress with increasing Reynolds number occurs for the wing at $z/c = 0.25$. This reduction is attributed to a reduction in disturbance growth rates when separation is almost entirely suppressed near the wing root at the higher Reynolds number (Fig. 5.7l).

Transient Flow Development

The transient flow development over the airfoil and wing during the ramp changes in free-stream velocity between Reynolds numbers of 5.4×10^4 and 7.4×10^4 is examined in this section. The discussion focuses on a comparison of the flow over the wing at $\alpha = 6°$ to the

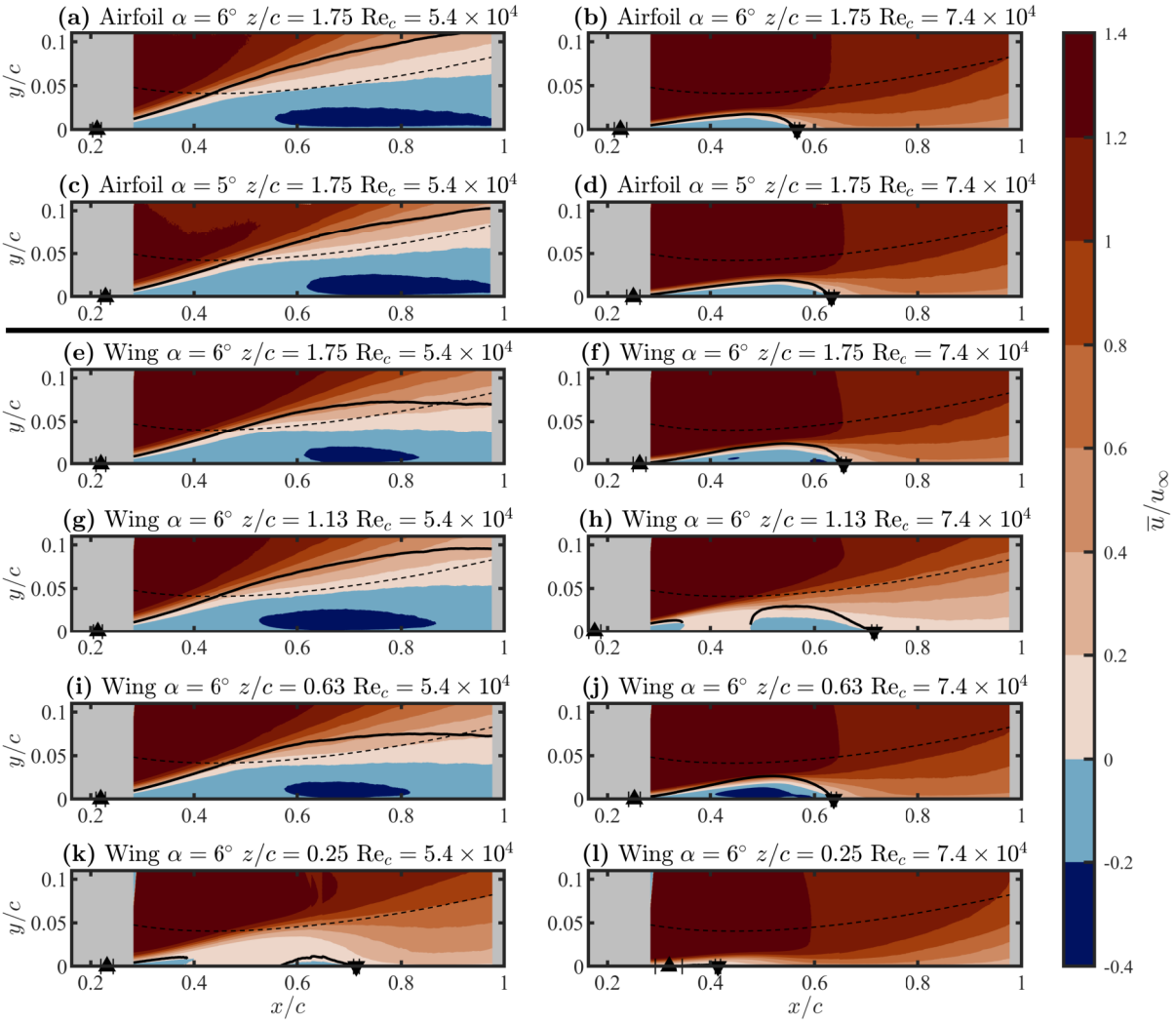


Figure 5.7: Mean streamwise velocity fields of the limiting flow states from side-view PIV. Solid lines: zero-net-streamwise mass flux line, dashed lines: intersection of top-view PIV measurement plane, ▲: separation location, ▼: reattachment location. Error bars indicate uncertainty interval (95% confidence).

airfoil at 5°, because the effective angle of attack near the wing root is approximately equal to 5°, and the resulting mean LSB size and location on the wing at $z/c = 0.63$ is most similar to that on the airfoil at $\alpha = 6°$ (Fig. 5.7). Contours of instantaneous streamwise velocity are plotted for single runs of the transient reattachment and stalling processes during the ramp up and ramp down in free-stream velocity in Fig. 5.9 and Fig. 5.10, respectively.

At the beginning of the ramp up, the recirculation region downstream of boundary layer separation contains a turbulent flow of slow-moving fluid over the majority of the span in the top-view PIV measurements on the wing and airfoil (Fig. 5.9). For the airfoil, the observed recirculation region extends up to approximately $0.1c$ from the test section wall at $z/c = 0$ (Fig. 5.9a). On the wing, the recirculation region is suppressed near the wing root

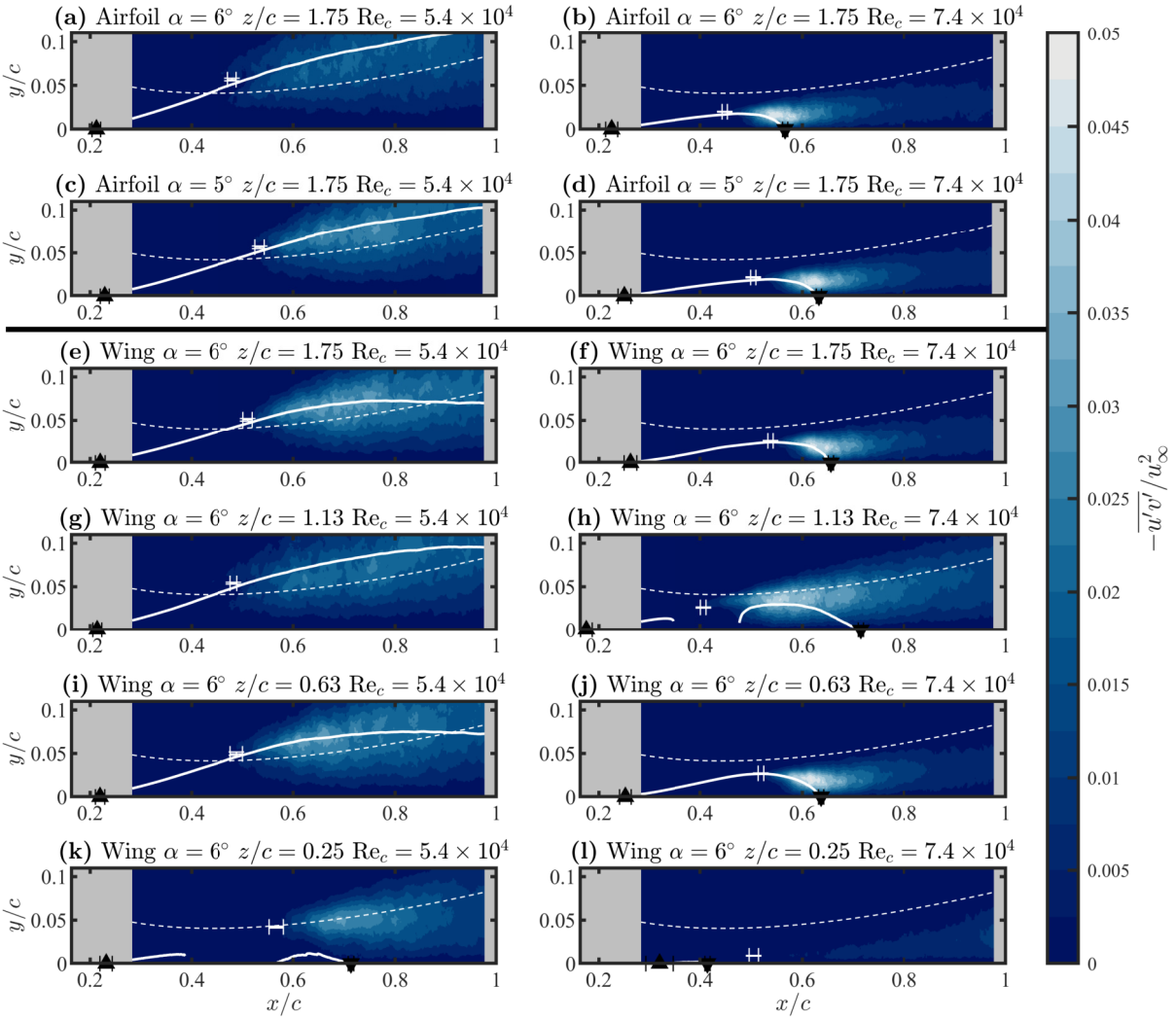


Figure 5.8: Reynolds shear stress fields of limiting flow states from side-view PIV. Solid lines: zero-net-streamwise mass flux line, dashed lines: intersection of top-view PIV measurement plane, ▲: separation location, ▼: reattachment location, white markers: transition location. Error bars indicate uncertainty interval (95% confidence).

for $z/c < 0.15$ and near the wing tip for $z/c > 2.2$ (Fig. 5.9b). As the free-stream velocity increases, the recirculation region contracts in its spanwise extent on both the airfoil and wing. For the wing during $0 < \mathcal{D} < 50$, the contraction occurs primarily from the wing tip. The increase in velocities measured within the turbulent flow region that occurs for the airfoil between $\mathcal{D} = 29$ and $\mathcal{D} = 41$, and for the wing between $\mathcal{D} = 41$ and $\mathcal{D} = 54$ suggests a reduction in the distance of the separated shear layer from the model surface. For the airfoil, a notable change in the flowfield occurs between $\mathcal{D} = 41$ and $\mathcal{D} = 54$, where the streamwise velocity rapidly increases over the entire recirculation region. In contrast, a more gradual progression towards the reattaching limiting state is observed for the wing.

In the reattaching limiting state, spanwise bands of increased velocity are observed for

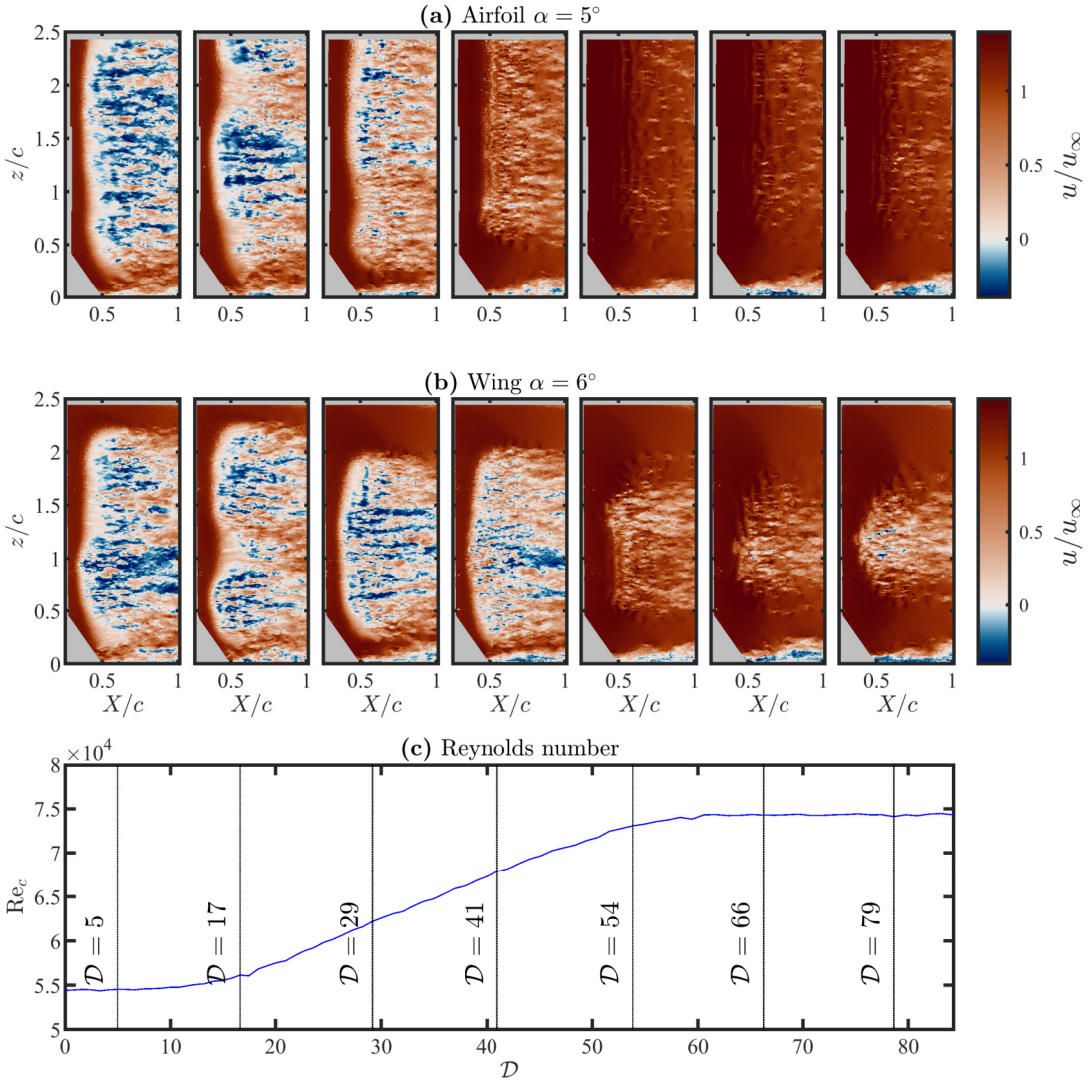


Figure 5.9: Instantaneous snapshots of streamwise velocity during ramp up of free-stream velocity. Black lines in (c) indicate the time instants of the snapshots in (a) and (b). Grey areas masked out due to noise from light reflections.

the airfoil, which are associated with spanwise vortex shedding from the LSB [e.g., 190]. On the wing, similar but shorter bands are seen near the edges of the central region of low-velocity turbulent flow because of the local increase in LSB thickness at $z/c \approx 1.13$ (Fig. 5.7h) that shifts the formed vortices above the plane of top-view measurements.

For the ramp down in free-stream velocity (Fig. 5.10), the flow field development is essentially reversed. On both the airfoil and wing, the ramp down begins with the LSB formed on the suction surface, and spanwise vortex shedding from the LSB being visible in

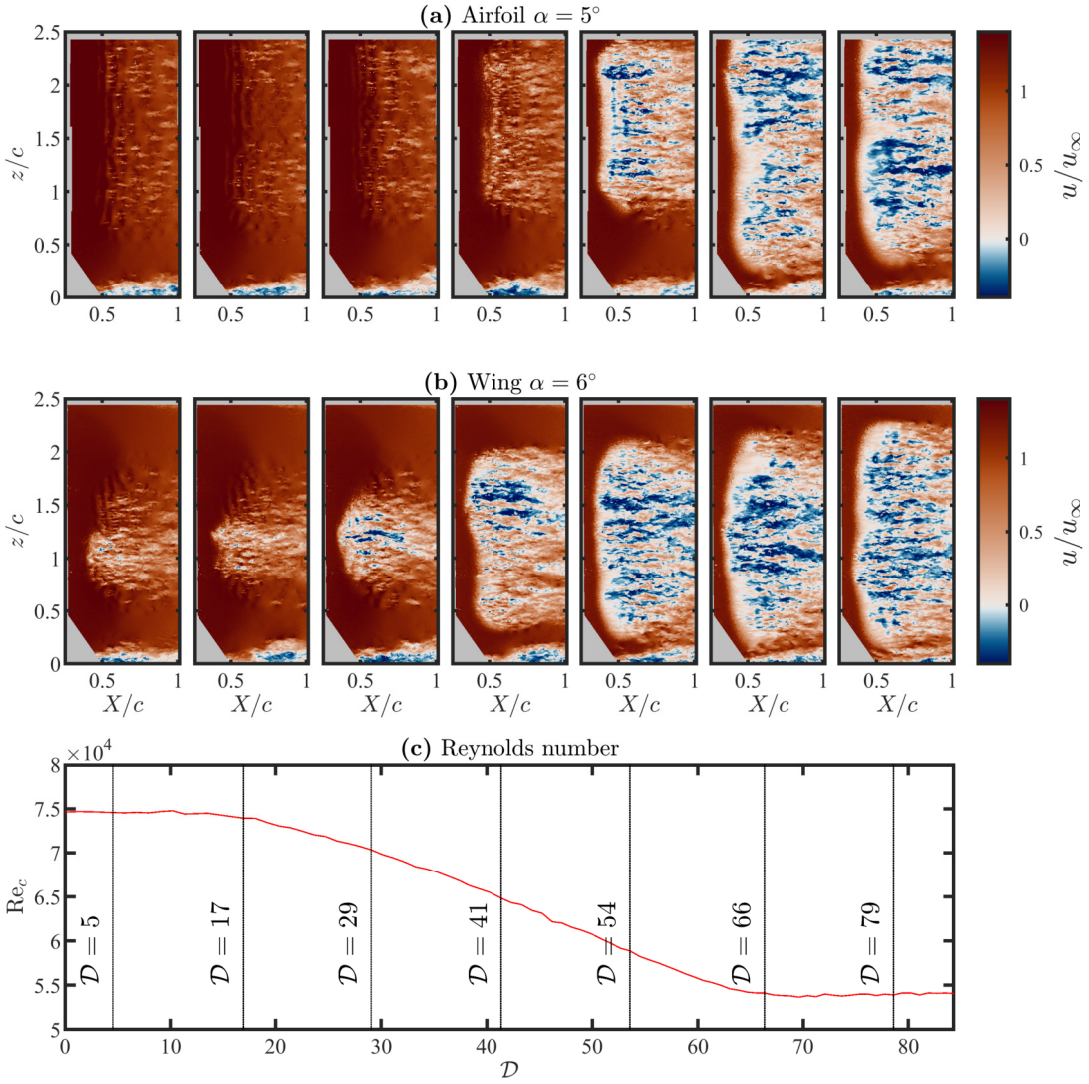


Figure 5.10: Instantaneous snapshots of streamwise velocity during ramp up of free-stream velocity. Black lines in (c) indicate the time instants of the snapshots in (a) and (b). Grey areas masked out due to noise from light reflections.

the top-view measurements. As the free-stream velocity decreases, a substantial region of turbulent reverse flow appears on the airfoil at $\mathcal{D} = 54$ (Fig. 5.10a), which subsequently spreads towards the test section wall at $z/c = 0$. On the wing, the transient flow field is characterised by an earlier cessation of reattachment near the midspan and a gradual spreading of the region of low-velocity turbulent flow towards the root and tip in the measurement plane.

To qualitatively explore repeatable features of the spanwise progression of LSB formation

and bursting, contours of the minimum streamwise velocity versus spanwise location and time are presented in Fig. 5.11 for the ensemble-averaged top view PIV measurements. The ensemble size is 20 runs. The minimum is taken over x from the ensemble-averaged flow-field at each instant in time. The regions of negative streamwise velocity illustrated by the two lowest contour levels can be used to roughly approximate the spanwise extent of the region where reattachment does not occur. For the airfoil during the ramp up in free-stream velocity (Fig. 5.11a), largely spanwise uniform LSB formation is indicated at $\mathcal{D} \approx 40$ by the relatively abrupt increase in minimum streamwise velocity across the span of the PIV measurements. During the ramp down for the airfoil (Fig. 5.11b), a more gradual decrease in minimum streamwise velocity occurs in the region influenced by end effects ($z/c < 1$). For the wing during the ramp up (Fig. 5.11c), there is a slow initial contraction in the spanwise extent of the separation region beginning from the wing tip for $0 \leq \mathcal{D} \leq 40$, before a relatively abrupt cessation of reverse flow at $\mathcal{D} \approx 40$ for $0.5 \leq x/c \leq 1.7$. In contrast, stall on the wing occurs more gradually, beginning near $z/c = 1.13$ at $\mathcal{D} = 25$ and spreading towards the wing root and tip (Fig. 5.11d).

The ensemble-averaged top view PIV measurements also display evidence of spanwise-travelling disturbances in the recirculation region. Because the streamwise velocity contours in Fig. 5.11 are plotted against spanwise position and time, spanwise-travelling disturbances appear as diagonal streaks in the contour plots. Specifically, diagonal bands of increased streamwise velocity are seen to originate from the edge of the recirculation region closest to the test section side-wall at $z/c \approx 0.5$ after LSB bursting on both the airfoil at $\mathcal{D} = 60$ (Fig. 5.11b) and on the wing at $\mathcal{D} = 42$ (Fig. 5.11d). When the spanwise-travelling disturbance on the wing reaches the side of the recirculation region closest to the wing tip ($z/c \approx 1.75$, $\mathcal{D} \approx 45$), there is a temporary pause in the spanwise expansion of the recirculation region towards the wing tip. This event temporally aligns with a transient increase in the ensemble-averaged lift coefficient (Fig. 5.3e). On the airfoil, a transient increase in lift is observed as the spanwise-travelling region of faster moving fluid reaches the midspan of the airfoil at $\mathcal{D} \approx 65$. As noted in the discussion of Fig. 5.3, the transient increase in lift is associated with the formation of a vortex from the leading edge shear layer. The spanwise motion of the region of faster moving flow on the wing from the root towards the tip suggests that leading edge vortex growth occurs more slowly near the wing tip, similar to the results of Visbal & Garmann [130]. The delayed increase in velocity at the midspan of the airfoil associated with the spanwise-travelling disturbance is consistent with the merging of two adjacent arch vortices as observed in the numerical simulations of Visbal & Garmann [130] for an airfoil between side-walls with $0.02c$ gaps, similar to the gaps between the airfoil and test section side-walls in the present study. The presence of these spanwise-travelling disturbances in the ensemble-average data suggests that they are characteristic of the LSB bursting process under these conditions.

Since the inherent run-to-run variability in the LSB formation and bursting processes leads to smearing in ensemble-averages, it is also informative to consider the top view results for a single ramp up or down of the free-stream velocity. Minimum streamwise velocity contours, analogous to those of the ensemble-average in Fig. 5.11, are plotted for single runs for the wing in Figs. 5.12a and 5.12b, and the corresponding instantaneous and

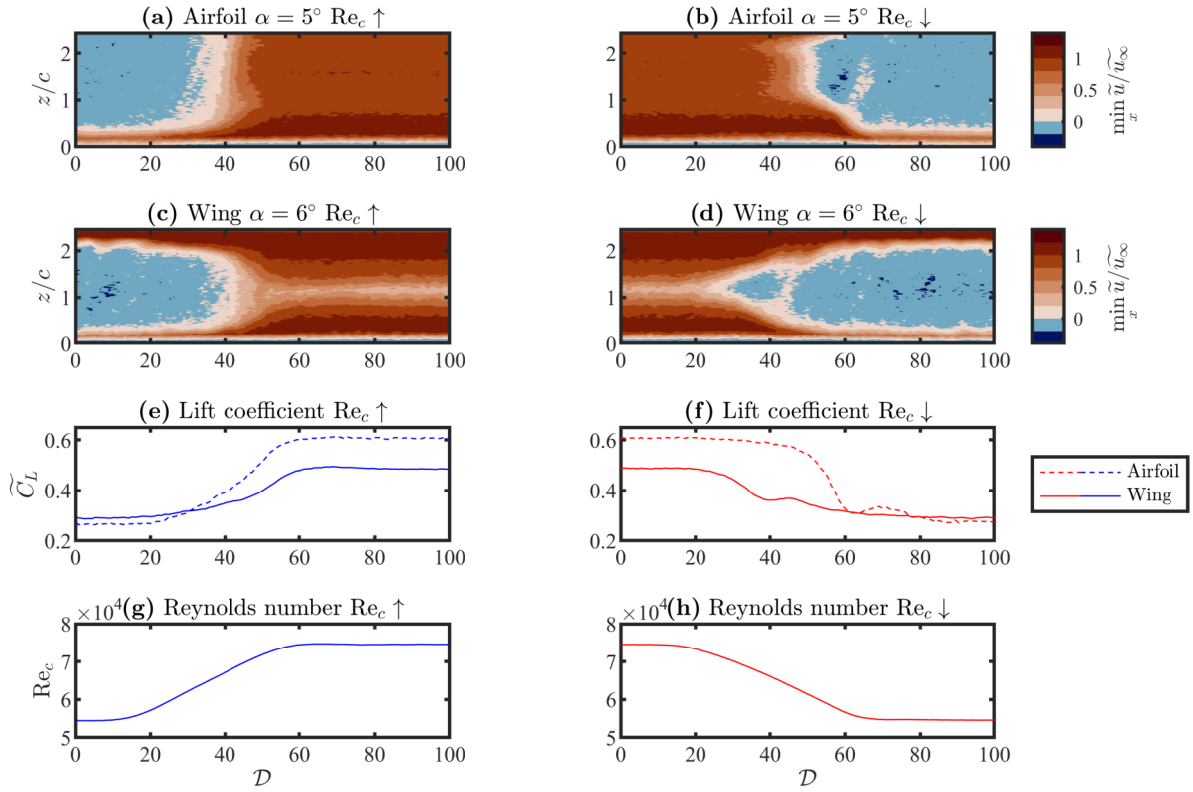


Figure 5.11: Contours of minimum ensemble-averaged streamwise velocity during ramp up (a,c), and ramp down (b,d) in free-stream velocity for airfoil (a,b) and wing (c,d).

ensemble-averaged lift coefficients are plotted in Figs. 5.12c and 5.12d. The results from the single ramp up presented largely resemble those of the ensemble-average (Fig. 5.11c). However, intermittent reverse flow is also present near the midspan after the end of the ramp up because the measurement plane intersects the turbulent shear layer at this location. The abrupt increase in velocity that occurs over a wide portion of the span at $\mathcal{D} = 55$ corresponds to an abrupt increase in instantaneous lift coefficient near the same time as the most rapid increase in the ensemble-averaged lift coefficient (Fig. 5.11c). The minimum streamwise velocity contours for the single ramp down for the wing (Fig. 5.12b) exhibit a notable decrease in the spanwise extent of reverse flow near $\mathcal{D} = 45$. As in the ensemble-averaged results, a spanwise-travelling region of relatively faster fluid forms near the wing root at $z/c = 0.5$, $\mathcal{D} = 38$ and propagates towards the wing tip as the separated flow region expands. As the region of faster fluid reaches the outboard end of the separated flow region, a transient contraction of the spanwise extent of reverse flow occurs. This contraction is accompanied by a local maximum in lift coefficient (Fig. 5.12d), indicative of the formation of a leading edge vortex. Subsequently, the separated flow region expands back towards the wing tip as the leading edge vortex is shed and the flow settles to the limiting stalled state. For both the ramp up and ramp down, the reduction in the spanwise width of the region of reverse flow correlates with an increase in the lift coefficient.

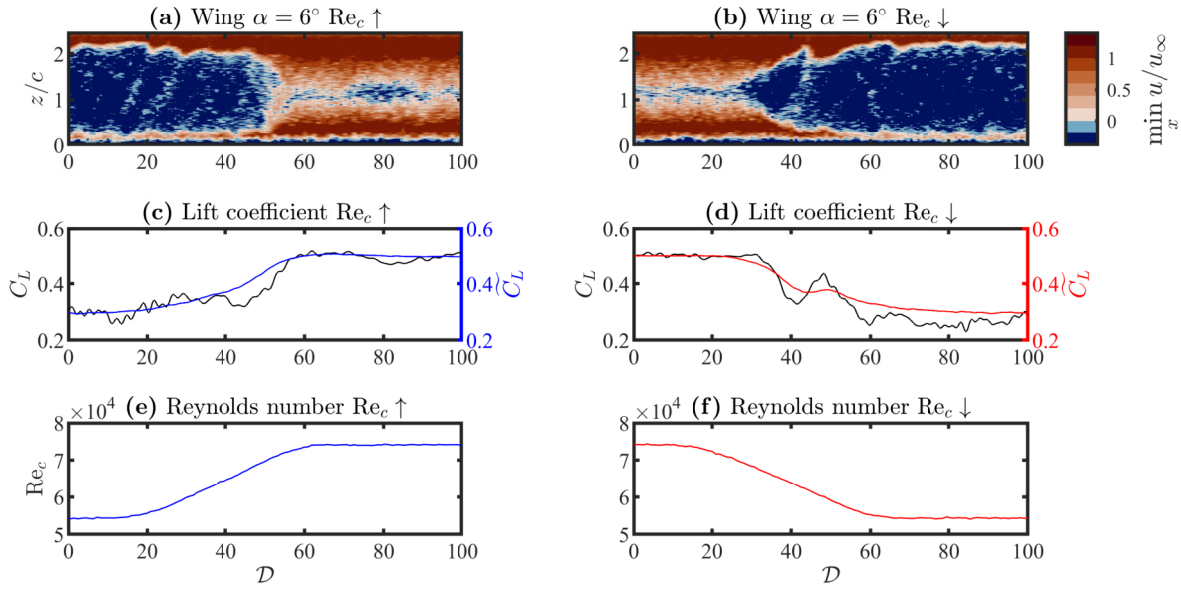


Figure 5.12: Contours of minimum streamwise velocity (a,b), lift coefficient (c,d), and Reynolds number (e,f) for ramp up (a,c,e) and ramp down (b,d,f) for the wing.

The changes in the extent of the separated flow region, position of the separated shear layer and the formation and bursting of an LSB inferred from the transient top view PIV measurements are confirmed using the transient side-view PIV measurements discussed hereafter. Instantaneous spanwise vorticity contours from the side view PIV measurements during the ramp up and ramp down in free-stream velocity are presented in Figs. 5.13 and 5.14, respectively, for the airfoil at $\alpha = 5^\circ$ and the wing at $\alpha = 6^\circ$. Note that the instantaneous spanwise vorticity snapshots at each spanwise location were recorded during separate runs, and are therefore uncorrelated. During the ramp up (Fig. 5.13), the spanwise vorticity fields reveal a reduction in the angle between the separated shear layer and the airfoil surface as the turbulent shear layer reattaches, whereas during the ramp down (Fig. 5.14), this angle increases. The results from the airfoil at $\alpha = 5^\circ$ (Figs. 5.13a and 5.14) largely resemble those from the wing at $z/c = 0.63$ and 1.75 (Figs. 5.13b, 5.13d, 5.14b, and 5.14d). At $z/c = 1.13$ (Figs. 5.13c and 5.14c), shear layer roll-up in the reattaching flow occurs farther upstream than on the airfoil and the other locations on the wing. The spanwise vorticity contours at $z/c = 0.25$ (Figs. 5.13e and 5.14e), which are influenced by wing root effects, also differ from those on the airfoil in that the distance of the shear layer from the surface is notably reduced when reattachment occurs.

Although the lift coefficient and top-view PIV measurements provide evidence of leading edge vortex shedding during the LSB bursting process, identification of the DSV using the λ_2 criterion [40] and visual inspection of spanwise vorticity contours was inconclusive due to the lack of time-resolved velocity data, the small wall-normal extent of the side-view PIV field of view, and the reduced coherence of vortical structures in the turbulent flow downstream of transition.

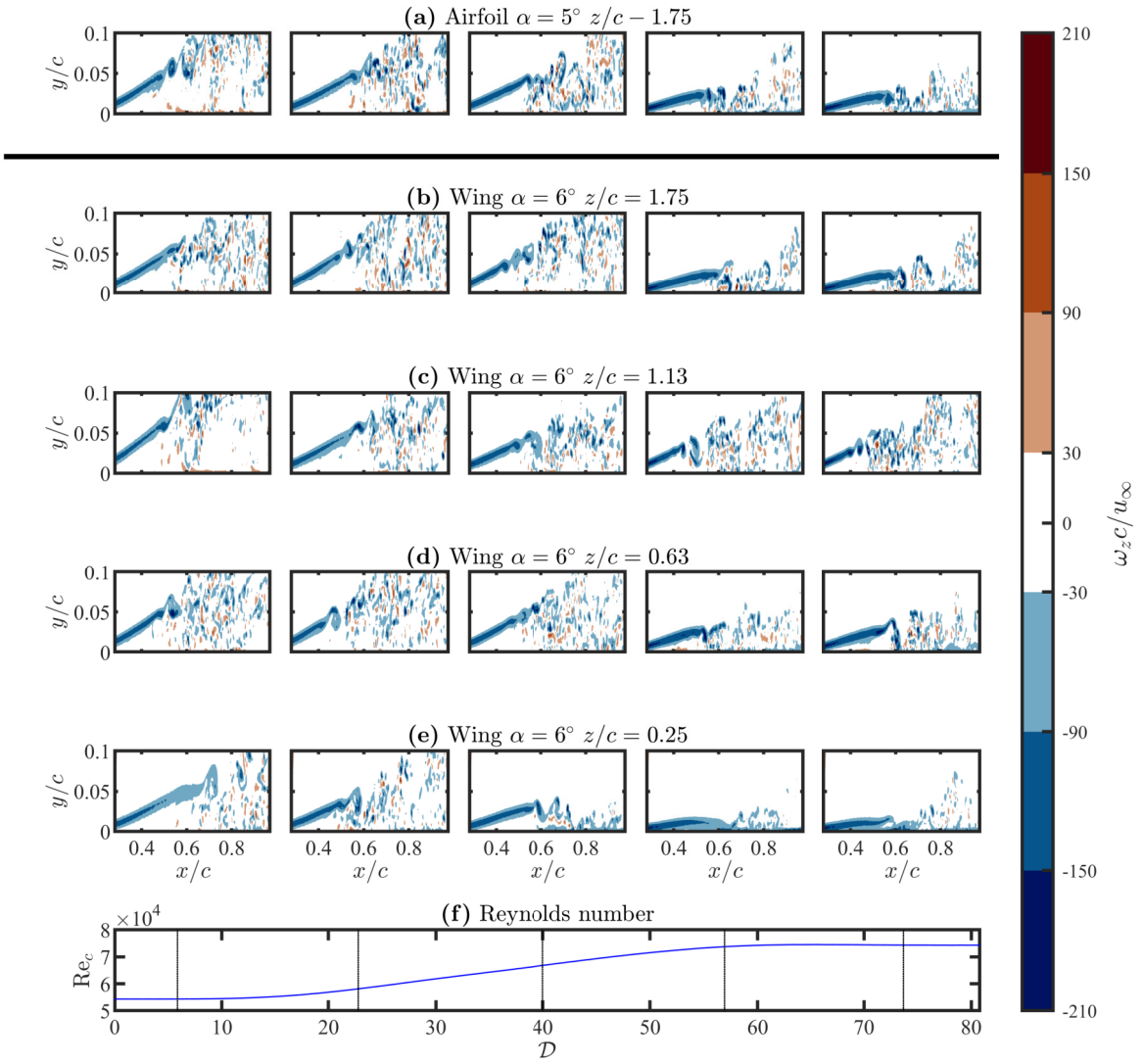


Figure 5.13: Instantaneous snapshots of spanwise vorticity during ramp up in free-stream velocity. Black lines in (c) indicate the time instants of the snapshots in (a-e).

The spanwise contractions and expansions of the separated flow region inferred from the top view PIV measurements (Figs. 5.9–5.12) during LSB formation and bursting, respectively, suggest that LSB formation and bursting occur at different times at different spanwise locations. Using data from the side view PIV measurement planes outside of direct end effects ($z/c \geq 0.63$), the spanwise variations of the locations of separation, transition, and reattachment on the airfoil and wing are examined in Fig. 5.15. The data presented in the figure were obtained by averaging the ensemble-average of these locations from 20 runs over a sliding temporal window of $5c/\widetilde{u_\infty}$ (Section 3.3).

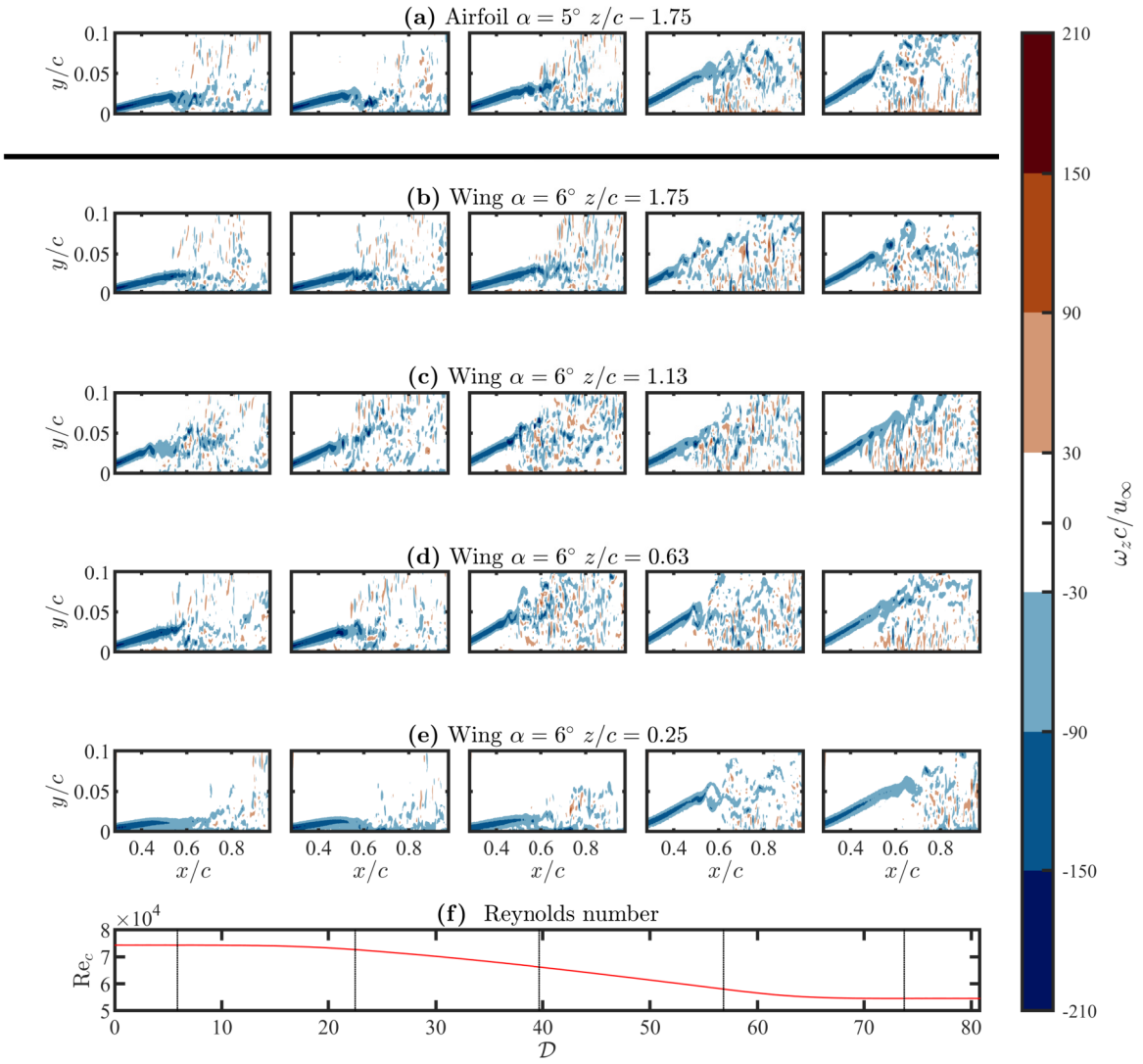


Figure 5.14: Instantaneous snapshots of spanwise vorticity during ramp down in free-stream velocity. Black lines in (c) indicate the time instants of the snapshots in (a-e).

During the ramp up in free-stream velocity for the airfoil, LSB formation is indicated by reattachment starting at $\mathcal{D} = 38$ (Fig. 5.15e). As the free-stream velocity increases, the transition location on the airfoil remains largely unchanged (Fig. 5.15c), although there is a small downstream movement of the separation point indicative of a decrease in adverse pressure gradient (Fig. 5.15a).

During the ramp up in free-stream velocity for the wing, reattachment occurs at $\mathcal{D} = 41$, 39, and 38 for $z/c = 0.63$, 1.13, and 1.75, respectively (Fig. 5.15e). The delay in LSB formation near the wing root is consistent with the expected spanwise progression of

reattachment on a rectangular stalled wing of uniform cross-section [42]. As the flow over the wing settles to the reattached state, there is a relatively small downstream shift in the locations of separation and transition at $z/c = 0.63$ and 1.75 (Figs. 5.15a and 5.15c). However, at $z.c = 1.13$, there is an upstream shift in separation and transition during the ramp up in free-stream velocity. This is reflected in the notably different LSB structure observed near the midspan of the wing (Fig. 5.7h).

During the ramp down in free-stream velocity for the airfoil, LSB bursting is marked by the cessation of reattachment at $\mathcal{D} = 50$ (Fig. 5.15f). Relative to the ramp up, the movement of the reattachment point is slower during the ramp down. For $55 \leq \mathcal{D} \leq 75$, there is a notable oscillation in the location of transition (Fig. 5.15c) centred near the time when there is a transient increase in lift coefficient (Fig. 5.3e). Transition reaches its farthest downstream location at $\mathcal{D} = 71$, while the local maximum in lift coefficient occurs at $\mathcal{D} = 70$. Thus, the temporary increase in lift coefficient for the airfoil during the ramp down is associated with a delay in transition. It should be noted that relatively minor movements of the location of separation on the airfoil are observed during the ramp down.

During the ramp down for the wing, there is a substantial spanwise variation in the time at which reattachment ceases (Fig. 5.15f). In agreement with the extent of reattachment inferred from top view PIV measurements, the reattachment locations calculated from side view PIV measurements indicate that reattachment ceases first near the midspan of the wing. This occurs at $\mathcal{D} = 28$ at $z/c = 1.13$ before reattachment ceases at $\mathcal{D} = 43$ and 55 at $z/c = 0.63$ and 1.75, respectively. These results are consistent with the spanwise expansion of the separated flow region on the wing during LSB bursting (Figs. 5.11d and 5.12b). The trends in the locations of separation and transition on the wing during the ramp down are largely the opposite of those during the ramp up. At $z/c = 1.13$, there is a measurable downstream movement in transition during the period $43 \leq \mathcal{D} \leq 55$ (Fig. 5.15d) where the lift coefficient plateaus (Fig. 5.3e) and the rate of spanwise expansion of the separated flow region towards the wing tip is reduced (Fig. 5.11d), implying lower disturbance growth rates in the separated flow during this time interval.

Because the reattachment process depends on transition in the separated shear layer, the wavelet transform of the wall-normal velocity fluctuations (Section 5.2.2) is employed to characterise the dynamics of the vortices shed from the separated shear layer during ramp changes in free-stream velocity. Figures 5.16 and 5.17 present ensemble-averaged wavelet amplitude scalograms for selected time instants during the ramp up and ramp down, respectively. The ensemble size is 20 runs. The scalograms illustrate how the magnitudes of the wall-normal velocity fluctuations at each time instant vary with respect to normalised wavenumber (kc) and streamwise location (x/c).

On the airfoil (Figs. 5.16a and 5.17a) the magnitudes of wall-normal velocity fluctuations upstream of the transition location are comparable to the noise level in the PIV measurements. A rapid increase in the amplitudes of the wall-normal velocity fluctuations is resolved near the transition location, with the largest amplitude fluctuations observed near the location of reattachment for conditions where an LSB forms. Downstream of the transition location, there is a progressive decrease in the wavenumber of the largest amplitude fluctuations. The decrease in wavenumber with downstream distance can be

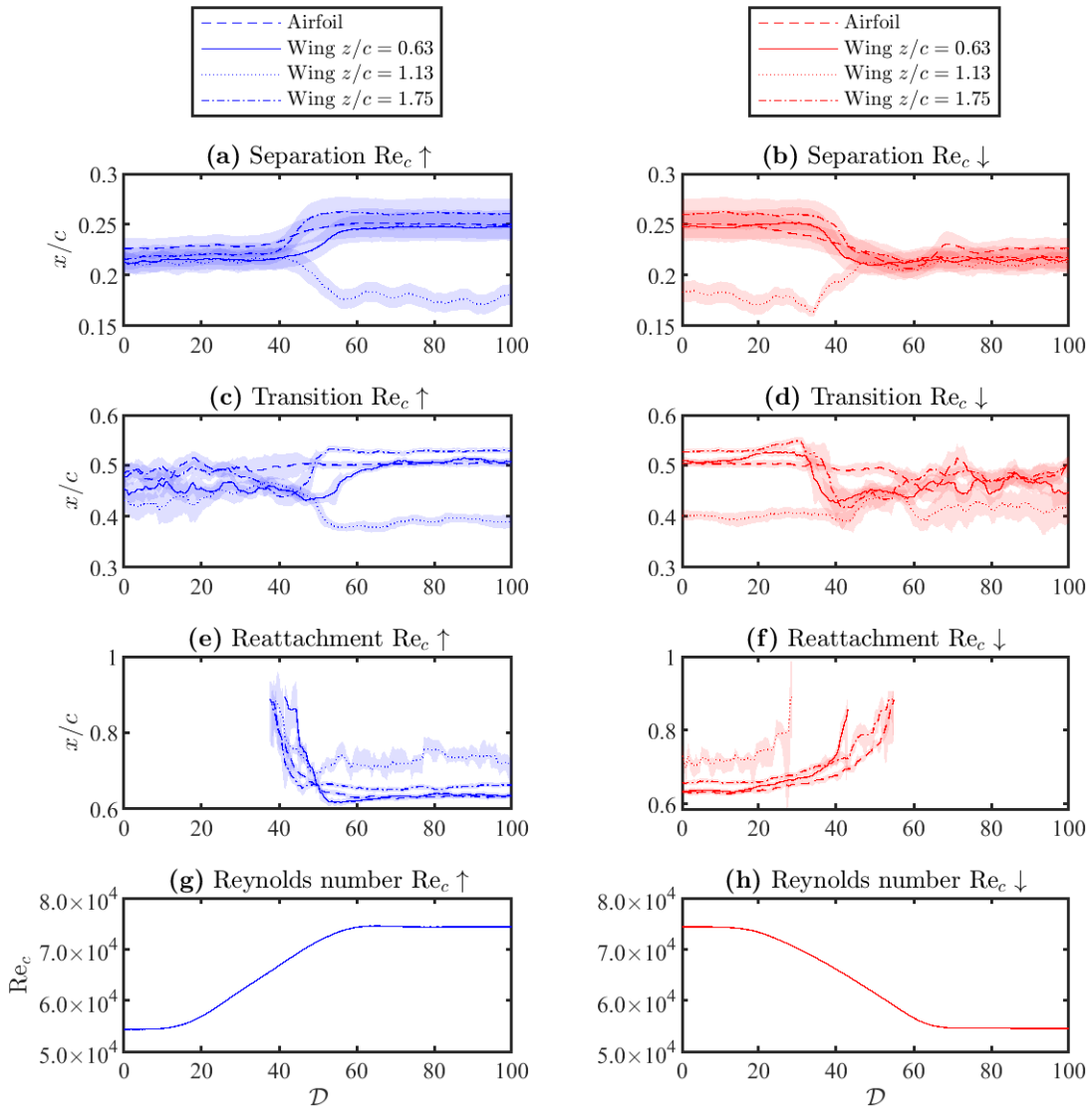


Figure 5.15: Transient movement of separation, transition, and reattachment locations for airfoil at $\alpha = 5°$ and finite wing at $\alpha = 6°$. Shaded areas indicate uncertainty interval (95% confidence)

attributed to the increasing thickness of the shear layer [e.g., 87]. During the ramp up and ramp down, there is an increase and decrease in the wavenumber of the largest amplitude fluctuations, respectively, which settles on $kc \approx 70$ and $kc \approx 100$ in the stalled and reattaching limiting states, respectively. These wavenumbers and the locations of maximum amplitude are consistent with the shear layer vortex shedding illustrated in Figs. 5.13a and 5.14a. The frequencies associated with these wavenumbers can be estimated by taking the mean streamwise velocity at the y coordinate equal to the displacement thickness and the x location of the maximum wavelet coefficient amplitude as the phase velocity. For the stalled and reattaching states of the airfoil, these frequencies are $9u_\infty/c$ and $12u_\infty/c$, respectively. During the ramp up, there is a relatively abrupt increase in the wavenumber and amplitude of the largest amplitude fluctuations between $\mathcal{D} = 40$ and 56, which corresponds to the time period where reattachment begins (Fig. 5.15e) and there is a rapid increase in lift (Fig. 5.3e). Likewise, during the ramp down, there is an abrupt decrease in the wavenumber and amplitude of the largest amplitude fluctuations between $\mathcal{D} = 40$ and 57, which corresponds to the time period where reattachment ceases and there is a rapid decrease in lift. A comparison of the middle panels in Figs. 5.16a and 5.17a reveals hysteresis in the shear layer velocity fluctuations, with larger amplitudes during the ramp down compared to the ramp up. Throughout the LSB formation and bursting process on the airfoil, the streamwise location of maximum wavelet amplitude remains largely constant, in agreement with the relatively small changes in transition location identified using the Reynolds shear stress-based transition criterion in Figs. 5.15c and 5.15d. The hysteresis in the amplitudes of velocity fluctuations is consistent with the lift coefficient hysteresis (Fig. 5.4), as larger amplitude fluctuations enable reattachment to persist at lower Reynolds numbers, increasing measured lift.

The duration of the time period over which the rapid changes in wavenumber and maximum velocity fluctuations occur ($< 17c/\widetilde{u_\infty}$) in Figs. 5.16 and 5.17 is comparable to the ensemble-averaged transient period of the lift coefficient (Fig. 5.5b) at this angle of attack, which is substantially shorter than the duration of the imposed change in free-stream velocity. These results suggest that, for quasi-steady changes in operating conditions, changes in disturbance wavenumbers and wavelet amplitudes are driven indirectly by the formation or bursting of the LSB, rather than directly by the change in Reynolds number.

The evolution of the wall-normal velocity fluctuations on the wing at $z/c = 0.63$ (Figs. 5.14d and 5.16d) and 1.75 (Figs. 5.14b and 5.16b) is largely similar to that on the airfoil. However, the changes in amplitude and wavenumber of the largest amplitude fluctuations at these two locations on the wing are more gradual than on the airfoil or at $z/c = 1.13$ on the wing (Figs. 5.14c and 5.16c). At $z/c = 1.13$, the wavenumber of the largest amplitude fluctuations when reattachment occurs ($kc \approx 125$) is greater than that observed at $z/c = 0.63$ and 1.75 ($kc \approx 90$). An upstream shift in the location and increase of the maximum fluctuation amplitudes also occurs at $z/c = 1.13$. These changes are attributed to the increase in LSB thickness at this location, since the larger distance of the velocity profile inflection point from the airfoil surface is expected to increase the wavenumber and growth rate of the most unstable disturbances [17]. At $z/c = 0.25$ on the wing (Figs. 5.16e and 5.17e), root effects cause the shear layer to remain closer to the wing

surface when the LSB forms. Such a reduction in the distance of the inflection point of the velocity profile from the wing surface is expected to decrease the growth rates of unstable disturbances [17], and this is reflected in the substantial reduction in measured amplitudes relative to the other planes when an LSB forms on the wing. The occurrence of lower disturbance growth rates closer to the wing root and tip, where the LSB is thinner, has also been observed at a higher Reynolds number [$Re_c = 1.25 \times 10^5$, 124]. The wavelet analysis of velocity fluctuations in the separated shear layer shows that the relatively gradual spanwise progression of LSB formation and bursting observed on the wing is associated with a more gradual change in the wavenumbers and amplitudes of velocity fluctuations in the regions near the root and tip. The hysteresis in velocity fluctuation amplitudes on the wing is less pronounced than on the airfoil, consistent with the observed reduction in lift coefficient hysteresis on the wing (Fig. 5.4). Because the base flow and the superimposed velocity fluctuations in reattaching flows are strongly coupled [e.g., 17, 191], the overall changes in LSB structure during formation and bursting should be considered interdependent on the transition dynamics.

The foregoing results show that substantial differences in LSB formation and bursting transients occur at different spanwise locations on the wing. However, in previous studies, bubble bursting criteria have been almost exclusively applied to two-dimensional flows [e.g., 6, 7, 30, 78, 82]. Therefore, it is of interest to evaluate the three-dimensional LSB forming on the wing using an established bursting criterion to understand how bursting criteria may be applied to real flows where three-dimensionality is always present to some extent. Because bursting can be caused by either a change in adverse pressure gradient or Reynolds number, the two-parameter criterion of Gaster [7] is employed here since it allows the relationship between these two effects to be examined.

In Fig. 5.18, the pressure gradient parameter $P = (\widetilde{\theta_s}^2/\nu)(\Delta u_e/\Delta x)$ is plotted versus momentum thickness Reynolds number at separation ($\widetilde{\mathrm{Re}_{\theta_s}}$) for the ensemble-averaged velocity field over 20 runs during the ramp changes in free-stream velocity. The results for the airfoil pertaining to $\alpha = 5°$ and those for the wing at $\alpha = 6°$ are presented for the planes outside of direct root effects ($z/c = 0.63$, 1.13, and 1.75). Although four momentum thickness components are required to describe the momentum deficit in a three-dimensional boundary layer, the mean spanwise velocities at these locations in the reattaching limiting state are less than 6% of the free-stream velocity, and the criterion of Gaster [7] has been applied in its two-dimensional form. Since the separation location falls just upstream of the PIV field of view for all cases presented, upstream linear extrapolation of the separation streamline was used to estimate the separation point location [e.g., 31]. The edge velocity and momentum thickness at separation (θ_s), required to calculate Re_{θ_s} and P were also computed from the PIV data using linear extrapolation. The mean inviscid velocity gradient over the LSB ($\Delta u_e/\Delta x$) was estimated from the inviscid velocity distribution over the airfoil calculated using the XFOIL software [192]. The solid black lines in the figure are the bursting line [7], above which LSBs are classified as long, and below which LSBs are classified as short. The bursting line of Gaster [7] extends only to a $P = -0.09$, which was deemed as the maximum value of P for which separation would occur on sharp-nosed airfoils of interest for aeronautical applications. The fact that separation occurs for higher

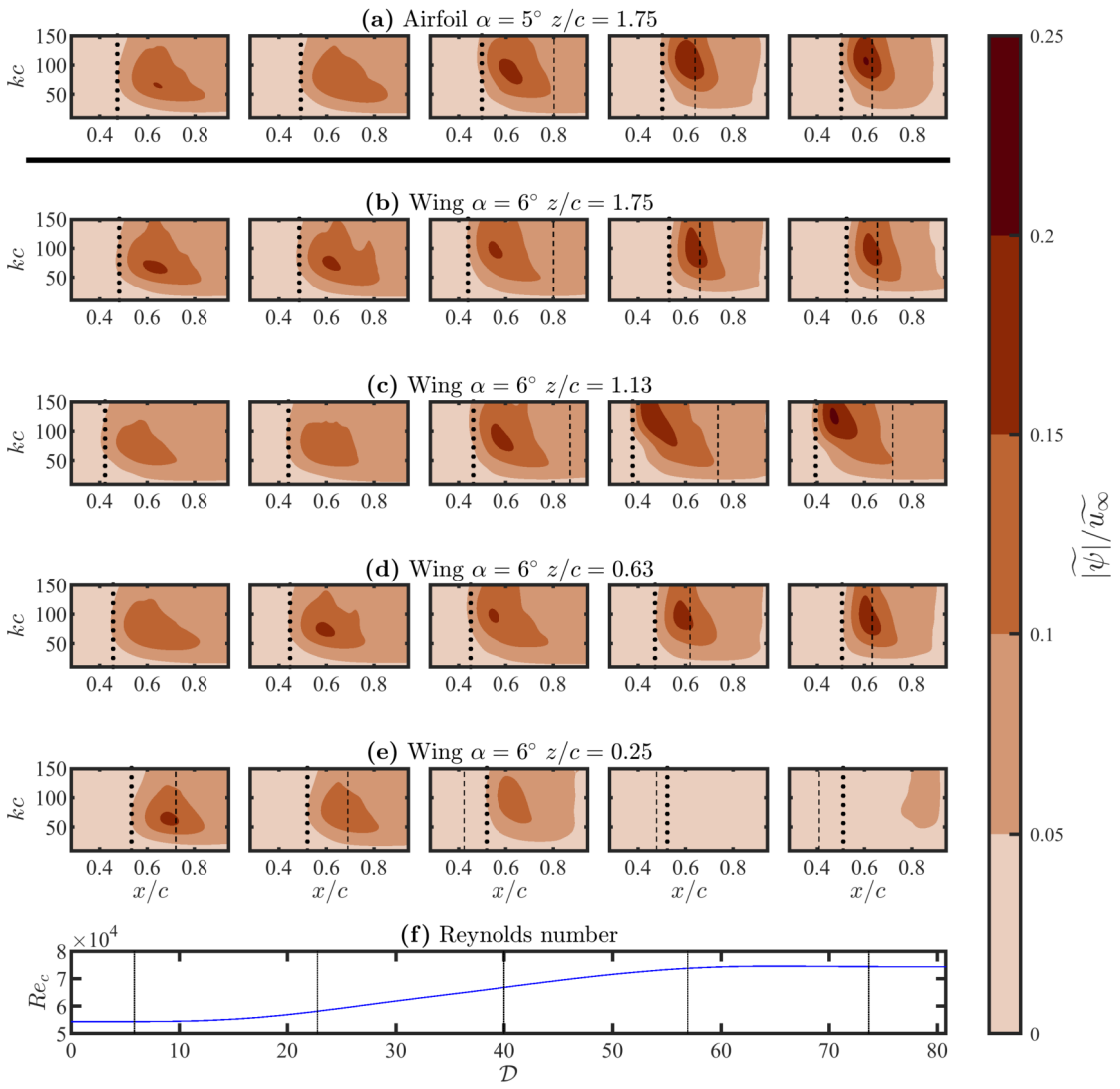


Figure 5.16: Ensemble-averaged wavelet amplitude scalograms of integrated wall-normal velocity fluctuations during ramp up in free-stream velocity. Dotted lines: transition location. Dashed lines: reattachment location. Black lines in (c) indicate the time instants of the snapshots in (a-e).

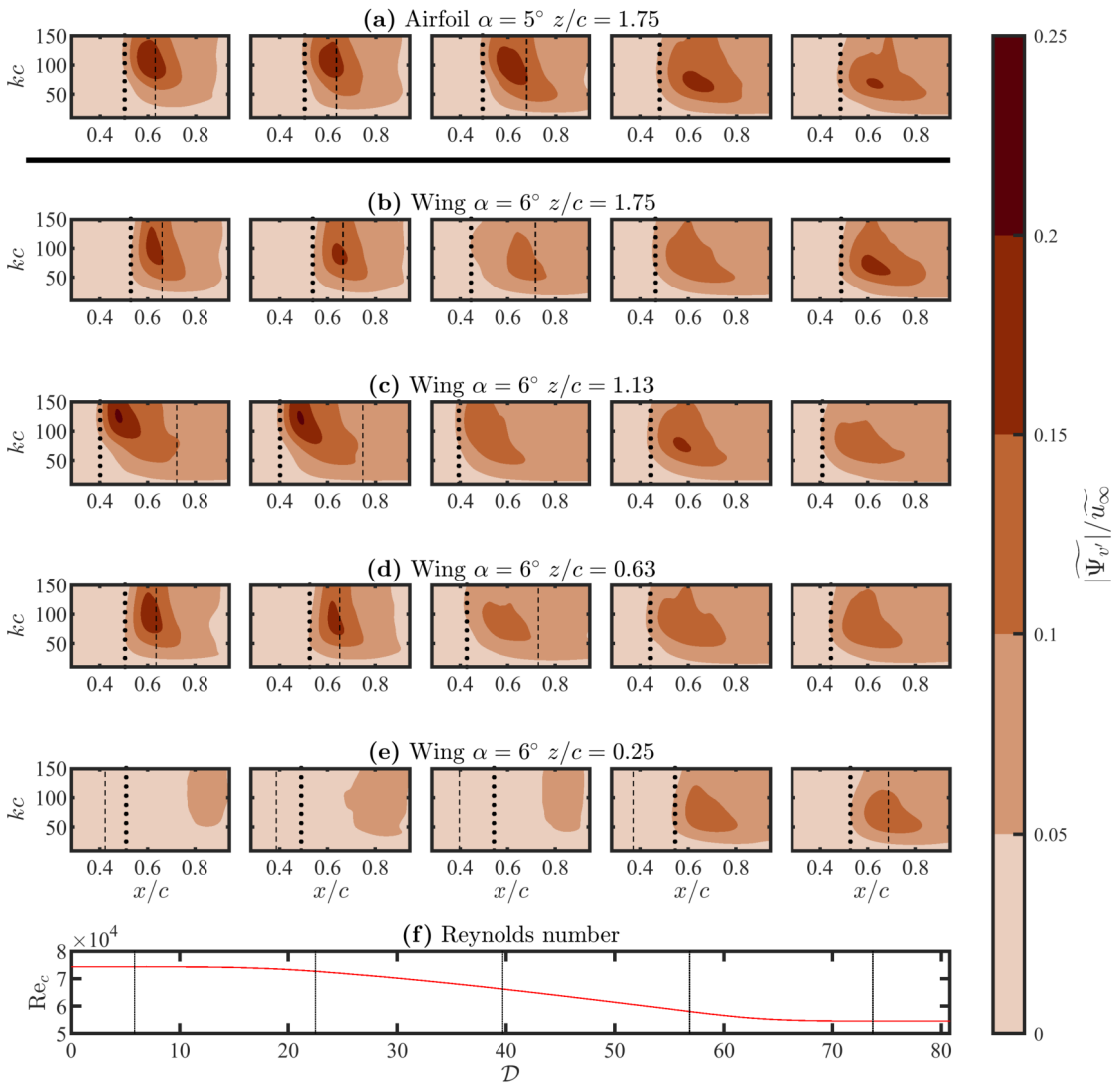


Figure 5.17: Ensemble-averaged wavelet amplitude scalograms of integrated wall-normal velocity fluctuations during ramp down in free-stream velocity. Dotted lines: transition location. Dashed lines: reattachment location. Black lines in (c) indicate the time instants of the snapshots in (a-e).

values of P on the airfoil and wing models is attributed to the relatively thick and rounded leading edge of the airfoil section employed in the present study [181].

The obtained data trajectories in the $P - \mathrm{Re}_{\theta_s}$ plane during the ramp up and ramp down in free-stream velocity are examined in Figs. 5.18a and 5.18b, respectively. The location of the LSB in the reattaching limiting state is indicated by the white $\times$ marker. When reattachment does not occur, the parameter P is undefined and only Re_{θ_s} can be calculated. Consequently, the value of Re_{θ_s} for the stalled limiting state is indicated by the vertical dashed line. The trajectory of the LSB from the initiation of reattachment up to the reattaching limiting state during the ramp up in free-stream velocity (or vice versa for the ramp down) is indicated by the black markers, and the uncertainty in the location of this trajectory is indicated by the shaded region that is coloured according to the corresponding chord Reynolds number (Re_c) to help connect the data to free-stream conditions during transients. As expected, the LSB in the reattaching limiting state on the airfoil is in the short bubble region, close to the bursting line. During the ramp up (Fig. 5.18a), the parameter P remains relatively constant from the initiation of reattachment until the reattaching limiting state is reached, while there is an increase in Re_{θ_s} from 116 to 134 that moves the LSB towards the short bubble region. During the ramp down, Re_{θ_s} decreases, moving the LSB towards the bursting line as P remains relatively constant until reattachment ceases at $\mathrm{Re}_{\theta_s} = 108$. For both the ramp up and ramp down for the airfoil, the trajectories of the LSBs form a shallow angle with the bursting line, typical of the "smooth-expansion" burst type described by [7].

Similar to the airfoil, the LSB in the reattaching limiting state on the wing at $z/c = 0.63$ and 1.75 (Figs. 5.18c and 5.18d and Figs. 5.18g and 5.18h) is within the short bubble regime, close to the bursting line. However, the LSB in the reattaching limiting state at $z/c = 1.13$ has significantly lower values of P and Re_{θ_s}, that place it outside of the short LSB region identified by Gaster [7]. Considering the substantial increase in the distance between transition and reattachment observed at $z/c = 1.13$ (Fig. 5.8f) that is characteristic of long LSBs [29], the LSB in the reattaching limiting state at this location is deemed long. The agreement between qualitative observations of the LSB structure and dynamics at this location and the criterion of Gaster [7] suggests that this criterion is applicable in mildly three-dimensional regions of LSBs on finite lifting surfaces. Although spontaneous LSB formation and bursting can occur on airfoils and wings at low Reynolds numbers in a steady free-stream near the stall conditions [193], the long LSB observed at $z/c = 1.13$ did not spontaneously change into a short LSB or massively separated flow under steady free-stream conditions at $\mathrm{Re}_c = 7.4 \times 10^4$. This observation is notable because, although the LSB forming on the wing in the reattaching limiting state is both short at some spanwise locations and long at others, this flow state is globally quasi-stable, and spontaneous switching between reattaching and fully stalled states does not occur at $\mathrm{Re}_c = 7.4 \times 10^4$. Thus, partial LSB bursting and formation of a long LSB over part of the wing is necessary but not sufficient to cause bursting of the entire LSB on the finite wing.

During the ramp up for the wing, there is an overall increase in Re_{θ_s} from the initiation of reattachment up to the reattaching limiting state at $z/c = 0.63$ and $z/c = 1.75$ (Figs. 5.18c and 5.18g), similar to the trend seen for the airfoil. However, there is an overall decrease

in Re_{θ_s} at $z/c = 1.13$ (Fig. 5.18c) that points to a different dynamics involved with the formation of a long LSB at the midspan of the wing. Also, large variations in Re_{θ_s} and P occur for the LSB at $z/c = 1.13$ after the ramp up in free-stream velocity is complete, as indicated by the dark red colour of the shaded region encompassing the limiting reattaching state. Unlike the airfoil, during the ramp down at $z/c = 0.63$ and 1.75 on the wing (Figs. 5.18c and 5.18d), there is a significant initial decrease in P and increase in Re_{θ_s} as the LSB initially moves into the long bubble regime, similar to the "violent burst" type of trajectory described by Gaster [7]. In this case, such a trajectory is the result of a large transient increase in momentum thickness that occurs between the time that reattachment ceases at $z/c = 1.13$ and the time that reattachment ceases at $z/c = 0.63$ and 1.75. As the flow approaches the stalled limiting state, there is a subsequent decrease in Re_{θ_s} and a return of P to a similar value as the reattaching limiting state at $z/c = 0.63$ and 1.75. Compared to the ramp up at $z/c = 1.13$, the ramp down at this z/c location features the LSB remaining relatively close to the reattaching limiting state before reattachment ceases, consistent with the small change in chord Reynolds number undergone before the separated flow region begins to expand from this spanwise location (Fig. 5.11d). The foregoing application of the bursting criterion of Gaster [7] to the LSB on the wing shows that this criterion correctly classifies the limiting LSB state as near bursting conditions. However, marked differences in the trajectories of the LSB in the $P - \mathrm{Re}_{\theta_s}$ plane are seen when comparing the airfoil to the wing, or when comparing different spanwise locations on the wing during the transient changes in free-stream velocity. The relatively shallow approach of the LSB trajectory to the bursting line on the airfoil (Fig. 5.18b) and on the wing near its midspan ($z/c = 1.13$, Fig. 5.18f) compared to the locations on the wing closer to the root and tip ($z/c = 0.63$ and 1.75 Figs. 5.18d and 5.18h) suggests that end effects may induce the "violent burst" type of trajectory characterised by an increase in Re_{θ_s} and P as the bursting line is approached. The application of the two-parameter bursting criterion of Gaster [7] to the transient flow over the wing model reveals that end effects may lead to substantial spanwise variations in quasi-steady and transient LSB classification on finite wings.

5.4 Discussion

It is instructive to compare the results of the current study with those from previous related investigations conducted on different airfoil geometries and flow parameters, so as to identify any general trends in the observed transient flow development and, when possible, the associated changes in aerodynamic loading.

The degree to which the measured flow field transients are dependent on the duration of the free-stream velocity ramp can be assessed by comparing the estimated transient periods from the present study (Fig. 5.5b) to the duration of stall and reattachment transients reported from other investigations. Because the lift response of the wing does not deviate substantially from quasi-steady behaviour (Figs. 5.4d–5.4f), this comparison focuses on the airfoil. Although there are relatively few previous studies that consider transient

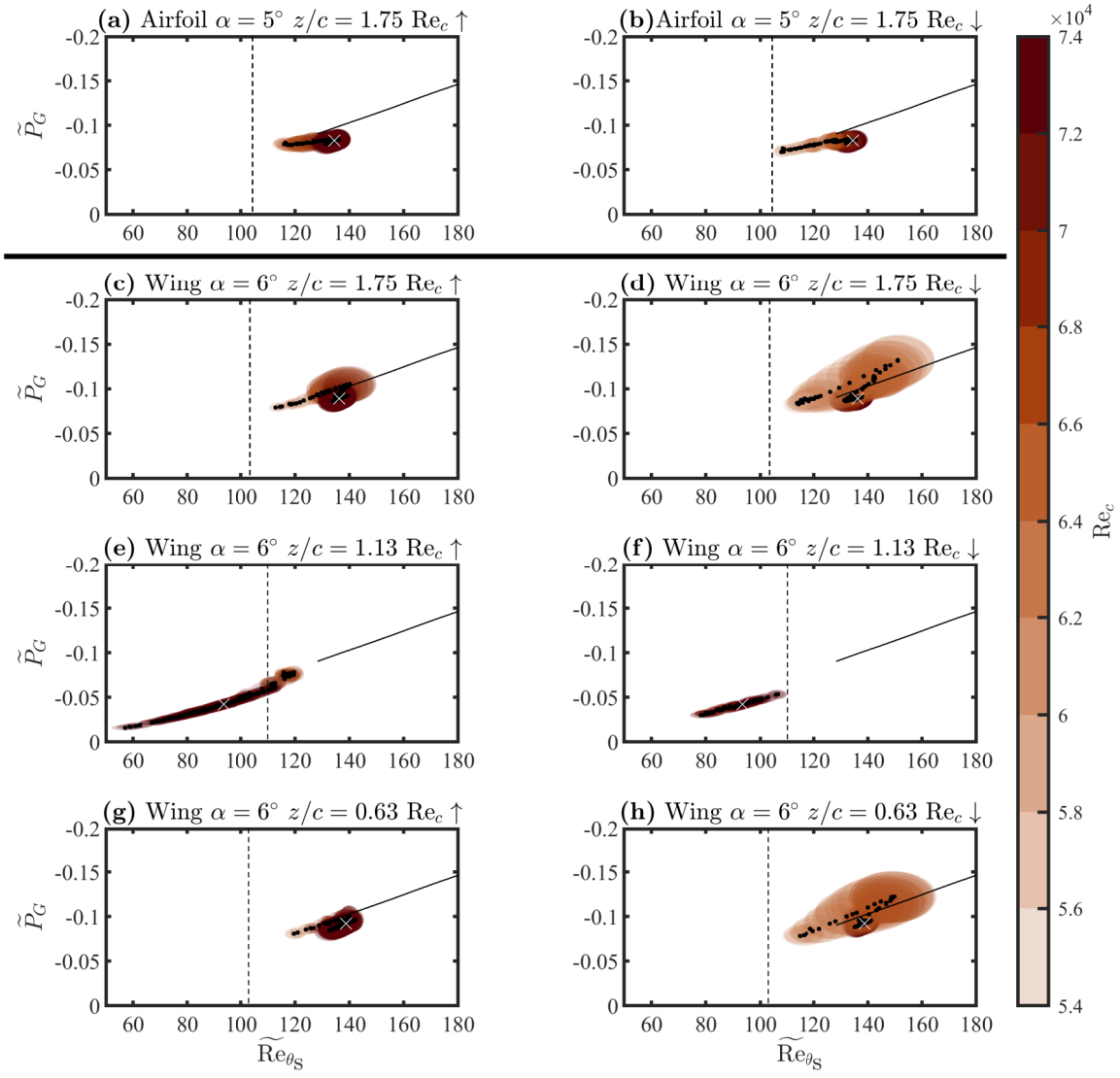


Figure 5.18: Gaster [7] bursting criterion during ramp changes in free-stream velocity. Solid line: bursting line. Dashed line: Re_{θ_s} for limiting stalled state. Black markers: LSB trajectory. White markers: LSB in reattaching limiting state. Shaded regions indicate uncertainty interval (95% confidence) and are coloured by Re_c.

free-stream velocity changes causing stall or reattachment on an airfoil, several studies have considered transients caused by pitching motions or active flow control strategies and are compared to the present study in Table 5.4. For studies of ramp-type pitching motions, the non-dimensional pitch rate, defined as $r = \dot{\alpha}c/(2u_\infty)$, where $\dot{\alpha}$ is the pitch rate in $\mathrm{rad\,s^{-1}}$, is listed. For the studies involving active flow control, the reattachment and stall transients are produced by turning the flow control off and on, respectively.

The results in Table 5.4 suggest that, across a variety of airfoil geometries and flow parameters, the stall transient durations tend to be longer than the reattachment transient durations, consistent with the present study. Additionally, the transient durations do not appear to strongly depend on Reynolds number. The range of transient durations observed in the present study overlaps those of both quasi-steady, unsteady, and impulsive changes in operating conditions from previous studies. This suggests that there is a minimum time required for reattachment of approximately $7c/u_\infty - 10c/u_\infty$, and for stall of $20c/u_\infty - 30c/u_\infty$, regardless of the type of imposed change in operating conditions.

The flow development over the wing in the stalled limiting state of the present study bears a strong resemblance to that observed on a semi-span NACA 0015 wing with aspect ratio four at a higher angle of attack and Reynolds number ($\alpha = 22°$, $\mathrm{Re}_c = 3.3 \times 10^5$) reported by Neal & Amitay [188]. In their study, three-dimensional end effects were seen to dominate the near-surface flow development within $0.75c$ of the wing tip and within $0.5c$ of the wing root. Similarly, reverse flow is not observed in the top-view PIV measurements of the present study within $0.5c$ of the wing root and tip (Fig. 5.6e), indicating the regions where three-dimensional end effects suppress the wall-normal extent of flow separation. The similarity of the spanwise extent of tip effects in the massively separated flow at different aspect ratios points to an insensitivity of overall structure of the stalled limiting state to this parameter when the aspect ratio is sufficiently large to separate the regions under direct end effects.

In the reattaching limiting state, the PIV measurements indicate that a three-dimensional LSB forms on the wing, with an increase in thickness near the midspan and a reduction in wall-normal extent towards the root and tip. This type of LSB structure is qualitatively similar to that described by Henk [194, fig. 6.2] resulting from the impulsive imposition of a three-dimensional pressure gradient on a flat plate. However, the results of experiments on the same wing geometry at higher Reynolds numbers [124] reveal a notably different spanwise structure to the LSB, with two local maxima in LSB thickness located in the intermediate regions between the areas dominated by end effects and the flow over the midspan. The maximum displacement thickness computed from the side-view PIV measurements of the present study at $z/c = 1.13$ is $\delta^* = 0.05$, compared to local maxima of $\delta^* \approx 0.01$ at $z/c = 0.35$ and 2.00 measured on the same wing model at $\mathrm{Re}_c = 1.25 \times 10^5$ [124]. Given the substantial change in maximum displacement thickness with Reynolds number coinciding with the location where reattachment first ceases during the LSB bursting transient, it is conjectured that LSB bursting may not initiate from near the midspan of the wing at higher Reynolds numbers where the maximum displacement thickness does not occur near the midspan. Instead, it is speculated that LSB bursting proceeds by the outboard progression of massive separation initiating closer to the wing root, as often occurs on wings at Reynolds

Table 5.4: Comparison of stall and reattachment durations from selected previous studies.

Study	Re_c	Profile	Type of unsteadiness	Transient duration $\times c/u_\infty$	
				Reattachment	Stall
Present Study	$4.8 \times 10^4 - 8.6 \times 10^4$	NACA 0018	Freestream velocity change	$10 - 22$	$22 - 30$
Le Fouest *et al.* [187]	7.5×10^4	NACA 0018	Pitching - $r = 0.001$		40
			Pitching - impulsive		22
Carusone *et al.* [37]	4.6×10^5	NACA 0015	Fluidic vortex generators	7	
Benard *et al.* [34]	1.9×10^5	NACA 0015	Leading edge plasma actuator	10	$30 - 160$
Green & Galbraith [64]	1.5×10^6	NACA 23012B	Pitching - $r = 0.009$	30	
			Pitching - $r = 0.048$	8	
Siauw *et al.* [180]	1.0×10^6	NACA 0015	Fluidic vortex generators	10	20
Kiefer *et al.* [63]	3.0×10^6	NACA 0021	Pitching - $0.0006 \leq r \leq 0.02$		20

numbers typical of manned aircraft [42]. Furthermore, during the LSB formation process on the wing, the side-view PIV measurements indicated that earlier reattachment occurred at the planes closer to the wing tip (Fig. 5.15), as expected for a rectangular wing. Thus, the initiation of LSB bursting at $z/c = 1.13$ is likely a consequence of the shape of the preceding LSB.

It is important to note that the imposed free-stream accelerations in this study were relatively small, with $|ac/u_\infty^2| \leq 0.011$. For faster free-stream accelerations, the magnitude of the free-stream streamwise pressure gradient is expected to become significant in the transient flow development. This may lead to more substantial lift hysteresis for the wing, such as that observed for a stalled wing in a periodic free-stream by [195], and to measurable differences in roll-up vortex size and shedding frequency for positive and negative free-stream accelerations, similar to the results of Nati *et al.* [87] and Gloutak *et al.* [196]. However, more rapid changes in free-stream velocity may not necessarily lead to more rapid LSB formation and bursting, because the more favourable pressure gradient during the ramp up has been shown to cause a delay in separation and transition, whereas the more adverse pressure gradient during the ramp down produces the opposite effect [85].

Although relatively few previous studies have considered the stall of a wing due to a change in free-stream velocity, the dynamic stall of pitching airfoils and wings has received greater attention [e.g., 55]. Dynamic stall may occur through the formation of a single dynamic stall vortex (DSV) that grows as it remains in place over the suction surface before being shed, or by the convective growth of a series of vortices. Mulleners & Raffel [57] termed these two modes of dynamic stall as the wake mode and shear layer mode, respectively. Typical DSV formation periods are on the order of c/u_∞ [57], which is sufficiently long to be captured by the side-view PIV, whose sampling frequency is $0.5c/u_\infty$. In the present investigation, the formation of a series of downstream convecting vortices and the absence of a stationary dynamic stall vortex during the ramp down in free-stream velocity suggests that the stall due to LSB bursting precipitated by the change in free-stream velocity can be classified as a shear layer mode stall.

The dynamic stall of finite aspect ratio wings has been investigated in multiple studies where wake mode dynamic stall was reported [e.g., 128, 130, 131]. Although the stall mode is different, there are similarities between the topological changes in flow development along the span in these studies and the present. The wake mode dynamic stall of a finite wing is characterised by DSV pinning at the leading edge of the wing tip as a result of downwash from the wing tip vortex that suppresses DSV formation in its vicinity [197]. This leads to the formation of an arch-shaped DSV [e.g., 129]. For semi-span wings, the arch shaped DSV curves back towards the wing surface near the root [129], reaching its greatest wall-normal distance from the wing surface near the midspan [198]. Similarly, the spanwise variation of the distance of the separated shear layer from the wing surface in the reattaching limiting state of the present study is expected to result in the formation of arch-shaped roll-up vortices in the LSB over the midspan of the wing. Near the wing tip and root, the downwash produced by the tip and wing root vortices suppress boundary layer separation and roll-up vortex formation. On finite wings undergoing dynamic stall, the suppression of boundary layer separation and DSV formation due to tip vortices has

been linked to a reduction in non-linear lift overshoot [128]. Analogously, the results of the present study indicate that the presence of a wing tip leads to a substantial reduction in lift hysteresis, rendering the lift response to the ramp change in free-stream velocity nearly quasi-steady.

5.5 Concluding Remarks

An experimental study on the formation and bursting of an LSB on a NACA 0018 airfoil and a finite wing with the same airfoil section was undertaken in a wind tunnel for angles of attack between 3° and 9°. Simultaneous direct force and particle image velocimetry measurements were employed to relate the lift produced by the airfoil and wing to transient flow field development over the suction surface. The lift coefficients and velocity field measurements of the airfoil and wing were compared at equivalent geometric and effective angles of attack. The formation and bursting of an LSB on the suction surface of the airfoil and wing models was triggered by imposing controlled ramp changes in free-stream velocity. With non-dimensional accelerations of $|ac/u_\infty^2| \leq 0.011$, the changes in free-stream velocity were essentially quasi-steady.

The results from the airfoil and wing at equivalent effective angles of attack are used to explore the influence of end effects on the transient process of LSB formation and bursting on the wing at a geometric angle of attack of 6°. The corresponding limiting Reynolds numbers for the ramp changes used for this case are $\mathrm{Re}_c = 5.4 \times 10^4$ and 7.4×10^4. At $\mathrm{Re}_c = 5.4 \times 10^4$, the airfoil and wing are stalled, and at $\mathrm{Re}_c = 7.4 \times 10^4$ reattachment occurs and a LSB forms on the suction surface of both models. The presence of wing root and tip effects leads to substantial three-dimensionality of the flow over wing. These end effects also cause notable changes in LSB thickness along the span of the wing in the reattaching limiting state, with the LSB becoming thickest near the midspan and thinner near the wing root and tip.

LSB bursting begins near the midspan on both the airfoil and wing. On the airfoil, cessation of reattachment spreads from the midspan rapidly towards the test section walls. On the wing, cessation of reattachment spreads more gradually from the location of maximum LSB thickness towards the root and tip. During LSB formation, reattachment occurs first near the ends of the airfoil and wing and spreads towards the midspan. The location of reattachment moves upstream more rapidly when the LSB forms during the ramp up than it moves downstream when the LSB bursts during the ramp down. The duration of the transient adjustment for the lift coefficient and flow development on the airfoil ranges from 10 to 22 convective time scales during LSB formation, and from 22 to 30 convective time scales for LSB bursting. This range of transient durations, and the longer duration of the bursting transient, are consistent with results reported for airfoils undergoing pitching or active flow control in previous studies. In contrast, the flow over the wing geometry does not substantially deviate from quasi-steady behaviour. As reflected in the observed transient flow development, the change in lift coefficient during LSB bursting is more gradual on the wing than on the airfoil. This is a result of more gradual spanwise

contraction and expansion of the region of fully separated flow during LSB formation and bursting, respectively. Contrary to the reduction in quasi-steady and transient stall Reynolds numbers expected to be caused by the reduction in effective angle of attack on the wing, an increase in the stall Reynolds number was observed relative to the airfoil at the same effective angle of attack. This finding is attributed to the increased distance of the separated shear layer from the surface in the three-dimensional LSB forming on the wing near the midspan, which inhibits turbulent shear layer reattachment.

Substantial Reynolds number hysteresis is observed for the lift coefficient of the airfoil during the ramp changes in free-stream velocity, taking the form of a counter-clockwise hysteresis loop, with the lift coefficient during the ramp up being lower than that during the ramp down. The lift produced by the wing during the ramp changes in free-stream velocity is less hysteretic than the airfoil, following the quasi-steady lift coefficients more closely. Consequently, the duration of lift coefficient deviations from quasi-steady values are reduced for the wing relative to the airfoil. The lift coefficient hysteresis is linked to hysteresis of the velocity fluctuations in the separated shear layer, with larger amplitude velocity fluctuations associated with the higher lift observed during the ramp down, and smaller amplitudes associated with lower lift during the ramp up.

During the ramp down at moderate angles of attack, the ensemble-averaged lift coefficients do not change monotonically despite the imposed monotonic change in free-stream velocity. For the airfoil and the wing, a local maximum occurs in the ensemble-averaged lift coefficient after the initial rapid loss of lift caused by LSB bursting. This local maximum in lift is linked to an oscillation in the spanwise and wall-normal extent of the recirculating flow region associated with a spanwise-travelling wave of higher velocity fluid. The presence of this phenomenon in the ensemble-average indicates that it is a repeatable process connected to the transient flow development triggered by the imposed change in free-stream velocity.

The LSB bursting criterion of Gaster [7] correctly identifies the LSB on the airfoil in the reattaching quasi-steady limiting state as near bursting. During the ramp up, the formed LSB on the airfoil moves from the long bubble regime to the short bubble regime. During the ramp down, the opposite is observed. The LSB on the wing in the reattaching limiting state is also classified as a short bubble near the root and tip. However, near the midspan, the LSB on the wing falls within the long regime. As a result, the relationship between the bursting criterion parameters during ramp changes in free-stream velocity vary with spanwise position on the wing. Therefore, a precise knowledge of the conditions under which LSB bursting and formation occurs and the associated changes in aerodynamic forces on finite wings at moderate angles of attack requires the consideration of three-dimensional effects.

Chapter 6

Comparison of Transient LSB Development During Changes in Angle of Attack and Reynolds Number

The influence of the type and rate of change of lifting surface operating conditions on LSB formation and bursting transients is studied through wind tunnel experiments on airfoil and finite wing models. Two types of transient changes in operation conditions are considered: i) changes in angle of attack at constant free-stream velocity, and ii) changes in free-stream velocity at constant angle of attack. The pitch rate is varied for the changes in angle of attack to investigate the influence of the time-scale of the change in the operating conditions on the LSB development. The evolution of the lift coefficient during changes in angle of attack is consistent with dynamic stall at higher Reynolds numbers, with a reduction in the time delay between the passing of the static stall condition and the loss of lift with increasing pitch rate. During an increase in angle of attack, the LSB moves upstream before rapidly bursting, whereas for a decrease in free-stream velocity the LSB undergoes a more gradual monotonic increase in length prior to bursting. The process of LSB formation is less sensitive to the type of change in operating conditions. The spanwise flow development during LSB formation and bursting is also insensitive to the type of change in operating conditions.

This chapter has been adapted from

Toppings, C. E. & Yarusevych, S. 2025 Transient dynamics of stall and reattachment at low Reynolds number. *Journal of Fluid Mechanics* **1011**, 1–35. DOI.

6.1 Introduction

The location of boundary layer transition at low chord Reynolds numbers is sensitive to changes in both free-stream velocity magnitude and direction [e.g., 84, 104, 199]. In Chapters 4–5, the effects of a quasi-steady change in operating conditions in the form of a change in free-stream velocity magnitude were investigated. In this chapter, the flow development during a change in free-stream velocity direction due to a change in angle of attack is compared to a change in free-stream velocity magnitude. If bursting is triggered by an increase in angle of attack, the LSB initially shortens and moves upstream as the roll-up vortex shedding frequency increases due to the stronger adverse pressure gradient and increase in boundary layer edge velocity [103]. This is in contrast to bursting during a decrease in Reynolds number, during which there is a downstream movement of the reattachment location and reduction in vortex shedding frequency prior to bursting, as demonstrated in Chapters 4 and 5.

Because LSB formation or bursting can be caused by changes in Reynolds number, angle of attack, or external disturbances, there are multiple pathways between short and long LSB flow configurations. However, our knowledge of how LSB formation and bursting dynamics are affected by the way in which the external operating conditions change remains limited beyond the well-studied LSB dynamics in quasi-steady conditions [e.g., 74]. This impedes more accurate prediction of LSB formation and bursting in unsteady real-world conditions. The objective of this chapter is to understand how the type and time-scale of a change in operating conditions affects transient LSB development, focusing on the relationship between the flow field development and the aerodynamic loads. The effect of varying pitch rate is also studied to understand how the duration of a change in operating conditions affects the duration of the flow response. A secondary objective is to elucidate the influence of finite aspect ratio on the LSB formation and bursting processes during different types of changes in operating conditions. These objectives are achieved through wind tunnel experiments on two-dimensional airfoil and finite wing models, employing lift force measurements simultaneously with PIV.

6.2 Description of Experiments

Experiments were performed in the recirculating wind tunnel at the University of Waterloo. An aspect ratio 2.5 wing model of chord $c = 0.2\,\mathrm{m}$ with a NACA 0018 cross-section was cantilevered vertically from the floor of the $0.61\,\mathrm{m} \times 0.61\,\mathrm{m}$ test section. A schematic of the model setup is presented in Fig. 6.1. A two-dimensional airfoil model was approximated by attaching an extension to the end of the wing model (dashed line in Fig. 6.1), so that the model spanned the entire height of the test section. The wing model and extension were machined from acrylic, polished iteratively with sandpaper to 1500 grit, and finally polished with a finer polishing paste.

The wing and airfoil models were subject to two types of unsteadiness: i) changes in angle of attack at constant Reynolds number and ii) changes in Reynolds number at constant

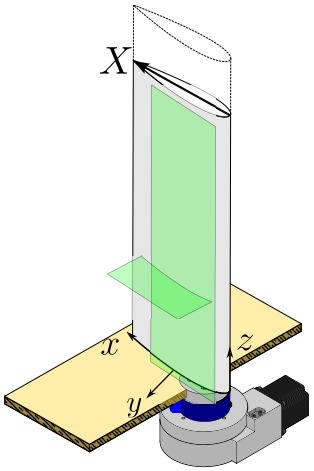


Figure 6.1: Model setup and coordinate system definition. PIV measurement planes in green.

angle of attack. The effect of the Reynolds number on the transient flow development and aerodynamic loading was considered in separate tests from the changes in angle of attack. The changes in angle of attack were performed between 10° and 13° at pitch rates within $3 \times 10^{-5} \leq |\dot{\alpha}c/2u_\infty| \leq 5 \times 10^{-3}$. The model was rotated about the quarter chord. The slowest pitch rate was selected to approximate a quasi-steady change in angle of attack [e.g., 187], whereas the fastest pitch rate was limited by the inertial forces of the model on the load cell. The time-history of the angle of attack for all pitch rates tested is shown in Figs. 6.2a and 6.2b, where the temporal data is presented in terms of the convective time $\mathcal{D} = \frac{1}{c}\int_0^t u_\infty(\tau)d\tau$, equivalent to the number of chord lengths that the free-stream has travelled at time t after the beginning of the commanded pitching motion or Reynolds number change. The Reynolds number was maintained at $1 \times 10^5 \pm 1.5 \times 10^3$ during the pitching motions.

Changes in Reynolds number were performed between $8 \times 10^4 \leq \mathrm{Re}_c \leq 1 \times 10^5$ by changing the wind tunnel fan speed at the maximum rate allowed by the electric drive motor (Figs. 6.2c and 6.2d). The $10\% - 90\%$ rise-time for the increase in Reynolds number was 39 convective time units, and the $90\% - 10\%$ fall-time for the decrease in Reynolds number was 49 convective time units. The maximum non-dimensional free-stream accelerations were $|\partial u/\partial t|\,(c/u_\infty^2) = 0.008$ and 0.007 for the ramp up and down, respectively, meaning that the imposed Reynolds number changes were virtually quasi-steady. The ramp changes in Reynolds number were highly repeatable with an ensemble standard deviation accommodated by the line width in Fig. 6.2. Time $t = 0$ is defined as the time that the rotary table or wind tunnel fan was commanded to begin changing the angle of attack or Reynolds number, respectively. The time lag between the commanded angle change and the beginning of the actual angle change measured by the encoder was negligible. However, the lag between the commanded fan speed change and measured change in Reynolds number was more substantial, yet consistent between runs. To account for this lag, Section 6.3.2 presents results that have been shifted in time according to the response of the measured lift

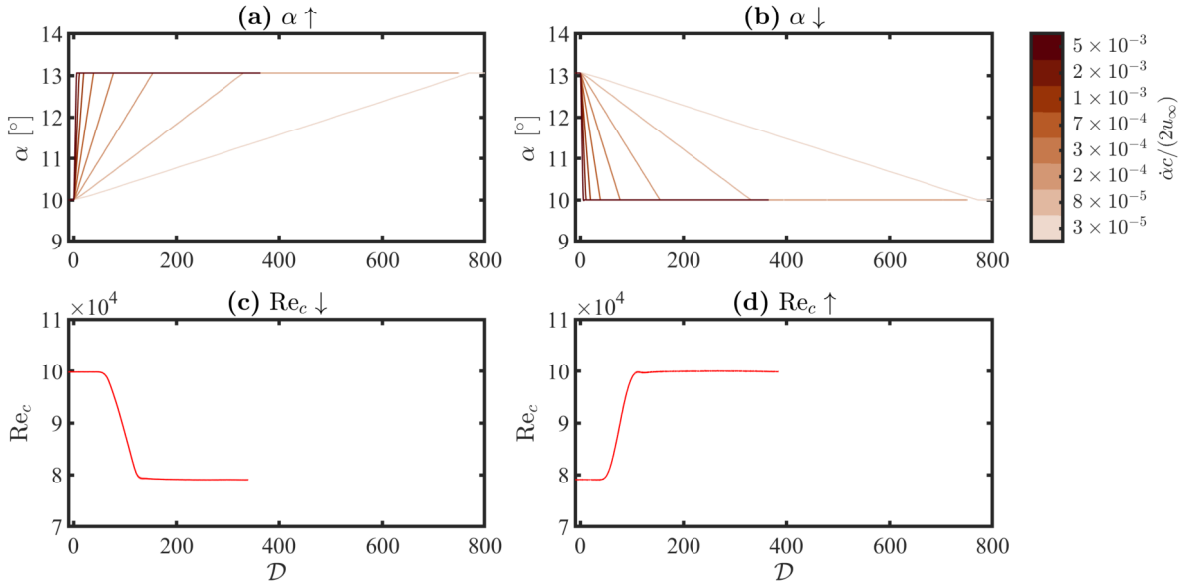


Figure 6.2: Controlled angle of attack (a,b), and Reynolds number (c,d) changes leading to LSB bursting (a,c), and formation (b,d) on the suction surface of the airfoil and wing models. Colours in (a) and (b) correspond to different pitch rates.

force. To obtain ensemble statistics, lift force and PIV measurements were performed for each pitch rate or Reynolds number change over an ensemble of 20 runs. Ensemble averages are denoted with a tilde ($\tilde{}$), and time averages are denoted with an over-bar ($\bar{}$). The measurements were performed as a cyclic motion, with measurements of increases in angle of attack or Reynolds number alternating with decreases in angle of attack or Reynolds number. Between each transient, the flow was allowed to stabilise for approximately $760c/u_\infty$. For the transient cases with simultaneous force and PIV measurements, the wind tunnel fan was turned off after each transient while the particle images were downloaded from the cameras. Before each PIV measurement, the wind tunnel fan was turned on and the flow was allowed to stabilise for approximately $386c/u_\infty$. Comparison of the mean velocity fields of the initial conditions obtained after turning on the wind tunnel from rest with those obtained at the end of transient pitching motions indicated that turning off the wind tunnel between transients had negligible effect on the initial conditions.

6.2.1 Measurement Techniques

The angle of attack of the wing and airfoil models was controlled through a stepper motor connected to a Velmex B48 rotary table and measured by an incremental encoder with a resolution of 0.036°. Angles of attack of the wing and airfoil models were set relative to the measured zero-lift angle. The uncertainty of the angle of attack is estimated to be 0.06° (95% confidence). The wing model was attached to the rotary table through a 6-axis JR3 30E12A4 load cell. The voltage signals from the load cell were amplified using a JR3 amplifier and recorded using a 24-bit National Instruments PCI-4472 data acquisition

card at a sampling rate of 10 kHz. The absolute uncertainty in instantaneous lift force measurements is estimated to be less than 0.2 N. However, since the assumed constant bias error of the load cell does not affect comparisons between force measurements, the presented uncertainties in aerodynamic coefficients account solely for random errors in the measurements. The reference velocity used in the calculation of lift coefficients was obtained from a single hot-wire anemometer located in the test section $2.75c$ upstream of the model. Two-component PIV measurements were acquired during the pitching motions at reduced pitch rates of $\dot{\alpha}c/(2u_\infty) = \pm 3 \times 10^{-4}$ and $\pm 5 \times 10^{-3}$ and during Reynolds number changes between $\mathrm{Re}_c = 8.0 \times 10^4$ and 1.0×10^5. For all PIV measurements, the flow was seeded with water-glycol fog particles measured with a particle analyser to have a mean diameter of approximately 0.7 µm. The particles were illuminated with a Photonics DM20-527 Nd:YLF pulsed laser forming a light sheet with a thickness of approximately $0.01c$. Spurious light reflections in the particle images were mitigated using ensemble minimum background subtraction. All particle images were processed using the multi-pass cross-correlation algorithm with window deformation as implemented in the DaVis 10 software. Erroneous vectors were removed using universal outlier detection [150].

The PIV measurements were performed in two orthogonal planes (Fig. 6.1). Measurements in each plane were obtained during separate runs. The plane tangent to and offset from the suction surface is termed the top-view plane. The laser sheet for the top-view plane was positioned parallel to the model chord and the minimum distance between the model surface and the laser sheet was 3 mm. Top-view particle images were acquired using a side-by-side arrangement of three LaVision sCMOS 5.5 megapixel cameras, operating in double-frame mode with a sampling frequency of 25 Hz and a laser pulse separation interval of 80 µs. All three cameras were equipped with Nikon 50 mm focal length lenses with the apertures set to $f/4$. The combined field of view of covered $0.03 < X/c < 0.77$ in the streamwise direction and $0 < z/c < 2.5$ in the spanwise direction, and the dimensionless magnification factor was 0.10. The maximum particle image displacement in the top-view images was 16 pixels. The initial and final correlation window sizes were 64px × 64px and 24px × 24px, respectively, yielding a vector pitch of $0.002c$. A total of 250 samples were acquired during each transient pitching motion or Reynolds number change. Data from the top-view PIV plane is presented in a chord-based coordinate system, with the origin at the model root leading edge, the X axis parallel to the chord, and the z axis parallel to the span (Fig. 6.1). The velocity components in the X and z directions are denoted as u and w, respectively.

The PIV measurement plane normal to the span of the model is termed the side-view plane. The laser sheet for the side-view plane was positioned at $z/c = 1.5$ and at $z/c = 1$ for measurements on the airfoil and wing, respectively. These locations were selected to reduce the influence of spanwise flow due to end effects on the two-component PIV measurements. Side-view particle images were acquired using time-resolved and non-time-resolved camera setups in separate runs. The time-resolved measurements employed two side-by-side Photron Fastcam SA4 1 megapixel cameras operated in double-frame mode with a laser pulse separation interval of 60 µs. The sampling frequency was 2500 Hz. The side-view cameras were equipped with 200 mm focal length Nikon micro lenses with the apertures

Parameter	Side-view	Top-view
Cameras	2× Photron Fastcam SA4	3× LaVision Imager sCMOS
Cropped sensor size	1024px × 512px	2560px × 2160px
Combined field of view	$0.37c \times 0.69c$	$0.74c \times 2.50c$
Lens focal length	200 mm	
Aperture	$f/4$	
Magnification factor	0.15	0.10
Sampling frequency	2500 Hz	25 Hz
Number of samples during transient conditions	5457	250
Number of samples in limiting conditions	5457	4000
Laser pulse separation	60 µs	
Maximum particle image displacement	18px	16px
Initial interrogation window size	24px × 24px	
Final interrogation window size	16px × 16px	
Vector pitch	$0.003c$	$0.002c$
Light source	Photonics DM20-527 Nd:YLF pulsed laser	
Light sheet thickness	2 mm	
Particles	1 µm diameter water-glycol fog	

Table 6.1: PIV parameters.

set to $f/4$. The combined field of view was $0.15 < x/c < 0.52$ in the streamwise direction and $0 < y/c < 0.7$ in the wall-normal direction, and the dimensionless magnification factor was 0.15. The maximum particle displacement was 18 pixels, and the initial and final correlation window sizes were 24px × 24px and 16px × 16px, yielding vector pitches of $0.003c$. A total of 5457 samples were acquired during each transient pitching motion or Reynolds number change and for steady-state measurements of the initial and final flow conditions. Essential PIV setup parameters are listed in Table 7.1. Data from the side-view PIV plane is presented in a surface-attached coordinate system, with the origin at the model root leading edge, the x axis tangent to the suction surface, the y axis normal to the suction surface, and the z axis parallel to the span (Fig. 6.1). The velocity components in the x, y, and z directions are denoted as u, v, and w, respectively.

The uncertainty in each velocity vector field was estimated using the correlation statistics method [149]. For the side-view PIV configuration, the uncertainty in the u and v velocity components in the vicinity of the separated shear layer is less than $0.1u_\infty$ at a confidence level of 95%. For the top-view PIV configuration, the uncertainty in the u and w velocity components in the vicinity of the separated shear layer is less than $0.13u_\infty$ at a confidence level of 95%. The higher uncertainty in the for the top-view measurements is attributed to the strong streamwise velocity gradient and out of plane particle motion where the separated shear layer intersects the top-view measurement plane.

6.2.2 Data processing techniques

To isolate the aerodynamic loads from the inertial loads acting on the load cell during pitching motions, the lift forces measured in quiescent conditions were subtracted from the lift forces obtained during flow measurements. The structural natural frequency of both the airfoil and wing models was measured to be approximately 12 Hz. To attenuate fluctuations in the measured force coefficients caused by random noise and structural vibrations, the

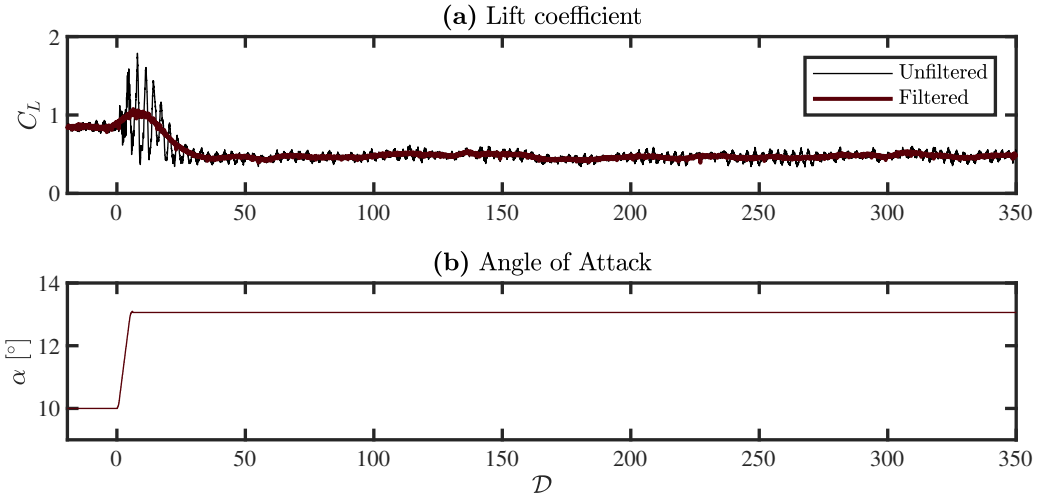


Figure 6.3: Unfiltered and filtered lift coefficients for the airfoil undergoing a pitch up manoeuvre at $\dot{\alpha}c/(2u_\infty) = 5 \times 10^3$. The forces measured in quiescent conditions have been subtracted from the forces used to calculate the unfiltered and filtered force coefficients.

lift coefficients were filtered using the empirical mode decomposition described by Huang *et al.* [200]. The filtering procedure used here involved subtracting the first six intrinsic mode functions (IMF) from the raw force coefficient data. Cubic spline interpolation was used to compute the signal envelope. The sifting process for each IMF was stopped when the relative tolerance between consecutive sifting results (SD) was less than 0.15 or at a maximum of 50 sifting iterations, whichever occurred first. The relative tolerance is defined as [200]:

$$SD = \sum_{t=0}^{T} \frac{(h_{k-1}(t) - h_k(t))^2}{h_{k-1}^2(t)} \tag{6.1}$$

where h_{k-1} is the result of the previous sifting iteration, h_k is the result of the current sifting iteration, and T is the sampling period. A comparison of the unfiltered lift coefficient data with the quiescent load subtracted and the filtered lift coefficient with the quiescent load subtracted for the airfoil undergoing a pitch up manoeuvre for $\dot{\alpha}c/(2u_\infty) = 5 \times 10^3$ is presented in Fig. 6.3 versus the non-dimensional convective time $\mathcal{D}$. The effective low-pass cut-off frequency of this filtering method is on the order of $0.1u_\infty/c$, corresponding to a period of approximately $10c/u_\infty$. The cut-off frequency is defined as the frequency for which the ratio of the squared amplitude of the output and input signals drops below a threshold of -3 dB.

To quantitatively compare the time-history of the lift coefficient between different transients, the duration of the step change in lift coefficient ($\Delta\mathcal{D}_{\text{step}}$) and the time delay of the reaction of the lift coefficient to the change in operating conditions ($\Delta\mathcal{D}_{\text{react}}$) were computed using a method based on that used by Le Fouest *et al.* [187]. In Figs. 6.4 and 6.5, which illustrate this method for a decrease in angle of attack and decrease in Reynolds number, respectively. The temporal evolution of the lift coefficients has been shifted by the time of passing the static reattachment condition ($\mathcal{D}_{sr}$, Fig. 6.4b) and the static stall

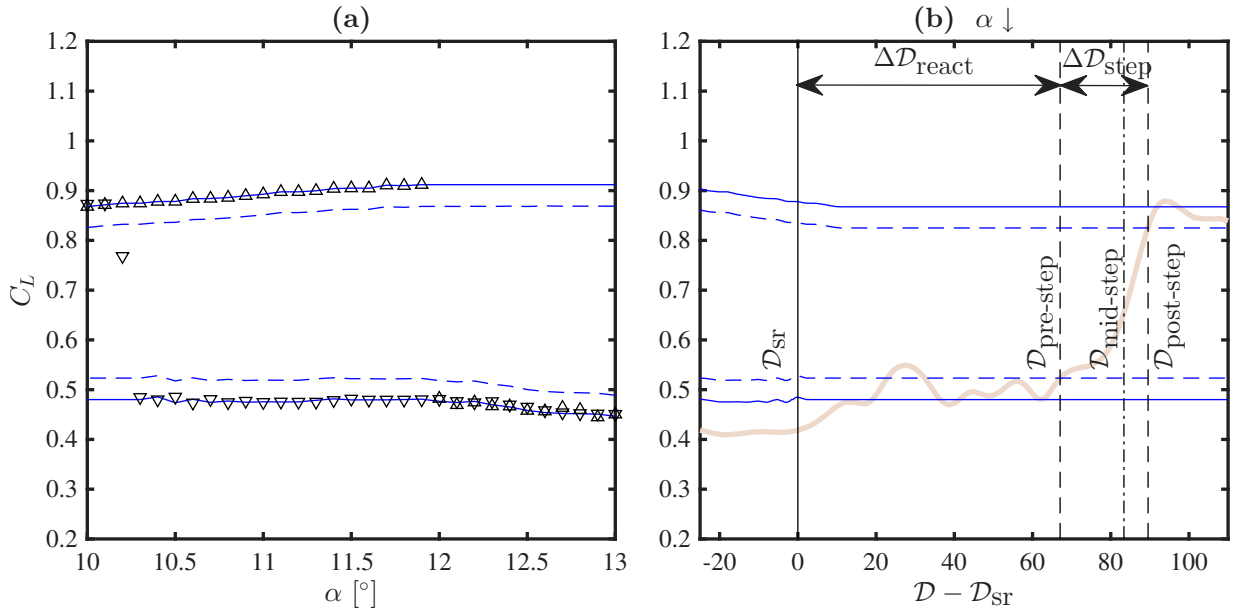


Figure 6.4: Definition of reaction and step times for pitching motion. Light brown line: lift coefficient during pitch down motion at $\dot{\alpha}c/\left(2u_\infty\right) = 3 \times 10^{-4}$, solid blue lines: pre-stall and post-stall lift coefficients, dashed blue lines: thresholds for defining $\mathcal{D}_{\text{pre-step}}$ and $\mathcal{D}_{\text{post-step}}$, $\triangle$: quasi-steady C_L for increasing α, $\triangledown$: quasi-steady C_L for decreasing α.

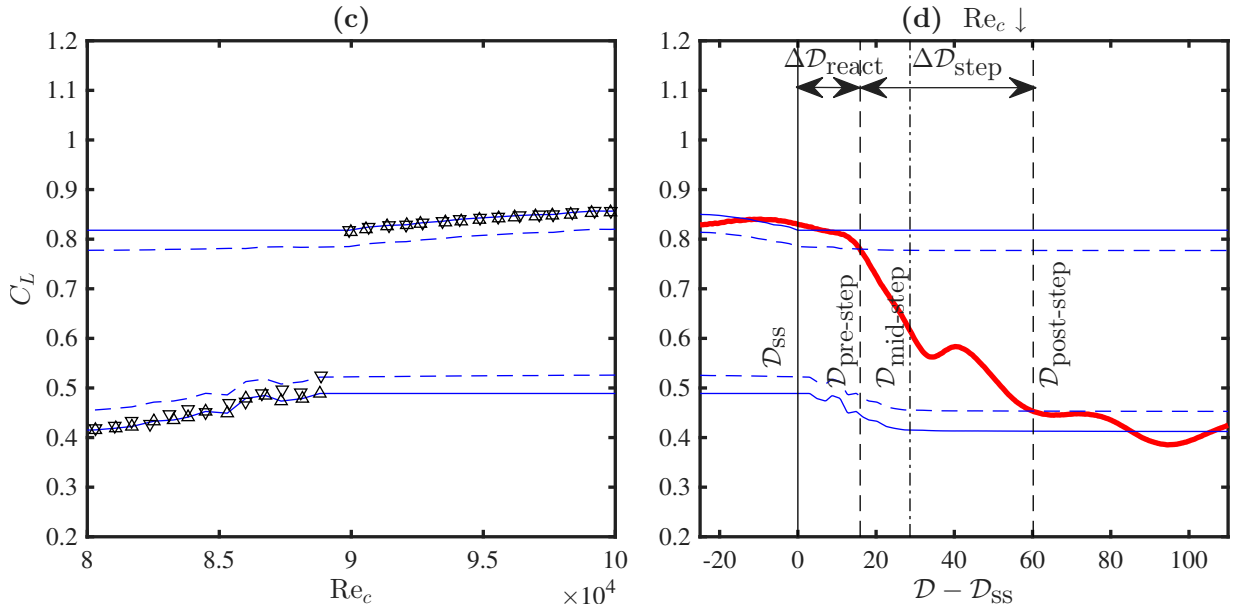


Figure 6.5: Definition of reaction and step times for Re_c change. Red line: lift coefficient during decrease in Re_c, solid blue lines: pre-stall and post-stall lift coefficients, dashed blue lines: thresholds for defining $\mathcal{D}_{\text{pre-step}}$ and $\mathcal{D}_{\text{post-step}}$, $\triangle$: quasi-steady C_L for increasing Re_c, $\triangledown$: quasi-steady C_L for decreasing Re_c.

condition ($\mathcal{D}_{ss}$ Fig. 6.5b), respectively. The static stall and reattachment angles of attack are defined as the angles of attack immediately preceding the largest magnitude rate of change of lift coefficient for increasing and decreasing angle of attack, respectively. Analogously, the static stall and reattachment Reynolds numbers are defined as the Reynolds numbers immediately following and preceding the largest magnitude rate of change of lift coefficient, respectively.

The step times ($\Delta\mathcal{D}_{\text{step}}$) are defined as the difference between the post-step time ($\mathcal{D}_{\text{post-step}}$), and the pre-step ($\mathcal{D}_{\text{pre-step}}$) time, which correspond to the end and the beginning of the step change in lift coefficient, respectively. The procedure for computing $\mathcal{D}_{\text{pre-step}}$ and $\mathcal{D}_{\text{post-step}}$ requires the definition of pre- and post-stall lift coefficients ($C_{L,\text{pre-stall}}$ and $C_{L,\text{post-stall}}$). Because the quasi-steady pre-stall and post-stall lift coefficients vary with angle of attack and Reynolds number, the employed stall and reattachment thresholds for the lift coefficient are also defined as functions of the angle of attack and Reynolds number using the following procedure. In the case of pitching transients, for angles of attack below the static stall angle, $C_{L,\text{pre-stall}}$ is defined equal to the quasi-steady lift coefficient during quasi-steady upward pitching. For angles of attack above the static stall angle, $C_{L,\text{pre-stall}}$ is defined equal to the lift coefficient at the static stall angle. Similarly, $C_{L,\text{post-stall}}$ is defined as equal to the quasi-steady lift coefficient during downward pitching for angles of attack greater than the quasi-steady reattachment angle, and equal to the lift coefficient at the quasi-steady reattachment angle for angles of attack less than the quasi-steady reattachment angle. These definitions of $C_{L,\text{pre-stall}}$ and $C_{L,\text{post-stall}}$ are plotted as solid blue lines in Fig. 6.4a. The pre-stall and post-stall lift coefficients for the transient changes in Reynolds number are defined analogously and plotted in Fig. 6.5a.

For transients leading to stall, the start of the step change in lift coefficient ($\mathcal{D}_{\text{pre-step}}$) is defined as the first time after the initiation of the change in operating conditions that the lift coefficient was less than $C_{L,\text{pre-stall}} - 0.1\,(C_{L,\text{pre-stall}} - C_{L,\text{post-stall}})$, and the end of the step change in lift coefficient ($\mathcal{D}_{\text{post-step}}$) is defined as the first time that the lift coefficient was less than $C_{L,\text{post-stall}} + 0.1\,(C_{L,\text{pre-stall}} - C_{L,\text{post-stall}})$. For the transients leading to reattachment, $\mathcal{D}_{\text{pre-step}}$ is defined as the last time that the lift coefficient was greater than $C_{L,\text{post-stall}} + 0.1\,(C_{L,\text{pre-stall}} - C_{L,\text{post-stall}})$, and $\mathcal{D}_{\text{post-step}}$ is defined as the first time that the lift coefficient was greater than $C_{L,\text{pre-stall}} - 0.1\,(C_{L,\text{pre-stall}} - C_{L,\text{post-stall}})$. These thresholds are plotted as dashed blue lines in Figs. 6.4 and 6.5. Representative runs for LSB formation and bursting are presented in Fig. 6.4b and Fig. 6.5b, respectively. The reaction delay ($\Delta\mathcal{D}_{\text{react}}$) is defined as the time difference between $\mathcal{D}_{\text{pre-step}}$ and the passing of the static stall or reattachment condition. The definitions of the start and end of the step changes where formulated with the goal of reducing erroneous measurements of $\Delta\mathcal{D}_{\text{react}}$ caused by the relatively large random fluctuations in lift coefficient that occur in the stalled limiting state.

In Section 6.3.2, ensemble statistics are presented after shifting data from individual runs in time using the mid-step time ($\mathcal{D}_{\text{mid-step}}$) so that the step change in lift coefficient occurs at the same time for each run. $\mathcal{D}_{\text{mid-step}}$ is defined as the first time the lift coefficient was equal to $1/2\,(C_{L,\text{post-stall}} + C_{L,\text{pre-stall}})$.

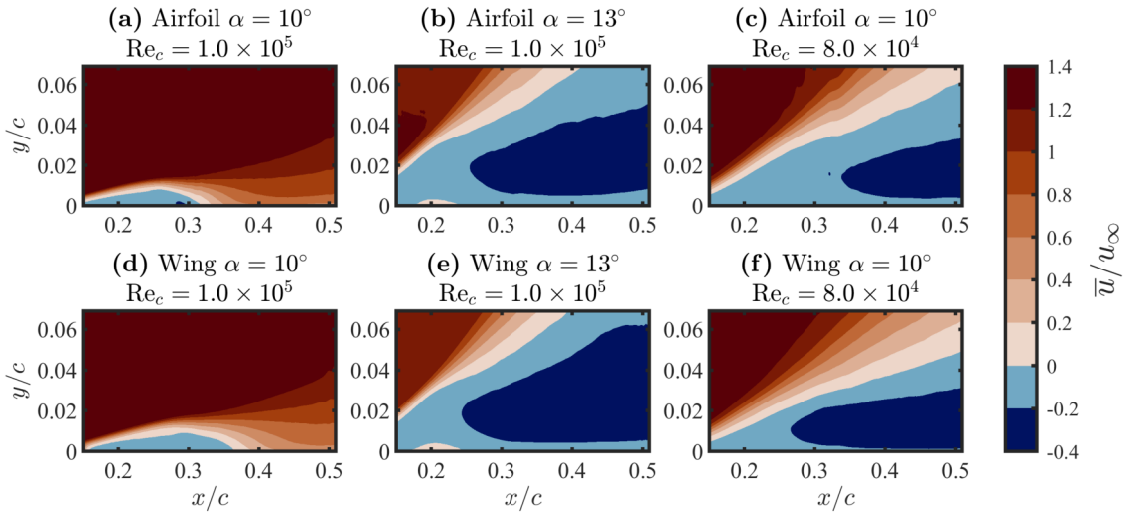


Figure 6.6: Mean streamwise velocity contours in steady conditions measured by side-view PIV configuration.

6.3 Results and Discussion

6.3.1 Limiting flow states

The transient changes in angle of attack and Reynolds number used to investigate LSB formation and bursting involve changes between statistically stationary limiting flow states. The wall-normal structure of the flow development on the airfoil and wing in the limiting flow states is illustrated by the contours of mean streamwise velocity from the side-view PIV presented in Fig. 6.6. The side view measurements were taken at $z/c = 1.5$ and $z/c = 1$ for the airfoil and wing models, respectively. At $\alpha = 10°$ and $\mathrm{Re}_c = 1.0 \times 10^5$ (Figs. 6.6a and 6.6d), the laminar boundary layer separates upstream of the field of view, and reattaches in the mean sense at $x/c = 0.32$ and $x/c = 0.37$ on the airfoil and wing models, respectively. The delay in reattachment on the wing relative to the airfoil is attributed to the reduction in effective angle of attack on the wing model caused by the presence of the wing tip, which reduces the streamwise adverse pressure gradient and is expected to delay separation and transition [114]. In the stalled limiting states (Figs. 6.6b, 6.6c, 6.6e, and 6.6f), reattachment does not occur, and the magnitude and spatial extent of reverse flow is substantially increased. The flow field development at $\alpha = 13°$ and $\mathrm{Re}_c = 1.0 \times 10^5$ (Figs. 6.6b and 6.6e) is largely similar to that at $\alpha = 10°$ and $\mathrm{Re}_c = 8.0 \times 10^4$ (Figs. 6.6c and 6.6f), except that the separated shear layer remains closer to the model surface at the lower Reynolds number.

Quasi-steady lift coefficient measurements for the wing and airfoil models versus angle of attack and Reynolds number are presented in Figs. 6.7 and 6.8, respectively. The expected reduction in quasi-steady lift of the finite wing relative to the airfoil at pre-stall angles of attack is evident from the lift polars in Fig. 6.7. The limiting flow states (coloured markers)

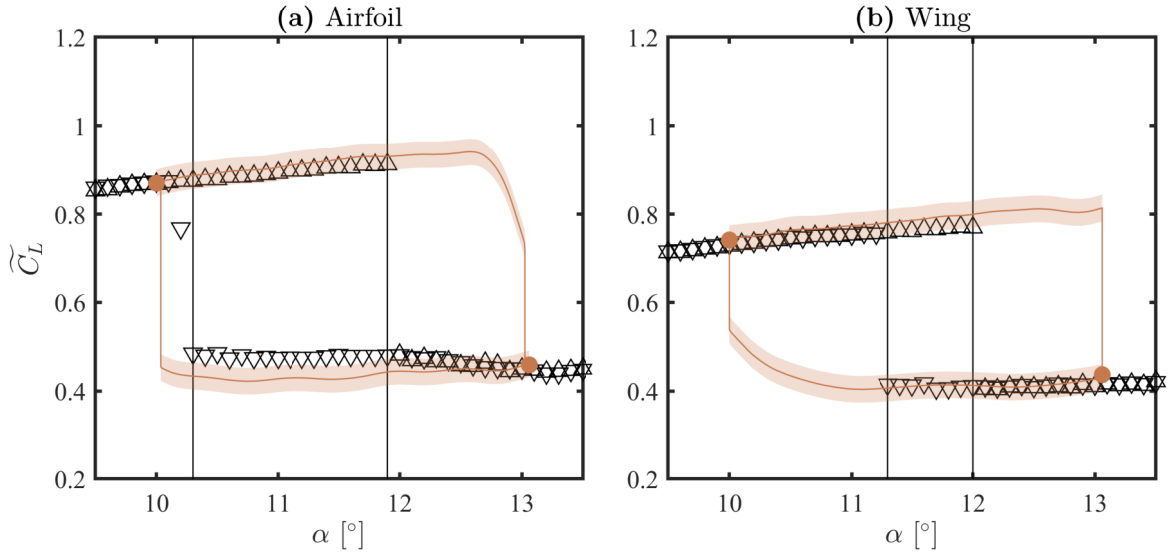


Figure 6.7: Quasi-steady (black markers), and transient (coloured lines) lift coefficients for pitching airfoil (a), and wing (b) at $\mathrm{Re}_c = 1 \times 10^5$ and $\dot{\alpha}c/(2u_\infty) = \pm 3 \times 10^{-4}$. $\triangle$: increasing α, $\triangledown$: decreasing α, black lines: static reattachment and stall angles, coloured markers: limiting flow states. Shaded areas denote uncertainty (95% confidence).

straddle the quasi-steady stall and reattachment angles and Reynolds numbers (vertical black lines, as defined in Section 6.2.2) for the airfoil and wing for changes in angle of attack (Fig. 6.7) and changes in Reynolds number (Fig. 6.8). The differences between the limiting flow states measured during transients and the quasi-steady measurements are within the experimental uncertainty. The static stall angles for increasing angle of attack for the airfoil and wing models are 11.9° and 12.0°, respectively, and the static reattachment angles for decreasing angle of attack are 10.3° and 11.3°, respectively. The static stall and reattachment Reynolds numbers are defined as the Reynolds numbers following or preceding the largest magnitude change in lift coefficient, respectively. The static stall Reynolds numbers for decreasing Reynolds number for the airfoil and wing are 9.0×10^4 and 8.8×10^4, respectively, and the static reattachment Reynolds numbers for increasing Reynolds number are 8.9×10^4 and 8.6×10^4, respectively. The increase in the stall and reattachment angles and decrease in the stall and reattachment Reynolds numbers of the wing relative to the airfoil is attributed to the reduction in effective angle of attack caused by the presence of the wing tip. For both models, there is substantial hysteresis in the lift coefficient for quasi-steady changes in angle of attack. The existence of a quasi-steady hysteresis loop is characteristic of lifting surfaces operating at low Reynolds numbers [e.g., 79] and suggests the presence of an LSB on both models under the conditions investigated. The area of the quasi-steady hysteresis loop of the airfoil is 2.6 times that of the wing. In contrast to the lift coefficient hysteresis observed for quasi-steady changes in angle of attack, no significant hysteresis was observed for quasi-steady changes in Reynolds number (Fig. 6.8).

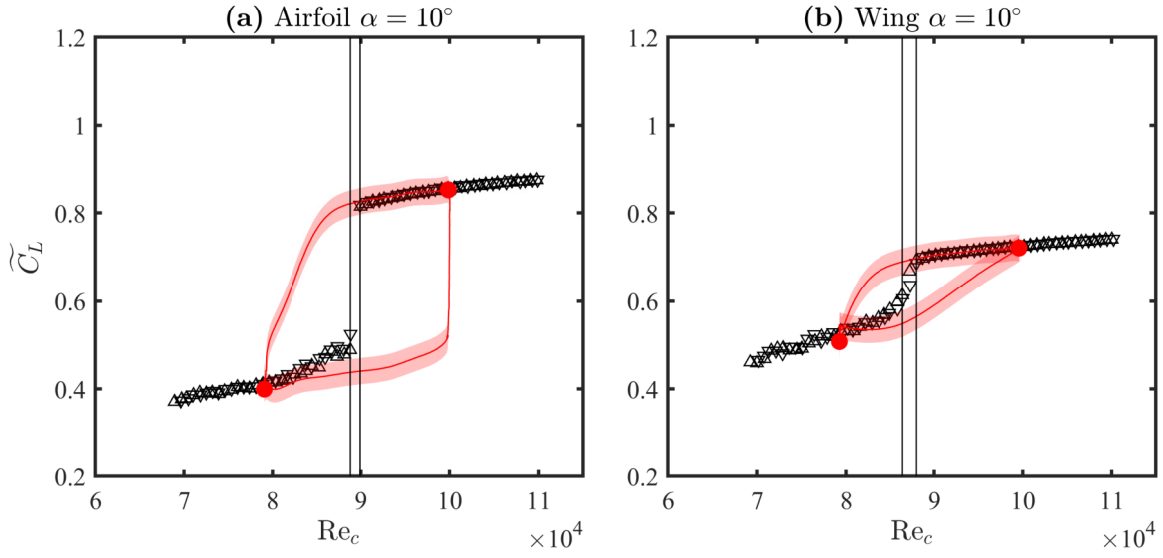


Figure 6.8: Quasi-steady (markers), and ensemble-averaged transient (red lines) lift coefficients for (a,c) airfoil and (b,d) wing for changes in Re_c. △: increasing Re_c, ▽: decreasing Re_c, black lines: static reattachment and stall Reynolds numbers, coloured markers: limiting flow states. Shaded areas denote uncertainty (95% confidence).

6.3.2 Transient Flow Development

The relationship between ensemble-averaged unsteady and quasi-steady lift coefficients of the airfoil and wing models are examined in Figs. 6.7 and 6.8. The pitching motion shown for comparison is that for $\dot{\alpha}c/(2u_\infty) = \pm 3 \times 10^{-4}$, which has a duration of $75c/u_\infty$ that is approximately equal to the duration of the transient Reynolds number change. The ensemble-averaged lift coefficients from the transient pitching motions exhibit an enlargement of the hysteresis loop compared to the quasi-steady measurements. The area of the transient hysteresis loop of the airfoil is 1.3 times that of the wing. Note that the uncertainty of the ensemble average (shaded area) is significantly less than the variations between individual runs because of the ensemble size of 20 runs. The nearly monotonic change in ensemble-averaged lift coefficient between $\alpha = 10°$ and 13° for upward pitching of the wing (Fig. 6.7b) indicates that stall does not occur until after the final angle of attack is reached. However, for the airfoil, loss of lift begins prior to reaching $\alpha = 13°$. As expected for lifting surfaces undergoing dynamic stall and reattachment, the transient pitching motions produce overshoots and undershoots relative to the quasi-steady lift coefficients [e.g., 55, 64].

Although there is no quasi-steady hysteresis in the lift coefficient with respect to Reynolds number, transient changes in Reynolds number exhibit hysteresis for the wing and the airfoil (Fig. 6.8). However, the reduction in effective angle of attack of the wing reduces the area of its hysteresis loop to approximately 1/4 of the area of the airfoil's hysteresis loop. This suggests that the difference in lift coefficient between the upper and lower branches of the hysteresis loop with respect to Reynolds number increases with increasing effective

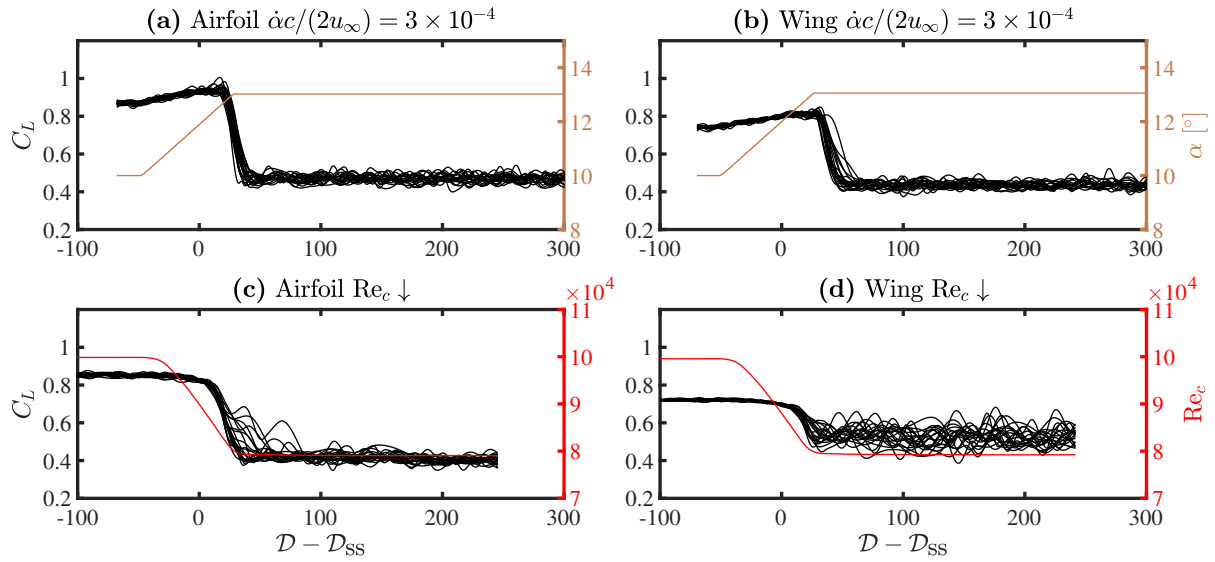


Figure 6.9: Lift coefficients from individual runs of the pitching motion with rate $\dot{\alpha}c/(2u_\infty) = 3 \times 10^{-5}$ and Reynolds number decrease.

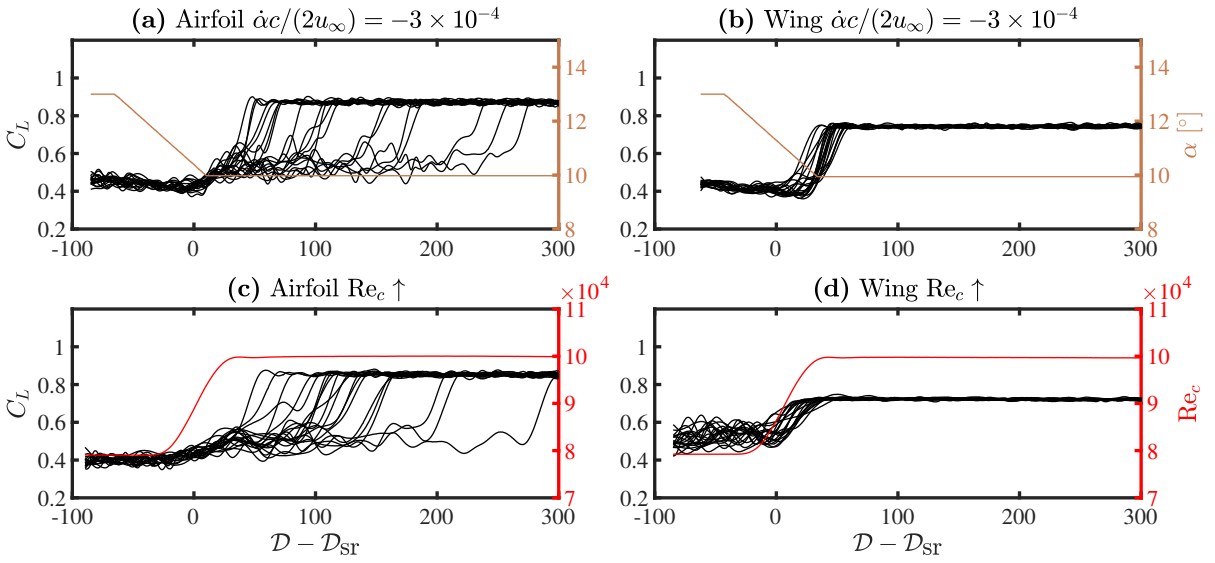


Figure 6.10: Lift coefficients from 20 individual runs of the pitching motion with rate $\dot{\alpha}c/(2u_\infty) = -3 \times 10^{-5}$ and Reynolds number increase.

angle of attack.

Lift coefficients obtained from 20 individual runs for the airfoil and wing during transients leading to stall are plotted in Fig. 6.9 versus the non-dimensional convective time. The uncertainty in instantaneous lift coefficient measurements is estimated to be less than 0.05. The pitching motions and Reynolds number changes in the figure have been shifted in time so that the static stall condition is passed at $\mathcal{D} - \mathcal{D}_{\mathrm{ss}} = 0$ for both types of changes in operating conditions. The stall process results in a step-like reduction in lift coefficient

after the static stall condition is passed, with relatively small variations between runs of the moment that the rapid loss of lift initiates. In Section 6.3.2 it will be shown that the step-change in lift is caused by bursting of the LSB on the suction surface. The variation in the timing of the initiation of the step-change, quantified by the standard deviations of $\Delta\mathcal{D}_{\text{react}}$ (defined in Section 6.2.2), are 2 and 3 convective time units for the pitching motions of the airfoil and wing, respectively, for both types of changes in operating conditions.

Lift coefficients obtained from 20 individual runs for the airfoil and wing during transients leading to reattachment are plotted in Fig. 6.10. The measurements have been shifted in time so that the static reattachment condition is passed at $\mathcal{D} - \mathcal{D}_{\text{sr}} = 0$ for both types of changes in operating conditions. The step-like increase in lift that occurs for downward pitching motions and Reynolds number increases will be shown in Section 6.3.2 to be caused by reattachment of the separated turbulent shear layer and formation of an LSB on the suction surface. There is a notably greater variation in the timing of the step-like increase in lift during reattachment compared to the rapid decrease in lift during stall, and the variation is greater for the airfoil (Figs. 6.10a and 6.10c) than for the wing (Figs. 6.10b and 6.10d).The standard deviations of $\Delta\mathcal{D}_{\text{react}}$ for the pitching motions of the airfoil and wing are 67 and 9, respectively. For the increase in Reynolds number the standard deviations of $\Delta\mathcal{D}_{\text{react}}$ for the airfoil and wing are 55 and 10, respectively. The greater variability in the onset of the lift increase for the airfoil than the wing was hypothesised to be related to the closer proximity of the airfoil reattachment angle of attack to the final angle of attack during downward pitching motions than for the wing (Fig. 6.7a). To test this hypothesis, pitching runs were also performed between $\alpha = 9°$ and $14°$. In those runs, discussed in more detail in Section 6.3.4, the timing of the onset of the step changes in lift for both models was less variable, supporting this hypothesis. The variation in timing of the lift response and its relationship to pitch rate is quantified in Section 6.3.5. Regardless of the precise timing of the lift recovery, the rate of change of the lift coefficient as the final limiting state is approached remains relatively consistent between runs. Therefore, to obtain ensemble flow-field statistics that reflect LSB formation and bursting dynamics, the ensemble statistics presented in the following section were computed after shifting the measurements from each run by $\mathcal{D}_{\text{mid-step}}$ (defined in Section 6.2.2), so that the step change in lift coefficient was approximately centred in time about $\mathcal{D} - \mathcal{D}_{\text{mid-step}} = 0$.

Laminar separation bubble dynamics

This section focusses on the transient dynamics of the LSB on the suction surface of the airfoil whose bursting and formation are linked to the step-changes in transient lift coefficients. The evolution of the streamwise LSB structure on the wing is similar to that of the airfoil and is omitted for brevity. A comparison of the flow-field development leading to LSB bursting on the airfoil for a pitching motion and Reynolds number change of duration approximately $75c/u_\infty$ is facilitated by the streamwise velocity and instantaneous vorticity fields presented in Figs. 6.11 and 6.12, respectively. The presented ensemble-average streamwise velocity fields from 20 runs have been averaged over a sliding temporal window of one convective time unit for better statistical convergence. Flow-fields are shown for

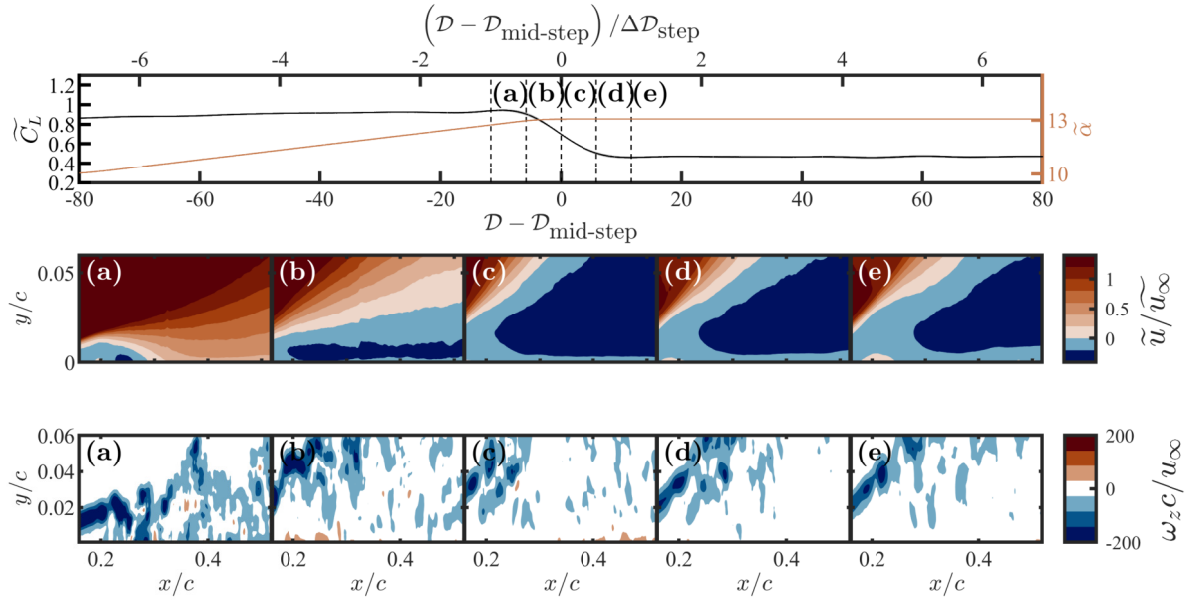


Figure 6.11: Ensemble-averaged lift coefficient and angle of attack (top row), streamwise velocity (middle row), and instantaneous spanwise vorticity (bottom row) contours from side-view PIV for $\dot{\alpha}c/(2u_\infty) = 3\times10^{-4}$. Shaded areas indicate uncertainty (95% confidence).

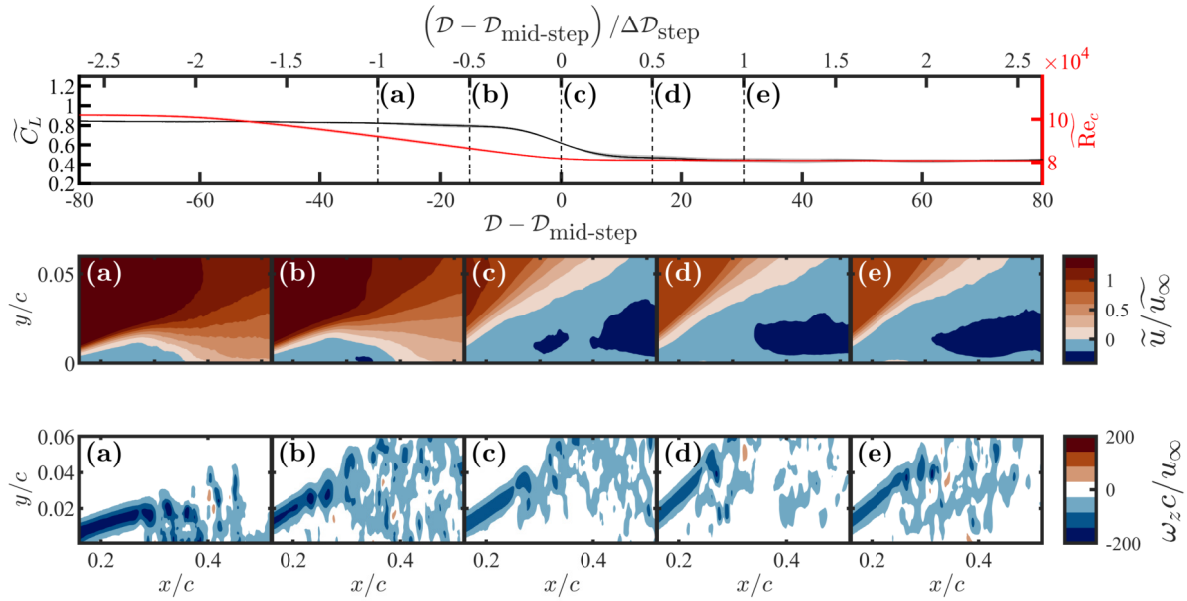


Figure 6.12: Ensemble-averaged lift coefficient and Reynolds number (top row), streamwise velocity (middle row), and instantaneous spanwise vorticity (bottom row) contours from side-view PIV for Reynolds number decrease. Shaded areas indicate uncertainty (95% confidence).

the LSB at $(D - D_{\text{mid-step}})/\Delta D_{\text{step}} = -1$, -0.5, 0, 0.5, and 1 in panels (a-e), respectively. These times correspond to flow conditions prior to, at the beginning of, in the middle of, at the end of, and after the step change in lift coefficient, respectively.

Prior to bursting during the pitching motion at $\dot{\alpha}c/(2u_\infty) = 3 \times 10^{-4}$ (Fig. 6.11a), reattachment occurs at $x/c \approx 0.30$, which is upstream of the reattachment location in the initial limiting LSB condition (cf. Fig. 6.6a) because of the stronger adverse pressure gradient at the increased angle of attack. The instantaneous vorticity contours show that the separated laminar shear layer rolls up into vortices at $x/c \approx 0.2$. When the loss of lift begins, (Fig. 6.11b), reattachment no longer occurs, leading to massive separation. The instantaneous vorticity contours indicate vortex roll-up occurring upstream of the field of view at this time. As the lift coefficient continues to decrease, the wall-normal extent of the reverse flow region increases (Fig. 6.11c).

In contrast to the pitching transient, the evolution of the LSB structure during the reduction in Reynolds number begins with a downstream movement of the reattachment point. When $(D - D_{\text{react}})/\Delta D_{\text{step}} = -1$ (Fig. 6.12a), reattachment occurs at $x/c \approxeq 0.36$ which is downstream of its location in the initial flow because of the delay in transition at the reduced Reynolds number. Reattachment persists, and the LSB continues to increase in length and thickness as the lift coefficient begins to decrease more rapidly at $(D - D_{\text{mid-step}})/\Delta D_{\text{step}} = -0.5$ (Fig. 6.12b). The instantaneous vorticity field at this time shows that the shear layer roll-up location is farther from the airfoil surface than previously. At the middle of the drop of the lift coefficient (Fig. 6.12c), reattachment no longer occurs and there is massive separation over the suction surface of the airfoil. For the reduction in Reynolds number, the location of shear layer roll-up in the stalled flow is farther downstream than for the increase in angle of attack, consistent with the expected reduction in the convective growth rates of disturbances at lower Reynolds numbers [e.g., 201].

A comparison of the flow-field development leading to LSB formation for a pitch down motion and Reynolds number increase at the same rates but opposite senses as those of Figs. 6.11 and 6.12 is facilitated by the streamwise velocity and instantaneous vorticity fields presented in Figs. 6.13 and 6.14, respectively. The time instants at which ensemble-averaged streamwise velocity and instantaneous vorticity are shown for both transients are defined in the same way as Figs. 6.11 and 6.12 using the shifted and normalised convective time ($(D - D_{\text{mid-step}})/\Delta D_{\text{step}}$). The full time series of the flow field measurements is available in movies 5 and 6, respectively.

For the pitch down motion (Fig. 6.13), the lift increase can be divided into two distinct periods: an initial slow increase in lift from $(D - D_{\text{mid-step}})/\Delta D_{\text{step}} = -1$ to 0 followed by a more rapid increase in lift from $(D - D_{\text{mid-step}})/\Delta D_{\text{step}} = 0$ to 0.5. A comparison of Figs. 6.13a and 6.13b suggests that the initial slow increase in lift is due to the relatively slow movement of the separated shear layer towards the airfoil surface. A more rapid lift increase occurs as reattachment begins between $(D - D_{\text{mid-step}})/\Delta D_{\text{step}} = 0$ and 0.5. (Figs. 6.13c and 6.13d). After the rapid increase in lift is complete, the size and location of the LSB and the trajectory of the separated shear layer remain largely unchanged (Fig. 6.13e).

For the Reynolds number increase (Fig. 6.14), the rate of lift increase between

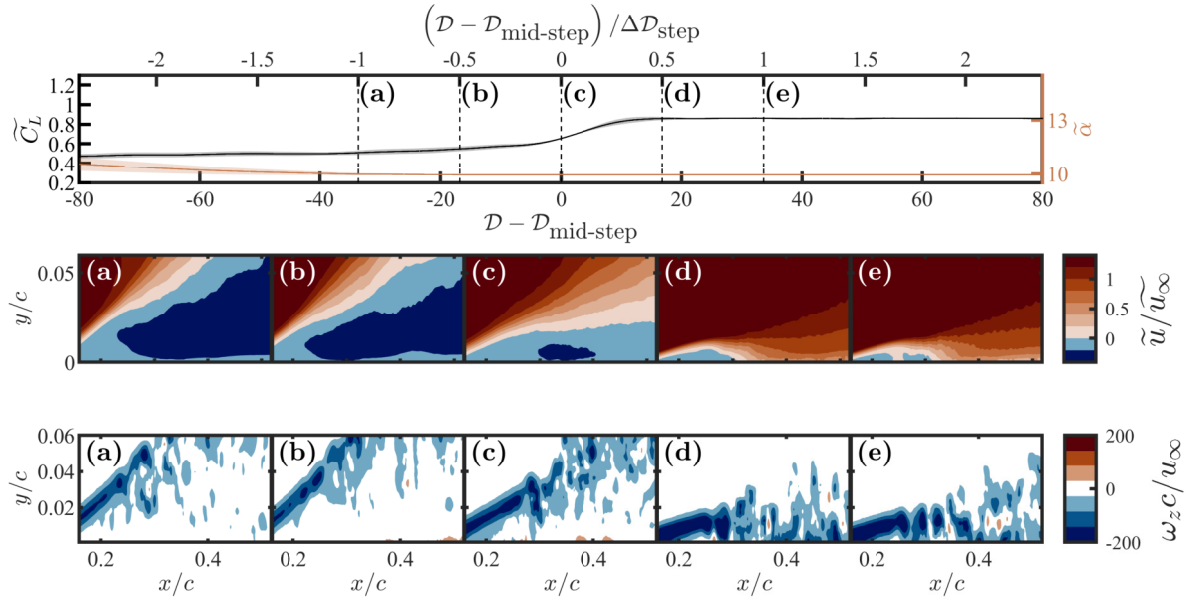


Figure 6.13: Ensemble-averaged lift coefficient and angle of attack (top row), streamwise velocity (middle row), and instantaneous spanwise vorticity (bottom row) contours from side-view PIV for $\dot{\alpha}c/(2u_\infty) = -3 \times 10^{-4}$. Shaded areas indicate uncertainty (95% confidence).

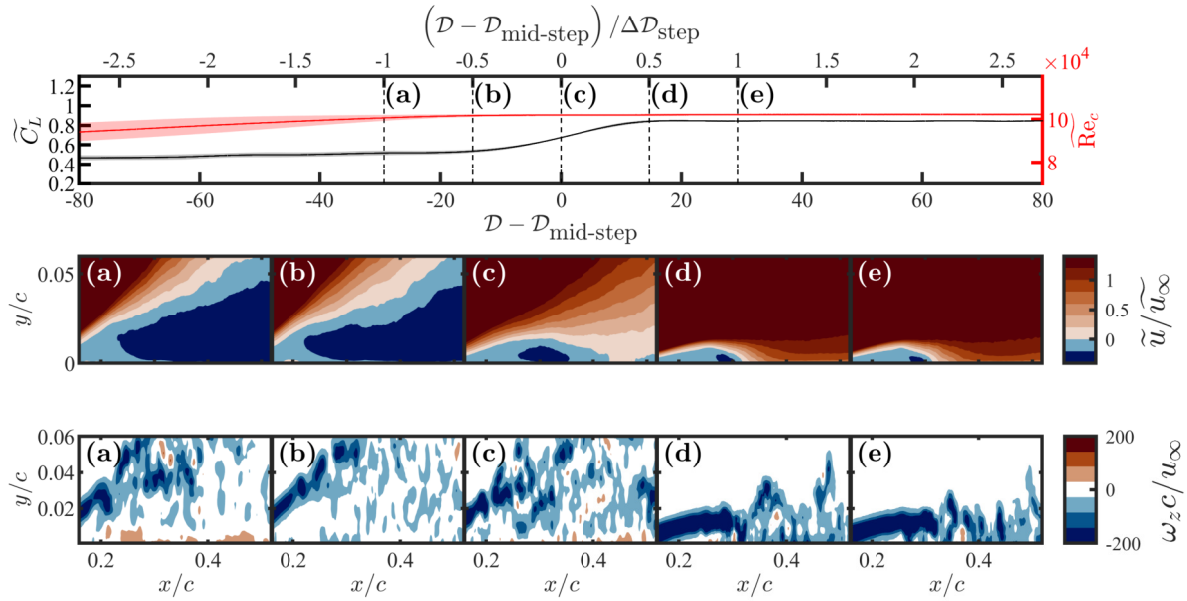


Figure 6.14: Ensemble-averaged lift coefficient and Reynolds number (top row), streamwise velocity (middle row) and instantaneous spanwise vorticity (bottom row) contours from side-view PIV for Reynolds number increase. Shaded areas indicate uncertainty (95% confidence). Full time-series available in movie 6.

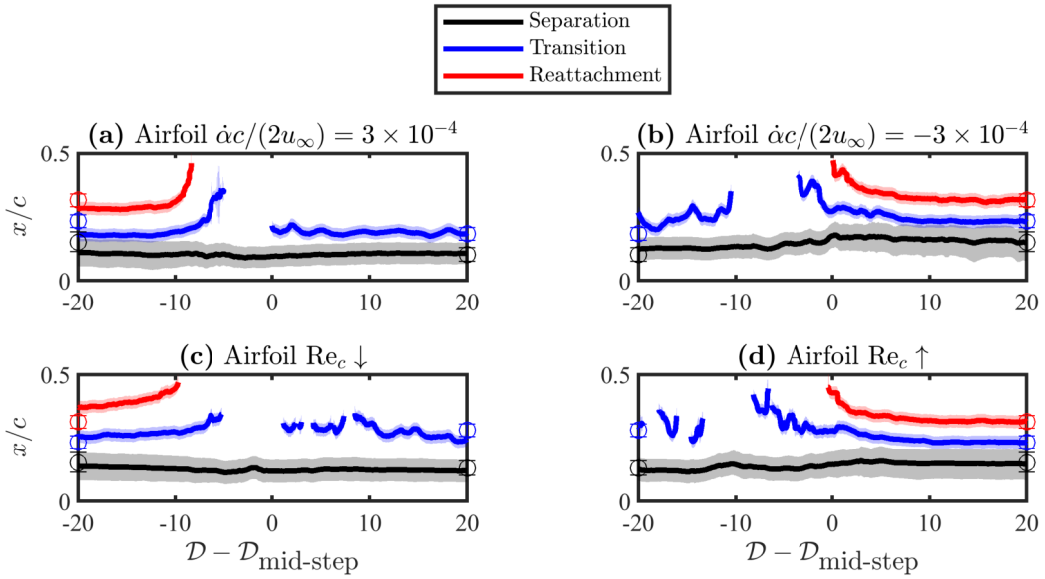


Figure 6.15: Transient locations of separation, transition, and reattachment during LSB bursting (a,c) and LSB formation (b,d) on airfoil. Shaded areas denote uncertainty (95% confidence). Markers indicate initial and final limiting conditions.

$(\mathcal{D} - \mathcal{D}_{\text{mid-step}})/\Delta\mathcal{D}_{\text{step}} = -1$ (Fig. 6.14a) and $(\mathcal{D} - \mathcal{D}_{\text{mid-step}})/\Delta\mathcal{D}_{\text{step}} = -0.5$ (Fig. 6.14a) is less than that for the decrease in angle of attack. However, there is still a relatively small reduction in the size of the reverse flow region during this period. As reattachment begins to occur at $\mathcal{D} - \mathcal{D}_{\text{mid-step}} = 0$ the lift coefficient increases more rapidly (Fig. 6.14c). As the flow settles to its final limiting condition, the separated shear layer continues to move towards the airfoil surface and the reattachment point moves upstream, settling at $x/c = 0.31$ (Figs. 6.14d and 6.14e). Similar to the downward pitching motion, the LSB remains relatively unchanged after $(\mathcal{D} - \mathcal{D}_{\text{mid-step}})/\Delta\mathcal{D}_{\text{step}} = 0.5$.

The transient streamwise evolution of the LSB structure on the airfoil is summarised in Fig. 6.15 which presents the laminar separation, transition, and turbulent reattachment locations plotted versus the non-dimensional time relative to the middle of the step change in lift coefficient ($\mathcal{D}_{\text{mid-step}}$, defined in Section 6.2.2) obtained from the ensemble-averaged side-view PIV measurements from 20 runs at the midspan of the model. The separation and reattachment locations were obtained from the locations where the zero-net-mass flux streamline intersects the airfoil surface. The relatively large uncertainty in the location of separation is a consequence of the need to extrapolate the zero-net-mass flux line upstream of the side-view PIV field of view to obtain the separation location. Similar to the transition criterion used by Hain *et al.* [170], the transition location was defined as the location where the Reynolds shear stress at the y coordinate equal to the displacement thickness ($y = \int_0^\delta (1 - u/u_e)\, dy$, where δ is the boundary layer thickness and u_e is the boundary layer edge velocity) first exceeds a threshold of $0.001u_\mathrm{e}^2$. Gaps in the time series of the transition location are present whenever the transition criterion is not satisfied within the PIV field of view. Because the high-speed PIV recording duration of approximately 80 convective

time units is shorter than the imposed changes in operating conditions, the PIV recordings do not contain the full pitching motion or Reynolds number change. Rather, the PIV recordings were triggered at different times for each type of transient to ensure that $\mathcal{D}_{\text{mid-step}}$ was contained in the recordings for each type of transient.

For the changes in operating conditions leading to stall (Figs. 6.15a and 6.15c), LSB bursting is indicated by the cessation of reattachment at $\mathcal{D} - \mathcal{D}_{\text{mid-step}} = -8.4$, and -9.7, respectively. In the reattaching limiting condition where an LSB forms on the airfoil, reattachment occurs at $x/c = 0.32$. For the pitching motion (Fig. 6.15a), the reattachment point moves upstream of its initial steady-state location as the angle of attack increases before rapidly moving downstream as the LSB bursts. In contrast, the LSB undergoing the decrease in Reynolds number (Fig. 6.15c) undergoes a gradual lengthening prior to bursting. The movement of the transition point during the bursting process largely follows the trend in the reattachment location for each type of change in operating conditions. This is an expected result given that reattachment depends on transition in the separated shear layer. After the rapid downstream movement of the transition location associated with the cessation of reattachment for the pitching motions, the transition location in the stalled flow re-establishes at a location similar to that prior to the rapid expansion of the LSB. The upstream movement of the transition location after LSB bursting is attributed to the reduction in stability of the separated shear layer as its trajectory moves away from the airfoil surface [17]. Relative to the movements of the transition and reattachment locations, the movement of the separation point during LSB bursting is relatively small.

For the changes in operating conditions leading to reattachment (Figs. 6.15b and 6.15d), a similar progression of the separation, transition, and reattachment locations is observed for both types of transient changes in operating conditions. The reattachment process consists of a gradual downstream movement of the separation point, and a gradual upstream movement of the transition point that begins near $D_{\text{mid-step}}$ and is followed by the initiation and gradual upstream movement of reattachment.

Substantial changes in the transition process are expected to accompany the bifurcation of the flow-field topology during the imposed changes in lifting surface operating conditions. The transition of the separated laminar shear layer is explored in Fig. 6.16, where the ensemble-averaged Reynolds shear stress obtained from 20 runs at the y coordinate equal to the displacement thickness is presented for pitching motions at $\dot{\alpha}c/(2u_\infty) = \pm 3 \times 10^{-4}$, $\dot{\alpha}c/(2u_\infty) = \pm 5 \times 10^{-3}$, and for changes in Reynolds number. The streamwise location of the transition criterion $-\widetilde{u'v'}/u_e^2 > 0.001$ is also plotted for reference with the white line. The Reynolds shear stress measurements for the transients were averaged over a temporal window of one convective time unit. Prior to ensemble-averaging, the data were shifted in time by $\mathcal{D}_{\text{mid-step}}$ (defined in Section 6.2.2) so that the step change in lift coefficient occurs at $\mathcal{D} - \mathcal{D}_{\text{mid-step}} = 0$. The initial and final panes in the figure illustrate the streamwise Reynolds shear stress distribution from steady state PIV measurements taken at the operating conditions preceding and following the transients, respectively. The white areas in the plots denote where the displacement thickness is greater than the y extent of the field of view, and serve to indicate massive separation from the airfoil. In the limiting LSB state, the largest Reynolds shear stress magnitude occurs at $x/c = 0.31$,

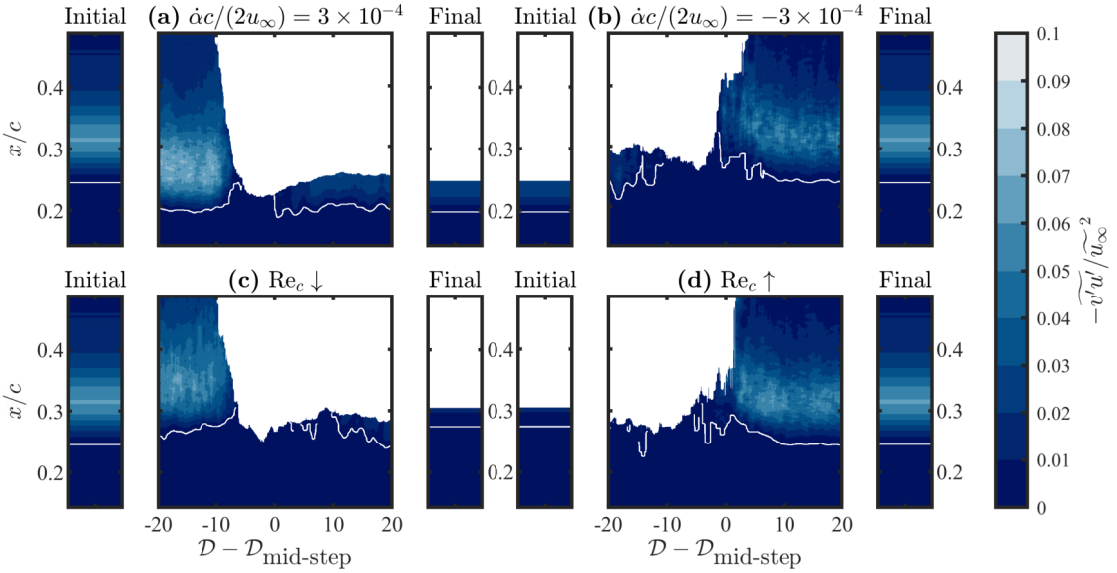


Figure 6.16: Contours of ensemble-averaged Reynolds shear stress during LSB bursting (a,c) and LSB formation (b,d) on airfoil. White line: transition location.

which corresponds to the location of reattachment (Fig. 6.15).

For the pitching motion leading to LSB bursting (Fig. 6.16a), the upstream movement of transition during the increase in angle of attack is associated with an upstream movement of the location of maximum Reynolds shear stress magnitude. After the LSB moves upstream and contracts, the location of the maximum Reynolds shear stress magnitude remains at a relatively consistent streamwise location prior to LSB bursting. In contrast, during the decrease in Reynolds number (Fig. 6.16c), there is a gradual downstream movement of the location of maximum Reynolds shear stress magnitude prior to cessation of reattachment. For both types of transients leading to LSB bursting, only after the onset of massive separation is there a substantial decrease in the maximum Reynolds shear stress magnitude measured within the PIV field of view. For the transients leading to LSB formation (Figs. 6.16b and 6.16d), a substantial increase in the maximum magnitude of Reynolds shear stress coincides with the upstream movement of the reattachment point after $\mathcal{D} - \mathcal{D}_{\text{mid-step}} = 0$. The subsequent upstream movement of the location of maximum Reynolds shear stress magnitude is consistent with the upstream movement of the transition point.

The transient Reynolds shear stress contours show that, for an increase in angle of attack, the transition process temporarily settles upstream at an unsustainable location prior to LSB bursting, whereas during a Reynolds number decrease, there is a more gradual downstream movement of the production of turbulent stresses. Although the type of imposed change in operating conditions affects the transition process during LSB bursting, similar trends in the location of maximum Reynolds shear stress magnitude are observed for both types of LSB formation transients investigated.

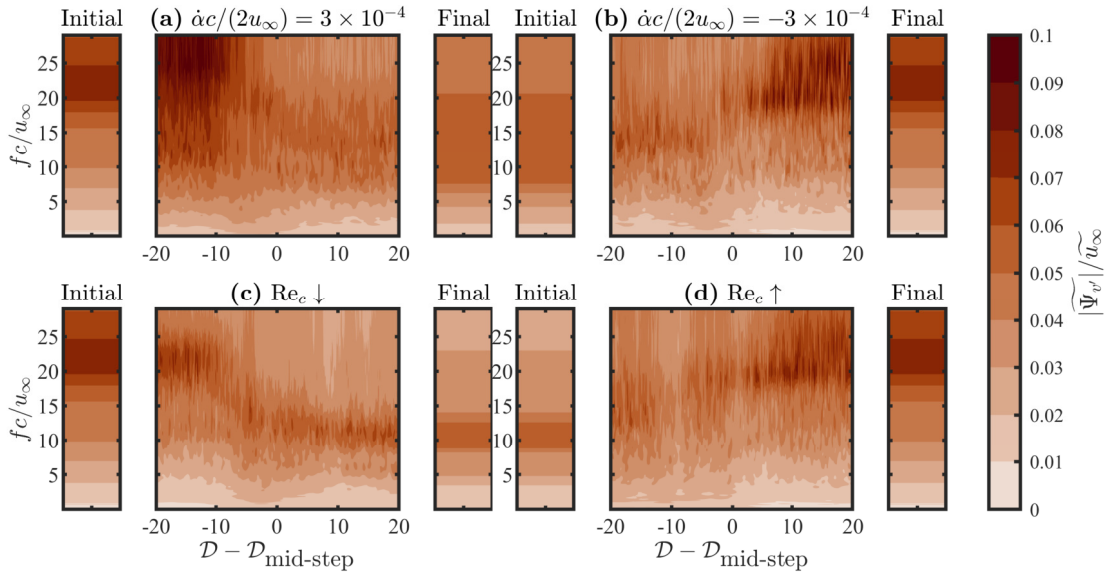


Figure 6.17: Contours of ensemble-averaged wavelet amplitude during LSB bursting (a,c) and LSB formation (b,d) on airfoil.

The transition to turbulence indicated by the production of Reynolds shear stress is fundamentally a consequence of the amplification of disturbances in the separated shear layer. To investigate how the temporal evolution of the frequency band of amplified disturbances in the separated shear layer is affected by the type of imposed transient, a wavelet analysis was performed on velocity fluctuations sampled at the y coordinate equal to the displacement thickness, which approximates the trajectory of the separated shear layer [75]. The wall-normal velocity fluctuations were used for the analysis because they are associated with the convection of roll-up vortices while being less sensitive to shear layer flapping. The wavelet magnitude ($\widetilde{\Psi_{v'}}$) scalograms presented in Fig. 6.17 are averaged over the ensemble of 20 PIV measurements, $0.14 < x/c < 0.38$, and a sliding temporal window of one convective time unit. Prior to ensemble-averaging, the data were shifted in time by $\mathcal{D}_{\text{mid-step}}$ (defined in Section 6.2.2) so that the step change in lift coefficient occurs at $\mathcal{D} - \mathcal{D}_{\text{mid-step}} = 0$. The mother wavelet used for the continuous wavelet transform was the Morse wavelet with a symmetry parameter of 3 and a duration of 11 [156]. In the same format as Fig. 6.16, the time-average wavelet magnitude scalograms of the initial and final steady state conditions are also plotted in Fig. 6.17. In the LSB limiting state at $\mathrm{Re}_c = 1.0 \times 10^5$ and $\alpha = 10°$, the most amplified frequency is approximately $fc/u_\infty = 23$. In the stalled limiting state at $\mathrm{Re}_c = 1.0 \times 10^5$ and $\alpha = 13°$, the most amplified frequency decreases to approximately $fc/u_\infty = 12$, and in the stalled limiting state at $\mathrm{Re}_c = 8.0 \times 10^4$ and $\alpha = 10°$, the most amplified frequency is approximately $fc/u_\infty = 10$. When non-dimensionalised by the airfoil projected chord, these frequencies correspond to approximately $fc \sin\alpha/u_\infty = 4$, 3, and 2, respectively.

For the pitching motion leading to LSB bursting, there is an increase in the most amplified frequency and a broadening of the band of amplified frequencies prior to the

cessation of reattachment. After cessation of reattachment, there is a relatively rapid reduction in disturbance amplitudes and a decrease in the most amplified frequency. In contrast, the band of amplified frequencies remains relatively narrow prior to cessation of reattachment during the Reynolds number decrease. For the transients leading to LSB formation (Figs. 6.17c and 6.17d), there is relatively gradual increase in the frequency of the most amplified disturbances prior to initiation of reattachment. Consistent with the foregoing results, the wavelet analysis of wall-normal velocity fluctuations in the separated shear layer demonstrates that the dynamics of LSB bursting depends on the type of imposed change in operating conditions to a greater extent than those of LSB formation.

6.3.3 Spanwise Flow Development

The spanwise flow development in each of the limiting flow states for the airfoil and wing models is illustrated by the instantaneous contours of streamwise velocity in Fig. 6.18. Note that the airfoil model extends across the entire test section to $z/c = 3$. For the airfoil and wing models at $\alpha = 10°$ and $\mathrm{Re}_c = 1.0 \times 10^5$ (Figs. 6.18a and 6.18d), the top-view measurement plane is located above the core of the separated shear layer, and spanwise bands of increased streamwise velocity are present between $0.2 \lesssim X/c \lesssim 0.5$ over the central portion of the models. These bands, which occur when the measurement plane intersects the top halves of vortices shed from the separated laminar shear layer [146], are evidence of coherent spanwise vortex shedding that is expected to occur when LSBs form on the models [e.g., 202]. Downstream of $X/c = 0.4$, these vortices undergo three-dimensional breakdown in the reattached turbulent boundary layer. For $z/c \lesssim 0.4$, spanwise vortex shedding is suppressed by the three-dimensional flow at the junction between the models and the test section wall. On the wing (Fig. 6.18d), vortex shedding and transition are also suppressed due to downwash from the wing tip vortex for $z/c \gtrsim 2.0$.

At the higher angle of attack of $\alpha = 13°$ (Figs. 6.18b and 6.18e), a large region of turbulent reverse flow is observed in the top-view measurements, indicating massive separation from the suction surface of the airfoil and wing. The stark change in streamwise velocity at $X/c \approxeq 0.2$ denotes the location where the core of the separated shear layer intersects the top-view measurement plane. On the wing (Fig. 6.18e), separation is suppressed in the vicinity of the wing tip. The flow development at the lower Reynolds number of $\mathrm{Re}_c = 8.0 \times 10^4$ (Figs. 6.18c and 6.18f) is similar to that observed at the higher Reynolds number and angle of attack, except that the velocities in the turbulent separated region are relatively higher, suggesting that the trajectory of the separated shear layer remains closer to the model surface under this condition. For all of the limiting stalled states of the airfoil and wing, there is an oblique region of higher velocity near the test section wall junction, indicating possible reattachment because of spanwise flow between the corner separation and the central region of massive separation.

The spanwise development of the separated flow on the wing and airfoil models during transients leading to LSB bursting is illustrated in Fig. 6.19, where contours of the minimum streamwise velocity from the ensemble average over 20 runs of the top view PIV measurements are plotted against spanwise position and time. The ensemble average was taken after

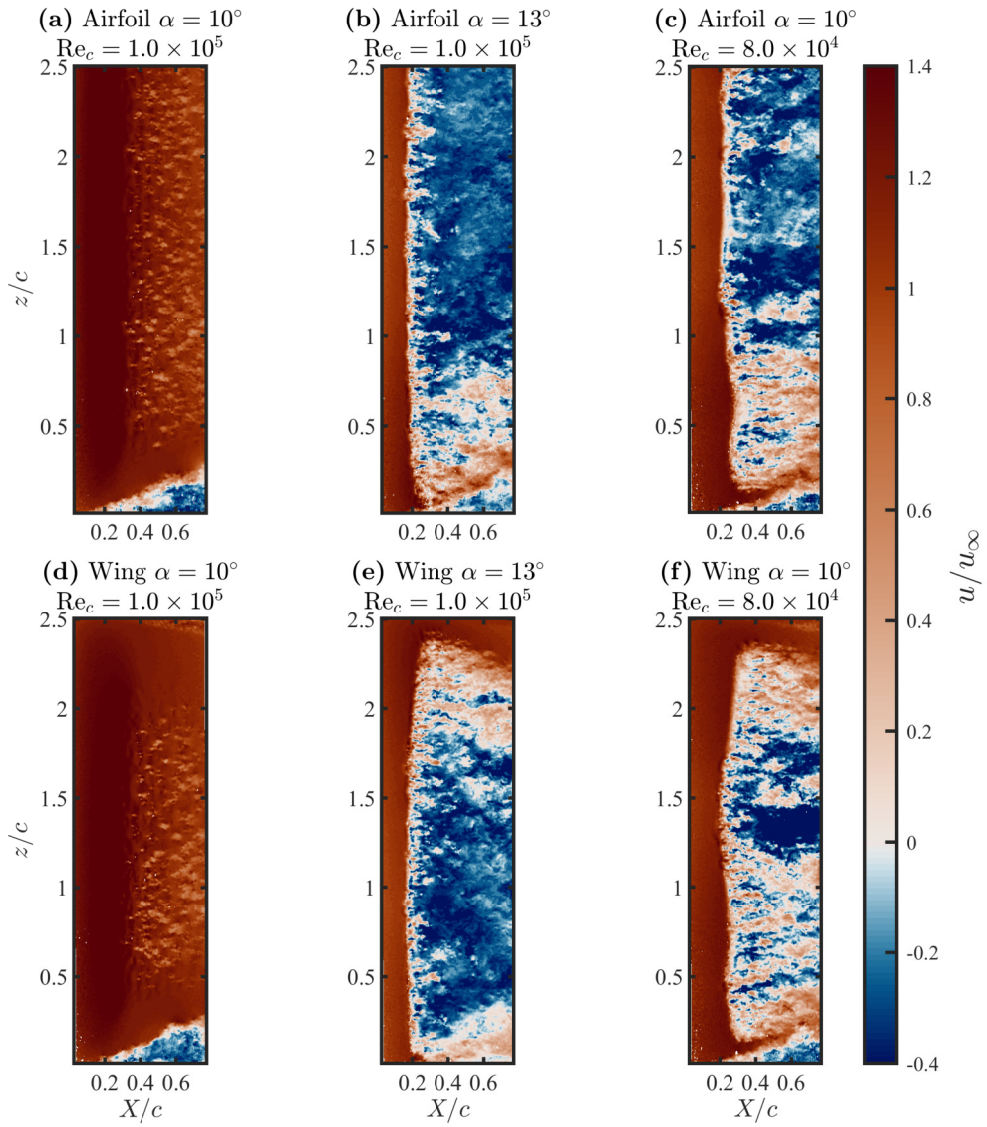


Figure 6.18: Streamwise velocity contours in steady conditions measured by top-view PIV configuration.

shifting each of the individual runs in time by $\mathcal{D}_{\text{mid-step}}$ (defined in Section 6.2.2) so that the step change in lift coefficient occurs at the same time ($\mathcal{D} - \mathcal{D}_{\text{mid-step}} = 0$) for each run. In Fig. 6.19, the minimum is taken over the streamwise (X) extent of the field of view so that the spanwise position of regions of reverse flow can be identified at a given time instant. The spanwise progression of LSB formation and bursting was found to be insensitive to pitch rate. Therefore, only measurements for a pitch rate of $\dot{\alpha}c/(2u_\infty) = \pm 3 \times 10^{-4}$ are presented here.

For both the airfoil and the wing, the initial reduction in the minimum streamwise

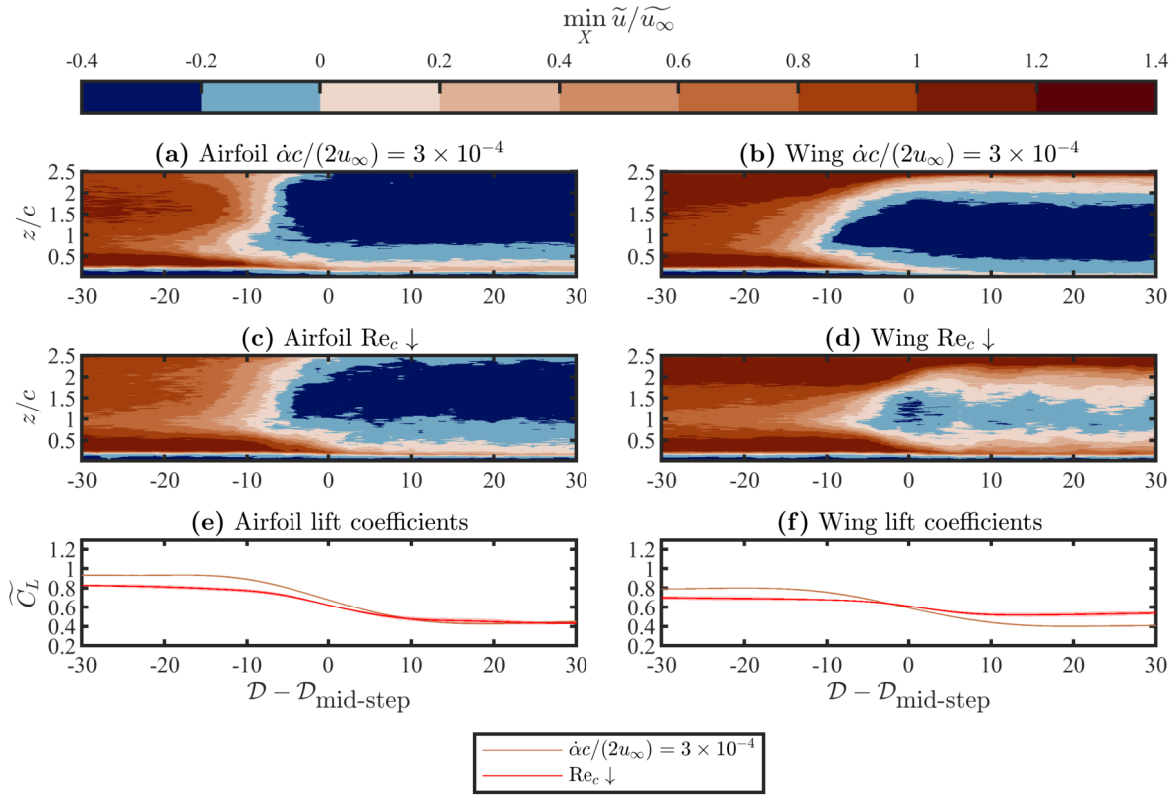


Figure 6.19: Contours of minimum ensemble-averaged streamwise velocity during LSB bursting.

velocity occurs at $z/c \approx 0.75$. The fact that the LSB bursts first at this location on both models is likely due to minute variations in the uniformity of the oncoming flow and/or the model surface that remain consistent for both model configurations. The main difference between the spanwise progression of the region of massive separation on the airfoil and wing during pitching motions is that the flow separates relatively abruptly across the span of the airfoil (Fig. 6.19a), whereas on the wing (Fig. 6.19b) there is a gradual expansion of the region of massive separation towards the wing tip, and separation is suppressed entirely in proximity of the wing tip. The similarity in the results from both pitch rates indicate that the spanwise progression of LSB bursting is not substantially affected by the pitch rate. During the reduction in Reynolds number leading to LSB bursting, the region of massive separation on the airfoil spreads more gradually toward the walls of the test section than for the pitching motions. On the wing, during the reduction in Reynolds number the initial location of LSB bursting and the initial progression of the region of massive separation towards the wing tip is similar to those of the pitching motions. However, the final spanwise extent of the region of massive separation after the reduction in Reynolds number is smaller than that after the increase in angle of attack because of the different limiting conditions for the two types of transients. Thus, the type of imposed transient does not substantially affect the initial spanwise progression of LSB bursting when the presence of the wing tip

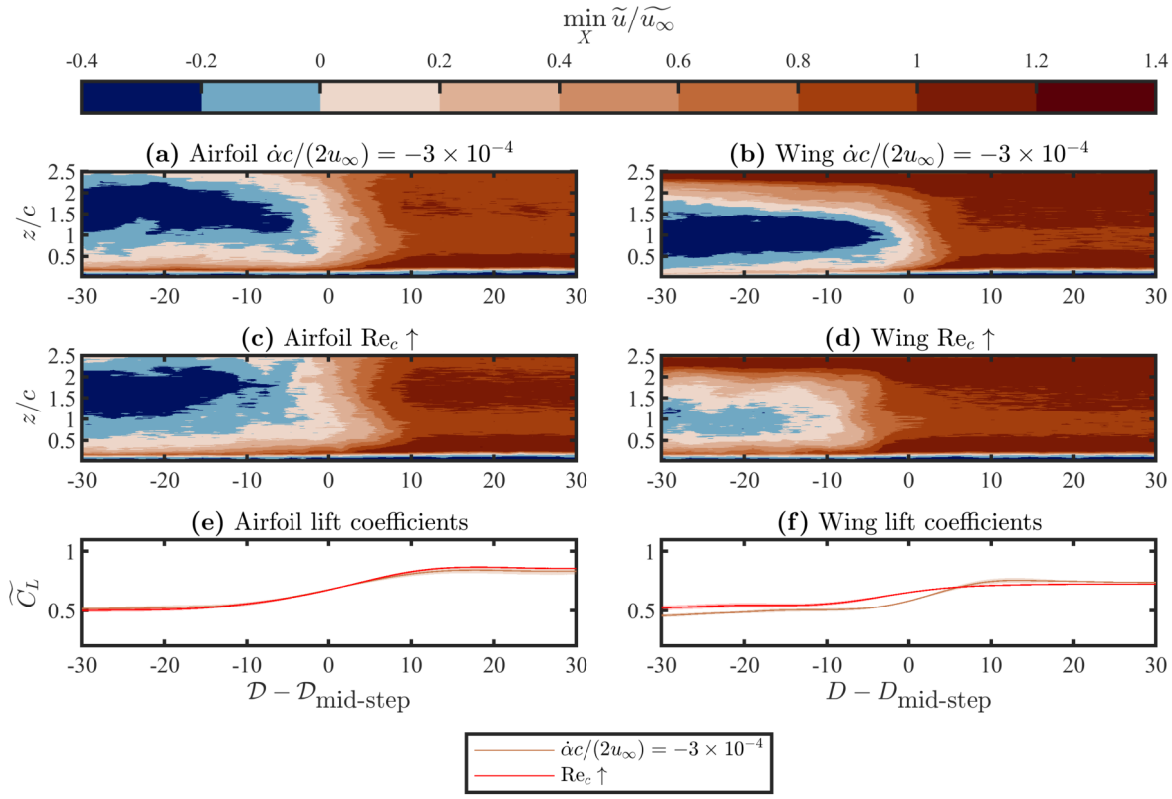


Figure 6.20: Contours of minimum ensemble-averaged streamwise velocity during LSB formation.

creates a preferential direction for the progression of stall across the span. For both models, the appearance of the region of massive separation coincides with the beginning of a rapid loss of lift (Figs. 6.19e and 6.19f).

In Fig. 6.20, contours of the minimum streamwise velocity from the ensemble average of the top view PIV measurements over 20 runs are presented for transients leading to LSB formation. As in Fig. 6.19, the minimum in Fig. 6.20 is computed over the streamwise extent of the field of view. For each of the transients of the airfoil (Figs. 6.20a and 6.20c), the region of massive separation contracts in its spanwise extent prior to cessation of reverse flow at the midspan. The cessation of reverse flow in the top view PIV measurements at the midspan of the airfoil coincides with a rapid increase in lift (Fig. 6.20e). The continued lift increase after the cessation of reverse flow in the top view measurements is attributed to the gradual reduction in extent of reverse flow closer to the model surface. The spanwise contraction of the region of massive separation prior to the cessation of reverse flow observed on the wing (Figs. 6.20b and 6.20d) is similar to that on the airfoil, although the region of massive separation is displaced towards the wing root, consistent with the increased effective angle of attack on this part of the wing. For each of the tested cases, the cessation of reverse flow on the wing precedes that on the airfoil. The differences in the time of cessation of reverse flow between the airfoil and wing are approximately 2, and 10 convective time units

for the pitching motion at $\dot{\alpha}c/(2u_\infty) = 3 \times 10^{-4}$ and for increasing Re_c, respectively. The expedited cessation of reverse flow in the top view measurements on the wing is attributed to downwash from the wing tip vortex which causes the separated shear layer to remain closer to the surface of the wing.

Overall, the ensemble-averaged top-view PIV measurements indicate that both changes in angle of attack and Reynolds number cause spanwise expansion and contraction of the region of massive separation during LSB bursting and formation, respectively. The presence of the wing tip has the effect of shifting the region of massive separation towards the root of the wing model.

6.3.4 Influence of limiting flow conditions

To investigate the influence of the particular limiting flow conditions of the present study on the transient aerodynamic loading, additional force measurements were performed for the airfoil during pitching motions between $\alpha = 9°$ and $14°$ at a pitch rate of $\dot{\alpha}c/(2u_\infty) = \pm 3 \times 10^{-4}$. The lift coefficients measured for individual runs of this wider angle change are plotted in Fig. 6.21. The data is shifted in time such that the static stall or reattachment condition is passed at $\mathcal{D} - \mathcal{D}_{\mathrm{ss}} = 0$ or $\mathcal{D} - \mathcal{D}_{\mathrm{sr}} = 0$, respectively. Lift coefficients from individual runs between $\alpha = 10°$ and $13°$ at the same pitch rate are reproduced in Fig. 6.21 for comparison.

For the downward pitching transient leading to reattachment (Fig. 6.21b), the larger separation between the quasi-steady reattachment condition and the limiting LSB flow state decreases the variance the timing of the rapid increase in lift. For the wider angle change, the lift recovery consistently occurs within $50c/u_\infty$ of the passing of the static reattachment condition, similar to the fastest increases in lift for the narrower angle range. For the upward pitching transient leading to stall (Fig. 6.21a), the timing of the rapid loss of lift is relatively unchanged between the two angle ranges, which is attributed to the greater separation of the static stall condition and the stalled limiting state (Fig. 6.7a). For the stall and reattachment transients, the minimum time at which the step change in lift coefficient occurs remains largely unchanged for the two angle ranges. This observation suggests that once the limiting states are sufficiently separated from the static stall or reattachment conditions, increasing the separation of the limiting states has a negligible effect on LSB formation and bursting and the consequent timing of the step changes in lift coefficient.

The influence of Reynolds number on the evolution of the lift coefficient is investigated by comparing the ensemble-averaged lift coefficient measurements over 20 runs for pitching between $\alpha = 10°$ and $13°$ from the present study with those obtained by Kiefer *et al.* [63] for transient pitch up motions from $\alpha = 19°$ to $29°$. The data from Kiefer *et al.* [63] pertain to a NACA 0021 airfoil at $\mathrm{Re}_c = 3.0 \times 10^6$. At that Reynolds number, Kiefer *et al.* [63] reported that an LSB did not form in the pre-stall condition. The data selected for comparison in Fig. 6.22 are those pitching motions with durations of 5 and 79 convective time units, which are similar to those of the present study for $\dot{\alpha}c/(2u_\infty) = 3 \times 10^{-4}$ and 5×10^{-3} of 6 and 77 convective time units, respectively. Note that because Kiefer *et al.* [63] used a sinusoidal

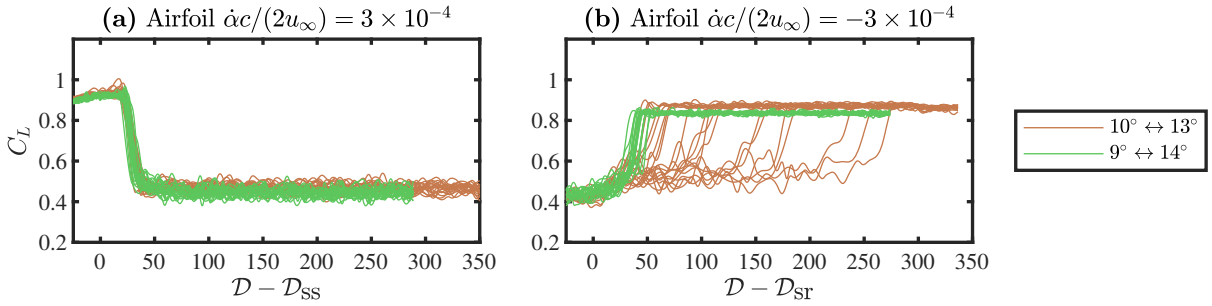


Figure 6.21: Comparison of transient lift coefficients of individual runs for pitching motions over narrow and wide angle ranges.

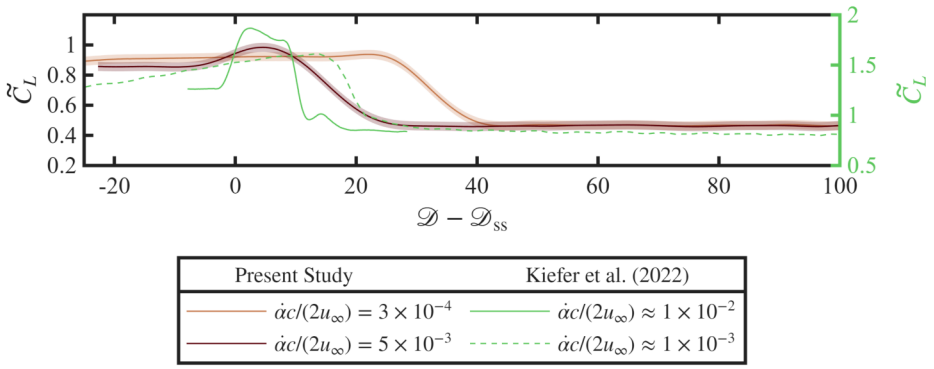


Figure 6.22: Comparison of pitching transients leading to stall with data from Kiefer *et al.* (2022). Shaded areas indicate uncertainty (95% Confidence)

motion profile instead of the linear ramp used in the present study, the maximum pitch rates from their study were higher for the same overall duration of the transient pitching motion. Although the data of Kiefer *et al.* [63] were obtained at a higher Reynolds number at which the lift coefficients and stall angle are substantially higher, the maximum lift overshoot and subsequent rapid loss of lift occur at similar times as the fastest pitch rate in the present study. This similarity supports the conclusion made by Mulleners & Raffel [57] and Le Fouest *et al.* [187] that the loading during the fastest pitching motions is initially governed by the time required for DSV formation, which is largely insensitive to Reynolds number and airfoil kinematics. For the longer duration transients, the onset of stall in the present study is substantially delayed when compared to the measurements of Kiefer *et al.* [63] at a higher Reynolds number. This suggests that Reynolds number effects are more significant for slower pitching motions, where the influence of the airfoil kinematics on unsteady lift development is weaker. For both pitch rates, the lift decrease is more rapid after the onset of stall for the data of Kiefer *et al.* [63] at the higher Reynolds number than for the present study. This suggests that the later stages of dynamic stall may be relatively more sensitive to the Reynolds number and airfoil kinematics.

The foregoing results demonstrate that the difference between the static stall or reattachment conditions and the initial and final flow states affect the timing of the decrease or

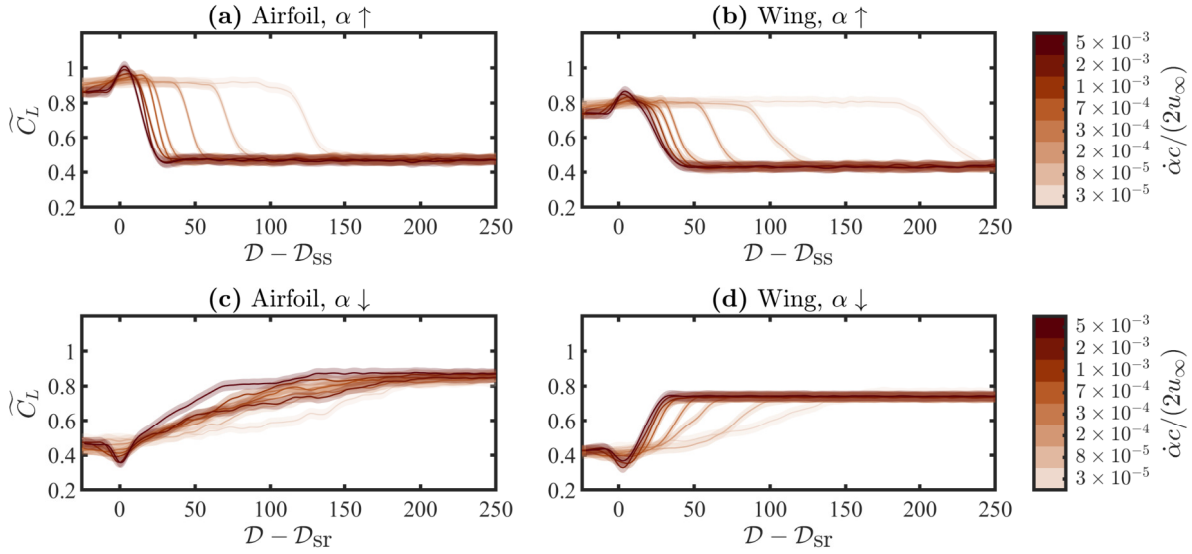


Figure 6.23: Ensemble averaged lift coefficient time-history during pitching motion for airfoil (a,c), and wing (b,d). Shaded areas indicate uncertainty (95% confidence).

increase in lift coefficient during transients leading to LSB bursting or formation, respectively. However, for a given type of imposed change in operating conditions, qualitative similarity in the initial time-history of the lift response exists across different Reynolds numbers and angles of attack. Although the timing of LSB bursting and reattachment vary depending on the operating conditions, the PIV measurements taken for a limited set of imposed transients are expected to be representative of the LSB bursting and formation processes that govern the onset of stall and reattachment.

6.3.5 Influence of pitch rate

The time evolution of the ensemble-averaged lift coefficients from 20 transient pitching motions is illustrated in Fig. 6.23. Because the duration of the transient pitching motions depends on pitch rate (Fig. 6.2), the passing of the static stall angle occurs at later times for slower pitch rates. To facilitate the comparison of lift coefficients between different cases, the data in Fig. 6.23 are shifted in time such that the static stall or reattachment condition is passed at $\mathcal{D} - \mathcal{D}_{ss} = 0$ or $\mathcal{D} - \mathcal{D}_{sr} = 0$, respectively. As the pitch rate is increased, stall occurs with a shorter delay after the passing of the static stall condition for the airfoil and wing (Figs. 6.23a and 6.23b), consistent with the results of Ayancik & Mulleners [203] and Kiefer *et al.* [63]. For the fastest pitch rates, substantial over- and under-shoots in the lift coefficients are observed during stall and reattachment on both models, consistent with the dynamic stall and reattachment processes observed at higher Reynolds numbers [e.g., 63, 64] and discussed in Section 6.3.4.

The ensemble-averaged lift coefficients during transients leading to LSB formation in Figs. 6.23c and 6.23d indicate that reattachment occurs more quickly after the static

reattachment condition is passed as the pitch rate is increased for both the airfoil and wing. The slower rate of change of the ensemble-averaged lift coefficients for slower pitch rates is a consequence of greater variability in the time at which the step increase in lift occurs in the individual runs at slower pitch rates (e.g. Fig. 6.10a). This variability is greater for the airfoil than the wing because of the closer proximity of the limiting LSB state for the airfoil to the static reattachment angle of the airfoil. The undershoot in lift coefficient for faster pitch rates resembles that measured by Green & Galbraith [64] for the normal force coefficient during a continuous decrease of the angle of attack through $\alpha = 0°$ at $\mathrm{Re}_c = 1.5 \times 10^6$. The undershoot in lift at faster pitch rates likely contributes to making the timing of the lift recovery more consistent, acting as an effective increase in the difference between the initial and static reattachment conditions.

To quantitatively compare the delay between the passing of the static stall or reattachment conditions and the start of the step change in lift coefficient for different pitch rates, the ensemble-average reaction delays ($\Delta\mathcal{D}_{\mathrm{react}}$ defined in Section 6.2.2), are presented in Fig. 6.24 for the ensemble of 20 runs obtained for all pitch rates tested. As the pitch rate is increased, the reaction delays for stall of the airfoil and stall and reattachment of the wing decrease asymptotically, converging towards the trend reported by Ayancik & Mulleners [203] for ramp-up and sinusoidal pitching motions at Reynolds numbers in the range of $7.5 \times 10^4 \leq \mathrm{Re}_c \leq 9.2 \times 10^5$ for various airfoil profiles and motion kinematics. The asymptotic decrease in reaction delay suggests that the time-evolution of the lift force is governed by the DSV formation process [203], with the details of transition having a relatively minor influence. At the highest pitch rate tested ($\dot{\alpha}c/(2u_\infty) = 5 \times 10^{-3}$), the airfoil stall reaction delay is $\Delta\mathcal{D}_{\mathrm{react}} = 11$, and that of the wing is $\Delta\mathcal{D}_{\mathrm{react}} = 19$. At each pitch rate, the reaction delay for stall of the wing is longer than that for the airfoil, indicating that the presence of end effects increases the reaction delay during stall. The reaction delays at the highest pitch rate are still significantly longer than the minimum stall reaction delay of approximately $\Delta\mathcal{D}_{\mathrm{react}} = 3$ observed by Le Fouest *et al.* [187] for a NACA0018 airfoil at $\mathrm{Re}_c = 7.5 \times 10^5$ and a reduced pitch rate of $\dot{\alpha}c/(2u_\infty) = 0.14$. This discrepancy is attributed to the relatively low effective cut-off frequency of the filtering procedure used to attenuate structural vibrations at the natural frequency of the model (Fig. 6.3).

Similar to the reaction delays for stall of the wing, the reaction delays for reattachment on the wing also show a decrease with increasing pitch rate before plateauing at a delay of approximately 10 convective time units because of the limited frequency response of the force measurement system. In contrast, the reaction delays for reattachment on the airfoil are notably longer and more variable for pitching between $\alpha = 10°$ and 13°. This result is attributed to the proximity of the limiting LSB condition to the static reattachment angle (Fig. 6.7a). In such case, the initiation of reattachment is likely to have a higher sensitivity to random minute perturbations of the flow in the test section. The substantially longer reaction delays for reattachment on the airfoil observed in the present study are a consequence of the particular limiting conditions investigated, and this is confirmed by the reaction delays for pitching motions of the airfoil between $\alpha = 9°$ and 14° (filled symbols), which are less variable and closer to those of the wing. Regardless of the limiting conditions,

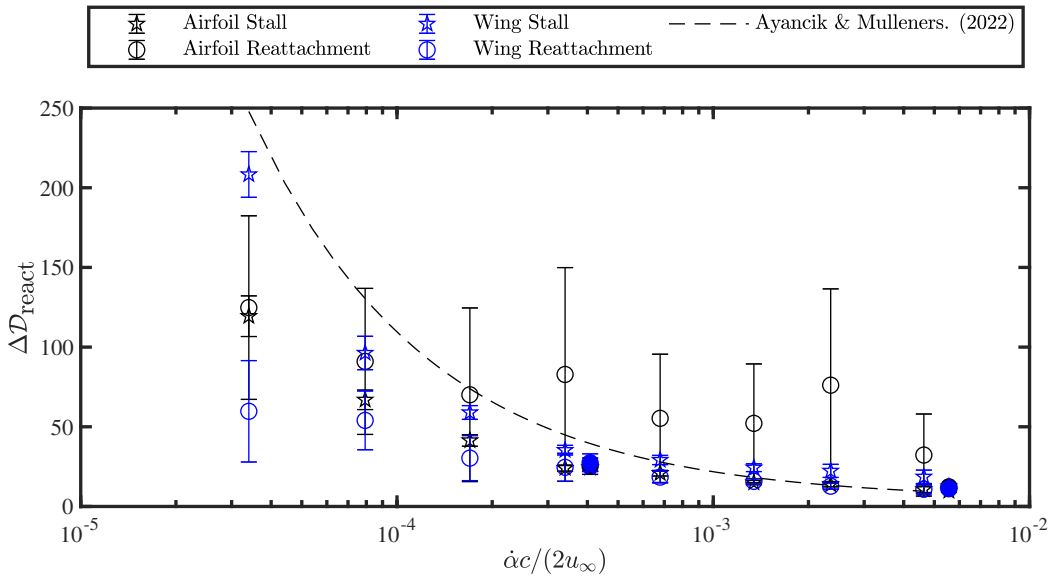


Figure 6.24: Reaction delay versus pitch rate for pitching between 10° and 13°. Error bars denote standard deviation. Filled symbols denote pitching between 9° and 14° and are offset in the horizontal direction for clarity.

there is still an overall trend towards shorter reaction delays for reattachment on the airfoil as the pitch rate increases.

The ensemble-average step times ($\Delta\mathcal{D}_{\text{step}}$ defined in Section 6.2.2), which describe the duration of the step change in lift coefficient, are presented in Fig. 6.25 for the ensemble of 20 runs for each pitch rate tested. The stall step times are largely insensitive to pitch rate, and are on the order of 10 convective time units. This is on the order of the shortest step times that can be expected to be resolved by the force measurement system. However, the present measurements of the step time are close to the mean drop time of 8 convective time units reported by Le Fouest *et al.* [187] for quasi-steady increases in angle of attack. The relatively short duration of the stall step times means that near the instant in time when the flow bifurcates between reattaching and stalled topologies there are substantial unsteady effects in the flow's response, even if the change in operating conditions is quasi-steady.

For reattachment on the wing, there is a reduction in step time with increasing pitch rate for $\dot{\alpha}c/(2u_\infty) < 3\times10^{-4}$. This is attributed to the reduction in effective angle of attack near the wing tip enabling reattachment to progress more gradually in the spanwise direction (Figs. 6.20b and 6.20d). For the airfoil, the ensemble-average and standard deviation of the reattachment step times are greater than those of stall across all of the pitch rates tested. Again, this is attributed to the proximity of the static reattachment condition to the final limiting flow state, since the step times for the wider angle change (filled symbols) are consistent with those of the wing.

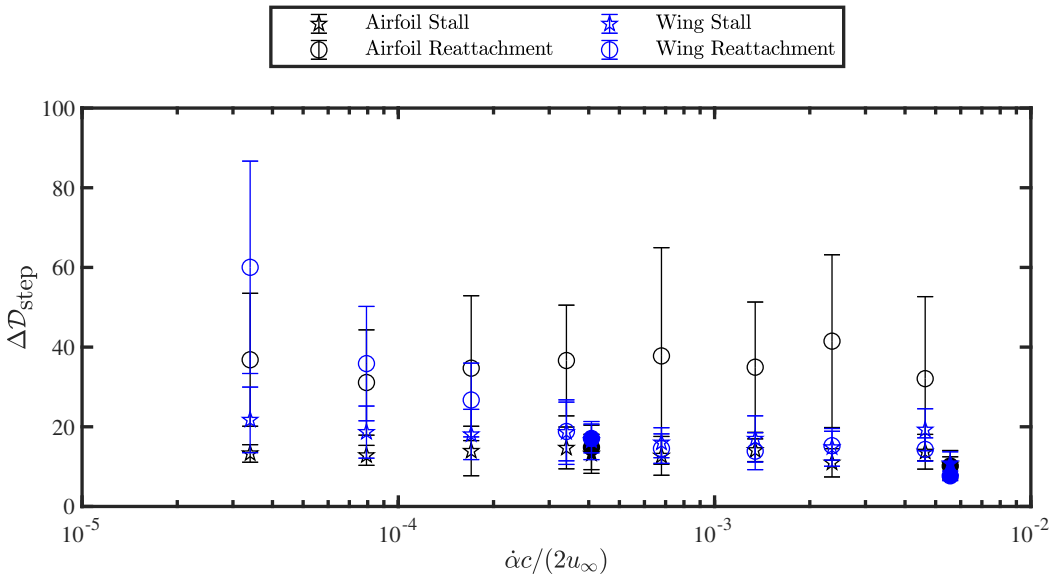


Figure 6.25: Step time versus pitch rate for pitching between 10° and 13°. Error bars denote standard deviation. Filled symbols denote pitching between 9° and 14° and are offset in the horizontal direction for clarity.

6.4 Concluding Remarks

Experiments were performed on an airfoil and wing model undergoing transient changes in operating conditions at aerodynamically low Reynolds numbers. Lift force and PIV measurements were performed during transient changes in angle of attack and Reynolds number to investigate the relationship between LSB bursting and formation and the transient aerodynamic loads.

For the wing and airfoil models, the lift coefficients exhibited hysteresis with respect to angle of attack for quasi-steady and transient pitching motions. Even though the quasi-steady lift coefficients did not exhibit significant hysteresis for Reynolds number changes, significant transient hysteresis of the lift coefficients with respect to Reynolds number was identified for both models.

LSB bursting and formation transients caused by a change in angle of attack at constant Reynolds number and a change in Reynolds number at constant angle of attack were compared in detail. The comparison was made for imposed changes in operating conditions with durations of approximately 75 convective time units. During an increase in angle of attack leading to LSB bursting, the transition location initially moves upstream, enabling the temporary formation of an LSB that is unsustainable against the stronger adverse pressure gradient and an overshoot in the lift coefficient. LSB bursting was subsequently initiated with a rapid downstream movement of the reattachment location, with a majority of the downstream movement occurring over a time period on the order of a single convective time unit. The bursting process was accompanied by a rapid loss of lift. In contrast, during a decrease in Reynolds number, there is a downstream movement in the transition location

that results in continuous LSB lengthening before the rapid decrease in lift coefficient. For both types of transients leading to LSB bursting, the cessation of reattachment coincided with a decrease in the maximum magnitude of Reynolds shear stress and a decrease in vortex shedding frequency. For the transients leading to LSB formation, namely a decrease in angle of attack or an increase in Reynolds number, the initiation of reattachment coincided with an increase in the rate of change of the lift coefficient, and was accompanied by a gradual increase in the roll-up vortex shedding frequency. The nature of the imposed change in operating conditions leading to LSB formation did not substantially affect the trends for the streamwise movement of the transition and reattachment points, which settled to their final limiting locations within approximately 15 convective time units from the onset of reattachment. The downstream movement of the separation point during LSB formation was more gradual than that of the transition and reattachment points. Whenever reattachment was present, the trends in the movement of the transition location were similar to those of the reattachment location for all transients. In conclusion, the type of change in lifting surface operating conditions has a greater influence on the transient lift forces and streamwise LSB development during LSB bursting than during LSB formation.

Using the top-view PIV configuration, the transient spanwise flow development was investigated on the airfoil and wing models for pitching motions and Reynolds number changes. On both the airfoil and wing models, LSB bursting resulted in a spanwise expansion of the region of massively separated flow from the midspan towards the ends of both models. On the airfoil, the onset of massive separation was more uniform across the span than on the wing, where stall initiated closer to the wing root and progressed toward the wing tip. During the transients leading to LSB formation, there was a spanwise contraction of the region of massive separation from the ends of the models towards the midspan. No significant differences in spanwise flow development were observed for different pitch rates. The spanwise flow development for Reynolds number changes was similar to that observed for pitching motions, except that the onset of massive separation during the Reynolds number decrease for the airfoil spread along the span more slowly than for the pitching motions.

The stall reaction delays of the airfoil and wing for pitching motions follow the asymptotic behaviour observed by [203], and are similar to those observed in experiments at higher Reynolds numbers [e.g., 63]. This suggests that the initial stages of dynamic stall for both types of lifting surfaces are largely governed by the formation and downstream convection of the DSV in a manner that is relatively Reynolds number insensitive, in agreement with previous studies. However, the degree to which the static stall or reattachment conditions were exceeded affected the timing of the lift force response to transient pitching motions, with a notable reduction in the variance of the reaction delay for reattachment on the airfoil for pitching motions with larger angular displacements. The relatively large variance in reaction delay for reattachment on the airfoil for the smaller angular displacement highlights the sensitivity of the transition process to airfoil kinematics and random external perturbations in unsteady conditions at low Reynolds numbers.

Chapter 7

Boundary Layer Transition on an Airfoil in Large-Scale Free-Stream Turbulence

The effects of high-intensity, large-scale free-stream turbulence on the aerodynamic loading and boundary layer flow field development on a NACA 0018 airfoil model are studied experimentally using direct force measurements and particle image velocimetry at a chord Reynolds number of 7×10^4*. An active turbulence grid was used to generate free-stream turbulence intensities of up to* 16% *at integral length scales on the order of the airfoil chord length. Relative to the clean flow condition with a free-stream turbulence intensity of* 0.1%*, elevated levels of free-stream turbulence intensity decrease the lift slope at low angles of attack, and increase the stall angle and maximum lift coefficient. At moderate angles of attack, high-intensity free-stream turbulence causes large variations in the location of transition, with laminar flow occasionally persisting over* 90% *of the chord length. At pre-stall angles of attack, high-intensity free-stream turbulence causes intermittent massive separation. Variations in the extent of turbulence in the suction surface boundary layer are correlated with large-scale fluctuations in oncoming velocity direction, demonstrating that the observed variability in transition location is related to large-scale oncoming flow disturbances impinging on the airfoil model.*

7.1 Introduction

Boundary layer transition in low-disturbance environments involves the exponential amplification of wave-like disturbances of the velocity field [67]. At higher levels of FSTI, transition may occur prior to saturation of the primary instability through bypass transition [204]. Most previous studies considering the effect of elevated FSTI on flows around airfoils and finite wings primarily focused on the effect of turbulence intensity [e.g., 91, 107–109, 146, 205, 206], whereas the effect of the streamwise integral length scale (Λ_{ux}) is less well understood [105].

The majority of previous studies on boundary layer transition in aerodynamically low Reynolds number flows have been limited to free-stream turbulence intensities below 10% and integral length scales less than the airfoil chord [e.g., 73, 105, 106, 108, 146, 175, 199, 206–208]. A limited number of studies have considered turbulence intensities of 10% or greater and integral length scales longer than the airfoil chord. Among those studies, Ravi *et al.* [110], Watkins *et al.* [135], Kay *et al.* [209], and Devinant *et al.* [210] focused on characterisation of the pressure distribution and loading on wings and airfoils, whereas Herbst *et al.* [111] and Herbst *et al.* [112] also reported on the time- and conditionally-averaged boundary layer development on the suction surface. For $Tu = 7\%$ and 12%, Ravi *et al.* [110] found that increasing the integral length scale at constant Tu from c to approximately $2c$ increased the maximum lift coefficient of a flat plate airfoil. Although Herbst *et al.* [112] observed an increase in maximum lift coefficient when increasing Λ_{ux} from $0.5c$ to c at $Tu = 10\%$ for an SD7003 wing, a further increase in Λ_{ux} to $2c$ did not cause a significant change in maximum lift coefficient. The difference between the results of Ravi *et al.* [110] and Herbst *et al.* [112] suggests that the lifting surface geometry may influence the effect of the integral length scale on aerodynamic loading. The effect of airfoil geometry on the lift coefficient in high-intensity, large-scale free-stream turbulence was investigated by Kay *et al.* [209] for a symmetrical and cambered airfoil for $1.3\% \leq Tu \leq 15\%$ at $5 \times 10^4 \leq \mathrm{Re}_c \leq 2 \times 10^5$ with streamwise integral length scales on the order of the airfoil chord. They inferred from surface pressure measurements that fluctuations in effective angle of attack beyond the static stall angle lead to intermittent dynamic stall events associated with the shedding of leading edge vorticity. These events corresponded to transient increases in lift coefficient which were stronger for the symmetric airfoil than for the cambered airfoil [209]. Devinant *et al.* [210] studied the loading on a wind turbine airfoil at FSTIs of up to 16%, and reported a decrease in the lift slope and a more gradual stall behaviour with increasing FSTI. The flow field around a fully stalled airfoil with $4\% \leq Tu \leq 16\%$ and $\Lambda_{ux} \sim c$ was investigated by Sicot *et al.* [211], who found that the variations in the suction surface boundary layer separation location and wake vortex shedding Strouhal number were insensitive to FSTI. Although the effect of free-stream turbulence on aerodynamic loading has been studied by several authors, the dynamics of the boundary layer transition process that cause the observed changes in lifting surface performance in large-scale high-intensity free-stream turbulence remain relatively unexplored. One consistent observation in experiments involving large-scale high-intensity turbulence has been intermittent separation and LSB formation [110–112, 209]. This is in contrast to

flows at relatively moderate turbulence intensities and length scales, in which the LSB is typically suppressed intransiently due to bypass transition [73, 146].

Better understanding of the boundary layer transition mechanisms on lifting surfaces in large-scale high-intensity free-stream turbulence is necessary to improve the performance and control of small unmanned aerial vehicles [12] and small wind turbines [13] that operate in atmospheric flows. Therefore, the objective of this chapter is to quantify the effects of high-intensity, large-scale free-stream turbulence on airfoil performance at low Reynolds numbers, and to correlate changes in the boundary layer transition dynamics to fluctuations in the oncoming flow. To achieve this objective, wind tunnel experiments were performed using a NACA 0018 airfoil model with an active turbulence grid placed upstream of the test section to generate relatively high free-stream turbulence intensities and large integral length scales. Direct aerodynamic force measurements and suction surface boundary layer velocity field measurements were employed to quantify airfoil performance and boundary layer transition dynamics, respectively.

7.2 Description of Experiments

Experiments were conducted in the recirculating wind tunnel at the University of Waterloo. The experimental setup is illustrated in Fig. 7.1. The test section is square, with a width and height of 0.61 m and a length of 2.44 m. The free-stream velocity was set based on a calibration of the pressure drop across the 9 : 1 contraction located upstream of the test section measured using a Setra model 239 pressure transducer. The relative uncertainty in the free-stream velocity is estimated to be 2% (95% confidence). The NACA 0018 airfoil used in this study had a chord length of $c = 0.1\,\mathrm{m}$ and spanned the height of the test section. To facilitate direct force measurements, the airfoil model was structurally isolated from the test section walls with gaps of approximately 4 mm at each end. The regions of three-dimensional flow caused by the presence of the tip gaps is expected to be limited to within one chord length of the ends of the model [124, 186]. The airfoil was machined from aluminium, polished with 1000 grit sandpaper, and anodised black to minimise light reflections. A stepper motor controlled rotary table with a resolution of 0.05° was used to set the angle of attack of the airfoil. The airfoil was connected to the rotary table through a 6-axis load cell. The absolute accuracy in force measurements from the load cell was 0.1 N. All experiments were performed at a chord Reynolds number of $\mathrm{Re}_c = 7.0 \times 10^4$, corresponding to a mean free-stream velocity of $\overline{u_\infty} = 10.7\,\mathrm{m\,s^{-1}}$.

7.2.1 Flow Measurements

Two-component particle image velocimetry (PIV) measurements were performed over the suction surface of the airfoil in two measurement planes shown in Fig. 7.2. The side-view measurement plane was normal to the span of the airfoil and located at the midspan of the model, and the top-view measurement plane was tangent to but offset from the suction surface of the airfoil. The minimum distance between the top-view measurement plane and

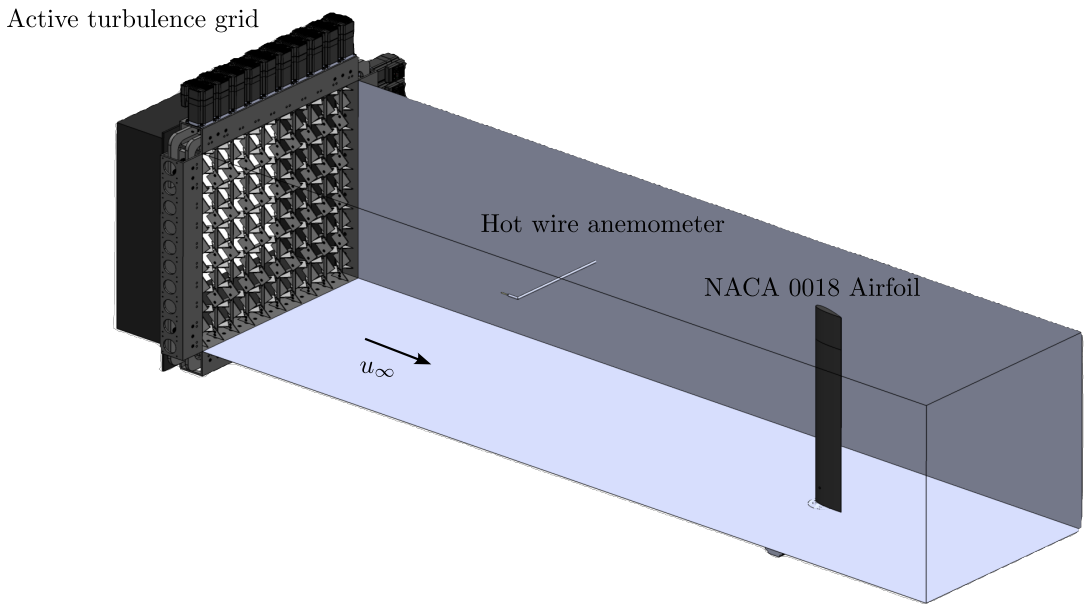


Figure 7.1: Experimental setup.

the airfoil was 2 mm. The PIV data is presented in a surface attached coordinate system whose origin is at the midspan leading edge, with the streamwise (x) axis tangent to the suction surface, the wall-normal (y) axis normal to the airfoil surface, and the spanwise (z) axis parallel to the span in the sense of a right-handed coordinate system. Particle images were obtained using a Photron Fastcam Nova R3-4K camera with a 105 mm focal length macro lens at an aperture of $f/2.8$. The flow was seeded with water-glycol fog particles of diameter $O(1\,\mu\text{m})$. The particles were illuminated by a Photonics Industries DM20-527 Nd:YLF pulsed laser operating in frame straddling mode, with a pulse separation of 15 µs. Image acquisition and processing was performed using the LaVision DaVis 10 software. Particle images were pre-processed using temporal minimum subtraction with a window length of 8 images. Local intensity normalisation with window sizes of 4×4 pixels and 32×32 pixels was used for the side-view and top-view images, respectively. Vector calculation was performed using an iterative cross-correlation algorithm with window deformation [148]. The vector fields for both measurement planes were post-processed using universal outlier detection [150]. For the side-view configuration, vectors were deleted if the correlation coefficient was less than 0.5. For the top-view configuration, vectors were deleted if the correlation peak ratio was less than 1.6. For both measurement planes, the maximum particle displacement was approximately 15 px, and the initial and final correlation window sizes were 24 px × 24 px and 16 px × 16 px, with 75% window overlap for the final iteration. The vector pitch of the final velocity fields was $0.0009c$ and $0.0007c$ for the side- and top-view PIV configurations, respectively.

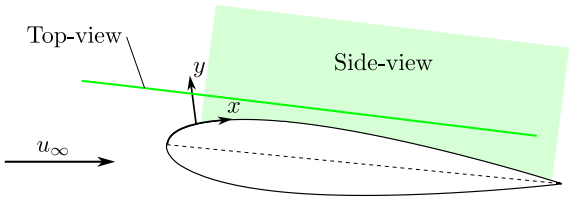


Figure 7.2: PIV measurement plane configurations and coordinate system definitions. The z axis is in the out-of-plane direction in the sense of a right-handed coordinate system.

In addition to the instantaneous velocity vector fields computed from image pairs, time-mean velocity fields were also calculated using the average correlation method [212] for improved spatial resolution in the boundary layer for the side-view configuration. The average correlation method involves averaging the correlation maps from all image pairs before determining the mean particle displacement from the correlation peak. For the average correlation method, the mean velocity field obtained from the standard PIV method was used to estimate the initial displacements, and the final correlation window size was 4 px $\times$ 4 px with 75% window overlap. The vector pitch of the mean velocity fields from the average correlation method was $0.0002c$.

For the side-view configuration, PIV measurements were taken at sampling frequencies of 3.9 kHz and 0.1 kHz to obtain time-resolved and statistical data, respectively. The size of the field of view and the sampling period were varied for different flow conditions and sampling frequencies and are tabulated in Tables 7.2 and 7.3. To correct for relative motion between the airfoil and the camera due to model vibrations at elevated FSTI, each side-view PIV image was aligned with the first image in the sequence based on the cross-correlation of the illuminated airfoil surface between images. For the top-view configuration, only non-time-resolved PIV measurements were acquired at 0.1 kHz. The size of the top-view field of view was $0.76c \times 0.42c$, and the sampling period was 11.99 s.

The uncertainty in the instantaneous PIV measurements was estimated using the correlation statistics method [149]. The root-mean-square (RMS) uncertainty (95% confidence) in the instantaneous streamwise (u) and wall-normal (v) velocity components was estimated to be less than $0.06\overline{u_\infty}$ outside of the airfoil boundary layer. Adjacent to the airfoil surface, stronger velocity gradients and light reflections increased the RMS uncertainty to no more than $0.3\overline{u_\infty}$. For the top-view configuration, the uncertainty in the instantaneous streamwise velocity component was less than $0.04\overline{u_\infty}$ over the majority of the field of view, increasing to no more than $0.18\overline{u_\infty}$ where the top-view measurement plane intersected the separated shear layer due to strong velocity gradients. The uncertainty in the instantaneous spanwise velocity measurements from the top-view configuration is also estimated to be less than $0.04\overline{u_\infty}$, increasing to no more than $0.12\overline{u_\infty}$ in the separated shear layer. The uncertainty of quantities derived from the PIV measurements was estimated using the methods described by Sciacchitano & Wieneke [167] and Moffat [168].

Table 7.1: PIV measurement parameters

Parameter	Value		
Camera	Photron Fastcam Nova R3-4K		
Lens Focal Length	105 mm		
Laser Pulse Separation	15 µs		
Aperture	$f/2.8$		
Light Source	Photonics DM20-527 Nd:YLF Pulsed Laser		
Particles	Water-Glycol Fog		
Maximum Particle Image Displacement	15 px		
Initial Correlation Window	24 px × 24 px		
	Side-view		Top-view
Magnification Factor	0.29		0.35
	Instantaneous	Average Correlation	
Final Correlation Window	16 px × 16 px	4 px × 4 px	16 px × 16 px
Vector Pitch	$0.0009c$	$0.0002c$	$0.0007c$
Final Correlation Window Overlap	75%	75%	75%
	Non-time-resolved		Time-resolved
Sampling Frequency	0.1 kHz		3.9 kHz

Table 7.2: PIV fields of view and sampling times for time resolved measurements.

Sampling Frequency	3.9 kHz			
Angle of Attack	$\alpha = 5°$		$\alpha = 12°$	
Active Turbulence Grid	No	Yes	No	Yes
Cropped Sensor Size	2175px × 351px	1916px × 415 px	1791px × 415px	2431px × 351 px
Field of View	$0.74c \times 0.09c$	$0.43c \times 0.06c$	$0.40c \times 0.07c$	$0.55c \times 0.06c$
Sampling Time	3.79 s	3.79 s	3.90 s	3.39 s

7.2.2 Free-stream Turbulence Generation

Free-stream turbulence was generated using an active turbulence grid consisting of 10 horizontal and 10 vertical steel shafts of diameter 7.94 mm upon which were fixed square aluminium wings with a diagonal of 56.96 mm (Fig. 7.1). The wings adjacent to the test section walls were triangular. The rotation of each shaft was controlled by a dedicated stepper motor. The free-stream turbulence intensity and streamwise integral length scale were estimated at the location of the airfoil leading edge in the empty test section based on measurements with a single normal hot-wire anemometer probe. During tests with the

Table 7.3: PIV fields of view and sampling times for non-time resolved measurements.

Sampling Frequency	0.1 kHz			
Angle of Attack	$\alpha = 5°$		$\alpha = 12°$	
Active Turbulence Grid	No	Yes	No	Yes
Cropped Sensor Size	3327px × 607px	3301px × 575px	3967px × 799px	3967px × 799px
Field of View	$0.73c \times 0.09c$	$0.75c \times 0.06c$	$0.88c \times 0.11c$	$0.90c \times 0.11c$
Sampling Time	55.98 s	59.09 s	35.68 s	35.68 s

airfoil mounted in the test section, free-stream velocity fluctuations were measured with a single normal hot-wire anemometer probe positioned at the centre of the test section $10c$ upstream of the airfoil. A summary of the turbulence intensity and integral length scales investigated is provided in Table 7.4, and Fig. 7.3 presents the power spectral density (PSD) of free-stream velocity fluctuations ($\mathcal{P}_{u'_\infty u'_\infty}$) for each case. The spectra were obtained using Welch's method [153] with a Hamming window of length 2^{16} samples and 50% window overlap from 300 s of data sampled at 20 kHz. Turbulence intensities and integral length scales were computed after band-pass filtering the hot-wire signal. The low-frequency cutoff of the filter was $0.005u_\infty/c$ and the high-frequency cutoff was the frequency at which the PSD fell below the measurement noise floor of $\mathcal{P}_{u'_\infty u'_\infty} = 10^{-8}$. The relative uncertainty in Tu was estimated to be less than 10% (i.e. the uncertainty for $Tu = 13\%$ is $< \pm 1.3\%$), following the approach outlined in Yavuzkurt [213]. The streamwise integral length scale was estimated from the streamwise integral time scale using the frozen turbulence hypothesis [214]:

$$\Lambda_{ux} = \overline{u_\infty} \int_0^\infty \rho_{u'_\infty u'_\infty}(t) dt \tag{7.1}$$

where $\rho_{u'_\infty u'_\infty}(t)$ is the temporal autocorrelation coefficient of the free-stream velocity fluctuations. Because estimates of $\rho_{u'_\infty u'_\infty}(t)$ obtained from finite length experimental data may not converge to 0 for large t, the streamwise integral time scale was computed by integrating an exponential fit to $\rho_{u'u'}(t)$ [215, 216]. The integral length scales computed from multiple shorter (60 s) segments of the hot-wire recordings were averaged to reduce the uncertainty in integral length scale estimates. The uncertainty in the reported integral length scales was estimated from the variance of the integral length scales for the shorter segments, and was less than $0.14c$. The spanwise integral length scale (Λ_{wz}) was estimated from an exponential fit to the spatial autocorrelation coefficient [e.g., 190, 216] of the spanwise velocity fluctuations of the top-view PIV measurements outside of the boundary layer near the leading edge of the airfoil. The spanwise velocity fluctuations were used for this estimate because they are expected to be less affected by the blocking effect of the airfoil [217] than the streamwise velocity fluctuations. The estimated values of Λ_{wz} were on the order of $0.1c$. In other investigations of active [138] and passive [218] grid-generated turbulence, integral length scales in the spanwise direction and those for spanwise velocity components in the streamwise direction have also been reported to be substantially smaller than the streamwise integral length scale.

Two different shaft motion protocols were used to generate different turbulence intensities. The grid motion parameters for these two protocols are summarised in Table 7.4. For $Tu = 4\%$ and 7%, the grid was operated in flapping mode such that the shafts oscillated about a mean angle of attack of zero. The amplitude and frequency of the shafts' oscillation were varied depending on the desired turbulence intensity and integral length scale, respectively. The frequency of oscillation of each shaft was varied according to a top-hat probability distribution to avoid exciting a single frequency of velocity fluctuations. The bounds of the top-hat distribution were $\pm 1/2$ of the mean frequency. To minimise the influence of oscillation frequency on the energy spectrum of the free-stream turbulence, the oscillation frequency of each shaft was continually re-sampled from the uniform distribution. To

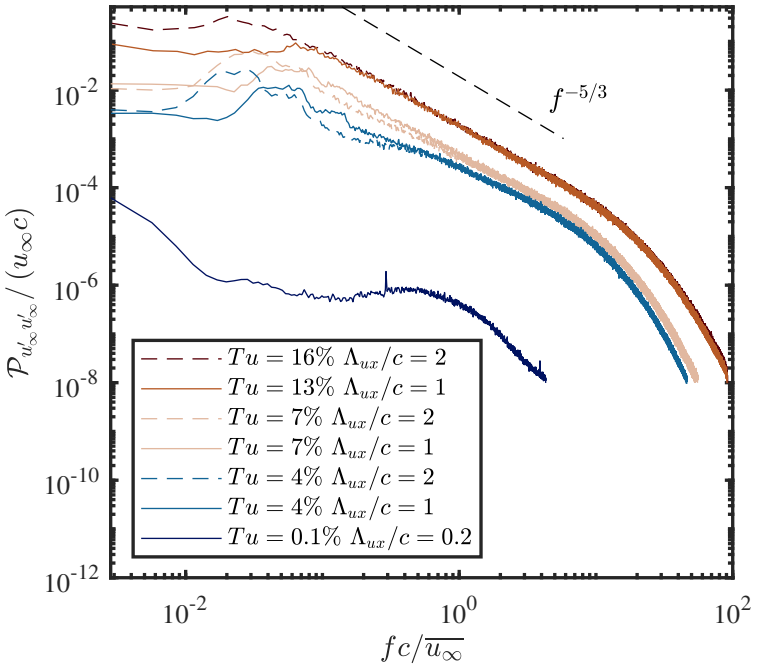


Figure 7.3: Free-stream turbulence spectra.

Table 7.4: Free-stream turbulence conditions and active grid parameters.

Tu [%]	Λ_{ux}/c	Flapping mode		Rotation mode	
		Amplitude [°]	Mean frequency [Hz]	Mean speed [rev/s]	Mean time interval [s]
0.1	0.1				
4	1	19	5.6		
4	2	19	2.6		
7	1	37	6.7		
7	2	35	3.1		
13	1			8.38	0.93
16	2			2.45	0.93

generate higher FSTI ($Tu = 13\%$ and $Tu = 16\%$), the grid was operated in rotation mode, where the shafts performed complete rotations at random rotational velocities for random intervals of time. The rotation speeds and time intervals were varied using top-hat probability distributions with bounds set at $\pm 1/2$ of the mean rotation speed and time interval, respectively. Measurements were also taken with the active turbulence grid removed from the test section. This condition is termed the clean flow, and the FSTI for the clean flow was $Tu = 0.1\%$.

7.2.3 Data Processing Techniques

Proper Orthogonal Decomposition

The snapshot method of POD (Section 3.4.3) is employed in this chapter to identify coherent structures from PIV data. Although the mean velocity field is often subtracted from the velocity data before performing the POD, in this chapter the mean is not subtracted because we require the POD modes to contain information about the mean flow [219] for the entropy-based transition detection method detailed in Section 7.2.3. The POD can be obtained from the singular value decomposition of the snapshot matrix whose rows represent the spatial locations of velocity measurements, and whose columns represent the individual snapshots [e.g., 162]. The uncertainty of the computed modal energies was estimated using the method described by Epps & Krivitzky [220]. Two different PODs were performed on the PIV data using different formulations of the snapshot matrix.

The first POD, termed the velocity profile POD (P-POD), was performed independently on the data obtained at each $x-$grid location in the side-view PIV field of view (i.e. $\mathbf{x} = y$ in Eq. 3.4, thus the data snapshots were the u and v velocity profiles at each streamwise location). This POD produced a set of spatial modes, modal energies, and temporal coefficients for each x location that describe the shape and time evolution of the velocity profile at that location.

The second POD, termed the velocity field POD (F-POD), was performed on the data from the entire side-view PIV field of view (i.e. $\mathbf{x} = [x, y]^T$ in Eq. 3.4, thus the data snapshots were the two-dimensional u and v velocity fields). This POD produced a single set of spatial modes and temporal coefficients for each PIV measurement run that describe the two-dimensional flow-field development.

Transition Detection

The transition from laminar to turbulent states involves an increase in the disorder of a flow [80]. The degree of disorder can be quantified by applying the concept of entropy from information theory [221] to the POD [222–224]. An ordered, laminar flow can be described by a relatively small number of POD modes, whereas a turbulent flow typically requires a relatively greater number of POD modes to account for the same fraction of the total kinetic energy [e.g., 159]. Thus, more information is required to describe a turbulent flow than a laminar flow. The quantity of information contained in the POD modes that describe a flow can be expressed in terms of entropy [223]. The entropy of the POD is zero when the velocity field can be exactly represented by a single POD mode. The entropy is maximum if the kinetic energy of the flow is evenly distributed among all POD modes. Thus, the entropy of the flow is related to the relative energy distribution of the POD modes. Aubry *et al.* [223] defined a global entropy E_g that is a constant for a given snapshot matrix, and spatial entropy $E_\mathrm{s}(t)$ that is a function of time. The global entropy E_g, is given by [223]:

$$E_\mathrm{g} = -\sum_{i=1}^{N} p_{g,i} \ln\left(p_{g,i}\right) \tag{7.2}$$

where $p_{g,i}$ are the relative modal energies, computed as:

$$p_{g,i} = \frac{\lambda_i^2}{\sum_{i=1}^{N} \lambda_i^2} \tag{7.3}$$

The global entropy is zero if the flow is steady, and the global entropy is maximised if all data snapshots are uncorrelated. The spatial entropy of the flow at a given instant in time is given by [223]:

$$E_s(t) = -\sum_{i=1}^{N} p_{s,i}(t) \ln\left(p_{s,i}(t)\right) \tag{7.4}$$

where $p_{s,i}(t)$ are computed as:

$$p_{s,i}(t) = \frac{\Theta_i^2(t)\lambda_i^2}{\sum_{i=1}^{N} \Theta_i^2(t)\lambda_i^2} \tag{7.5}$$

Note that, unlike Aubry *et al.* [223], the relative energies $p_{s,i}(t)$ in the definition of the spatial entropy have been computed using $\Theta_i^2(t)\lambda_i^2$ instead of $\Theta_i(t)\lambda_i$ to maintain symmetry with the definition of global entropy [e.g., 225]. The spatial entropy is zero if only one $\Theta_i(t)$ is non-zero, that is, if the velocity field at time t can be exactly represented by a single POD mode. The spatial entropy is maximum if $\Theta_i^2(t)\lambda_i^2$ is constant for all i, that is, if the kinetic energy of the flow is evenly distributed among all modes at time t. Since turbulent flows are characterised by a redistribution of energy from larger to smaller spatio-temporal scales, the global and spatial entropies increase as the flow becomes more turbulent.

The global entropy computed from the P-POD quantifies the degree of disorder in both the wall-normal direction and time at each x location. The spatial entropy of the P-POD at each x location quantifies the degree of spatial disorder of the velocity profile as a function of time. Since the spatial entropy can be computed separately on the P-POD for each x location, the spatial disorder of the velocity profile can be plotted in the $x - t$ plane. The global entropy of the F-POD quantifies the degree of disorder of the two-dimensional flow field within the entire field of view in space and time. The spatial entropy of the F-POD quantifies the degree of spatial disorder of the PIV flow-field as a function of time.

The main advantage of using entropy to measure the degree of turbulence in the flow compared to traditional methods of calculating the intermittency factor [e.g., 226] is that the computation of entropy from the POD is an entirely data-driven procedure that does not require the computation of temporal derivatives from time-resolved data. However, to distinguish laminar from turbulent flow, selection of a threshold that separates these two flow regimes is unavoidable. Although Abdelsamie *et al.* [222] demonstrated that transition occurs at similar values of global entropy for numerical simulations of widely varying flow configurations, in the present study, the entropy threshold separating laminar and turbulent flow regimes was determined empirically from the PIV data. The selection of the transition threshold is detailed in Section 7.3.3.

Unlike methods that define the instantaneous transition location using integral boundary layer quantities [e.g., 176] or Reynolds stresses computed over a sliding temporal window

[e.g., 1], defining the instantaneous transition location using the spatial entropy from the P-POD (Eq. 7.4) does not require temporal windowing. Consequently, the spatial entropy from the P-POD has the potential to more precisely differentiate between unsteady laminar and turbulent flows.

7.3 Results

7.3.1 Aerodynamic Forces

Lift and drag coefficient polars for the airfoil under all tested conditions of free-stream turbulence are presented in Fig. 7.4. The lift coefficient from thin airfoil theory is also plotted for comparison. The maximum solid blockage was less than 7%, for which the errors in lift coefficients due to blockage are expected to be less than 10% [227]. The reduction in lift coefficient relative to a true two-dimensional airfoil due to the presence of the gaps between the tips of the model and the test section walls is estimated to be on the order of 0.1 based on the results of Marchman [186]. In the clean flow ($Tu = 0.1\%$), the pre-stall lift is highly non-linear with respect to the angle of attack and exceeds that predicted by thin airfoil theory for $\alpha \leq 6°$. Non-linear lift at moderate angles of attack is typical of airfoils operating at aerodynamically low Reynolds numbers [e.g., 228, 229], and is attributed to the increased local suction that occurs due to the presence of a short LSB [16]. Bursting of the LSB for $\alpha > 8°$ leads to an abrupt stall, decreasing lift and increasing drag.

When the FSTI is increased to 4%, the stall angle increases substantially, and the lift at low angles of attack is relatively more linear, in agreement with the effects of moderate FSTI observed in previous studies [209, 230]. These changes are attributed to the free-stream turbulence causing expedited transition, which reduces the size of the LSB and its associated pressure plateau [e.g., 146]. There are no significant differences in pre-stall lift as the FSTI increases from $Tu = 4\%$ to 7%, but the post-stall decrease in lift becomes less abrupt. At $Tu = 13\%$, there is a substantial reduction in lift at pre-stall angles of attack, and the post-stall decrease in lift and increase in drag become notably more gradual. These changes are attributed to a continued reduction in the extent of separated flow at very high free-stream turbulence intensities, which will be explored in Section 7.3.3. The observed decrease in lift slope and more gradual stall with increasing FSTI are in agreement with the measurements of Devinant *et al.* [210]. There is no significant change in airfoil performance between integral length scales of $\Lambda_{u,x}/c = 1$ and 2 at pre-stall angles of attack (compare solid and dashed lines). For $Tu = 7\%$, there is a decrease in post-stall lift at the larger length scale. It is speculated that this decrease may be caused by a delay in transition due to a reduction in the amplitudes of velocity fluctuations in the free-stream at the length scales to which the boundary layer is most receptive.

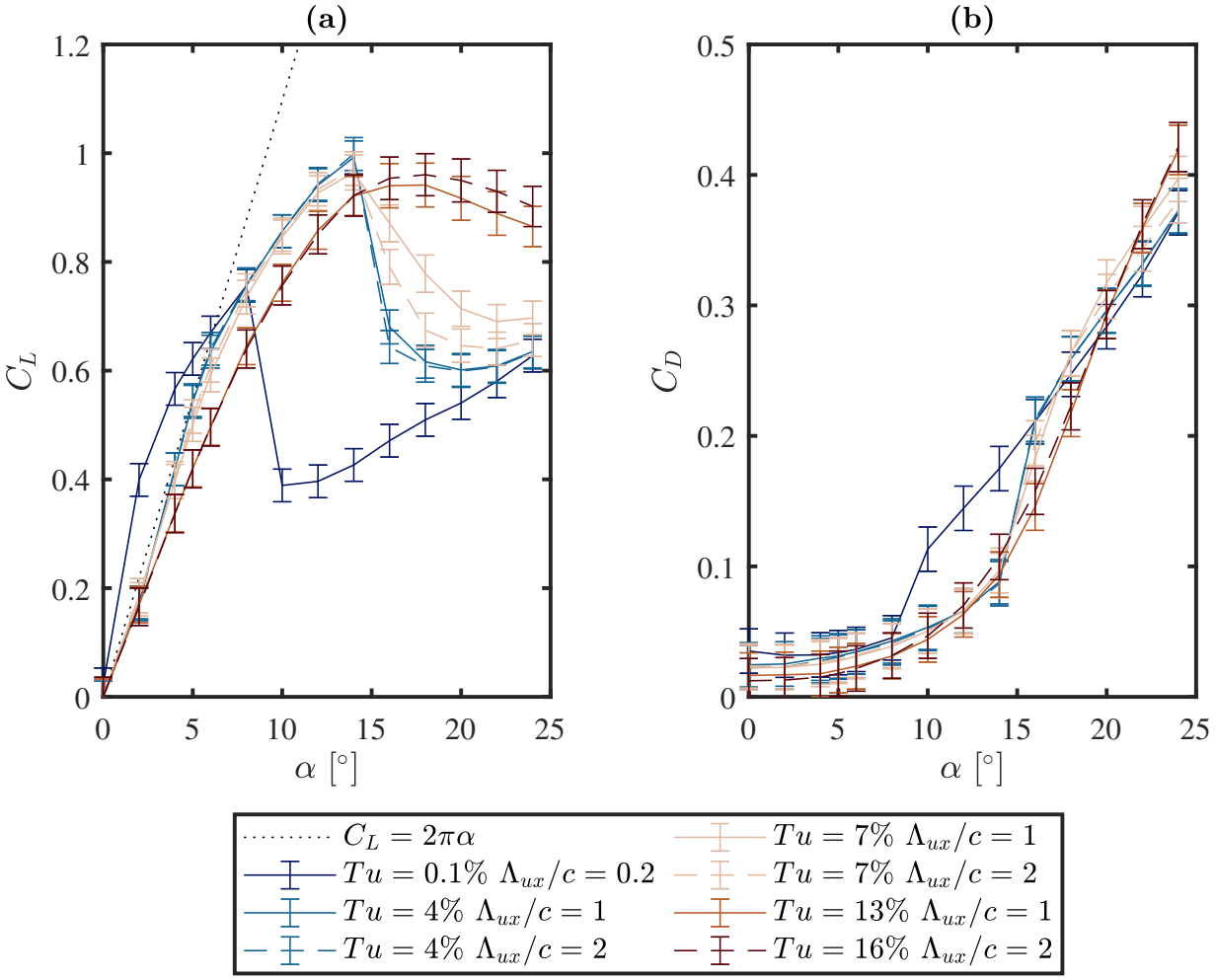


Figure 7.4: Lift (a) and drag (b) coefficients. Error bars denote uncertainty (95% confidence)

7.3.2 Overview of Boundary Layer Transition

To investigate the mechanisms responsible for the changes in airfoil performance at high FSTI with large integral length scales, side-view PIV measurements of the suction surface boundary layer were obtained at $\alpha = 5°$, which is within 2° of the angle of maximum lift to drag ratio for all tested cases, and at $\alpha = 12°$, which represents an angle at which performance is severely degraded at low FSTI.

The boundary layer transition process on the suction surface of the airfoil at $\alpha = 5°$ is illustrated using instantaneous snapshots of spanwise vorticity ($\omega_z = \partial v/\partial x - \partial u/\partial y$) in Fig. 7.5 for $Tu = 0.1\%$, 7%, and 13%. The snapshots are separated by $0.06c/\overline{u_\infty}$, and are ordered with increasing time from top to bottom. The spanwise vorticity was computed from the circulation on the contour of the 8 neighbouring velocity vectors around every PIV grid point [231] and smoothed using a 3×3 spatial average.

In the clean flow (Fig. 7.5a), due to the relatively low amplitudes of incoming disturbances,

the boundary layer remains laminar over a substantial distance, leading to laminar boundary layer separation in the region of adverse pressure gradient. The separated laminar shear layer rolls up into relatively large-scale coherent vortices near $x/c = 0.55$ as a consequence of the Kelvin-Helmholtz instability mechanism [e.g., 17, 77]. The increase in wall-normal momentum transport produced by the vortices leads to reattachment, and a turbulent boundary layer develops as the spanwise vortices break down into small-scale turbulence for $x/c > 0.6$. This transition scenario is consistent with the features typical of short LSBs [29]. The location of shear layer roll-up is observed to remain relatively consistent in time.

With increasing FSTI (Figs. 7.5b and 7.5c), higher amplitudes of boundary layer disturbances are generally expected to lead to earlier transition in a time-averaged sense [e.g., 105, 175]. The location of transition in the vorticity field snapshots can be inferred from the onset of relatively small-scale spatial variations in spanwise vorticity. Interestingly, the snapshots in Fig. 7.5 show that substantially greater variations in the location of transition occur with increasing FSTI. For $Tu = 13\%$, the variations in transition location are large enough to cause the boundary layer to occasionally remain laminar across the entire PIV field of view (Fig. 7.5c, bottom panel). It is likely that these variations are a consequence of the relatively large integral length scale of the free-stream turbulence, which leads to temporal variations in effective angle of attack and incoming flow velocity. The relationship between the variations in transition location and large-scale free-stream velocity fluctuations will be investigated in detail in Section 7.3.5.

In addition to the location of transition, the FSTI also affects the development of vortical structures formed in the transition process [e.g., 73]. Whereas the roll-up vortices formed in the clean flow are relatively large and coherent, the breakdown of the laminar shear layer at $Tu = 7\%$ involves less organised, finer-scale structures (Fig. 7.5b). At $Tu = 13\%$, the inclined regions of increased vorticity within the boundary layer are consistent with the lift-up of low speed streaks that eventually decay into turbulent spots [232]. The presence of streaks is evidence that bypass transition occurs at $Tu = 13\%$. The snapshots presented in Fig. 7.5 illustrate that large-scale free-stream turbulence can cause substantial changes in the mean flow development and the transition dynamics relative to the clean flow.

7.3.3 Mean Flow Development

Mean streamwise velocity ($\overline{u}$), standard deviation of streamwise velocity (S_u), and standard deviation of wall-normal velocity (S_v) fields for $Tu = 0.1\%$, 7% and 13% at an integral length scale of $\Lambda_{u,x}/c = 1$ are presented in Figs. 7.6 and 7.7 for $\alpha = 5°$ and 12°, respectively. The mean streamwise velocity fields were obtained from the average correlation method, whereas the other fields were computed from the average of the instantaneous PIV vector fields. Also plotted is the mean displacement thickness, defined as $\overline{\delta^*} = \int_0^{\overline{\delta}} (1 - \overline{u}/\overline{u_e})\, dy$, where δ is taken as the wall-normal distance to the location of the maximum streamwise velocity (u_e) at a given x location. The inset plots in Figs. 7.6b, 7.6c, 7.7b, and 7.7c show the near-wall structure of the mean flow with an enlarged y/c scale. The results for $Tu = 3\%$ are similar to those for $Tu = 5\%$ and are not shown for brevity. Likewise, there are no notable differences between the mean and fluctuating flow fields for $\Lambda_{u,x}/c = 2$ and

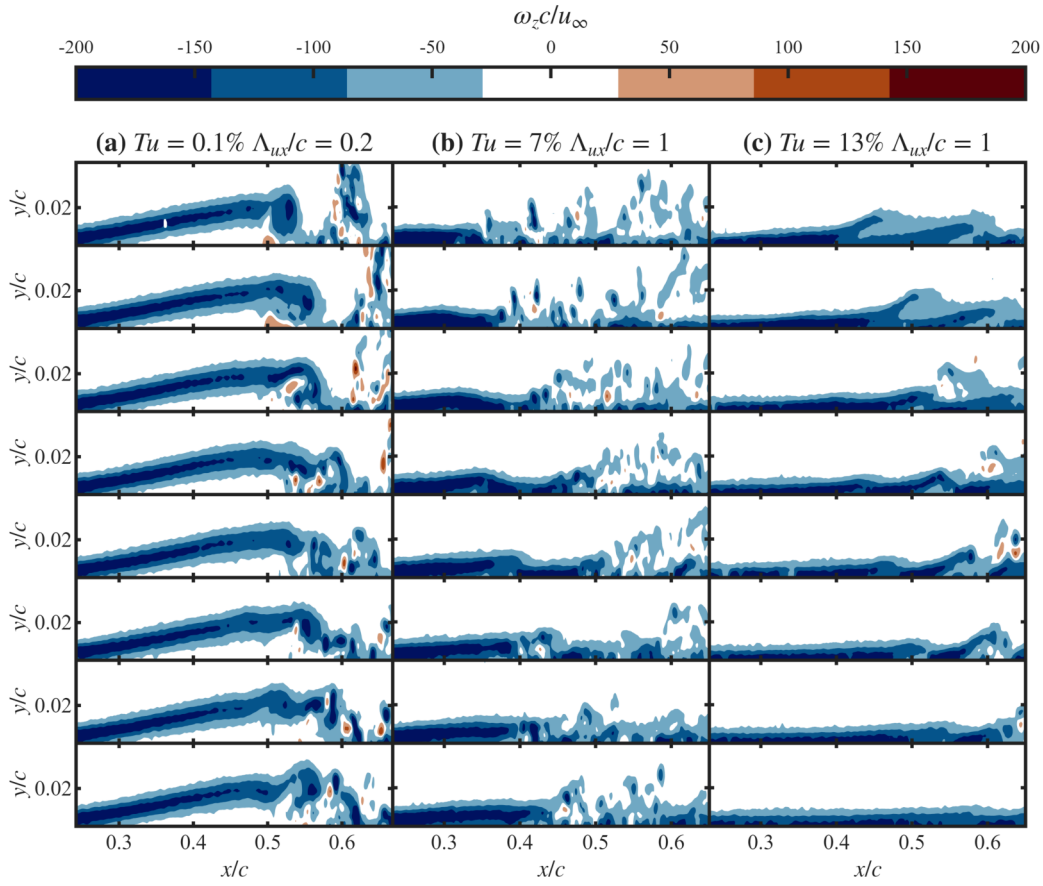


Figure 7.5: Instantaneous snapshots of spanwise vorticity. Time increases from top to bottom, and the snapshot separation is $0.06c/u_\infty$

those shown for $\Lambda_{u,x}/c = 1$, consistent with the measured lift coefficients (Fig. 7.4).

The measurements in the clean flow for $\alpha = 5°$ (Fig. 7.6a) show the development of a relatively thick LSB on the suction surface of the airfoil. The blue contours in the mean streamwise velocity plot outline the extent of mean reverse flow in the LSB, with separation at $x/c = 0.25$ and reattachment at $x/c = 0.58$. Transition of the separated shear layer is evidenced by the rapid increase in velocity fluctuations that occurs near the location of maximum bubble thickness ($x/c = 0.49$). The ratio of the lengths of the laminar and turbulent portions of the LSB is 2.7, suggesting that this LSB should be classified as short [29].

At $\alpha = 5°$ and $Tu = 7\%$ (Fig. 7.6b), the reverse flow region is nearly eliminated. However, the increase in streamwise velocity at $y/c \approx 0.0025$ for $0.5 < x/c < 0.55$ is similar to the flow structure seen near the reattachment location in the clean flow, and suggests that a thin LSB may intermittently form at $Tu = 7\%$. Furthermore, the local maximum in streamwise velocity fluctuations and increase in wall-normal velocity fluctuations that

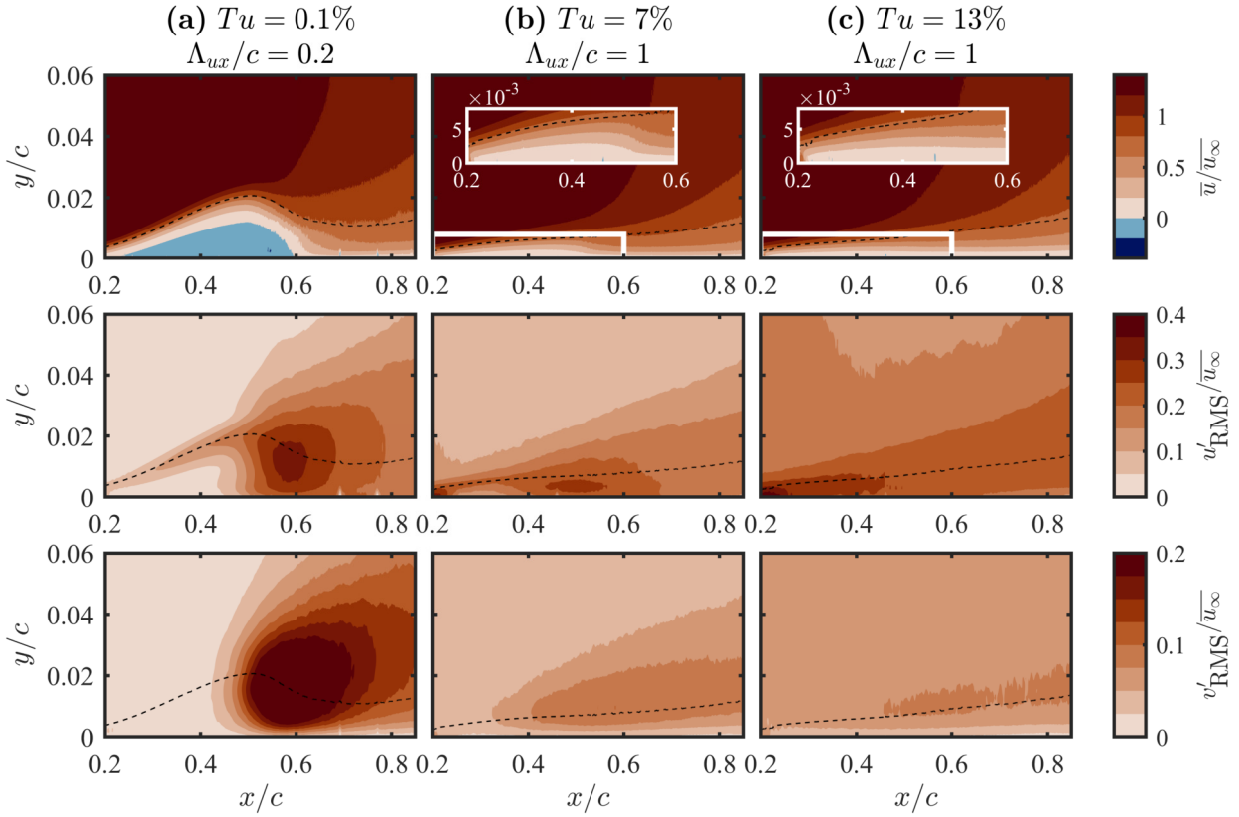


Figure 7.6: Mean streamwise velocity (top row), streamwise RMS velocity fluctuations (middle row), and wall-normal RMS velocity fluctuations (bottom row) for $\alpha = 5°$. Dashed lines: $\overline{\delta*}$.

occurs near $x/c = 0.5$ is consistent with LSB formation, since vortex shedding from the separated shear layer is expected to cause an increase in streamwise and wall-normal velocity fluctuations near the reattachment location [176, 233]. Evidence of vortex shedding in the POD spatial modes for these conditions will be discussed in Section 7.3.4.

At $\alpha = 5°$ and $Tu = 13\%$ (Fig. 7.6c), the FSTI is sufficiently high that the presence of an LSB is not evident in the mean or fluctuating velocity fields. The region of increased streamwise velocity fluctuations near the wall for $x/c \leq 0.5$ without a corresponding increase in wall-normal velocity fluctuations suggests that transition at this level of FSTI is dominated by streak formation and breakdown rather than separated shear layer roll-up.

The mean flow fields presented in Fig. 7.6 show that increasing the FSTI progressively decreases the extent of separated flow at $\alpha = 5°$. Because the LSB produces a low-pressure plateau in the surface pressure distribution [20], the decrease in lift coefficient with increasing FSTI is largely attributed to the reduction in streamwise extent of the LSB.

The reason for the substantial change in airfoil performance at $\alpha = 12°$ with varying FSTI (Fig. 7.4) is evident from the mean flow fields for this angle of attack presented in Fig. 7.7. For the clean flow (Fig. 7.7a), the reduced lift and increased drag is due to massive separation from the suction surface of the airfoil. In this case, the amplitudes of free-stream

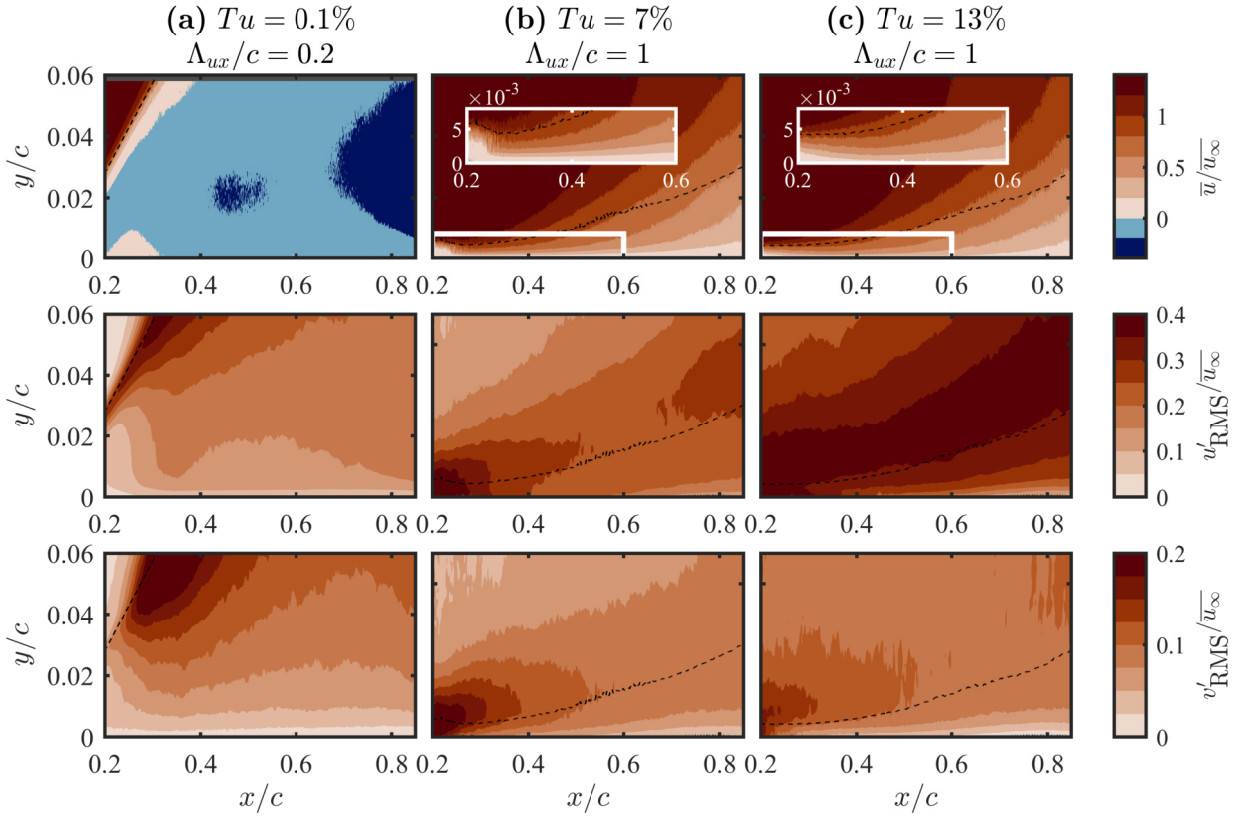


Figure 7.7: Mean streamwise velocity (top row), streamwise RMS velocity fluctuations (middle row) and wall-normal RMS velocity fluctuations (bottom row) for $\alpha = 12°$. Dashed lines: $\overline{\delta*}$.

disturbances are too low for transition to occur rapidly enough to enable reattachment.

At $Tu = 7\%$, the extent of separation is substantially reduced because of more rapid boundary layer transition (Fig. 7.7b). However, a thin region of mean reverse flow was detected at the upstream end of the field of view for $Tu = 7\%$, and the streamwise velocity contours in the inset are consistent with those expected near the reattachment location of an LSB. Thus, a thin laminar separation bubble persists on the airfoil for $Tu = 7\%$. The presence of the LSB is consistent with the region of stronger wall-normal velocity fluctuations near the airfoil surface for $x/c < 0.2$. The persistence of mean laminar separation up to at least $Tu = 7\%$ is attributed to the relatively low Reynolds number and strong adverse pressure gradient for the airfoil at $\alpha = 12°$. At $Tu = 13\%$, no reverse flow was detected in the PIV measurements (Fig. 7.7c). However, the increase in streamwise velocity near the wall and plateau in δ^* for $x/c < 0.4$ suggest that a thin LSB may form upstream of the field of view.

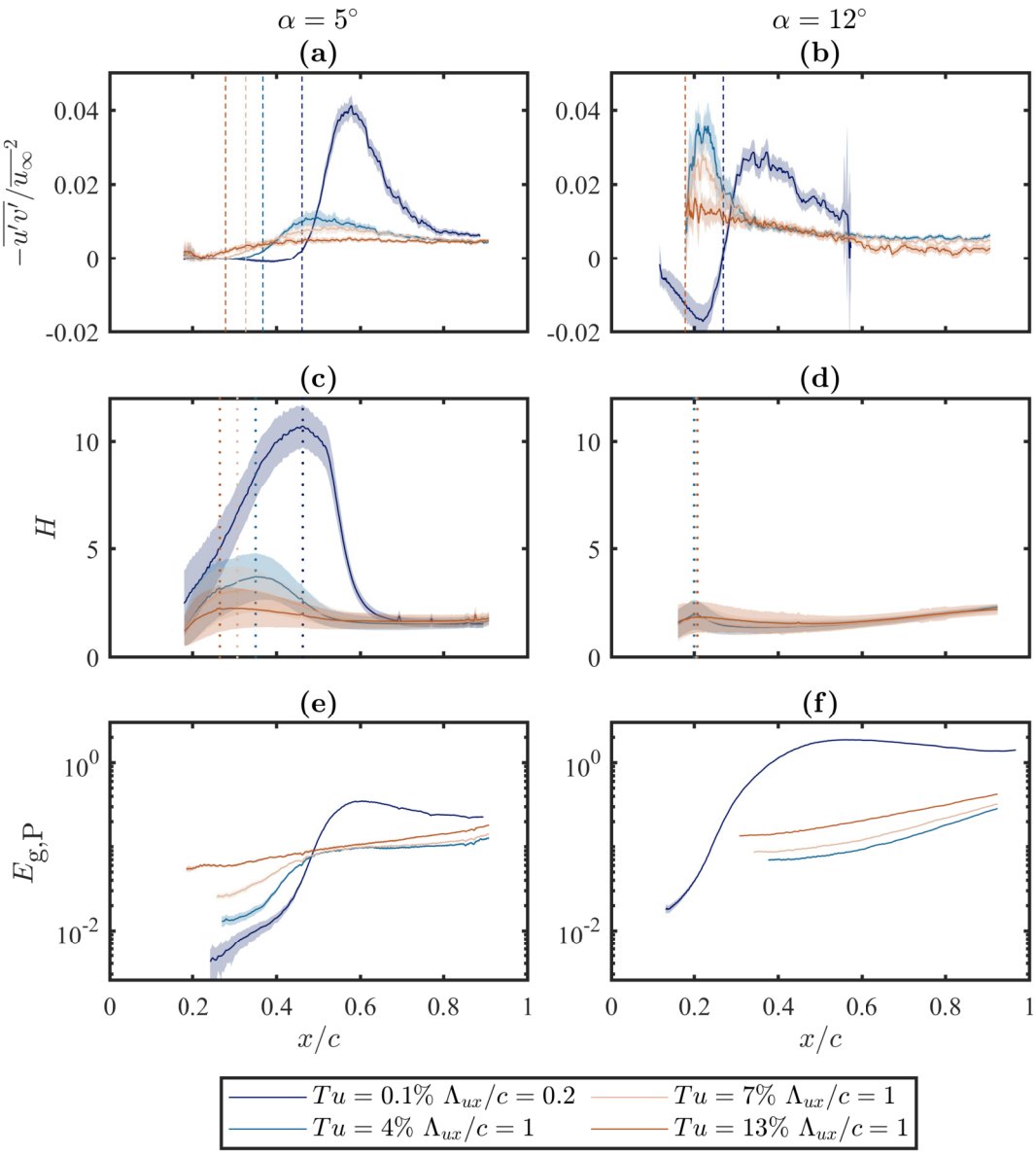


Figure 7.8: Reynolds shear stress at $y = \delta^*$ (a,b), shape factor (c,d), and global entropy from P-POD (e,f) at $\alpha = 5°$ (a,c,e) and $\alpha = 12°$ (b,d,f). Dashed lines: $-\overline{u'v'} = 0.001u_e^2$, dotted lines: maximum shape factor, shaded areas: uncertainty (95% confidence).

Mean Transition

In this section, the relationship between transition and time-averaged suction surface boundary layer properties is explored. It serves to define a transition threshold for the entropy-based transition detection method that is consistent with other boundary layer transition indicators commonly applied in low-Reynolds number flows over airfoils. The entropy-based method is used because it is desired to characterise instantaneous variations in the transition location in Section 7.3.4 without requiring temporal windowing for calculation of Reynolds shear stresses or integral boundary layer parameters. Figures 7.8a and 7.8b present the Reynolds shear stress ($-\overline{u'v'}$) measured at $y = \delta^*$ for $\alpha = 5°$ and 12°, respectively. The shape factors ($H = \overline{\delta^*}/\overline{\theta}$, where $\overline{\theta} = \int_0^{\overline{\delta}} \overline{u}/\overline{u_e}(1 - \overline{u}/\overline{u_e})dy$) for $\alpha = 5°$ and 12° are plotted in Figs. 7.8c and 7.8d, respectively.

Because a rapid increase in the magnitude of the Reynolds shear stress is indicative of transition, several transition criteria for low-Reynolds number boundary layers have been formulated based on the Reynolds shear stress [e.g., 104, 171, 234]. Moreover, the streamwise location of maximum Reynolds shear stress has been shown to occur near the location of reattachment in LSBs [e.g., 235]. The location where $-\overline{u'v'}$ first exceeds $0.001u_e^2$ is indicated by the dashed lines in Figs. 7.8a and 7.8b. This threshold for $-\overline{u'v'}$ is based on the transition threshold used by Ol *et al.* [171] and Hain *et al.* [170]. Other researchers have used the location of maximum shape factor to define the mean location of transition in LSBs [e.g., 176, 236]. The locations of the most upstream local maximum of the shape factor are indicated by the dotted lines in Figs. 7.8c and 7.8d.

At $\alpha = 5°$, a rapid increase in $-\overline{u'v'}$ begins near $x/c = 0.44$ for the clean flow condition (Fig. 7.8a), which agrees well with the location of maximum shape factor for the clean flow (Fig. 7.8d). A similar correlation between the locations of most rapid Reynolds shear stress growth and maximum shape factor is also apparent from the results at $Tu = 4\%$ and 7% for $\alpha = 5°$. Relative to the clean flow, the locations of maximum Reynolds shear stress and shape factor for $Tu = 4\%$ and 7% are shifted upstream, indicating earlier transition. The continued presence of a maximum in the Reynolds shear stress distribution for $Tu = 4\%$ and 7% provide further evidence of the presence of a thin LSB for elevated FSTI at $\alpha = 5°$. Notably, there is also reasonable agreement between the Reynolds shear stress transition location criterion and the location of maximum shape factor for $Tu = 13\%$, despite the absence of measurable reverse flow for this condition (Fig. 7.6c).

At $\alpha = 12°$ and $Tu = 0.1\%$, the flow is massively separated, and transition occurs near $x/c = 0.3$ where there is a rapid increase in Reynolds shear stress (Fig. 7.8b). When the FSTI is increased to $Tu = 4\%$ and $Tu = 5\%$, the maximum Reynolds shear stress occurs near the upstream end of the field of view for $Tu = 4\%$ and 7%. The location of the maximum in $-\overline{u'v'}$ for these conditions suggests that the boundary layer separates and transitions upstream of the field of view and reattaches near $x/c = 0.25$, supporting the assertion made previously that the wall-normal velocity fluctuations in this region (Figs. 7.6b and 7.6c) are related to vortex shedding from an LSB. For $\alpha = 12°$, the shape factor for the clean flow is not plotted since it cannot be accurately estimated when the separated shear layer is outside of the PIV field of view. Although it is within the experimental uncertainty,

for the cases of elevated FSTI at $\alpha = 12°$, there is a local maximum followed by a decrease in shape factor near $x/c = 0.25$ that is consistent with boundary layer transition occurring near the upstream end of the PIV field of view in an LSB.

The mean transition locations determined from the Reynolds shear stress threshold and the location of the first local maximum of the shape factor are in reasonable agreement for all considered flow conditions, and indicate an upstream movement of the mean transition location with increasing FSTI and angle of attack. However, it is desired to characterise instantaneous variations in the transition location without requiring temporal windowing or time resolved data. For this purpose, an entropy-based transition criterion is used. Unlike methods that define the instantaneous transition location using integral boundary layer quantities [e.g., 176] or Reynolds stresses computed over a sliding temporal window [e.g., 1], defining the instantaneous transition location using the spatial entropy from the P-POD (Eq. 7.4) does not require temporal windowing. Consequently, the spatial entropy from the P-POD has the potential to more precisely differentiate between unsteady laminar and turbulent flows.

Streamwise distributions of global entropy computed from the P-POD ($E_{\mathrm{g,P}}$) are plotted in Figs. 7.8e and 7.8f, for the clean flow and elevated FSTI at $\alpha = 5°$ and $12°$, respectively. Because noise in the PIV measurements of the thin boundary layer at the upstream end of the field of view contributes to erroneously high values of entropy in that region, the global entropy is only plotted downstream of the location of minimum global entropy. For the clean flow at both $\alpha = 5°$ and $12°$, there is a relatively rapid increase in global entropy near the transition locations identified from the Reynolds shear stress threshold. There is also a more rapid increase in the global entropy near the locations of transition identified from the shape factor for $Tu = 4\%$ and $Tu = 7\%$ at $\alpha = 5°$. This suggests that a transition threshold can be defined based on the global entropy. We choose to define the entropy threshold for transition ($E_{\mathrm{g,t}}$) as the value of the global entropy at the location of maximum shape factor at $\alpha = 5°$, since the location of maximum shape factor can be objectively measured for each level of FSTI. A specific threshold for each level of FSTI is used to mitigate the influence of the entropy of the free-stream turbulence on boundary layer transition detection. The instantaneous transition criterion can be expressed as $E_{\mathrm{s,P}} > E_{\mathrm{g,t}}$. For $Tu = 13\%$ at $\alpha = 5°$ an obvious increase in the slope of the global entropy does not occur near the location of maximum shape factor. However, it will be shown that the intermittency factor distributions determined with the entropy threshold defined from the location of maximum shape factor at $\alpha = 5°$ are in qualitative agreement with the observed transition dynamics for each flow condition investigated. To make estimation of the transition location (x_t) more robust to noise in the PIV measurements, we require that the instantaneous transition criterion be met over a total cumulative distance of at least $0.15c$ downstream of the location where the criterion was first met. Furthermore, x_t was smoothed with a moving median filter with window length $0.14c/\overline{u_\infty}$. By applying the transition threshold to the spatial entropy of the P-POD, turbulent flow can be identified as a function of time and streamwise location.

The mean transition locations determined from the instantaneous entropy-based transition criterion $E_{\mathrm{s,P}} > E_{\mathrm{g,t}}$ are compared with the location of maximum shape factor in

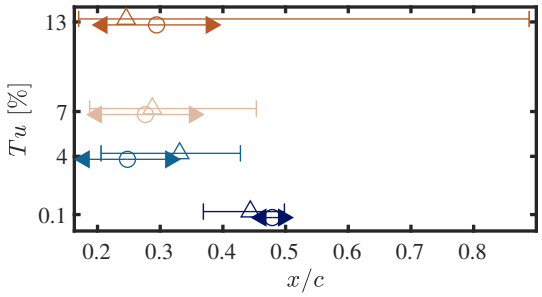


Figure 7.9: Locations of maximum shape factor (△) and mean transition location (○) for $\alpha = 5°$, $\Lambda_{ux}/c = 1$. Arrows denote standard deviation, error bars denote uncertainty (95% confidence).

Fig. 7.9 for $\alpha = 5°$ and $\Lambda_{ux}/c = 1$, where the mean transition location falls within the field of view for all levels the of FSTI investigated. The standard deviations of the transition locations (S_{x_t}) are indicated by the arrows, and the uncertainty in the locations of maximum shape factor are indicated by the error bars. The mean transition locations computed from the entropy-based criterion are all within the uncertainty intervals of the locations of maximum shape factor. When the FSTI is increased from $Tu = 0.1\%$ to 4%, there is a significant upstream movement in the transition location, expected to result from bypass transition [e.g., 105]. However, the differences in mean transition locations among the cases of elevated FSTI determined using the entropy-based criterion are sensitive to the chosen transition thresholds, since the streamwise increase in entropy for these cases is more gradual (Fig. 7.8e). It should be noted that the limited streamwise extent of the field of view is a significant source of bias in the estimates of $\overline{x_t}$ and S_{x_t}. Specifically, upstream excursions of x_t from the field of view at elevated FSTI bias the estimates of $\overline{x_t}$ downstream of their true locations, and reduce the measured S_{x_t}. Therefore, we refrain from drawing definitive conclusions about the change in mean transition locations between cases of elevated FSTI using the spatial entropy method. However, a more detailed exploration of the variations in the transition location in Section 7.3.4 will show that the instantaneous transition location becomes more variable with increasing FSTI. At $\alpha = 12°$, the mean transition location ($\overline{x_t}$) is upstream of the PIV field of view for all cases except the clean flow, for which it is located at $\overline{x_t}/c = 0.22$. Increasing the integral length scale to $\Lambda_{ux}/c = 2$ produced no substantial changes in the locations of maximum shape factor or in $\overline{x_t}$ and its standard deviation. The following discussion explores the unsteady transition dynamics responsible for the variations in transition location.

7.3.4 Transition Dynamics

The effect of the adverse pressure gradient, which is stronger at higher angles of attack, on the instantaneous transition dynamics at low and high FSTIs is visualised using the contours of instantaneous spanwise vorticity for $Tu = 0.1\%$ and 13% in Fig. 7.10. At both angles of attack for $Tu = 0.1\%$ (Figs. 7.10a and 7.10b), the separated laminar shear layer rolls up into relatively large-scale coherent vortices. At $\alpha = 5°$ (Fig. 7.10a) an LSB forms,

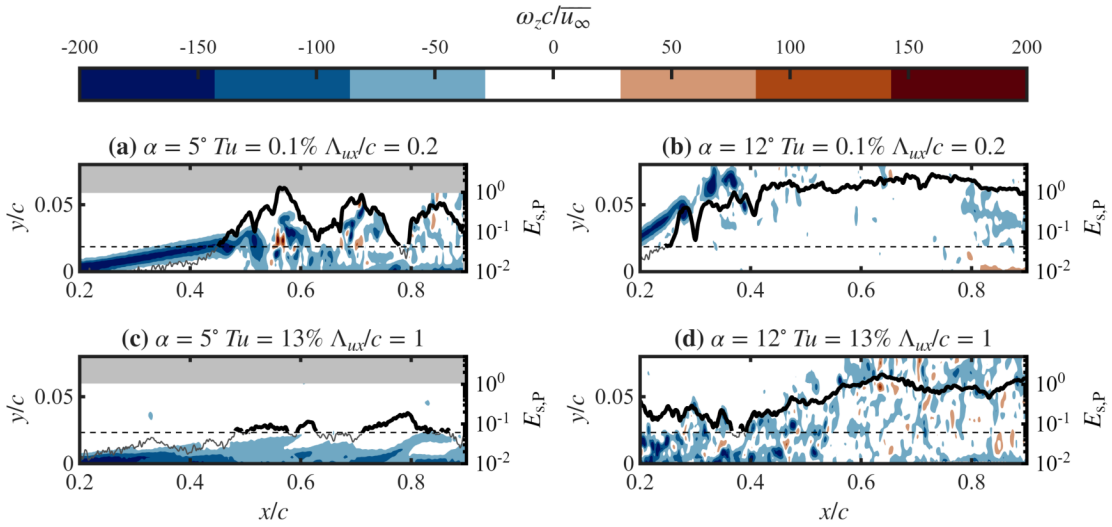


Figure 7.10: Instantaneous spanwise vorticity. Grey areas are outside the PIV field of view. Thick solid line: $E_{s,P}$ from P-POD in turbulent regions, thin solid line: $E_{s,P}$ from P-POD in laminar regions, dashed line: $E_{g,t}$.

but at $\alpha = 12°$ (Fig. 7.10b), the developing turbulent shear layer is unable to overcome the adverse pressure gradient and remains separated. At $Tu = 13\%$ (Figs. 7.10c and 7.10d), separation is suppressed due to bypass transition. The inclined structures at $x/c = 0.5$ and 0.8 in (Fig. 7.10c) are evidence of streak formation [232] at the lower angle of attack. For $Tu = 13\%$ and $\alpha = 12°$ (Fig. 7.10d), the stronger adverse pressure gradient causes earlier breakdown to small-scale turbulence within the boundary layer [e.g., 237], and no evidence of streaks is observed in this snapshot.

The relationship between vortical structures in the transitional boundary layer and the spatial entropy computed from the P-POD at each streamwise location is demonstrated in Fig. 7.10. Relative to the laminar flow in the upstream portion of the LSB at $\alpha = 5°$ and $Tu = 1\%$ (Fig. 7.10a), entropy is increased by the presence of small-scale turbulence (Fig. 7.10d), streaks (Fig. 7.10c), and breakdown of shear layer roll-up vortices (Fig. 7.10a). The relationship between these flow features and the computed spatial entropy confirms that the entropy tends to increase as the boundary layer transitions from laminar to turbulent states. Qualitatively, the transition thresholds (dashed lines in Fig. 7.5) demarcate reasonably well more laminar and more turbulent flow regions in various airfoil operating conditions.

In Section 7.3.3, the persistence of an LSB at elevated FSTI was inferred from the time-averaged flow-fields. Another indicator of the presence of an LSB is the periodic shedding of roll-up vortices from the separated shear layer near the location of mean reattachment. These coherent vortices can be characterised from their associated spatial F-POD modes [163, 233]. Furthermore, the effect of FSTI on the most energetic coherent structures in the boundary layer can be elucidated from a comparison of the F-POD spatial

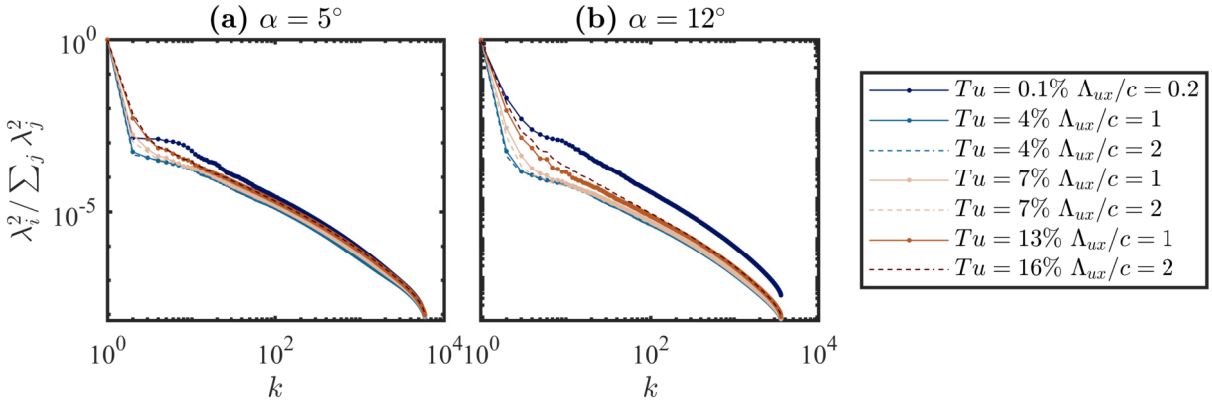


Figure 7.11: Relative energy of POD modes from F-POD.

modes from different flow conditions.

The relative modal energies for the F-POD ($\lambda_i^2 / \sum_i \lambda_i^2$), which describe the proportion of the flow's kinetic energy that is associated with each spatial mode, are presented in Fig. 7.11. The F-POD was performed on the non-time-resolved PIV measurements because these measurements cover a larger field of view. The streamwise component of the first ten spatial modes ($\mathbf{\Phi}_i(\mathbf{x})$) are presented in Figs. 7.12 and 7.13 for angles of attack of $\alpha = 5°$ and 12°, respectively, for the clean flow and for elevated FSTI with $\Lambda_{ux}/c = 1$. The spatial modes for $\Lambda_{ux}/c = 2$ (not shown for brevity) are similar to those for $\Lambda_{ux}/c = 1$, and their relative energy content is also similar as shown in Fig. 7.11. Thus, a change in integral length scale from $\Lambda_{ux}/c = 1$ to 2 does not cause a substantial change in the spatial structure or relative energy content of coherent structures in the airfoil boundary layer. Since the POD was performed without subtracting the mean flow field, the first F-POD mode, which contains over 85% of the total energy in all cases, describes a flow-field that is similar but not identical to the mean flow [e.g., 219]. The higher modes, which each contain less than 4% of the total energy, describe spatially coherent velocity fluctuations whose spatial scale decreases with increasing mode index.

For the clean flow at $\alpha = 5°$ (Fig. 7.12a), spatial modes 3 through 10 display spatially periodic velocity fluctuations beginning near the location of maximum LSB thickness, which are typical of vortex shedding from an LSB [e.g., 233, 238]. At $Tu = 4\%$ (Fig. 7.12b), similar spatially periodic structures are present in the near-wall region of modes 4 through 10, providing further evidence of vortex shedding from a thin LSB under these operating conditions. Mode 2 for $Tu = 4\%$ describes a variation in the streamwise velocity gradient of the outer flow that is correlated to a modulation of the boundary layer. This mode is consistent with the expected response of an LSB to a change in pressure gradient. For example, if the time coefficient of this mode is positive, this mode describes a streamwise acceleration of the outer flow. The associated reduction in adverse pressure gradient would be expected to delay separation, transition, and reattachment, leading to a downstream movement of the LSB, and this is consistent with the increase in streamwise velocity near the wall for $x/c < 0.4$ and reduction in streamwise velocity near the wall for $0.4 < x/c < 0.65$

present in this spatial mode. Accounting for the reversal of sign, the similarity of the second spatial modes for the cases of $Tu = 4\%$, 7%, and 13% suggests that a thin LSB may intermittently form in all of these cases. Indeed, mode 10 for $Tu = 7\%$ (Fig. 7.12c) also displays spatially periodic structures in the boundary layer that are typical of vortex shedding from an LSB.

Mode 3 for $Tu = 4\%$ describes a large-scale change in the outer flow that is correlated to a streamwise elongated region within the boundary layer, suggestive of the streaky structures formed during bypass transition [238]. Like the second modes, the overall spatial structure of the third modes is also analogous for $Tu = 4\%$, 7% and 13%, albeit reversed in sign. For $Tu = 7\%$ (Fig. 7.12c), the fourth mode also displays a relatively large wavelength change in the outer flow that is correlated to a streamwise elongated and inclined structure within the boundary layer. For $Tu = 13\%$ (Fig. 7.12d), modes 5 and 8 also contain similar elongated and inclined structures that are expected to form during bypass transition [232].

For the clean flow at $\alpha = 12°$ (Fig. 7.13a), the second mode is related to oscillations in the trajectory of the separated shear layer [e.g., 239]. Similar to the clean flow at $\alpha = 5°$, the spatial POD modes for $\alpha = 12°$ are related to periodic vortex shedding from the separated shear layer at progressively smaller scales for $4 \leq k \leq 10$. For $Tu = 4\%$ at $\alpha = 12°$ (Fig. 7.13b) modes 6 to 10 exhibit streamwise periodic structures in the boundary layer that are indicative of vortex shedding from an LSB located upstream of the field of view. The second spatial modes for $Tu = 4\%$, 7%, and 13% at $\alpha = 12°$ are analogous and describe a large scale change in the streamwise velocity gradient of the outer flow, similar to the second modes for these levels of FSTI at $\alpha = 5°$. The third modes for elevated FSTI at $\alpha = 12°$ describe streamwise elongated and inclined structures suggestive of streaks.

The comparison of F-POD spatial modes pertaining to different flow conditions reveals how the FSTI affects the spatial structure of the most energetic coherent structures in the boundary layer. The relatively small-scale structures associated with shear layer vortex shedding are progressively relegated to lower relative energy content and structures with relatively longer streamwise length scales gain a greater portion of the overall turbulent kinetic energy as the FSTI is increased. The modes with longer streamwise length scales contain elongated oblique structures near the airfoil surface, consistent with the streaks that are expected to form during bypass transition. However, the F-POD modes suggest that a thin LSB may persist to at least $Tu = 7\%$, for which the signature of a spatially periodic vortex train is present near the wall in mode 10 at both angles of attack. The second F-POD modes for each of the cases of elevated FSTI describe a change in the streamwise pressure gradient. The relationship of the second modes to the streamwise pressure gradient will be used to infer changes in effective angle of attack in Section 7.3.5.

The observation of relatively small-scale streamwise-periodic structures consistent with vortex shedding from the separated shear layer in the F-POD modes suggest that a thin LSB may form on the airfoil at relatively high FSTIs in large-scale freestream turbulence. Spectral analysis was performed on the wall-normal velocity fluctuations at $y = \delta^*$ to investigate the effect of large-scale high-intensity free-stream turbulence on the frequencies and wavenumbers associated with the vortex shedding from the separated shear layer, since the characteristics of the shed vortices affect the ability of the separated shear layer

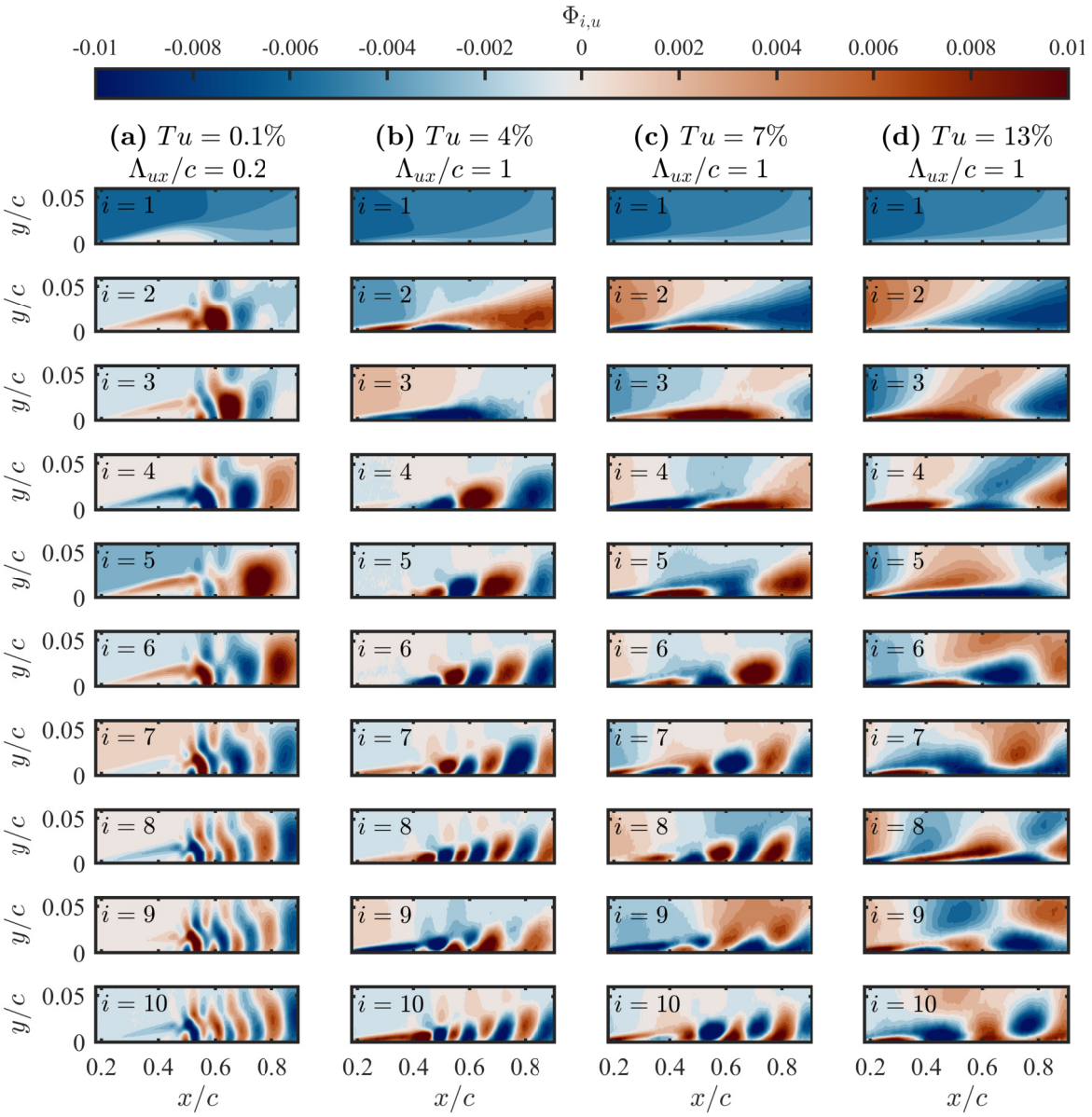


Figure 7.12: Streamwise component of POD spatial modes for $\alpha = 5°$ and $\Lambda_{ux}/c = 1$.

to reattach [e.g., 29, 78]. The wall normal velocity fluctuations at $y = \delta^*$ form a two-dimensional dataset that is a function of time and streamwise location. For the clean flow at $\alpha = 12°$ in the streamwise region where $y = \delta^*$ is outside of the field of view, the wall-normal velocity fluctuation data were extracted at the upper edge of field of view. The power spectral density of the wall-normal fluctuating velocity component ($\mathcal{P}_{v'v'}$) is plotted in Fig. 7.14 versus frequency and wavenumber. The power spectral density was estimated by averaging the squared magnitude of the two-dimensional Fourier transform obtained using windows of 128 and 256 samples in the temporal and streamwise dimensions, respectively, with 50% window overlap. This windowing procedure is a generalisation of the method of

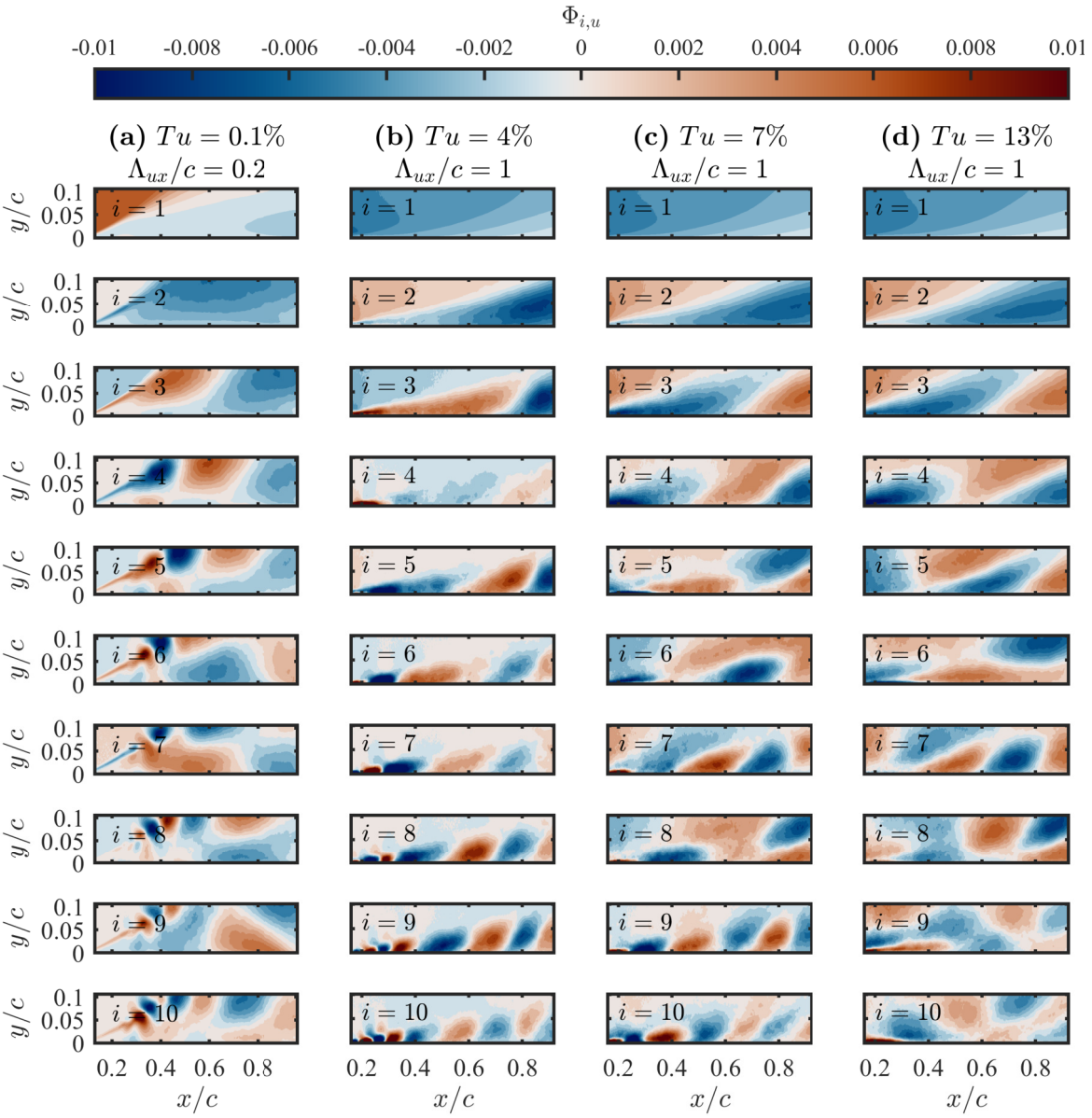


Figure 7.13: Streamwise component of POD spatial modes for $\alpha = 12°$.

Welch [153] to two dimensional data. The presented power spectral density estimates are the result of averaging over a total of 460 windows: 2 windows in the streamwise dimension and 230 windows in the temporal dimension. The frequency resolution is $0.3\overline{u_\infty}/c$, the wavenumber resolution is $30/c$, and the relative uncertainty in power spectral density is less than 8% (95% confidence). The data are normalised using the mean boundary layer edge velocity ($\overline{u_e}$) at the upstream limit of the PIV field of view, which is near the location of boundary layer separation for those cases where there is an LSB or massively separated flow (Figs. 7.6 and 7.7).

At $\alpha = 5°$ (Fig. 7.14a), vortex shedding from the LSB in the clean flow produces a peak

at $fc/\overline{u_e} = 6.6$ ($fc/\overline{u_\infty} = 9.8$) and $kc = 110$, which is consistent with the fundamental frequencies and wavenumbers for vortex shedding from LSBs at similar chord Reynolds numbers [1]. The estimated wavenumber corresponds to a streamwise wavelength of $0.06c$, which is in agreement with the streamwise wavelength of the stuctures near the location of maximum LSB height ($x/c = 0.49$) in POD modes 6 through 10 for the clean flow (Fig. 7.12a). Relative to the clean flow, there is a reduction in the frequency, wavenumber, and amplitude of the fundamental vortex shedding peak for the cases of elevated FSTI. The reduction in frequency and wavenumber of the vortex shedding peak is attributed to the reduction in the distance of the separated shear layer from the airfoil surface, which is expected to reduce the frequency and wavenumber of the most amplified disturbances [e.g., 17]. The reduction in amplitude of the vortex shedding peak is attributed to bypass transition, which leads to more rapid breakdown of the spanwise roll-up vortices into three-dimensional turbulence [73]. Furthermore, the streaks formed due to free-stream turbulence are expected to produce larger streamwise velocity fluctuations than wall-normal velocity fluctuations [e.g., 232], consistent with the fluctuating velocity statistics presented in Figs. 7.6 and 7.7. However, the discernible spectral peak of the wall-normal velocity fluctuations for $Tu = 7\%$ at $fc/u_e = 5.7$ and $kc = 84$ (Fig. 7.14e) provides additional evidence that an LSB with periodic vortex shedding may persist at this FSTI.

At $\alpha = 12°$, there are relatively stronger and more broadband wall-normal velocity fluctuations in the clean flow (Fig. 7.14b) because the greater separation angle reduces the stability of the separated shear layer [e.g., 17]. Similar to the results from the lower angle of attack, increasing the FSTI at $\alpha = 12°$ also decreases the amplitudes of wall-normal velocity fluctuations. This is consistent with the more rapid breakdown of the roll-up vortices into three-dimensional turbulence at elevated FSTI observed in previous studies where bypass transition mechanisms become dominant [e.g., 73, 105, 240]. The absence of a distinct spectral peak for the cases of elevated FSTI at $\alpha = 12°$ is attributed to the the upstream movement of the vortex roll-up location relative to the PIV field of view at this angle of attack, with the consequence of earlier vortex breakdown and reduced coherence of wall-normal velocity fluctuations in the field of view.

In all of the spectra presented in Fig. 7.14, the amplitude of wall-normal velocity fluctuations is greatest along a convective ridge [e.g., 241]. The convective speed of these fluctuations, which is approximately equal to the vortex convection speed for cases where coherent vortex shedding occurs, was estimated from a linear fit to the highest amplitude wavenumber for each frequency. The uncertainty in estimated convection speeds is estimated to be $0.1u_e$ from the variations in convection speeds obtained with various window widths for the power spectral density estimation. At $\alpha = 5°$, the convective speed is within $0.4 \leq u_e \leq 0.5$, consistent with the convective speeds expected for shear layer roll-up vortices in LSBs [19]. At $\alpha = 12°$, the convective speed remains at $0.5u_e$ for both the clean flow condition, where the flow is massively separated, and for the attached flow conditions at elevated FSTI. Although the frequency content of wall-normal velocity fluctuations in the boundary layer becomes more broadband with increasing FSTI, the results of the frequency-wavenumber analysis suggest that the angle of attack and FSTI have a negligible effect on the convection speed of coherent structures formed in the transition process when

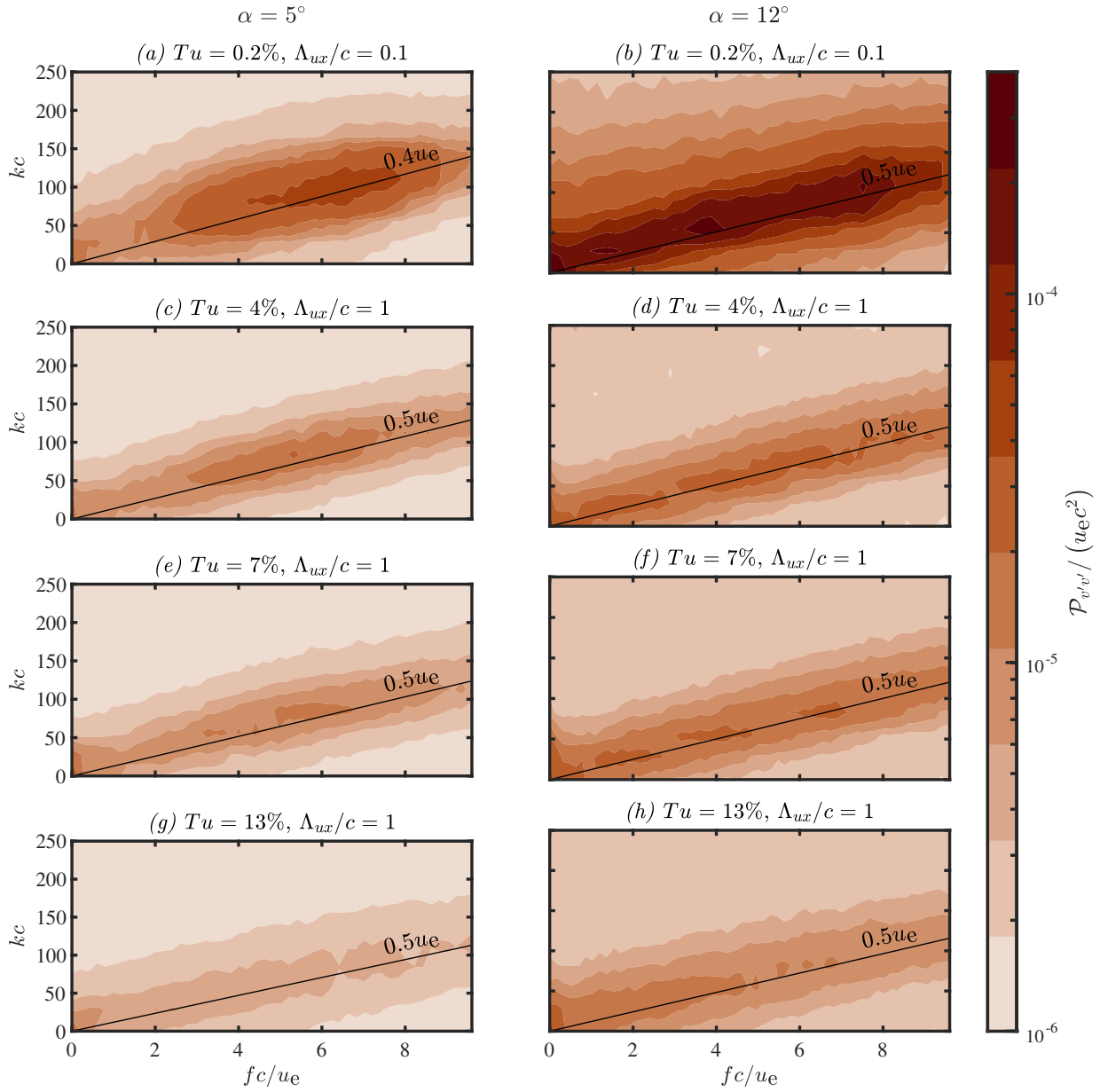


Figure 7.14: Frequency-wavenumber power spectral density of wall-normal velocity fluctuations at $y = \delta^*$ for clean flow and elevated FSTI with $\Lambda_{ux}/c = 1$ at $\alpha = 5°$ (a,c,e,g) and $\alpha = 12°$ (b,d,f,h),

normalised by the boundary layer edge velocity. The measured convection speeds are in agreement with the universal roll-up frequency scaling proposed by Yarusevych *et al.* [19].

To illustrate the temporal variations in transition location that occur at elevated FSTI, the spatial entropy from the P-POD is plotted versus time and streamwise location in Figs. 7.15 and 7.16 for $Tu = 0.1\%$, 7% and 13% at $\alpha = 5°$ and 12°, respectively. The entropy contours in these figures were obtained from time-resolved PIV measurements. All spatial entropy values below the transition threshold ($E_{s,P}/E_{g,t} < 1$) are covered by

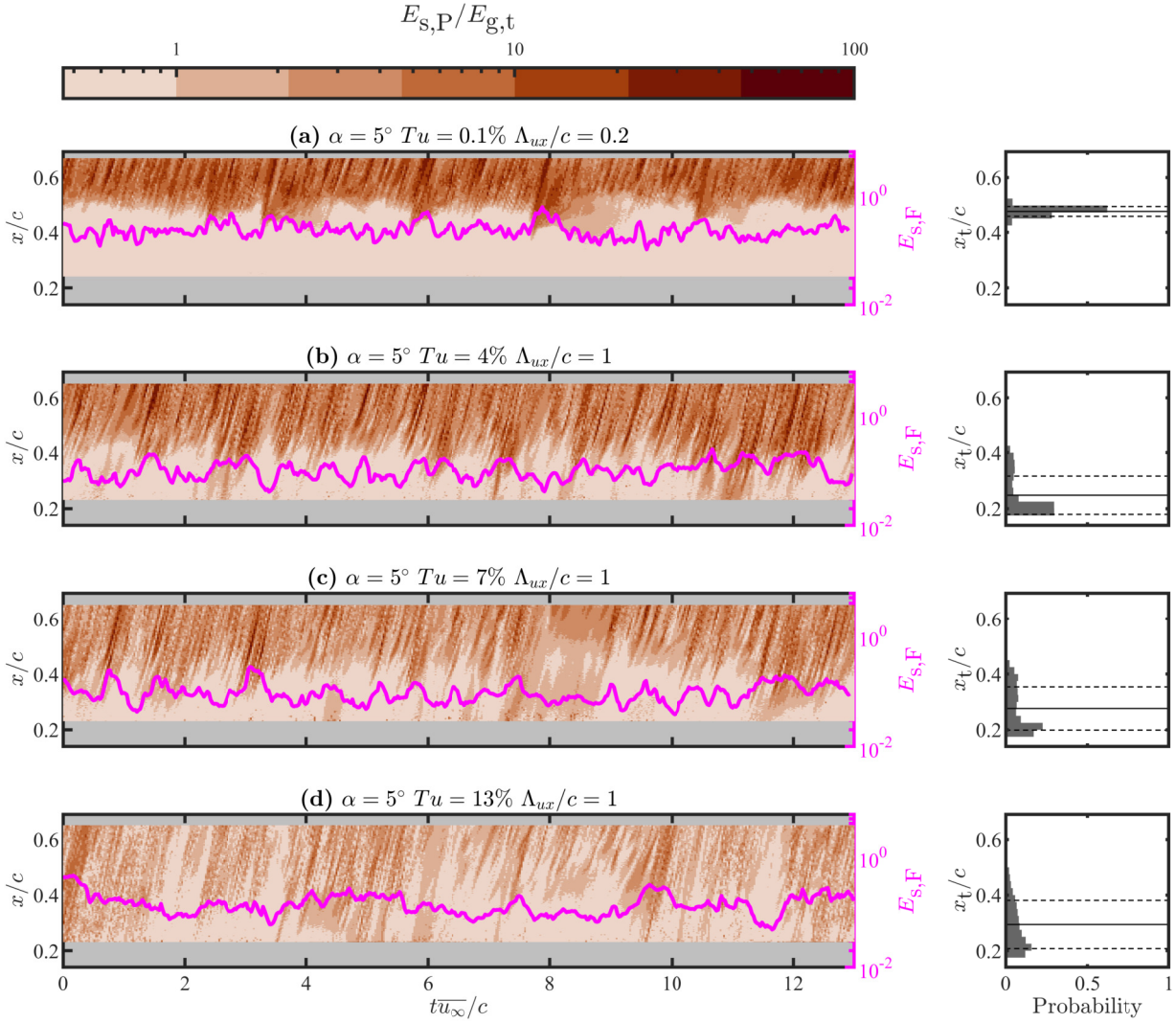


Figure 7.15: Right column: contours of spatial entropy from P-POD at $\alpha = 5°$. Grey areas are outside the PIV field of view. Magenta lines: spatial entropy from F-POD. Right column: histogram of x_t, Solid lines: $\overline{x_t}$, dashed lines: $\overline{x_t} \pm S_{x_t}$.

the lowest contour level. The overall entropy of the entire velocity field at each moment in time is quantified by the spatial entropy computed from the F-POD ($E_{s,F}$), plotted as magenta lines in Figs. 7.15 and 7.16. Histograms of the instantaneous location of x_t from non-time-resolved data over a wider field of view are provided in the right column for each level of FSTI. The probabilities in the histograms are defined as the fraction of the time that the transition location is within each bin of width $0.025c$.

In the clean flow at $\alpha = 5°$ (Fig. 7.15a), there is a rapid increase in entropy at $x/c \approx 0.5$, corresponding to the onset of transition near the location of maximum LSB thickness (Fig. 7.6a). For this case, the transition location determined from the entropy-based criterion remains relatively constant, with a mean of $\overline{x_t}/c = 0.48$ and a standard deviation

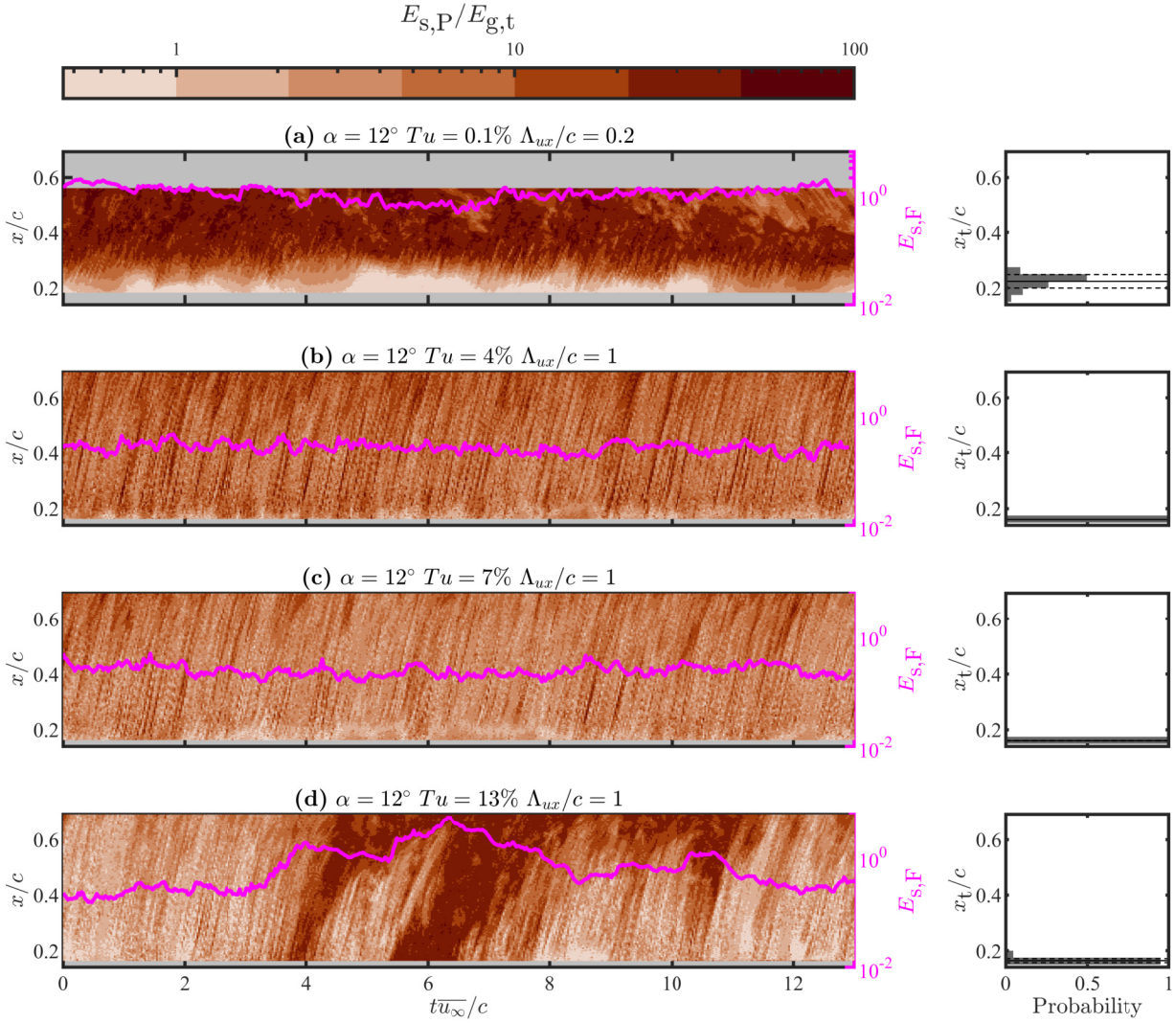


Figure 7.16: Right column: contours of spatial entropy from P-POD at $\alpha = 12°$. Grey areas are outside the PIV field of view. Magenta lines: spatial entropy from F-POD. Right column: histogram of x_t, Solid lines: $\overline{x_t}$, dashed lines: $\overline{x_t} \pm S_{x_t}$.

of $S_{x_\mathrm{t}}/c = 0.02$ as shown in the histogram. The boundary layer consistently remains turbulent downstream of the mean reattachment location of the LSB ($x/c = 0.6$ Fig. 7.6a). Regions of the boundary layer with higher spatial disorder indicative of turbulent flow appear as oblique ridges of higher entropy. The slope of the ridges in the plot is proportional to their convective speed. The convective speed of the high-entropy ridges is approximately $0.4\overline{u_\mathrm{e}}$ ($0.7\overline{u_\infty}$), which is consistent with the convective speed of the shear layer roll-up vortices estimated from the frequency wavenumber spectrum Fig. 7.14. The consistency of the estimated convective speeds of the wall-normal velocity fluctuations and the spatial entropy fluctuations holds for varying flow conditions, confirming the suitability of spatial entropy as a spatio-temporally localised indicator of velocity field disturbances.

For $\alpha = 5°$ with elevated FSTI (Figs. 7.15b–7.15d), the mean streamwise location of transition is relatively unaffected by FSTI beyond $Tu = 4\%$, but becomes more variable in time as the FSTI is increased. For example, for $Tu = 13\%$ (Fig. 7.15d) at $t\overline{u_\infty}/c = 9.5$, transition occurs upstream of the PIV field of view and at $t\overline{u_\infty}/c = 11.8$, laminar flow persists across the entire streamwise extent of the field of view. The mean measured transition locations for $Tu = 4\%$, 7%, and 13% are $\overline{x_t}/c = 0.25$, 0.28, and 0.30, respectively, and the standard deviations are $S_{x_t}/c = 0.07$, 0.08, and 0.09, respectively.

The overall level of disorder in the flow over the entire field of view can be quantified by the spatial entropy obtained from the F-POD (magenta lines in Figs. 7.15 and 7.16). When the transition location moves upstream, the spatial entropy from the F-POD tends to increase. The spatial entropy from the F-POD will be used in Section 7.3.4 to correlate overall changes in the disorder of the flow over the suction surface of the airfoil to free-stream velocity fluctuations upstream of the airfoil.

Similar to the foregoing results for the clean flow at $\alpha = 5°$, the transition location also remains relatively consistent for the clean flow at $\alpha = 12°$ (Fig. 7.16). However, the separated shear layer transitions further upstream at the higher angle of attack because the more adverse pressure gradient causes earlier separation, which destabilizes the shear layer [e.g., 15]. This is consistent with the earlier shear layer roll-up in Fig. 7.10b. For all levels of elevated FSTI at $\alpha = 12°$ (Figs. 7.16b–7.16d), the mean computed transition location is near the upstream limit of the field of view. Therefore, the standard deviations of the transition locations (dashed lines in Fig. 7.16) are likely underestimated. For the cases of $Tu = 4\%$ and 7% (Figs. 7.16b and 7.16c), the computed transition location is upstream of $x/c = 0.175$ for more than 98% of the measurement period. Intermittent periods of reduced spatial entropy indicative of laminar flow still occur in the attached boundary layer at $\alpha = 12°$, notably at $Tu = 13\%$ (Fig. 7.16d). However, the spatial and temporal extent of these laminar periods are substantially reduced compared to those for elevated FSTI at $\alpha = 5°$. For $Tu = 13\%$ at $\alpha = 12°$, there are also notable intermittent periods of substantially increased spatial entropy. It will be shown later that these periods are related to intermittent massive separation of the suction surface boundary layer.

Using the spatial entropy from the P-POD ($E_{s,P}$) and the transition thresholds ($E_{g,t}$), the intermittency factor (γ) can be calculated. The intermittency factor is defined as the fraction of time that $E_{s,P} > E_{g,t}$, and thus indicates the probability that the flow is turbulent at a given streamwise location [e.g., 226]. The intermittency factor is plotted in Fig. 7.17 for locations downstream of the minimum global entropy. The locations of maximum shape factor at $\alpha = 5°$ used to define the transition thresholds are indicated by the dashed lines in Fig. 7.17a. For all levels of FSTI at $\alpha = 5°$, $\gamma \approx 0.25$ at the location of maximum shape factor. In the clean flow at both $\alpha = 5°$ and 12°, the intermittency factor rapidly increases from $\gamma \approx 0$ to $\gamma \approx 1$ over a distance of approximately $0.15c$. The reduction in intermittency factor for elevated FSTI relative to the clean flow for $x/c > 0.5$ at $\alpha = 5°$ is consistent with the increased variability in transition location and intermittent periods of laminar flow for elevated FSTI in Fig. 7.15. For $x/c < 0.8$ at $\alpha = 12°$ (Fig. 7.17b), there is a decrease in intermittency factor with increasing FSTI, consistent with the larger variations in spatial entropy with increasing FSTI in Fig. 7.16. Overall, as the FSTI is increased, the

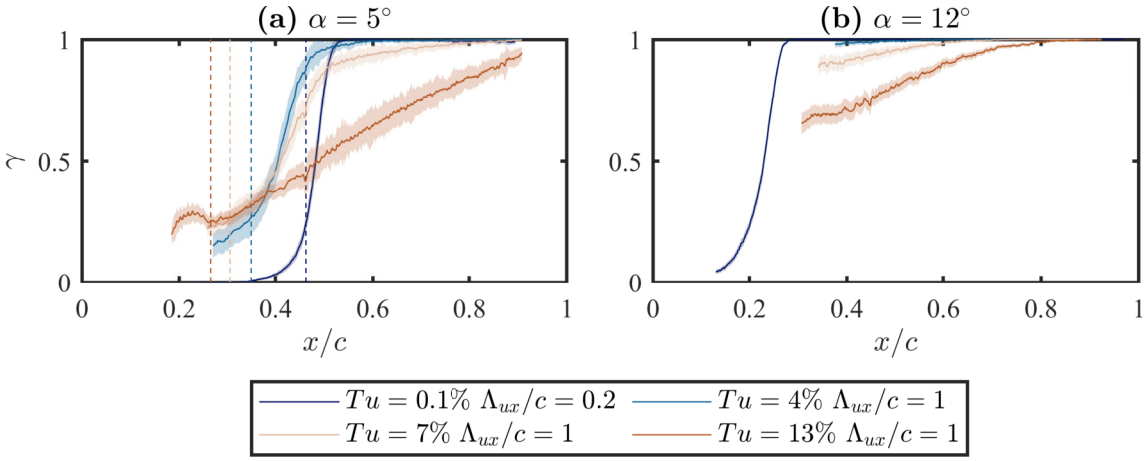


Figure 7.17: Intermittency factor for clean flow and elevated FSTI with $\Lambda_{ux}/c = 1$. Dashed lines: location of maximum shape factor. Shaded areas indicate uncertainty (95% confidence).

maximum rate of change of the intermittency factor becomes more gradual, indicating a higher probability of laminar flow persisting downstream of the mean transition location.

To characterise the frequencies associated with the large variations in transition location observed for $\alpha = 5°$, the power spectral density of the spatial entropy fluctuations from the P-POD ($\mathcal{P}_{E'_{s,P}E'_{s,P}}$) performed on the non-time-resolved PIV measurements for $\alpha = 5°$ are presented in Figs. 7.18a and 7.18b, for $\Lambda_{ux}/c = 1$ and 2 respectively. The spectra presented in Fig. 7.18 were obtained after averaging the spectra over $0.4 < x/c < 0.5$, where relatively large amplitude and low-frequency variations in spatial entropy occur for all levels of FSTI tested (Fig. 7.15). The clean flow with $\Lambda_{ux}/c = 0.2$ is shown in both plots for reference. The spectra were obtained using Welch's method with a Hamming window of length 128 samples and 50% window overlap, yielding a frequency resolution of 0.007 Hz.

In the clean flow, the transition location is relatively steady, and there are no substantial peaks in the spatial entropy spectrum. For increasing FSTI, there is an increase in the amplitudes of spatial entropy fluctuations, consistent with the low-frequency variability in the transition location observed for high FSTI (Fig. 7.15). For $Tu = 4\%$ and 7%, increasing the integral length scale from $\Lambda_{ux}/c = 1$ to 2 has the effect of shifting the largest amplitude fluctuations to lower frequencies. For $\Lambda_{ux}/c = 1$, there are prominent peaks at $fc/u_\infty = 0.06$ and 0.08, for $Tu = 4\%$ and 7%, respectively (Fig. 7.18a). These peaks are consistent with the frequencies of the largest amplitude free-stream velocity fluctuations for these conditions (cf. Fig. 7.3). For $\Lambda_{ux}/c = 2$, the frequencies of the largest amplitude spatial entropy fluctuations are reduced to $fc/u_\infty = 0.03$ for both $Tu = 4\%$ and 7% (Fig. 7.18b), consistent with the reduction in frequency of the largest amplitude free-stream velocity fluctuations. There is also a reduction in the frequency of the largest amplitude spatial entropy fluctuations for the case of $Tu = 16\%$, $\Lambda_{ux} = 2$ relative to $Tu = 13\%$, $\Lambda_{ux} = 1$. Considering that the change of integral length scale had a negligible influence on the mean flow, these results suggest that variations in Λ_{ux}, when $\Lambda_{ux} \sim c$, do not directly

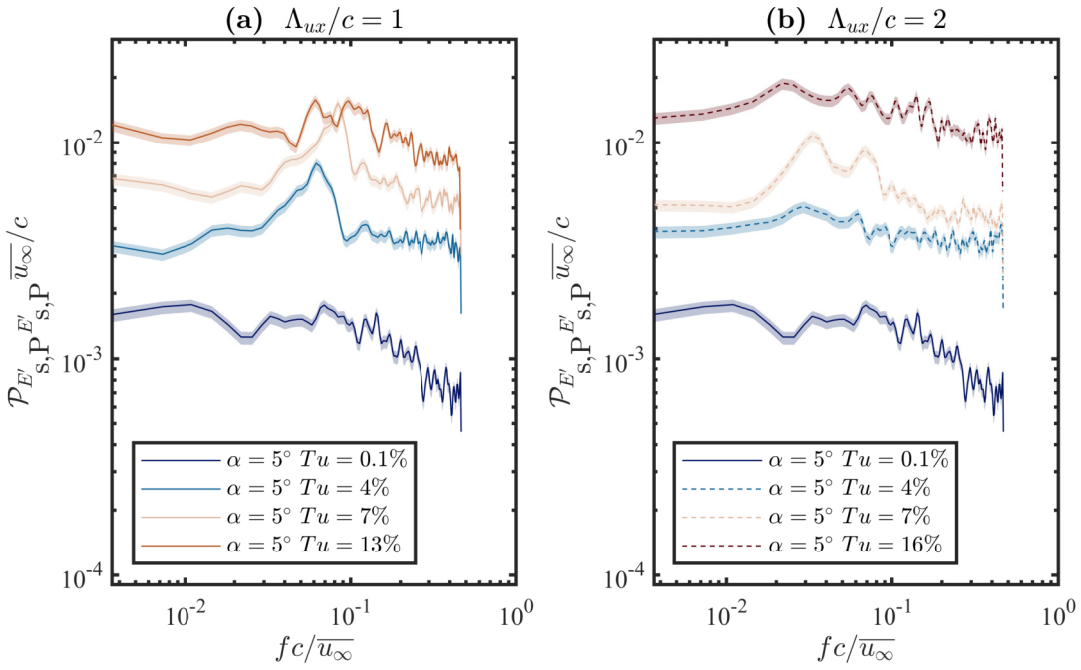


Figure 7.18: Power spectral density of spatial entropy fluctuations from P-POD averaged over $0.4 < x/c < 0.5$ for $\alpha = 5°$.

affect transition through the receptivity process. Instead, when $\Lambda_{ux} \sim c$, changes in Λ_{ux} influence the frequency at which variations of the global flow development occur about the mean.

The relationship between the flow field development and the spatial entropy computed from the F-POD (lines in Figs. 7.15 and 7.16) is demonstrated in Fig. 7.19, which presents instantaneous contours of streamwise velocity for the PIV snapshots of the 1$^{\mathrm{st}}$ percentile of $E_{\mathrm{s,F}}$ (Figs. 7.19a and 7.19b) and the 99$^{\mathrm{th}}$ percentile of $E_{\mathrm{s,F}}$ (Figs. 7.19c and 7.19d) at $Tu = 13\%$. Recall, the value of $E_{\mathrm{s,F}}$ computed from the F-POD quantifies the spatial disorder in the flow over the entire field of view. In the PIV snapshots of the 1$^{\mathrm{st}}$ percentile of $E_{\mathrm{s,F}}$, the boundary layer remains thin and laminar over a substantial portion of the field of view. For the snapshots of the 99$^{\mathrm{th}}$ percentile of $E_{\mathrm{s,F}}$, the boundary layer is relatively thicker, and at $\alpha = 12°$ reverse flow covers a substantial portion of the field of view. Figure 7.19d confirms that the periods of relatively higher spatial entropy for $\alpha = 12°$ and $Tu = 13\%$ in Fig. 7.16d are associated with intermittent massive separation from the airfoil surface. It is likely that these periods of massive separation are partly responsible for the measured reduction in time-averaged lift coefficient for $Tu = 13\%$ and 16% relative to $Tu = 4\%$ and 7% at $\alpha = 12°$ (Fig. 7.4).

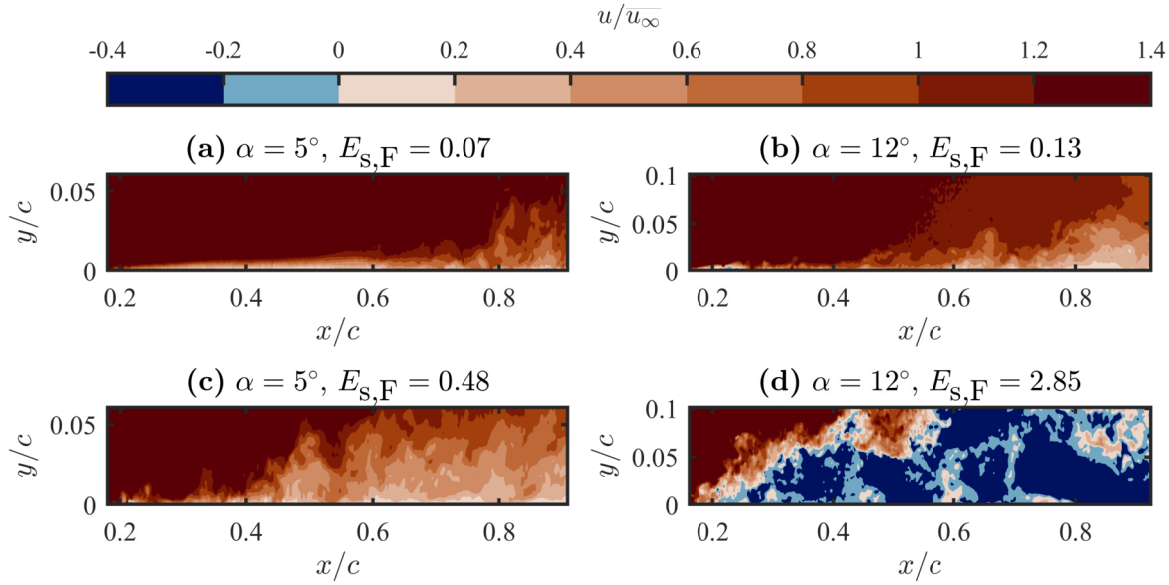


Figure 7.19: Instantaneous streamwise velocity measurements for the 1st percentile of $E_{s,F}$ (a,b) and the 99th percentile of $E_{s,F}$ (c,d) from the F-POD observed at $\alpha = 5°$ (a,c) and $\alpha = 12°$ (b,d) for $Tu = 13\%$, $\Lambda_{ux}/c = 1$.

7.3.5 Correlation of Oncoming Disturbances to Boundary Layer Development

Measurements from the hotwire anemometer placed $10c$ upstream of the airfoil and synchronised with the PIV system are used to explore the relationship of the oncoming velocity magnitude to the flow over the suction surface of the airfoil. The correlation coefficient between the velocity magnitude measured by the hotwire and the mean streamwise velocity averaged over the PIV field of view ($\langle u \rangle$) is plotted in Figs. 7.20a and 7.20b versus time lag for $\alpha = 5°$ and 12°, respectively. Data was used from the PIV measurements at 100 Hz for better statistical convergence at the expense of temporal resolution. The results show a positive peak at $t\overline{u_\infty}/c \approx 10$ for all levels of elevated FSTI at both $\alpha = 5°$ and 12°. Since the hotwire was positioned a distance of $10c$ upstream of the quarter-chord of the airfoil, this peak corresponds to disturbances in the oncoming flow that convect at the free-stream velocity and are sufficiently large to maintain their temporal coherence over that distance. The negative correlation peaks that occur at $tu_\infty/c \approx 5$ and 15 are attributed to inevitable opposite-sign changes of incoming flow velocity preceding and following that responsible for the dominant correlation peak. For example, due to the requirement for continuity, a significant, large-scale increase in free-stream velocity must be preceded or followed by a decrease in free-stream velocity to maintain the overall average flow rate through the test section.

Because of the closed test section, the active grid also produces pressure waves that likely affect the boundary layer development on the airfoil [e.g., 242]. The time lag for a pressure wave to propagate from the hotwire to the airfoil is $t\overline{u_\infty}/c \approx 0.003$. Although the influence

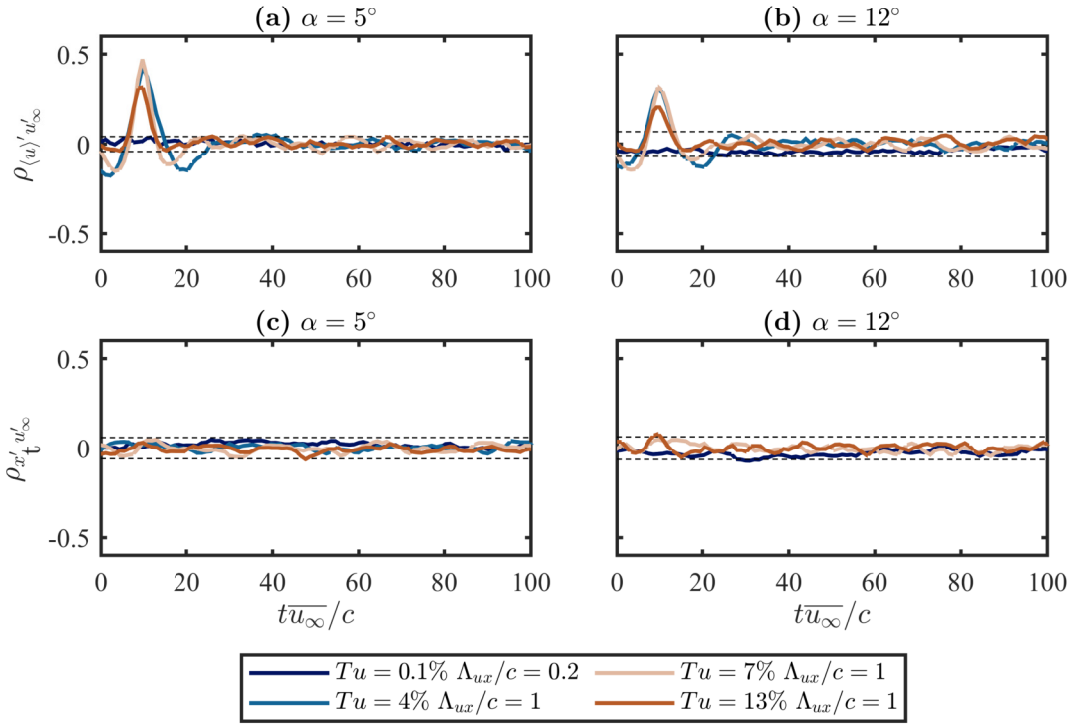


Figure 7.20: Correlation coefficient between upstream hotwire anemometer velocity and spatially averaged streamwise velocity from side-view PIV (a,b) and transition location from P-POD (c,d). Values outside the dashed lines are significant at a 95% confidence level.

of such pressure waves on the airfoil boundary layer cannot be discounted, the convective correlation peaks at $t\overline{u_\infty}/c \approx 10$ are substantially larger in magnitude than the correlations for $t\overline{u_\infty}/c \approx 0.003$. This suggests that convective vortical structures in the oncoming flow are primarily responsible for the variations in boundary layer development on the suction surface of the airfoil. In the clean flow, there are no significant correlations between the oncoming flow velocity magnitude and the spatially averaged velocity magnitude of the PIV measurements due to the order of magnitude lower FSTI.

The correlation coefficients between the upstream velocity magnitude and the transition location determined using the entropy-based method from the P-POD (Section 7.3.3) are presented in Figs. 7.20c and 7.20d. Note that, for the case of $Tu = 4\%$ at $\alpha = 12°$, no correlation coefficient could be computed because the transition location was always upstream of the side-view PIV field of view. The correlations are largely insignificant for all time lags at a 95% confidence level. Furthermore, no statistically significant correlations between the oncoming velocity magnitude and the turbulent kinetic energy within the boundary layer were found when the velocity fluctuations were normalised by the spatially averaged velocity within the boundary layer to account for the expected increase in turbulent kinetic energy with increasing free-stream velocity. Thus, it is unlikely that large-scale fluctuations in effective oncoming velocity magnitude are responsible for the the intermittent

periods of expedited and delayed transition observed at high FSTI.

In addition to fluctuations in the free-stream velocity magnitude, large-scale free-stream turbulence also leads to fluctuations in effective angle of attack, which may influence the boundary layer transition process on the airfoil [e.g., 111, 209]. The variations in effective angle of attack due to fluctuations in free-stream velocity direction were characterised from estimated variations in the suction surface pressure coefficients. The estimations were performed for $\alpha = 5°$, where the boundary layer remains relatively thin and massive separation is unlikely to occur. The instantaneous surface pressure coefficient at a given x location was estimated from the local instantaneous boundary layer edge velocity as $C_p = 1 - (u_e/\overline{u_\infty})^2$, assuming that the wall-normal pressure gradient may be neglected within the boundary layer [e.g., 243]. The free-stream velocity used for calculating the pressure coefficients was the mean free-stream velocity ($\overline{u}_\infty$) obtained from a calibration of the pressure drop across the wind tunnel contraction upstream of the active grid.

The mean surface pressure coefficient distributions for $\alpha = 5°$ are plotted in Fig. 7.21, along with inviscid surface pressure distributions for angles of attack of $\alpha = 0°$, $5°$, and $10°$ computed using the XFOIL software [192]. The mean surface pressure coefficients for the clean flow with $\Lambda_{ux}/c = 0.2$ are plotted in both Figs. 7.21a and 7.21b for reference. The maximum uncertainty in the estimated mean pressure coefficients is less than 0.2. In the clean flow, the $\overline{C_P}$ distribution initially follows the inviscid distribution at the geometric angle of attack of $\alpha = 5°$, before diverging near the boundary layer separation point and plateauing. A relatively rapid pressure recovery occurs between the location of maximum LSB thickness and the mean reattachment point, consistent with the surface pressure distribution expected of a short LSB [20]. For elevated FSTI, the pressure plateau is suppressed and the pressure distributions follow that for the inviscid flow at $\alpha = 5°$ more closely, consistent with the thinning of the LSB. However, there is still an increase in suction relative to the inviscid flow for $Tu = 4\%$ and 7%, suggesting that an LSB persists.

Previously, it was shown that the second POD mode for the cases of elevated FSTI was related to the streamwise pressure gradient. Since increases in effective angle of attack are expected to lead to a more adverse streamwise pressure gradient, variations in the effective angle of attack at elevated FSTI were characterised using conditional averaging of the estimated pressure coefficient distributions based on the temporal coefficient of the second POD mode. The surface pressure distributions of the conditional averages of snapshots for Θ_2 falling below or above the mean value by more than one standard deviation are plotted in Figs. 7.22a and 7.22b as dashed and dash-dotted lines, respectively, for the cases of elevated FSTI. Depending on the sign of the second spatial POD mode (Fig. 7.12), the C_p distributions conditioned on $\Theta_2 < \overline{\Theta_2} - S_{\Theta_2}$ and $\Theta_2 < \overline{\Theta_2} - S_{\Theta_2}$ show either a decrease or increase in pressure gradient consistent with a change in effective angle of attack. For $Tu = 13\%$ (Fig. 7.22a) and $Tu = 16\%$ (Fig. 7.22b), the conditional pressure distributions begin to approach the inviscid pressure distributions for $\alpha = 10°$, and $\alpha = 0°$. The pressure gradients of the conditional averages for $Tu = 16\%$ are consistent with changes in effective angle of attack of nearly $\pm 5°$ relative to the airfoil's fixed geometric angle of attack of $\alpha = 5°$. This range of effective angle of attack variation is in reasonable agreement with the results of Kay *et al.* [209], who reported standard deviations of the effective angle of

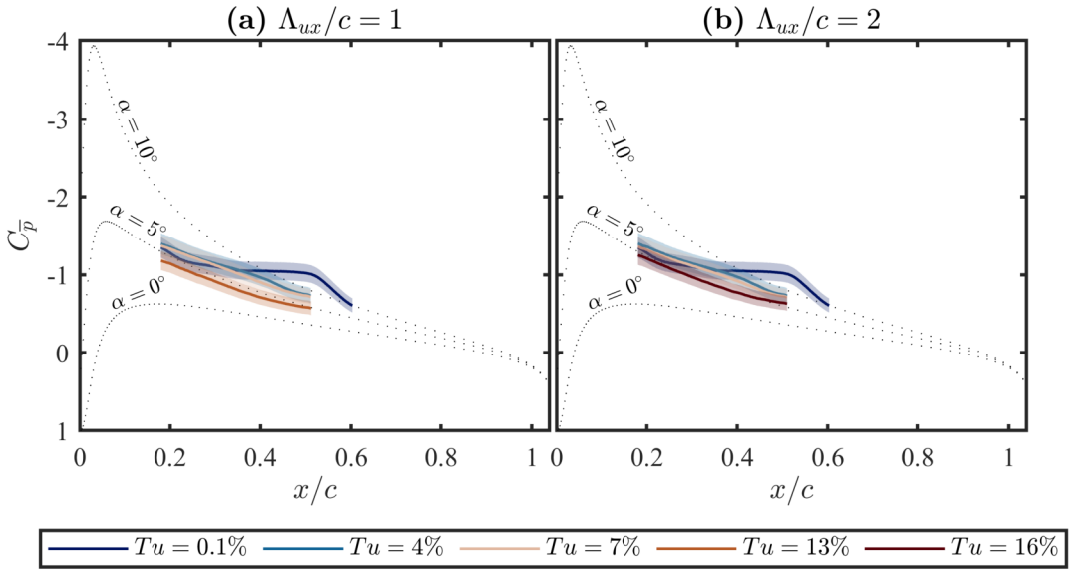


Figure 7.21: Estimated mean surface pressure distributions at $\alpha = 5°$. Shaded areas denote uncertainty (95% confidence). Dotted lines: inviscid surface pressure distributions from XFOIL [192].

attack of 2.4° and 6.9° for $Tu = 5\%$ and 15%, respectively. For $Tu = 4\%$ and 7%, the variations in effective angle of attack in the present study are more difficult to estimate from a comparison with inviscid surface pressure distributions due to the increase in suction caused by the relatively larger LSB forming at these FSTIs. However, the conditional surface pressure distributions from these cases are consistent with the expected increase in effective angle of attack variation with increasing FSTI. Note, the differences in the surface pressure distributions for $\Lambda_{ux}/c = 1$ and 2 at constant FSTI ($Tu = 4\%$ and 7%) are within the experimental uncertainty. This finding implies changes in Λ_{ux}, when Λ_{ux} remains on the order of the airfoil chord, do not substantially affect the effective angle of attack variations experienced by the airfoil.

Figure 7.22 demonstrates that substantial changes in pressure gradient occur at high FSTI that are likely associated with changes in effective angle of attack. When the second POD mode for the cases of elevated FSTI is related to a large-scale change in the edge velocity gradient (cf. Figs. 7.12 and 7.13), and therefore to a large-scale change in surface pressure distribution, the temporal coefficient of the second POD mode (Θ_2) is expected to be correlated to the spatial entropy from the F-POD. This is because stronger adverse pressure gradients lead to earlier boundary layer transition [176], causing an increase in disorder within the flow-field. The relationship between Θ_2 and the spatial entropy from the F-POD is shown in Fig. 7.23 for the cases of elevated FSTI. If the degree of disorder within the flow-field was independent of the second POD mode, the distribution of the data points in each scatter plot would have reflective symmetry about $\Theta_2 = 0$. In all cases, the scatter plots are visibly asymmetric about $\Theta_2 = 0$, and the correlations between Θ_2 and $S_{s,P}$ are significant at a 95% confidence level as verified by statistical P-value evaluation. The

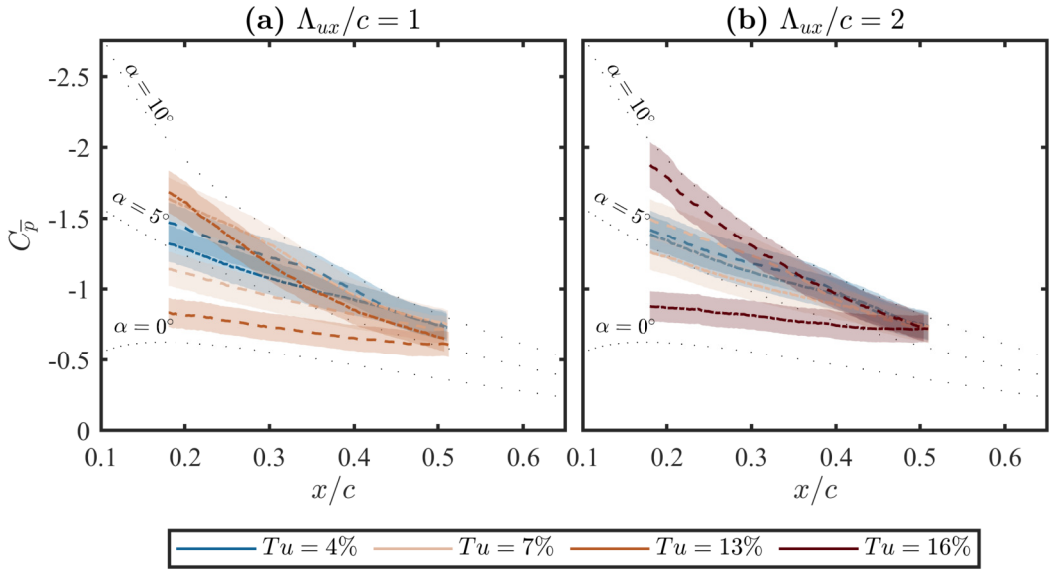


Figure 7.22: Estimated conditional surface pressure distributions at $\alpha = 5°$. Dashed lines: conditional average of $\Theta_2 < \overline{\Theta_2} - S_{\Theta_2}$, dash-dotted lines: conditional average of $\Theta_2 > \overline{\Theta_2} + S_{\Theta_2}$, dotted lines: inviscid surface pressure distributions from XFOIL [192].

sign of the correlation coefficients ($\rho_{\Theta_2 S_{s,F}}$) vary according to the sign of the spatial modes, but are all consistent with increasing spatial entropy with increasing adverse pressure gradient when accounting for the sign of the spatial modes (cf. Fig. 7.12 for $\Lambda_{u,x}/c = 1$). Weaker but still statistically significant correlations were found directly between Θ_2 and x_t, consistent with the tendency for earlier transition during periods of stronger adverse pressure gradient. Thus, the observed correlations between Θ_2 and the spatial entropy suggest that the variations in effective angle of attack caused by large-scale free-stream turbulence are linked to the relatively large variations in transition location and boundary layer thickness observed at high FSTI.

The prevalent effect of angle of attack fluctuations compared to that of the velocity magnitude is consistent with the much higher sensitivity of the transition process to comparable relative changes in angle of attack than chord Reynolds number for quasi-steady conditions [74, 244]. For example, the data of Boutilier & Yarusevych [74] indicate that for a NACA 0018 operating at $\mathrm{Re}_c = 1 \times 10^5$ and $\alpha = 5°$, a 50% increase in Re_c would cause a $0.05c$ upstream movement in transition location, compared to a $0.1c$ upstream movement for a 50% increase in angle of attack. Furthermore, the inferred relative fluctuations in angle of attack at high FSTI are substantially higher than those in chord Reynolds number. For example, at $Tu = 16\%$, $\Lambda_{ux}/c = 2$, the relative fluctuations in effective chord Reynolds number are on the order of 10%. In contrast, an order of $0.1\overline{u_\infty}$ fluctuations in vertical velocity component correspond to approximately $\arctan(0.1) \approx 6°$ fluctuations in the angle of attack (i.e., $\sim 100\%$ of the geometric angle of attack). Thus, the relative fluctuations in angle of attack are an order of magnitude higher than those in Reynolds number for this test case.

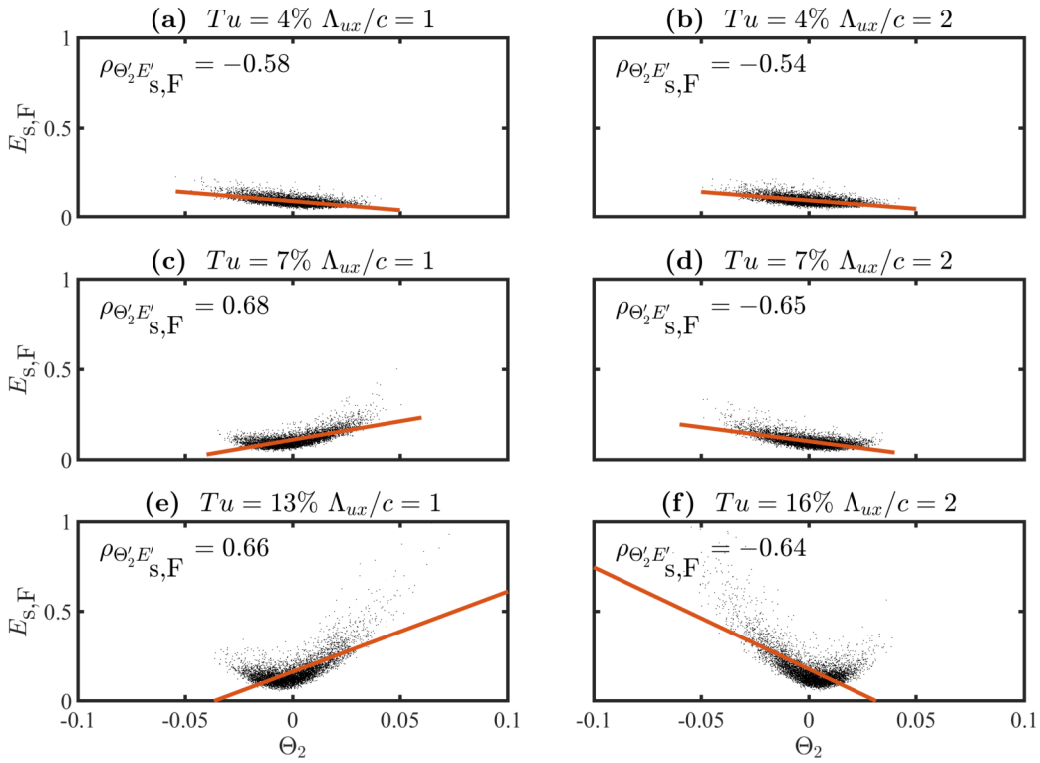


Figure 7.23: Correlation between the temporal coefficient of the second mode Θ_2 and spatial entropy $E_{s,F}$ from F-POD. Red lines show best linear fit.

7.4 Concluding Remarks

Wind tunnel tests were performed on a NACA 0018 airfoil model operating at a chord Reynolds number of $\mathrm{Re}_c = 7.0 \times 10^4$. Free-stream turbulence was generated using an active turbulence grid at intensities of up to $Tu = 16\%$. The integral length scale of the elevated free-stream turbulence was fixed at $\Lambda_{ux}/c = 1$ and 2. The mean aerodynamic loads on the airfoil were measured using a force balance and the velocity field at the midspan of the airfoil on the suction surface was measured using two-component PIV at angles of attack of $\alpha = 5°$ and 12°.

A laminar separation bubble formed on the airfoil in the clean flow at $\alpha = 5°$. The LSB became thinner as the FSTI was increased. Although mean reverse flow was not detected for $Tu = 7\%$, LSB formation likely persisted at this level of FSTI since a local maximum of the shape factor occurred in the vicinity of the mean transition location. Evidence of this LSB was also seen in the mean and fluctuating velocity fields, which exhibited features consistent with those observed in the reattachment region of the LSB in the clean flow. Furthermore, a spectral peak consistent with vortex shedding from the separated shear layer was observed in the wall-normal velocity fluctuations for $Tu = 7\%$. At $Tu = 13\%$, the FSTI was sufficiently high that these features of LSB formation were no longer seen. However, a

local maximum in the shape factor persisted at $Tu = 13\%$. The spatial POD modes of the measured velocity fields indicated that the most energetic coherent structures in the clean flow were those formed from roll-up of the separated shear layer. With increasing FSTI, the modes related to shear layer roll-up vortices were progressively superseded in relative energy content by modes containing structures with relatively larger streamwise length scales. These modes showed similarity with elongated streaks typical of bypass transition and relatively large-scale modulations of the outer flow velocity.

At $\alpha = 12°$, the airfoil was stalled in the clean flow. Increasing the FSTI caused the separated shear layer to reattach, leading to the formation of an LSB with measurable reverse flow. Due to the stronger adverse pressure gradient at the higher angle of attack, the LSB formed sufficiently far upstream that it was not completely eliminated by bypass transition and evidence of LSB formation at $Tu = 13\%$ was found in the mean and fluctuating velocity fields for $\alpha = 12°$. The persistence of the LSB at an FSTI of $Tu = 13\%$ is notable because this FSTI is substantially higher than the levels of FSTI whose effects on LSBs have been studied previously [e.g., 72, 105, 175, 176].

Consistent with prior studies of the effects of free-stream turbulence on airfoil performance at aerodynamically low-Reynolds numbers [e.g., 106, 146, 206, 208], elevated free-stream turbulence increased the stall angle and maximum lift coefficient relative to the clean flow because of an advancement of the mean boundary layer transition location. At moderate angles of attack, free-stream turbulence decreased the lift coefficient relative to the clean flow due to suppression of the suction surface LSB.

Despite the expected and observed upstream advancement of the mean boundary layer transition location with increasing FSTI, at the large integral length scales ($\Lambda_{ux} \sim c$) considered in this study, increasing the FSTI caused notable intermittent periods of substantially delayed transition at $\alpha = 5°$. In some of these periods, the boundary layer remained laminar over a majority of the suction surface. This observation highlights the importance of both the intensity and length scale of free-stream turbulence on the boundary layer development. The spatial entropy of the POD modes of measured velocity profiles was used to identify the instantaneous location of boundary layer transition. The variations in instantaneous transition location became greater as the FSTI was increased, leading to a reduction in the slope of the intermittency factor. Although the mean flow was attached to the suction surface for elevated FSTI at $\alpha = 12°$, periods of intermittent massive separation were observed to occur for $Tu = 13\%$ at this angle of attack. At both angles of attack investigated with PIV measurements, the spatial entropy of the entire field of view was demonstrated to provide an indication of the spatial extent of turbulent flow.

The correlation between the observed instantaneous variations in the boundary layer development and oncoming velocity magnitude fluctuations in the free-stream was investigated. However, no significant correlation was found between large-scale variations in oncoming velocity magnitude and the boundary layer transition process. In contrast, variations in the spatial extent of turbulence in the boundary layer were linked to changes in effective angle of attack caused by oncoming large-scale coherent structures. This was demonstrated through the correlation between the temporal coefficient of the second POD mode, which described the streamwise pressure gradient, and the spatial entropy of the velocity field. Increases in

the streamwise adverse pressure gradient, expected to occur during increases in effective angle of attack, were correlated with higher spatial entropy, indicating earlier transition. Thus, large-scale fluctuations in effective angle of attack likely cause substantial variations of the transition location on the suction surface of the airfoil when $\Lambda_{ux} \sim c$. By comparing the surface pressure coefficient distributions estimated from PIV measurements to those calculated for inviscid flow, it was estimated that the effective angle of attack undergoes fluctuations with an amplitude of more than 5° at the highest levels of FSTI tested. These fluctuations in effective angle of attack lead to intermittent massive separation at pre-stall angles of attack, which reduces airfoil performance relative to lower FSTIs.

Changing the integral length scale from $\Lambda_{ux}/c = 1$ to 2 had a negligible effect on the mean flow fields, the lift and drag coefficients, and the magnitude of the variations in effective angle of attack. This is in contrast with previous studies at smaller integral length scales ($\Lambda_{ux} \sim 0.1c$), which have reported measurable changes in pre-stall aerodynamic performance [106] and boundary layer disturbance growth rates [105] with relatively small changes in integral length scale. This suggests that the transition process is more sensitive to changes in integral length scale when $\Lambda_{ux} \ll c$, but is less so when $\Lambda_{ux} \sim c$. However, in the present experiments, changing the integral length scale changed the frequency at which variations about the mean flow occurred. Thus, incoming flow disturbances with characteristic lengths on the order of the airfoil chord do not directly affect boundary layer transition through the receptivity process, but rather through variations in global airfoil operating conditions.

Chapter 8

Conclusions & Recommendations

The most important findings are summarised and recommendations for future research are provided.

Motivated by the identified knowledge gap between steady, two-dimensional flows in the LSB literature and the unsteady, three-dimensional flows relevant to low-Reynolds number devices, a series of wind tunnel experiments were performed on airfoils and finite wings in unsteady operating conditions. The objectives of these experiments, as outlined in Chapter 1, are repeated here and the progress towards achieving each objective is summarised. Limitations of the present study are also identified, and recommendations for future work are given.

Objective 1: Characterise LSB structure and shear layer transition dynamics during LSB formation and bursting transients on a lifting surface during a change in free-stream velocity magnitude or angle of attack.

The experiments discussed in Chapter 4 focused on LSB formation and bursting caused by a change in free-stream velocity magnitude, whereas the experiments discussed in Chapter 6 focused on LSB formation and bursting caused by a change in angle of attack. Additionally, the LSB formation and bursting transients caused by a change in free-stream velocity were compared and contrasted with those caused by a change in angle of attack in Chapter 6.

In Chapter 4, a two-dimensional airfoil geometry was approximated using an airfoil model that spanned the entire width of the wind tunnel test section. The airfoil was placed at an angle of attack of 6° and subjected to ramp changes in free-stream velocity between limiting chord Reynolds numbers of 4.0×10^4 and 6.0×10^4, at which the flow over the airfoil was massively separated or formed a short LSB, respectively. The temporal development of the suction surface boundary layer during the ramp changes in free-stream velocity was investigated using PIV measurements. The transient changes in LSB structure during the ramp changes in free-stream velocity were characterised in terms of the movement of the dividing streamline and the evolution of the boundary layer thickness. The transient dynamics of the transition process during changes in free-stream velocity were characterised in terms of the development of the Reynolds shear stress along the separated shear layer and the changes in the frequencies and wavenumbers of shear layer disturbances.

The duration of the ramp changes in free-stream velocity in Chapter 4 was approximately 50 convective time units, rendering the temporal acceleration of the free-stream negligible compared to the spatial velocity gradients of the flow near the airfoil. Although the ramp up in free-stream velocity took approximately 50 convective time units, the most notable changes to the flow field during the LSB formation process occurred over a shorter time period of approximately 20 convective time units within which reattachment commenced and the newly formed LSB decreased in length. During this period, there was a relatively rapid decrease in separation angle and increase in magnitude of Reynolds shear stress in the separated shear layer. For the decreasing ramp change in free-stream velocity, the initially present LSB gradually expanded before bursting and bifurcating into a massively separated flow. The cessation of reattachment was accompanied by a decrease in the magnitude of Reynolds shear stresses. Before settling to the final massively separated flow state, large oscillations in the separation angle were observed. Consequently, the time required to reach the final statistically stationary flow state after LSB bursting was approximately 1.5 times

longer than that required for LSB formation. The longer duration of the transient leading to stall is consistent with the results of previous studies on transient flow development on lifting surfaces [e.g., 25, 34, 180]. During LSB formation and bursting transients caused by a ramp change in free-stream velocity, there was a continuous gradual change in the frequencies and wavenumbers of the most amplified disturbances in the separated shear layer.

In Chapter 6, a finite wing and two-dimensional airfoil at a chord Reynolds number of 1×10^5 were subject to ramp changes in angle of attack between 10° and 13°, at which the flow over both models formed a short LSB or was massively separated, respectively. The finite wing and airfoil models in Chapter 6 were also subject to ramp changes in free-stream velocity between $\mathrm{Re}_c = 8 \times 10^4$ and 1×10^5 at a constant angle of attack of 10°. At the lower Reynolds number, the flow was massively separated on both models. PIV measurements were performed to characterise the suction surface flow development during the ramp changes in free-stream velocity and angle of attack. The transient dynamics of the transition process during changes in free-stream velocity and angle of attack were characterised in terms of the development of the Reynolds shear stress along the separated shear layer and the changes in the frequencies of shear layer disturbances. Direct force measurements were also used in Chapter 6 to relate the flow-field development to the aerodynamic loads.

In Chapter 6, it was found that the time histories of the lift coefficients for LSB bursting during increases in angle of attack were similar to those reported from other experiments at higher Reynolds numbers. This suggests that the details of the transition process do not have a substantial influence on the loading after LSB bursting occurs. However, the dynamics of transition in the LSB are an important factor in determining the conditions under which bursting initiates. The delay between the passing of the static stall or reattachment conditions and the onset of LSB bursting or formation, respectively, was found to be sensitive to the degree to which the static stall or reattachment conditions were exceeded. Angle of attack changes with larger angular displacement were found to reduce the variance in the timing of bursting or reattachment. This points to a reduced sensitivity of LSB formation and bursting to minute random disturbances when subjected to larger amplitude variations in operating conditions.

In Chapter 6, a comparison of the LSB formation and bursting processes was made between ramp changes in free-stream velocity and ramp changes in angle of attack with durations of approximately 75 convective time units for both types of changes in operating conditions. Differences and similarities in the time history of the aerodynamic loads, ensemble-averaged LSB structure, and shear layer dynamics were identified between the two types of transient changes in operating conditions. For both types of changes in operating conditions, hysteresis was observed in the transient lift coefficients. During the ramp increase in angle of attack, the lift coefficient initially exceeded the maximum lift coefficient attained in steady conditions, as expected for a dynamically pitching lifting surface [55]. During the overshoot of the lift coefficient, the LSB on the suction surface persisted temporarily, moving upstream and shortening while the frequency of vortex shedding from the separated shear layer increased. Subsequently, there was a decrease in the magnitude of Reynolds

shear stress in the separated shear layer as the LSB expanded and burst. In contrast, LSB bursting during a decrease in Reynolds number did not produce a lift overshoot and there was a monotonic downstream movement in the location of reattachment, decrease in vortex shedding frequency and Reynolds shear stress, and expansion of the LSB prior to bursting. However, the LSB formation process was similar for both types of changes in operating conditions, beginning with an upstream movement of transition and increase in Reynolds shear stress, before the establishment and upstream movement of reattachment. The initiation of reattachment coincided with an increase in the rate of change of the lift coefficient. For both types of transients leading to LSB formation, the LSB reached its final location within 15 convective time units of the initiation of reattachment.

Although the initial conditions for the angle of attack changes and free-stream velocity changes that were compared in Chapter 6 were identical, the stall conditions for the two types of transients were different in terms of the specific chord Reynolds number and angle of attack where the static stall conditions were passed. If the angle of attack for the ramp change in Reynolds number were increased, the static stall Reynolds number and angle of attack for the two types of transients could be matched. This equivalency would facilitate a more direct comparison between the two types of transients, and such measurements may be useful for developing generalised LSB bursting criteria that are valid for various types of changes in operating conditions.

Objective 2: Quantify the influence of three-dimensional end effects on the aerodynamic forces produced during LSB formation and bursting, and relate these forces to the LSB flow field development.

In Chapter 5, a two-dimensional airfoil and finite wing at an equivalent angle of attack were both subjected to ramp changes in free-stream velocity so that the influence of the different end conditions on the LSB formation and bursting transients could be studied. In Chapter 6, the influence of end effects on LSB formation and bursting transients for a two-dimensional airfoil and finite wing were investigated during ramp changes in angle of attack and compared to the end effects observed during ramp changes in free-stream velocity.

The experiments discussed in Chapter 5 employed simultaneous PIV and direct force measurements to investigate the transient flow development and aerodynamic loading on an airfoil and wing model at an equivalent effective angle of attack of 5° during ramp changes in free-stream velocity between chord Reynolds numbers of 5.4×10^4 and 7.4×10^4. At these Reynolds numbers, the flow over the airfoil and wing was massively separated, or formed a short LSB, respectively. A comparison of the results from the airfoil and wing model enabled the effect of the presence of the wing tip on the transient loading to be quantified. PIV measurements performed at multiple locations along the span of the models were used to characterise the spanwise extent of the LSB during formation and bursting transients and the spanwise variations in shear layer disturbances that lead to transition.

The experiments in Chapter 5 revealed that during LSB formation on the wing and airfoil, reattachment occurred first near the ends of the models, and lastly near the midspan.

The accelerated LSB formation near the side-walls of the airfoil and the root of the wing was likely related to higher disturbance amplitudes caused by the turbulent side-wall boundary layers leading to earlier transition of the separated shear layer. The accelerated reattachment near the tip was attributed to the smaller effective angle of attack near the wing tip. The spanwise progression of LSB bursting was essentially the opposite of LSB formation. During bursting, the region of massive separation expanded from near the midspan towards the model ends. The spanwise progression of LSB bursting and reattachment was more gradual on the wing model than on the airfoil, and this was also reflected in the rate of change of the lift coefficient for the wing, which was more gradual than that of the airfoil. Whereas the loading on the airfoil deviated substantially from quasi-steady loading during ramp changes in free-stream velocity, the loading on the wing did not substantially deviate from quasi-steady loading during ramp changes in free-stream velocity at relatively low angles of attack ($\lesssim 5°$). During changes in free-stream velocity at higher angles of attack or during changes in angle of attack, more substantial deviations from quasi-steady loading were observed for the wing, although these deviations were not as great as those of the airfoil. The relatively more gradual changes in flow field development and aerodynamic loads observed for the wing were attributed to the spanwise variation in effective angle of attack on the wing, which enables a short LSB and a long LSB or massively separated flow to coexist at different spanwise locations during changes in operating conditions. The observed coexistence of both short and long LSBs at different spanwise locations on the wing indicates that three-dimensional effects need to be considered when applying LSB bursting criteria to finite wings.

In Chapter 6, the influence of three-dimensional end effects on LSB formation and bursting during a ramp change in angle of attack between 10° and 13° was studied on a two-dimensional airfoil and finite wing at a chord Reynolds number of 1×10^5. The LSB formation and bursting transients were also studied during a ramp change in free-stream velocity between chord Reynolds numbers of 8×10^4 and 1×10^5 at a constant angle of attack of 10°. The spanwise progression of LSB formation and bursting was similar for each type of model during both changes in free-stream velocity and angle of attack, except that the spanwise progression of massive separation was more gradual during decreases in Reynolds number than during increases in angle of attack.

In this thesis, only one finite wing geometry was considered with a relatively low aspect ratio of 2.5, meaning that the portion of the span over which three-dimensional effects were significant was relatively large compared to higher aspect ratios. On the aspect ratio 2.5 wing, LSB bursting was observed to initiate near the midspan of the wing. On wings of greater aspect ratio where root effects influence a relatively smaller proportion of the span, it is expected that the bursting process would initiate closer to the wing root than to the midspan because of the increase in effective angle of attack at the wing root. Future work should consider the effect of aspect ratio on the dynamics of LSB formation and bursting. In addition to the aspect ratio, wing plan-form also influences the spanwise variation in effective angle of attack. Future work should also investigate how wing plan-form affects the severity of the changes in aerodynamic loads during transient changes in operating conditions.

Objective 3: Quantify the influence of the time and length scale of an imposed change in operating conditions on boundary layer transition dynamics.

In Chapter 6, the influence of the time scale of an imposed change in operating conditions was studied by varying the non-dimensional pitch rate of the ramp changes in angle of attack within the range $3 \times 10^{-5} \leq \dot{\alpha}c/2u_\infty \leq 5 \times 10^{-3}$. For the changes in angle of attack considered in Chapter 6, a decrease in the duration of time between the passing of the static reattachment or stall angle and the onset of LSB bursting was observed with increasing pitch rate, consistent with prior studies of dynamic stall and reattachment [e.g., 63, 90]. The minimum time required for the LSB to form or burst was on the order of 10 convective time units, consistent with the time scales required for DSV formation [e.g., 187]. As the pitch rate was increased, the LSB persisted to higher angles of attack and became shorter prior to bursting. There was also a greater over- or under-shoot in the lift coefficient with increasing pitch rate relative to the quasi-steady lift coefficients during LSB bursting or formation, respectively. This overshoot is also consistent with previous studies at higher Reynolds numbers [63, 64]. The consistency of the results in this thesis with those obtained in different facilities at different Reynolds numbers suggests that the details of the boundary layer and separated shear layer transition process do not substantially affect the time-history of the aerodynamic loads once the LSB has burst or formed during a change in angle of attack. Also, it was found that the rate of change of the angle of attack had a negligible influence on the spanwise progression of LSB formation and bursting on the finite wing and airfoil models studied in Chapter 6.

Although this thesis considered variations in the time scales of imposed unsteadiness for angle of attack changes, the influence of the rate of change of the free-stream velocity was not investigated systematically because of the limited free-stream accelerations that could be produced by the wind tunnel fan. These limits constrained the changes in free-stream velocity to quasi-steady changes, with accelerations was less than $\pm 0.015 u_\infty^2/c$. Therefore, it was not possible to investigate LSB formation and bursting with strong free-stream pressure gradients, which are expected to occur during rapid large-scale gusts in atmospheric turbulence in urban environments [e.g., 245]. Future work should consider the effect of such pressure gradients on transient LSB dynamics. Time-resolved surface pressure measurements performed by Greenblatt *et al.* [85] suggest that rapidly increasing free-stream velocities may lead to LSB bursting due to delayed transition, opposite to the flow behaviour observed during the quasi-steady free-stream accelerations of the present study.

The effective length scales of the controlled ramp changes in free-stream velocity and angle of attack studied in this thesis can be estimated from the product of their time duration and the free-stream velocity, and were limited to $\gtrsim 10c$. However, the effects of unsteadiness with smaller spatial scales on the order of c can be inferred from the experiments discussed in Chapter 7 that were performed in high-intensity free-stream turbulence with integral length scales of $\lambda_{ux}/c = 1$ and 2. Although the frequency of variations in the transition location was dependent on the integral length scale, no substantial changes in mean flow field development and aerodynamic loading were observed between integral length scales of $\lambda_{ux}/c = 1$ and 2. This suggests that the primary effect of unsteadiness in the free-stream

with length scales on the order of the airfoil chord, like those of larger length scales, is to change the instantaneous operating conditions of the airfoil, rather than to directly affect boundary layer transition through the receptivity process.

Objective 4: Correlate oncoming free-stream disturbances in turbulent free-stream environments to variations in boundary layer development and the resulting aerodynamic forces.

In Chapter 7, an active turbulence grid was used to generate free-stream turbulence intensities of up to 16% with integral length scales on the order of the airfoil model chord, which are representative of the conditions that small aircraft and small wind turbines are expected to encounter in the atmosphere. PIV measurements of the suction surface boundary layer development over an airfoil model in the turbulent free-stream were performed for angles of attack of 5° and 12° at a Reynolds number of 7×10^4. Simultaneously with the PIV measurements, a hotwire anemometer placed upstream of the airfoil was used to characterise the oncoming disturbances so that variations in boundary layer development could be linked to free-stream velocity fluctuations.

Elevated FSTI caused a reduction in the length and thickness of the LSB relative to the clean flow. Under conditions where the separated laminar shear layer did not reattach in the clean flow, elevated FSTI enabled reattachment. Evidence of LSB formation was observed for FSTIs of up to 13%. POD analysis of the velocity field measurements showed that, as the FSTI was increased, the relative energy content of streaky structures associated with bypass transition progressively increased. As the FSTI was increased, larger variations in the location of boundary layer transition were observed. At $Tu = 13\%$, laminar flow occasionally persisted across the entire field of view. These variations in transition location were linked to large-scale fluctuations in oncoming velocity direction. Specifically, increases in effective angle of attack were correlated with expedited boundary layer transition.

In this experimental set-up, simultaneous measurement of aerodynamic forces and PIV was impractical because large amplitude vibrations of the airfoil model at elevated FSTI caused notable model vibrations. This problem was remedied by supporting the airfoil at both ends. However, direct force measurements require the model to be simply supported by only the load cell. Consequently, the only force measurements that were obtained were not during PIV measurements. This limited the conclusions that can be made about the relationship between the flow development and forces to a statistical comparison only. Furthermore, the increased amplitude of vibrations when the model was simply supported for force measurements may alter the flow development from that observed during the PIV measurements, because low-Reynolds number flows are known to be sensitive to model vibrations [e.g., 246]. It is recommended that future experiments at elevated FSTI use a more rigidly mounted airfoil to alleviate these problems caused by model vibration.

The use of a single-wire hotwire anemometer limited the characterisation of oncoming disturbances to changes in velocity magnitude only. It is recommended that future work be undertaken using a directionally sensitive velocimetry technique, such as x-wire hotwire anemometry, to understand in more detail how instantaneous changes in flow direction

affect the boundary layer development in conditions of elevated FSTI. Furthermore, a wider range of free-stream integral length scales should be investigated, because the scale above which the boundary layer ceases to be receptive to vortical structures in the free-stream remains unknown.

Letter(s) of Copyright Permission

SPRINGER NATURE LICENSE
TERMS AND CONDITIONS

May 06, 2025

This Agreement between Connor Toppings ("You") and Springer Nature ("Springer Nature") consists of your license details and the terms and conditions provided by Springer Nature and Copyright Clearance Center.

License Number	6023061190656
License date	May 06, 2025
Licensed Content Publisher	Springer Nature
Licensed Content Publication	Experiments in Fluids
Licensed Content Title	Transient dynamics of laminar separation bubble formation and bursting
Licensed Content Author	Connor Toppings et al
Licensed Content Date	Feb 23, 2023
Type of Use	Thesis/Dissertation
Requestor type	academic/university or research institute
Format	electronic
Portion	full article/chapter
Will you be translating?	no

References

[1] Toppings, C. E. & Yarusevych, S. 2023 Transient dynamics of laminar separation bubble formation and bursting. *Experiments in Fluids* **64** (3), 57. DOI. ↩

[2] Toppings, C. E. & Yarusevych, S. 2024 Laminar separation bubble formation and bursting on a finite wing. *Journal of Fluid Mechanics* **986**, A26. DOI. ↩

[3] Toppings, C. E. & Yarusevych, S. 2025 Transient dynamics of stall and reattachment at low Reynolds number. *Journal of Fluid Mechanics* **1011**, 1–35. DOI. ↩

[4] Crameri, F. Scientific colour maps. 2018. DOI. ↩

[5] Crameri, F., Shephard, G. E., & Heron, P. J. 2020 The misuse of colour in science communication. *Nature Communications* **11** (1), 1–10. DOI. ↩

[6] Diwan, S. S., Chetan, S. J., & Ramesh, O. N. 2006 On the Bursting Criterion for Laminar Separation Bubbles. In Govindarajan, R., editor, *Fluid Mechanics and its Applications*. Vol. 78, pp. 401–407. Springer Netherlands. DOI. ↩

[7] Gaster, M. 1967 The Structure and Behaviour of Laminar Separation Bubbles. *Tech. rep.* Reports and Memoranda 3595, Aeronautical Research Council, London, pp. 1–33. ↩

[8] Lissaman, P. B. S. 1983 Low-Reynolds-Number Airfoils. *Annual Review of Fluid Mechanics* **15** (1), 223–239. DOI. ↩

[9] Prandtl, L. 1904 Über Flüssigkeitsbewegung bei sehr kleiner Reibung. In *Verhandlungen des III. Internationalen Mathematiker-Kongresses*, Heidelberg. ↩

[10] Schlichting, H. & Gersten, K. 2017 *Boundary-Layer Theory*. 9th ed. Springer Berlin Heidelberg. DOI. ↩

[11] Carmichael, B. H. 1981 Low Reynolds Number Airfoil Survey. *Tech. rep.* NASA CR-165803, Low Energy Transportation Systems, Capistrano Beach, CA. ↩

[12] Mueller, T. J. & DeLaurier, J. D. 2003 Aerodynamics of Small Vehicles. *Annual Review of Fluid Mechanics* **35** (1), 89–111. DOI. ↩

[13] Wood, D. H. 2011 Small Wind Turbines. In *Advances in Wind Energy Conversion Technology*, pp. 195–211. Springer-Verlag. ↩

[14] Hodson, H. P. & Howell, R. J. 2005 The role of transition in high-lift low-pressure turbines for aeroengines. *Progress in Aerospace Sciences* **41** (6), 419–454. DOI. ↩

[15] Diwan, S. S. & Ramesh, O. N. 2009 On the origin of the inflectional instability of a laminar separation bubble. *Journal of Fluid Mechanics* **629**, 263–298. DOI. ↩

[16] Tani, I. 1964 Low-speed flows involving bubble separations. *Progress in Aerospace Sciences* **5**, 70–103. DOI. ↩

[17] Dovgal, A., Kozlov, V., & Michalke, A. 1994 Laminar boundary layer separation: Instability and associated phenomena. *Progress in Aerospace Sciences* **30** (1), 61–94. DOI. ↩

[18] Michelis, T., Yarusevych, S., & Kotsonis, M. 2018 On the origin of spanwise vortex deformations in laminar separation bubbles. *Journal of Fluid Mechanics* **841**, 81–108. DOI. ↩

[19] Yarusevych, S., Sullivan, P. E., & Kawall, J. G. 2009 On vortex shedding from an airfoil in low-Reynolds-number flows. *Journal of Fluid Mechanics* **632**, 245–271. DOI. ↩

[20] Horton, H. P. 1968 *Laminar Separation Bubbles in Two and Three Dimensional Incompressible Flow*. Ph.D. Thesis, University of London, London. ↩

[21] Marxen, O., Lang, M., & Rist, U. 2013 Vortex formation and vortex breakup in a laminar separation bubble. *Journal of Fluid Mechanics* **728**, 58–90. DOI. ↩

[22] Alam, M. & Sandham, N. D. 2000 Direct numerical simulation of 'short' laminar separation bubbles with turbulent reattachment. *Journal of Fluid Mechanics* **403**, 223–250. DOI. ↩

[23] Rodríguez, D., Gennaro, E. M., & Juniper, M. P. 2013 The Two Classes of Primary Modal Instability in Laminar Separation Bubbles. *Journal of Fluid Mechanics* **734**, 1–11. DOI. ↩

[24] Rodríguez, D. & Theofilis, V. 2010 Structural changes of laminar separation bubbles induced by global linear instability. *Journal of Fluid Mechanics* **655**, 280–305. DOI. ↩

[25] Yarusevych, S. & Kotsonis, M. 2017 Steady and transient response of a laminar separation bubble to controlled disturbances. *Journal of Fluid Mechanics* **813**, 955–990. DOI. ↩

[26] Jones, A. R., Cetiner, O., & Smith, M. J. 2022 Physics and Modeling of Large Flow Disturbances: Discrete Gust Encounters for Modern Air Vehicles. *Annual Review of Fluid Mechanics* **54**, 469–493. DOI. ↩

[27] Centiner-Yildirim, O. & Jones, A. R. 2020 Unsteady Aerodynamic Response of Rigid Wings in Gust Encounters. *Tech. rep.* October, NATO Science and Technology Organization, Brussels. ISBN. ↩

[28] Watkins, S., Milbank, J., Loxton, B. J., & Melbourne, W. H. 2006 Atmospheric winds and their implications for microair vehicles. *AIAA Journal* **44** (11), 2591–2600. DOI. ↩

[29] Marxen, O. & Henningson, D. S. 2011 The Effect of Small-Amplitude Convective Disturbances on the Size and Bursting of a Laminar Separation Bubble. *Journal of Fluid Mechanics* **671**, 1–33. DOI. ↩

[30] Horton, H. P. 1969 A semi-empirical theory for the growth and bursting of laminar separation bubbles. *Tech. rep.* 1073, Aeronautical Research Council, London, p. 37. URL. ↩

[31] Kurelek, J. W., Tuna, B. A., Yarusevych, S., & Kotsonis, M. 2021 Three-Dimensional Development of Coherent Structures in a Two-Dimensional Laminar Separation Bubble. *AIAA Journal* **59** (2), 493–505. DOI. ↩

[32] Post, M. L. & Corke, T. C. 2006 Separation control using plasma actuators: Dynamic stall vortex control on oscillating airfoil. *AIAA Journal* **44** (12), 3125–3135. DOI. ↩

[33] Corke, T. C., Bowles, P. O., He, C., & Matlis, E. H. 2011 Sensing and control of flow separation using plasma actuators. *Philosophical Transactions of the Royal Society A: Mathematical, Physical and Engineering Sciences* **369** (1940), 1459–1475. DOI. ↩

[34] Benard, N., Cattafesta, L. N., Moreau, E., Griffin, J., & Bonnet, J. P. 2011 On the benefits of hysteresis effects for closed-loop separation control using plasma actuation. *Physics of Fluids* **23** (8). DOI. ↩

[35] Sato, M., Nonomura, T., Okada, K., Asada, K., Aono, H., Yakeno, A., Abe, Y., & Fujii, K. 2015 Mechanisms for laminar separated-flow control using dielectric-barrier-discharge plasma actuator at low Reynolds number. *Physics of Fluids* **27** (11). DOI. ↩

[36] Kurelek, J. W., Kotsonis, M., & Yarusevych, S. 2018 Transition in a separation bubble under tonal and broadband acoustic excitation. *Journal of Fluid Mechanics* **853**, 1–36. DOI. ↩

[37] Carusone, A., Sicot, C., Bonnet, J. P., & Borée, J. 2021 Transient dynamical effects induced by single-pulse fluidic actuation over an airfoil. *Experiments in Fluids* **62** (2), 1–16. DOI. ↩

[38] Ho, H. H., Shirinzad, A., Essel, E. E., & Sullivan, P. E. 2024 Synthetic Jet Actuators for Active Flow Control: A Review. *Fluids* **9** (12), 1–35. DOI. ↩

[39] Munson, B. R., Okiichi, T. H., Huebsch, W. W., & Rothmayer, A. P. 2013 *Fundamentals of Fluid Mechanics*. 7th ed. John Wiley & Sons. ISBN. ↩

[40] Jeong, J. & Hussain, F. 1995 On the identification of a vortex. *Journal of Fluid Mechanics* **285**, 69–94. DOI. ↩

[41] Kaushik, M. 2019 *Finite Wing Theory*. Springer Singapore, pp. 145–168. DOI. ↩

[42] Gudmundsson, S. 2014 The Anatomy of the Wing. In *General Aviation Aircraft Design*, part 9, pp. 299–399. Elsevier. DOI. ↩

[43] Bertin, J. J. & Smith, M. L. 1979 Characteristic Parameters for Airfoil and Wing Aerodynamics. In *Aerodynamics for Engineers*, part 3, pp. 76–105. ↩

[44] Kretov, A. & Tiniakov, D. 2022 Evaluation of the Mass and Aerodynamic Efficiency of a High Aspect Ratio Wing for Prospective Passenger Aircraft. *Aerospace* **9** (9), 1–17. DOI. ↩

[45] Spall, R. E., Phillips, W. F., & Pincock, B. B. 2013 Numerical analysis of multiple, thin-sail geometries based on Prandtl's lifting-line theory. *Computers and Fluids* **82**, 29–37. DOI. ↩

[46] Svorcan, J., Wang, J. M., & Griffin, K. P. 2022 Current state and future trends in boundary layer control on lifting surfaces. *Advances in Mechanical Engineering* **14** (7), 1–23. DOI. ↩

[47] Awasthi, M., Moreau, D., & Doolan, C. 2018 Flow structure of a low aspect ratio wall-mounted airfoil operating in a low Reynolds number flow. *Experimental Thermal and Fluid Science* **99**, 94–116. DOI. ↩

[48] Houghton, E., Carpenter, P., Collicott, S. H., Valentine, D. T., Houghton, E., Carpenter, P., Collicott, S. H., & Valentine, D. T. 2013 Chapter 5 – Wing Theory. In *Aerodynamics for Engineering Students*, pp. 269–347. DOI. ↩

[49] Toppings, C. E. 2021 *Laminar Separation Bubble Dynamics on a Finite Wing*. Master Thesis, University of Waterloo. ↩

[50] Currie, I. 1993 *Fundamental Mechanics of Fluids*. 2nd ed. McGraw-Hill. ISBN. ↩

[51] Melvill Jones, B. 1934 Stalling. *The Journal of the Royal Aeronautical Society* **38** (285), 753–770. DOI. ↩

[52] Ericsson, L. E. & Reding, J. P. 1988 Fluid mechanics of dynamic stall part I. Unsteady flow concepts. *Journal of Fluids and Structures* **2** (1), 1–33. DOI. ↩

[53] McCune, J. E. & Tavares, T. S. 1993 Perspective: Unsteady Wing Theory—The Karman/Sears Legacy. *Journal of Fluids Engineering* **115** (4), 548–560. DOI. ↩

[54] Von Kármán, T. & Sears, W. R. 1938 Airfoil Theory for Non-Uniform Motion. *Journal of the Aeronautical Sciences* **5** (10), 379–390. DOI. ↩

[55] McCroskey, W. J. 1981 The phenomenon of dynamic stall. *Tech. rep.* NASA-TM-81264, NASA Ames Research Center, Moffat Field, CA. ↩

[56] McCroskey, W. J. 1982 Unsteady Airfoils. *Annual Review of Fluid Mechanics* **14** (1), 285–311. DOI. ↩

[57] Mulleners, K. & Raffel, M. 2013 Dynamic stall development. *Experiments in Fluids* **54** (2), 1469. DOI. ↩

[58] Corke, T. C. & Thomas, F. O. 2015 Dynamic stall in pitching airfoils: Aerodynamic damping and compressibility effects. *Annual Review of Fluid Mechanics* **47**, 479–505. DOI. ↩

[59] Carr, L. W., McAlister, K. W., & McCroskey, W. J. 1977 Analysis of the development of dynamic stall based on oscillating airfoil experiments. *Tech. rep.* NASA TN D-8382, pp. 1–99. ISBN. ↩

[60] Visbal, M. R. & Garmann, D. J. 2019 Comparison of pitch versus plunge maneuvers of a finite wing. *AIAA Aviation 2019 Forum* (June), 1–17. DOI. ↩

[61] Aihara, Y., Koyama, H., & Murashige, A. 1985 Transient aerodynamic characteristics of a two-dimensional airfoil during stepwise incidence variation. *Journal of Aircraft* **22** (8), 661–668. DOI. ↩

[62] Gupta, R. & Ansell, P. J. 2019 Unsteady flow physics of airfoil dynamic stall. *AIAA Journal* **57** (1), 165–175. DOI. ↩

[63] Kiefer, J., Brunner, C. E., Hansen, M. O., & Hultmark, M. 2022 Dynamic stall at high Reynolds numbers induced by ramp-type pitching motions. *Journal of Fluid Mechanics* **938**, 1–22. DOI. ↩

[64] Green, R. B. & Galbraith, R. A. M. 1995 Dynamic recovery to fully attached aerofoil flow from deep stall. *AIAA Journal* **33** (8), 1433–1440. DOI. ↩

[65] Sheng, W., Galbraith, R. A. M., & Coton, F. N. 2007 Return from Aerofoil Stall During Ramp-Down Pitching Motions. *Journal of Aircraft* **44** (6), 1856–1864. DOI. ↩

[66] Kachanov, Y. S. 1994 Physical Mechanisms of Laminar-Boundary-Layer Transition. *Annual Review of Fluid Mechanics* **26** (1), 411–482. DOI. ↩

[67] Saric, W. S., Reed, H. L., & Kerschen, E. J. 2002 Boundary-Layer Receptivity to Freestream Disturbances. *Annual Review of Fluid Mechanics* **34** (1), 291–319. DOI. ↩

[68] Klebanoff, P. S., Tidstrom, K. D., & Sargent, L. M. 1962 The three-dimensional nature of boundary-layer instability. *Journal of Fluid Mechanics* **12** (1), 1–34. DOI. ↩

[69] Saric, W. S., Carpenter, A. L., & Reed, H. L. 2011 Passive control of transition in three-dimensional boundary layers, with emphasis on discrete roughness elements. *Philosophical Transactions of the Royal Society A: Mathematical, Physical and Engineering Sciences* **369** (1940), 1352–1364. DOI. ↩

[70] Lord Rayleigh. 1879 On the Stability, or Instability, of certain Fluid Motions. *Proceedings of the London Mathematical Society* **s1-11** (1), 57–72. DOI. ↩

[71] Michelis, T., Kotsonis, M., & Yarusevych, S. 2018 Spanwise flow development within a laminar separation bubble under natural and forced transition. *Experimental Thermal and Fluid Science* **96** (January), 169–179. DOI. ↩

[72] Istvan, M. S. & Yarusevych, S. 2018 Effects of free-stream turbulence intensity on transition in a laminar separation bubble formed over an airfoil. *Experiments in Fluids* **59** (3), 52. DOI. ↩

[73] Hosseinverdi, S. & Fasel, H. F. 2019 Numerical investigation of laminar–turbulent transition in laminar separation bubbles: the effect of free-stream turbulence. *Journal of Fluid Mechanics* **858**, 714–759. DOI. ↩

[74] Boutilier, M. S. H. & Yarusevych, S. 2012 Parametric study of separation and transition characteristics over an airfoil at low Reynolds numbers. *Experiments in Fluids* **52** (6), 1491–1506. DOI. ↩

[75] Boutilier, M. S. H. & Yarusevych, S. 2012 Separated shear layer transition over an airfoil at a low Reynolds number. *Physics of Fluids* **24** (8), 084105. DOI. ↩

[76] McCullough, G. B. & Gault, D. E. 1951 Examples of Three Representative Types of Airfoil-Section Stall at Low Speed. *Tech. rep.* NACA TN-2502. DOI. ↩

[77] Ho, C.-M. & Huerre, P. 1984 Perturbed Free Shear Layers. *Annual Review of Fluid Mechanics* **16** (1), 365–422. DOI. ↩

[78] Serna, J. & Lazaro, B. J. 2015 On the bursting condition for transitional separation bubbles. *Aerospace Science and Technology* **44**, 43–50. DOI. ↩

[79] Mueller, T. J. 1985 The influence of laminar separation and transition on low Reynolds number airfoil hysteresis. *Journal of Aircraft* **22** (9), 763–770. DOI. ↩

[80] Lesieur, M. 2008 *Turbulence in Fluids*. Fluid Mechanics and its Applications. Springer Netherlands. DOI. ↩

[81] Thwaites, B. 1949 Approximate Calculation of the Laminar Boundary Layer. *Aeronautical Quarterly* **1** (3), 245–280. DOI. ↩

[82] Mitra, A. & Ramesh, O. N. 2019 New Correlation for the Prediction of Bursting of a Laminar Separation Bubble. *AIAA Journal* **57** (4), 1400–1408. DOI. ↩

[83] Alferez, N., Mary, I., & Lamballais, E. 2013 Study of Stall Development Around an Airfoil by Means of High Fidelity Large Eddy Simulation. *Flow, Turbulence and Combustion* **91** (3), 623–641. DOI. ↩

[84] Ellsworth, R. H. & Mueller, T. J. 1991 Airfoil Boundary Layer Measurements at Low Re in an Accelerating Flow from a Nonzero Velocity. *Experiments in Fluids* **11** (6), 368–374. DOI. ↩

[85] Greenblatt, D., Müller-Vahl, H., & Strangfeld, C. 2023 Laminar separation bubble bursting in a surging stream. *Physical Review Fluids* **8** (1), L012102. DOI. ↩

[86] Matsubara, M. & Alfredsson, P. H. 2001 Disturbance growth in boundary layers subjected to free-stream turbulence. *Journal of Fluid Mechanics* **430**, 149–168. DOI. ↩

[87] Nati, A., de Kat, R., Scarano, F., & van Oudheusden, B. W. 2015 Dynamic pitching effect on a laminar separation bubble. *Experiments in Fluids* **56** (9), 172. DOI. ↩

[88] Brendel, M. & Mueller, T. J. 1988 Boundary-layer measurements on an airfoil at low Reynolds numbers. *Journal of Aircraft* **25** (7), 612–617. DOI. ↩

[89] Wissink, J. G. & Rodi, W. 2003 DNS of a Laminar Separation Bubble in the Presence of Oscillating External Flow. *Flow, Turbulence and Combustion* **71** (1-4), 311–331. DOI. ↩

[90] Rezapour, S. & Mulleners, K. 2025 Dynamic stall reattachment revisited 1–19. arXiv: 2505.12798. URL. ↩

[91] Hoffmann, J. A. 1991 Effects of freestream turbulence on the performance characteristics of an airfoil. *AIAA Journal* **29** (9), 1353–1354. DOI. ↩

[92] Mora, D. O. & Obligado, M. 2020 Estimating the integral length scale on turbulent flows from the zero crossings of the longitudinal velocity fluctuation. *Experiments in Fluids* **61** (9), 1–10. arXiv: 2005.06055. DOI. ↩

[93] Halstead, D. E. 1996 *Boundary layer development in multi-stage low-pressure turbines*. PhD thesis, Iowa State University. ↩

[94] Brandt, L., Schlatter, P., & Henningson, D. S. 2004 Transition in boundary layers subject to free-stream turbulence. *Journal of Fluid Mechanics* **517**, 167–198. DOI. ↩

[95] Morkovin, M. V. 1985 Bypass Transition to Turbulence and Research Desiderata. In *NASA Lewis Research Center Transition in Turbines*. ↩

[96] Zhao, Y. & Sandberg, R. D. 2020 Bypass transition in boundary layers subject to strong pressure gradient and curvature effects. *Journal of Fluid Mechanics* **888**, A4. DOI. ↩

[97] Mamidala, S. B., Weingärtner, A., & Fransson, J. H. 2022 Leading-edge pressure gradient effect on boundary layer receptivity to free-stream turbulence. *Journal of Fluid Mechanics* **935**. DOI. ↩

[98] Brandt, L. 2014 The lift-up effect: The linear mechanism behind transition and turbulence in shear flows. *European Journal of Mechanics, B/Fluids* **47**, 80–96. arXiv: 1403.4657. DOI. ↩

[99] Fransson, J. H. & Shahinfar, S. 2020 On the effect of free-stream turbulence on boundary-layer transition. *Journal of Fluid Mechanics* DOI. ↩

[100] Ovchinnikov, V., Choudhari, M. M., & Piomelli, U. 2008 Numerical simulations of boundary-layer bypass transition due to high-amplitude free-stream turbulence. *Journal of Fluid Mechanics* **613**, 135–169. DOI. ↩

[101] Nagarajan, S., K., L. S., & Ferziger, J. H. 2007 Leading-edge effects in bypass transition. *Journal of Fluid Mechanics* **572**, 471–504. DOI. ↩

[102] Hernon, D., Walsh, E. J., & Mceligot, D. M. 2007 Experimental investigation into the routes to bypass transition and the shear-sheltering phenomenon. *Journal of Fluid Mechanics* **591**, 461–479. DOI. ↩

[103] Burgmann, S., Dannemann, J., & Schröder, W. 2008 Time-resolved and volumetric PIV measurements of a transitional separation bubble on an SD7003 airfoil. *Experiments in Fluids* **44** (4), 609–622. DOI. ↩

[104] Burgmann, S. & Schröder, W. 2008 Investigation of the vortex induced unsteadiness of a separation bubble via time-resolved and scanning PIV measurements. *Experiments in Fluids* **45** (4), 675–691. DOI. ↩

[105] Jaroslawski, T., Forte, M., Vermeersch, O., Moschetta, J.-M., & Gowree, E. R. 2023 Disturbance growth in a laminar separation bubble subjected to free-stream turbulence. *Journal of Fluid Mechanics* **956**, A33. DOI. ↩

[106] Cao, N., Ting, D. S.-K., & Carriveau, R. 2011 The Performance of a High-Lift Airfoil in Turbulent Wind. *Wind Engineering* **35** (2), 179–196. DOI. ↩

[107] Damiola, L., Siddiqui, M. F., Runacres, M. C., & De Troyer, T. 2023 Influence of free-stream turbulence intensity on static and dynamic stall of a NACA 0018 aerofoil. *Journal of Wind Engineering and Industrial Aerodynamics* **232** (September 2022), 105270. DOI. ↩

[108] Wang, S., Zhou, Y., Alam, M. M., & Yang, H. 2014 Turbulent intensity and Reynolds number effects on an airfoil at low Reynolds numbers. *Physics of Fluids* **26** (11). DOI. ↩

[109] Maldonado, V., Castillo, L., Thormann, A., & Meneveau, C. 2015 The role of free stream turbulence with large integral scale on the aerodynamic performance of an experimental low Reynolds number S809 wind turbine blade. *Journal of Wind Engineering and Industrial Aerodynamics* **142**, 246–257. DOI. ↩

[110] Ravi, S., Watkins, S., Watmuff, J., Massey, K., Peterson, P., & Marino, M. 2012 Influence of Large-Scale Freestream Turbulence on the Performance of a Thin Airfoil. *AIAA Journal* **50** (11), 2448–2459. DOI. ↩

[111] Herbst, S. L., Kähler, C. J., & Hain, R. 2018 Influence of large-scale free-stream turbulence on an SD7003 airfoil at low Reynolds numbers. In *2018 Applied Aerodynamics Conference*, number 3490, Reston, Virginia. American Institute of Aeronautics and Astronautics. DOI. ↩

[112] Herbst, S. L., Hain, R., & Kähler, C. J. 2020 Low Aspect Ratio Wing Under Large-Scale Turbulent Inflow Conditions at Low Reynolds Numbers. In *Notes on Numerical Fluid Mechanics and Multidisciplinary Design*. Vol. 142, pp. 653–662. Springer Verlag. DOI. ↩

[113] Pelletier, A. & Mueller, T. J. 2000 Low Reynolds Number Aerodynamics of Low-Aspect-Ratio, Thin/Flat/Cambered-Plate Wings. *Journal of Aircraft* **37** (5), 825–832. DOI. ↩

[114] Bastedo, W. G. & Mueller, T. J. 1986 Spanwise variation of laminar separation bubbles on wings at low Reynolds number. *Journal of Aircraft* **23** (9), 687–694. DOI. ↩

[115] Toppings, C. E., Kurelek, J. W., & Yarusevych, S. 2021 Laminar Separation Bubble Development on a Finite Wing. *AIAA Journal* **59** (8), 2855–2867. DOI. ↩

[116] Toppings, C. E. & Yarusevych, S. 2021 Structure and dynamics of a laminar separation bubble near a wingtip. *Journal of Fluid Mechanics* **929**, A39. DOI. ↩

[117] Chen, Z. J., Qin, N., & Nowakowski, A. F. 2013 Three-Dimensional Laminar-Separation Bubble on a Cambered Thin Wing at Low Reynolds Numbers. *Journal of Aircraft* **50** (1), 152–163. DOI. ↩

[118] Marchman, J. F. & Abtahi, A. 1985 Aerodynamics of an aspect ratio 8 wing at low Reynolds numbers. *Journal of Aircraft* **22** (7), 628–634. DOI. ↩

[119] Huang, R. F. & Lin, C. L. 1995 Vortex shedding and shear-layer instability of wing at low-Reynolds numbers. *AIAA Journal* **33** (8), 1398–1403. DOI. ↩

[120] Simpson, R. L. 2001 Junction Flows. *Annual Review of Fluid Mechanics* **33** (1), 415–443. DOI. ↩

[121] Traub, L. W. & Cooper, E. 2008 Experimental Investigation of Pressure Measurement and Airfoil Characteristics at Low Reynolds Numbers. *Journal of Aircraft* **45** (4), 1322–1333. DOI. ↩

[122] Delafin, P., Deniset, F., & Astolfi, J. 2014 Effect of the laminar separation bubble induced transition on the hydrodynamic performance of a hydrofoil. *European Journal of Mechanics - B/Fluids* **46**, 190–200. DOI. ↩

[123] Pelletier, A. & Mueller, T. J. 2001 Effect of Endplates on Two-Dimensional Airfoil Testing at Low Reynolds Number. *Journal of Aircraft* **38** (6), 1056–1059. DOI. ↩

[124] Toppings, C. E. & Yarusevych, S. 2022 Structure and dynamics of a laminar separation bubble near a wing root: towards reconstructing the complete LSB topology on a finite wing. *Journal of Fluid Mechanics* **944**, A14. DOI. ↩

[125] Devenport, W. J. & Simpson, R. L. 1990 Time-dependent and time-averaged turbulence structure near the nose of a wing-body junction. *Journal of Fluid Mechanics* **210** (23), 23–55. DOI. ↩

[126] Gand, F., Deck, S., Brunet, V., & Sagaut, P. 2010 Flow dynamics past a simplified wing body junction. *Physics of Fluids* **22** (11), 115111. DOI. ↩

[127] Schulz, H. D., Gallus, H. E., & Lakshminarayana, B. 1990 Three-Dimensional Separated Flow Field in the Endwall Region of an Annular Compressor Cascade in the Presence of Rotor-Stator Interaction: Part 1—Quasi-Steady Flow Field and Comparison With Steady-State Data. *Journal of Turbomachinery* **112** (4), 669–678. DOI. ↩

[128] Andreu Angulo, I. & Ansell, P. J. 2019 Influence of Aspect Ratio on Dynamic Stall of a Finite Wing. *AIAA Journal* **57** (7), 2722–2733. DOI. ↩

[129] Visbal, M. R. & Garmann, D. J. 2019 Dynamic Stall of a Finite-Aspect-Ratio Wing. *AIAA Journal* **57** (3), 962–977. DOI. ↩

[130] Visbal, M. R. & Garmann, D. J. 2019 Investigation of spanwise end effects on dynamic stall of a pitching wing section. *Journal of Aircraft* **56** (6), 2118–2130. DOI. ↩

[131] Hammer, P. R., Garmann, D. J., & Visbal, M. R. 2022 Effect of Aspect Ratio on Finite-Wing Dynamic Stall. *AIAA Journal* **60** (12), 6581–6593. DOI. ↩

[132] Kurelek, J. W. 2016 *Transition in a Laminar Separation Bubble and the Effect of Acoustic Excitation*. Master Thesis, University of Waterloo. ↩

[133] Kurelek, J. W. 2021 *The Vortex Dynamics of Laminar Separation Bubbles*. PhD thesis, University of Waterloo. ↩

[134] Simmons, L. F. G. & Salter, C. 1934 Experimental investigation and analysis of the velocity variations in turbulent flow. *Proceedings of the Royal Society of London. Series A, Containing Papers of a Mathematical and Physical Character* **145** (854), 212–234. DOI. ↩

[135] Watkins, S., Ravi, S., & Loxton, B. 2010 The effect of turbulence on the aerodynamics of low Reynolds number wings. *Engineering Letters* **18** (3). ↩

[136] Isaza, J. C., Salazar, R., & Warhaft, Z. 2014 On grid-generated turbulence in the near- and far field regions. *Journal of Fluid Mechanics* **753**, 402–426. DOI. ↩

[137] Makita, H. 1991 Realization of a large-scale turbulence field in a small wind tunnel. *Fluid Dynamics Research* **8** (1-4), 53–64. DOI. ↩

[138] Hearst, R. J. & Lavoie, P. 2015 The effect of active grid initial conditions on high Reynolds number turbulence. *Experiments in Fluids* **56** (10), 185. DOI. ↩

[139] Batchelor, G. K. & Townsend, A. A. 1948 Decay of isotropic turbulence in the initial period. *Proceedings of the Royal Society of London. Series A. Mathematical and Physical Sciences* **193** (1035), 539–558. DOI. ↩

[140] Comte-Bellot, G. & Corrsin, S. 1966 The use of a contraction to improve the isotropy of grid-generated turbulence. *Journal of Fluid Mechanics* **25** (4), 657–682. DOI. ↩

[141] Cekli, H. E. & Water, W. V. D. 2010 Tailoring turbulence with an active grid. *Experiments in Fluids* **49** (2), 409–416. DOI. ↩

[142] Thormann, A. & Meneveau, C. 2014 Decay of homogeneous, nearly isotropic turbulence behind active fractal grids. *Physics of Fluids* **26** (2). DOI. ↩

[143] Gerakopulos, R. J. 2011 *Investigating flow over an airfoil at low Reynolds numbers using novel time-resolved surface pressure measurements*. Master Thesis, University of Waterloo. ↩

[144] Lambert, A. & Yarusevych, S. 2019 Effect of angle of attack on vortex dynamics in laminar separation bubbles. *Physics of Fluids* **31** (6), 064105. DOI. ↩

[145] Kirk, T. M. & Yarusevych, S. 2017 Vortex shedding within laminar separation bubbles forming over an airfoil. *Experiments in Fluids* **58** (5), 43. DOI. ↩

[146] Istvan, M. S., Kurelek, J. W., & Yarusevych, S. 2018 Turbulence Intensity Effects on Laminar Separation Bubbles Formed over an Airfoil. *AIAA Journal* **56** (4), 1335–1347. DOI. ↩

[147] Raffel, M., Willert, C. E., Wereley, S. T., & Kompenhans, J. 2018 *Particle Image Velocimetry*, number 1. Springer Berlin Heidelberg, p. 680. DOI. ↩

[148] Scarano, F. & Riethmuller, M. L. 2000 Advances in iterative multigrid PIV image processing. *Experiments in Fluids* **29** (7), S051–S060. DOI. ↩

[149] Wieneke, B. 2015 PIV uncertainty quantification from correlation statistics. *Measurement Science and Technology* **26** (7), 074002. DOI. ↩

[150] Westerweel, J. & Scarano, F. 2005 Universal outlier detection for PIV data. *Experiments in Fluids* **39** (6), 1096–1100. DOI. ↩

[151] Tavoularis, S. 2005 *Measurement in Fluid Mechanics*. Cambridge University Press. ↩

[152] Landau, H. 1967 Sampling, data transmission, and the Nyquist rate. *Proceedings of the IEEE* **55** (10), 1701–1706. DOI. ↩

[153] Welch, P. 1967 The use of fast Fourier transform for the estimation of power spectra: A method based on time averaging over short, modified periodograms. *IEEE Transactions on Audio and Electroacoustics* **15** (2), 70–73. DOI. ↩

[154] Solomon, M. O. 1991 PSD Computations Using Welch's Method. *Tech. rep.* SAND91-1533, Sandia National Laboratories, p. 64. ↩

[155] Guo, T., Zhang, T., Lim, E., Lopez-Benitez, M., Ma, F., & Yu, L. 2022 A Review of Wavelet Analysis and Its Applications: Challenges and Opportunities. *IEEE Access* **10**, 58869–58903. DOI. ↩

[156] Lilly, J. M. & Olhede, S. C. 2012 Generalized Morse Wavelets as a Superfamily of Analytic Wavelets. *IEEE Transactions on Signal Processing* **60** (11), 6036–6041. arXiv: 1203.3380. DOI. ↩

[157] Lilly, J. M. 2017 Element analysis: A wavelet-based method for analysing time-localized events in noisy time series. *Proceedings of the Royal Society A: Mathematical, Physical and Engineering Sciences* **473** (2200). arXiv: 1703.04882. DOI. ↩

[158] Lilly, J. M. & Olhede, S. C. 2009 Higher-order properties of analytic wavelets. *IEEE Transactions on Signal Processing* **57** (1), 146–160. arXiv: 0802.2377. DOI. ↩

[159] Taira, K., Brunton, S. L., Dawson, S. T. M., Rowley, C. W., Colonius, T., McKeon, B. J., Schmidt, O. T., Gordeyev, S. V., Theofilis, V., & Ukeiley, L. S. 2017 Modal Analysis of Fluid Flows: An Overview. *AIAA Journal* **55** (12), 4013–4041. DOI. ↩

[160] Berkooz, G. 1993 The Proper Orthogonal Decomposition in the Analysis of Turbulent Flows. *Annual Review of Fluid Mechanics* **25** (1), 539–575. DOI. ↩

[161] Sirovich, L. 1987 Turbulence and the dynamics of coherent structures. I. Coherent structures. *Quarterly of Applied Mathematics* **45** (3), 561–571. DOI. ↩

[162] Chatterjee, A. 2000 An introduction to the proper orthogonal decomposition. *Current Science* **78** (7), 808–817. ↩

[163] Legrand, M., Nogueira, J., & Lecuona, A. 2011 Flow temporal reconstruction from non-time-resolved data part I: mathematic fundamentals. *Experiments in Fluids* **51** (4), 1047–1055. DOI. ↩

[164] Sciacchitano, A. Uncertainty quantification in particle image velocimetry. (9). 2019. DOI. ↩

[165] Walpole, R. E., Myers, R. H., Myers, S. L., & Ye, K. 2012 *Probability & Statistics for Engineers & Scientists*. 9th ed. Pearson Prentice Hall. ISBN. ↩

[166] Widrow, B. & Kollár, I. 2008 Statistical Analysis of the Quantization Noise. In *Quantization Noise: Roundoff Error in Digital Computation, Signal Processing, Control, and Communications*, part 5, pp. 93–112. DOI. ↩

[167] Sciacchitano, A. & Wieneke, B. 2016 PIV uncertainty propagation. *Measurement Science and Technology* **27** (8), 084006. DOI. ↩

[168] Moffat, R. J. 1988 Describing the uncertainties in experimental results. *Experimental Thermal and Fluid Science* **1** (1), 3–17. DOI. ↩

[169] O'Meara, M. M. & Mueller, T. J. 1987 Laminar separation bubble characteristics on an airfoil at low Reynolds numbers. *AIAA Journal* **25** (8), 1033–1041. DOI. ↩

[170] Hain, R., Kähler, C. J., & Radespiel, R. 2009 Dynamics of laminar separation bubbles at low-Reynolds-number aerofoils. *Journal of Fluid Mechanics* **630**, 129–153. DOI. ↩

[171] Ol, M., McCauliffe, B., Hanff, E., Scholz, U., & Kähler, C. J. 2005 Comparison of Laminar Separation Bubble Measurements on a Low Reynolds Number Airfoil in Three Facilities. In *35th AIAA Fluid Dynamics Conference and Exhibit*, Reston, Virigina. American Institute of Aeronautics and Astronautics. DOI. ↩

[172] Hristov, G. & Ansell, P. J. 2018 Poststall Hysteresis and Flowfield Unsteadiness on a NACA 0012 Airfoil. *AIAA Journal* **56** (7), 2528–2539. DOI. ↩

[173] Kurelek, J. W., Yarusevych, S., & Kotsonis, M. 2019 Vortex merging in a laminar separation bubble under natural and forced conditions. *Physical Review Fluids* **4** (6), 063903. DOI. ↩

[174] Franklin, G. F., Powell, J. D., & Emami-Naeini, A. 2014 Dynamic Response. In *Feedback Control of Dynamic Systems*, p. 129. 7th ed. Pearson. ↩

[175] Simoni, D., Lengani, D., Ubaldi, M., Zunino, P., & Dellacasagrande, M. 2017 Inspection of the dynamic properties of laminar separation bubbles: free-stream turbulence intensity effects for different Reynolds numbers. *Experiments in Fluids* **58** (6), 66. DOI. ↩

[176] Dellacasagrande, M., Barsi, D., Lengani, D., Simoni, D., & Verdoya, J. 2020 Response of a flat plate laminar separation bubble to Reynolds number, free-stream turbulence and adverse pressure gradient variation. *Experiments in Fluids* **61** (6), 128. DOI. ↩

[177] Van Ingen, J. L. 1991 Research on Laminar Separation Bubbles at Delft University of Technology. In *Separated Flows and Jets*, pp. 537–556. Springer Berlin Heidelberg. DOI. ↩

[178] IEEE. 2003 IEEE Standard on Transitions, Pulses, and Related Waveforms. URL: http://ieeexplore.ieee.org/document/5511873/. DOI. ↩

[179] Amitay, M. & Glezer, A. 2002 Controlled transients of flow reattachment over stalled airfoils. *International Journal of Heat and Fluid Flow* **23** (5), 690–699. DOI. ↩

[180] Siauw, W., Bonnet, J.-P., Tensi, J., Cordier, L., Noack, B., & Cattafesta, L. 2010 Transient dynamics of the flow around a NACA 0015 airfoil using fluidic vortex generators. *International Journal of Heat and Fluid Flow* **31** (3), 450–459. DOI. ↩

[181] Owen, P. R. & Klanfer, R. 1953 On the Laminar Boundary Layer Separation from the Leading Edge of a Thin Airfoil. *Tech. rep.* Aero 2508, Royal Aircraft Establishment. ↩

[182] Paarmann, L. D. 2001 *Design and Analysis of Analog Filters*. The International Series in Engineering and Computer Science. Kluwer Academic Publishers. DOI. ↩

[183] Broeren, A. P. & Bragg, M. B. 2001 Spanwise Variation in the Unsteady Stalling Flowfields of Two-Dimensional Airfoil Models. *AIAA Journal* **39** (9), 1641–1651. DOI. ↩

[184] Rosti, M. E., Omidyeganeh, M., & Pinelli, A. 2016 Direct numerical simulation of the flow around an aerofoil in ramp-up motion. *Physics of Fluids* **28** (2). DOI. ↩

[185] Zaman, K. B. M. Q. & McKinzie, D. J. 1991 Control of laminar separation over airfoils by acoustic excitation. *AIAA Journal* **29** (7), 1075–1083. DOI. ↩

[186] Marchman, J. F. 1987 Aerodynamic testing at low Reynolds numbers. *Journal of Aircraft* **24** (2), 107–114. DOI. ↩

[187] Le Fouest, S., Deparday, J., & Mulleners, K. 2021 The dynamics and timescales of static stall. *Journal of Fluids and Structures* **104**, 103304. arXiv: 2102.04485. DOI. ↩

[188] Neal, J. M. & Amitay, M. 2023 Three-dimensional separation over unswept cantilevered wings at a moderate Reynolds number. *Physical Review Fluids* **8** (1), 014703. DOI. ↩

[189] Miozzi, M., Capone, A., Costantini, M., Fratto, L., Klein, C., & Di Felice, F. 2019 Skin friction and coherent structures within a laminar separation bubble. *Experiments in Fluids* **60** (1), 13. DOI. ↩

[190] Kurelek, J. W., Lambert, A. R., & Yarusevych, S. 2016 Coherent Structures in the Transition Process of a Laminar Separation Bubble. *AIAA Journal* **54** (8), 2295–2309. DOI. ↩

[191] Sandham, N. D. 2008 Transitional separation bubbles and unsteady aspects of aerofoil stall. *Aeronautical Journal* **112** (1133), 395–404. DOI. ↩

[192] Drela, M. 1989 XFOIL: An Analysis and Design System for Low Reynolds Number Airfoils. In Mueller, T. J., editor, *Low Reynolds Number Aerodynamics*, pp. 1–12. Springer Berlin Heidelberg. DOI. ↩

[193] Zaman, K. B. M. Q., Mckinzie, D. J., & Rumsey, C. L. 1989 A natural low-frequency oscillation of the flow over an airfoil near stalling conditions. *Journal of Fluid Mechanics* **202**, 403–442. DOI. ↩

[194] Henk, R. W. 1990 *An Experimental Investigation of the Fluid Mechanics of an Unsteady, Three-Dimensional Separation*. PhD thesis, Stanford University. ISBN. ↩

[195] Gloutak, D. A., Jansen, K. E., & Farnsworth, J. A. 2022 Impact of Streamwise Gusts on the Aerodynamic Performance of a Finite-Span Wing. In *AIAA SCITECH 2022 Forum*, pp. 1–17, Reston, Virginia. American Institute of Aeronautics and Astronautics. DOI. ↩

[196] Gloutak, D. A., Jansen, K., & Farnsworth, J. A. 2023 Vortex Dynamics of a Separated Wing in a Time- Varying Freestream. *Experiments in Fluids* 0–9. DOI. ↩

[197] Coton, F. N. & Galbraith, R. A. D. 1999 Experimental study of dynamic stall on a finite wing. *Aeronautical Journal* **103** (1023), 229–236. DOI. ↩

[198] Schreck, S. J. & Hellin, H. E. 1994 Unsteady vortex dynamics and surface pressure topologies on a finite pitching wing. *Journal of Aircraft* **31** (4), 899–907. DOI. ↩

[199] Coull, J. D. & Hodson, H. P. 2011 Unsteady boundary-layer transition in low-pressure turbines. *Journal of Fluid Mechanics* **681** (1), 370–410. DOI. ↩

[200] Huang, N. E., Shen, Z., Long, S. R., Wu, M. C., Shih, H. H., Zheng, Q., Yen, N.-C., Tung, C. C., & Liu, H. H. 1998 The empirical mode decomposition and the Hilbert spectrum for nonlinear and non-stationary time series analysis. *Proceedings of the Royal Society of London. Series A: Mathematical, Physical and Engineering Sciences* **454** (1971), 903–995. DOI. ↩

[201] Schmid, P. J. & Henningson, D. S. 2001 *Stability and Transition in Shear Flows*, vol. 142 of *Applied Mathematical Sciences*. Springer New York. DOI. ↩

[202] Häggmark, C. P., Bakchinov, A. A., & Alfredsson, P. H. 2000 Experiments on a two–dimensional laminar separation bubble. *Philosophical Transactions of the Royal Society of London. Series A: Mathematical, Physical and Engineering Sciences* **358** (1777), 3193–3205. Duck, P. W. & Ruban, A. I., editors. DOI. ↩

[203] Ayancik, F. & Mulleners, K. 2022 All you need is time to generalise the Goman–Khrabrov dynamic stall model. *Journal of Fluid Mechanics* **942**, R8. arXiv: 2110.08516. DOI. ↩

[204] Reshotko, E. 2001 Transient growth: A factor in bypass transition. *Physics of Fluids* **13** (5), 1067–1075. DOI. ↩

[205] Sytsma, M. J. & Ukeiley, L. 2013 Mean Loads from Wind-Tunnel Turbulence on Low-Aspect-Ratio Flat Plates. *Journal of Aircraft* **50** (3), 863–870. DOI. ↩

[206] Li, L. & Hearst, R. J. 2021 The influence of freestream turbulence on the temporal pressure distribution and lift of an airfoil. *Journal of Wind Engineering and Industrial Aerodynamics* **209** (November 2020), 104456. DOI. ↩

[207] Yaras, M. I. 2002 Measurements of the Effects of Freestream Turbulence on Separation-Bubble Transition. In *Volume 3: Turbo Expo 2002, Parts A and B*, vol. 3 A, pp. 647–660. ASMEDC. DOI. ↩

[208] Mahallati, A., McAuliffe, B. R., Sjolander, S. A., & Praisner, T. J. 2012 Aerodynamics of a Low-Pressure Turbine Airfoil at Low Reynolds Numbers-Part I: Steady Flow Measurements. *Journal of Turbomachinery* **135** (1), 1–9. DOI. ↩

[209] Kay, N. J., Richards, P. J., & Sharma, R. N. 2020 Influence of turbulence on cambered and symmetrical airfoils at low Reynolds numbers. *AIAA Journal* **58** (5), 1913–1925. DOI. ↩

[210] Devinant, P., Laverne, T., & Hureau, J. 2002 Experimental study of wind-turbine airfoil aerodynamics in high turbulence. *Journal of Wind Engineering and Industrial Aerodynamics* **90** (6), 689–707. DOI. ↩

[211] Sicot, C., Aubrun, S., Loyer, S., & Devinant, P. 2006 Unsteady characteristics of the static stall of an airfoil subjected to freestream turbulence level up to 16%. *Experiments in Fluids* **41** (4), 641–648. DOI. ↩

[212] Meinhart, C. D., Wereley, S. T., & Santiago, J. G. 2000 A piv algorithm for estimating time-averaged velocity fields. *Journal of Fluids Engineering, Transactions of the ASME* **122** (2), 285–289. DOI. ↩

[213] Yavuzkurt, S. 1984 A Guide to Uncertainty Analysis of Hot-Wire Data. *Journal of Fluids Engineering* **106** (2), 181–186. DOI. ↩

[214] Taylor, G. I. 1938 The Spectrum of Turbulence. *Proceedings of the Royal Society A: Mathematical, Physical and Engineering Sciences* **164** (919), 476–490. DOI. ↩

[215] Schrader, P. 1993 Computing the statistical stability of integral length scale measurements by autoregressive simulation. *Journal of Wind Engineering and Industrial Aerodynamics* **46-47** (6), 487–496. DOI. ↩

[216] Gomes-Fernandes, R., Ganapathisubramani, B., & Vassilicos, J. C. 2012 Particle image velocimetry study of fractal-generated turbulence. *Journal of Fluid Mechanics* **711**, 306–336. DOI. ↩

[217] Hunt, J. C. 1973 *A theory of turbulent flow round two-dimensional bluff bodies*, vol. 61 of number 4, pp. 625–706. DOI. ↩

[218] Valente, P. C. & Vassilicos, J. C. 2011 The decay of turbulence generated by a class of multiscale grids. *Journal of Fluid Mechanics* **687**, 300–340. arXiv: 1101.0709. DOI. ↩

[219] Chen, H., Reuss, D. L., & Sick, V. 2012 On the use and interpretation of proper orthogonal decomposition of in-cylinder engine flows. *Measurement Science and Technology* **23** (8). DOI. ↩

[220] Epps, B. P. & Krivitzky, E. M. 2019 Singular value decomposition of noisy data: mode corruption. *Experiments in Fluids* **60** (8), 121. DOI. ↩

[221] Shannon, C. E. 1949 Communication in the Presence of Noise. *Proceedings of the IRE* **37** (1), 10–21. DOI. ↩

[222] Abdelsamie, A., Janiga, G., & Thévenin, D. 2017 Spectral entropy as a flow state indicator. *International Journal of Heat and Fluid Flow* **68** (September), 102–113. DOI. ↩

[223] Aubry, N., Guyonnet, R., & Lima, R. 1991 Spatiotemporal analysis of complex signals: Theory and applications. *Journal of Statistical Physics* **64** (3-4), 683–739. DOI. ↩

[224] Uruba, V. 2019 Energy and entropy in turbulence decompositions. *Entropy* **21** (2). DOI. ↩

[225] Li, Y., Yano, J. I., & Lin, Y. 2019 Is atmospheric convection organised?: information entropy analysis. *Geophysical and Astrophysical Fluid Dynamics* **113** (5-6), 553–573. DOI. ↩

[226] Hedley, T. B. & Keffer, J. F. 1974 Turbulent/non-turbulent decisions in an intermittent flow. *Journal of Fluid Mechanics* **64** (4), 625–644. DOI. ↩

[227] Boutilier, M. S. H. & Yarusevych, S. 2012 Effects of End Plates and Blockage on Low-Reynolds-Number Flows Over Airfoils. *AIAA Journal* **50** (7), 1547–1559. DOI. ↩

[228] Winslow, J., Otsuka, H., Govindarajan, B., & Chopra, I. 2018 Basic understanding of airfoil characteristics at low Reynolds numbers (104–105). *Journal of Aircraft* **55** (3), 1050–1061. DOI. ↩

[229] Ohtake, T., Nakae, Y., & Motohashi, T. 2007 Nonlinearity of the Aerodynamic Characteristics of NACA0012 Aerofoil at Low Reynolds Numbers. *Journal of the Japan Society for Aeronautical and Space Sciences* **55** (644), 439–445. DOI. ↩

[230] Hrynuk, J. T., Olson, D., Stutz, C., & Jackson, J. 2024 Effects of Turbulence on NACA 0012 Airfoil Performance at Low Reynolds Number. *AIAA Journal* **62** (1), 409–417. DOI. ↩

[231] Reuss, D. L., Adrian, R. J., Landreth, C. C., French, D. T., & Fansler, T. D. 1989 Instantaneous Planar Measurements of Velocity and Large-Scale Vorticity and Strain Rate in an Engine Using Particle-Image Velocimetry. In *SAE Technical Papers*, vol. 98. DOI. ↩

[232] Nolan, K. P. & Walsh, E. J. 2012 Particle image velocimetry measurements of a transitional boundary layer under free stream turbulence. *Journal of Fluid Mechanics* **702**, 215–238. DOI. ↩

[233] Lengani, D., Simoni, D., Ubaldi, M., & Zunino, P. 2014 POD analysis of the unsteady behavior of a laminar separation bubble. *Experimental Thermal and Fluid Science* **58**, 70–79. DOI. ↩

[234] Lang, M., Rist, U., Wagner, S., Lang, M., & Wagner, S. 2004 Investigations on Controlled Transition Development in a Laminar Separation Bubble by Means of LDA and PIV. *Experiments in Fluids* **36** (1), 43–52. DOI. ↩

[235] Lengani, D., Simoni, D., Ubaldi, M., Zunino, P., & Bertini, F. 2017 Analysis of the Reynolds stress component production in a laminar separation bubble. *International Journal of Heat and Fluid Flow* **64**, 112–119. DOI. ↩

[236] Michelis, T., Yarusevych, S., & Kotsonis, M. 2017 Response of a laminar separation bubble to impulsive forcing. *Journal of Fluid Mechanics* **820**, 633–666. DOI. ↩

[237] Litvinenko, Y. A., Chernoray, V. G., Kozlov, V. V., Grek, G. R., Löfdahl, L., & Chun, H. H. 2005 Adverse pressure gradient effect on nonlinear varicose instability of a streaky structure in an unswept wing boundary layer. *Physics of Fluids* **17** (11), 1–3. DOI. ↩

[238] Lengani, D. & Simoni, D. 2015 Recognition of coherent structures in the boundary layer of a low-pressure-turbine blade for different free-stream turbulence intensity levels. *International Journal of Heat and Fluid Flow* **54**, 1–13. DOI. ↩

[239] Fang, X. & Wang, Z. 2024 On the low-frequency flapping motion in flow separation. *Journal of Fluid Mechanics* **984**, A76. DOI. ↩

[240] Aniffa, M., Caesar, V., Dabaria, V., & Mandal, A. 2023 Characteristics of geometry-and pressure-induced laminar separation bubbles at an enhanced level of free-stream turbulence. *Journal of Fluid Mechanics* **957**, A19. DOI. ↩

[241] Abraham, B. M. & Keith, W. L. 1996 Direct Measurements of Turbulent Boundary Layer Wall Pressure Wavenumber - Frequency Spectra. *ASME International Mechanical Engineering Congress and Exposition, Proceedings (IMECE)* **1996-V** (March), 177–187. DOI. ↩

[242] Collins, F. G. & Zelenevitz, J. 1975 Influence of Sound upon Separated Flow over Wings. *AIAA Journal* **13** (3), 408–410. DOI. ↩

[243] Diwan, S. S. & Ramesh, O. N. 2012 Relevance of local parallel theory to the linear stability of laminar separation bubbles. *Journal of Fluid Mechanics* **698**, 468–478. DOI. ↩

[244] Park, D., Shim, H., & Lee, Y. 2020 PIV Measurement of Separation Bubble on an Airfoil at Low Reynolds Numbers. *Journal of Aerospace Engineering* **33** (1), 1–17. DOI. ↩

[245] Mohamed, A., Watkins, S., OL, M. V., & Jones, A. R. 2021 Flight-Relevant Gusts: Computation-Derived Guidelines for Micro Air Vehicle Ground Test Unsteady Aerodynamics. *Journal of Aircraft* **58** (3), 693–699. DOI. ↩

[246] Yarusevych, S., Kawall, J. G., & Sullivan, P. E. 2006 Airfoil performance at low Reynolds numbers in the presence of periodic disturbances. *Journal of Fluids Engineering, Transactions of the ASME* **128** (3), 587–595. DOI. ↩

[247] Comte-Bellot, G. 1976 Hot-wire anemometry. *Annual Review of Fluid Mechanics* **8**, 209–231. ↩

[248] Benedict, L. H. & Gould, R. D. 1996 Towards better uncertainty estimates for turbulence statistics. *Experiments in Fluids* **22** (2), 129–136. DOI. ↩

[249] Manolakis, D., Ingle, V., & Kagon, S. 2000 Nonparametric Power Spectrum Estimation. In *Statistical and Adaptive Signal Processing*, part 5. McGraw-Hill. ↩

Appendices

Appendix A

Uncertainty Estimation

Specifics of the methods used to obtain uncertainty estimates for quantities presented in Chapters 4–7 are provided. Maximum uncertainties for all plotted quantities are tabulated.

This appendix provides details of the uncertainty estimation for the quantities reported in Chapters 4–7. A summary of the maximum uncertainties in all reported quantities is provided in Table A.1.

A.1 Experimental Conditions

A.1.1 Free-stream Velocity

The free-stream velocity in the recirculating wind tunnel at the University of Waterloo was set using a calibrated relationship between the measured pressure drop across the 9 : 1 contraction upstream of the test section and the free-stream dynamic pressure in the test section. Mathematically, the free-stream velocity in the test section can be written as:

$$u_\infty = \sqrt{\frac{2C_{\text{cont}}\Delta P}{\rho}} \tag{A.1}$$

where ΔP is the pressure drop across the contraction and C_{cont} is a coefficient obtained from calibration. The uncertainty in u_∞ can be expressed as a function of the uncertainties in C_{cont}, ΔP, and ρ using the linear error propagation formula (Eq. 3.12) in a straightforward manner. The major sources of uncertainty contributing to the uncertainty in the free-stream velocity are the uncertainty in pressure measurements, uncertainty in the calibration between measured pressure drop and free-stream dynamic pressure, and uncertainty in ambient air density.

The contraction pressure drop was measured with a Setra Model 239 differential pressure transducer with a range of $\pm 250\,\text{Pa}$ and an uncertainty of $0.7\,\text{Pa}$. The uncertainty in the calibration constant C_{cont} was estimated to be no more than 0.05 from the variations observed across multiple calibration tests. The air density was computed from the measured barometric pressure and temperature using the ideal gas law, and its uncertainty was estimated to be $\pm 9 \times 10^{-3}\,\text{kg}\,\text{m}^{-3}$ using Eq. 3.12. The temperature was measured in the return duct of the wind tunnel using a K-type thermocouple with an uncertainty of $\pm 2\,^\circ\text{C}$, and the barometric pressure was measured using a barometer with an uncertainty of $\pm 13\,\text{Pa}$. The overall uncertainty in the free-stream velocity was no more than than $0.3\,\text{m}\,\text{s}^{-1}$ across the range of conditions investigated.

The chord Reynolds number was calculated from the free-stream velocity, airfoil chord length, and kinematic viscosity. The chord lengths of the airfoil and wing models were accurate to within approximately 0.5%. The kinematic viscosity was calculated from the measured ambient temperature using a linear fit. The uncertainty in kinematic viscosity due to the uncertainty in temperature was estimated to be $2 \times 10^{-7}\,\text{m}\,\text{s}^{-2}$. The overall uncertainty in Reynolds number was no more than 4×10^3 across the range of conditions investigated.

A.1.2 Turbulence Intensity

The free-stream turbulence intensity was measured in the empty test section using a single hot-wire anemometer. Prior to hot-wire measurements, the hot-wire voltage signal was calibrated against the mean free-stream velocity measured using a Pitot-static probe. A least-squares fourth-order polynomial fit was computed to relate the hot-wire voltage signal to the free-stream velocity. Because the heat flux from the hot-wire is sensitive to the ambient temperature [247], re-calibration of the hot-wire was performed every day that hot-wire measurements were taken. Following the methodology of Yavuzkurt [213], the relative uncertainty of the hot-wire calibration was estimated to be 14%. Because the single hot-wire sensor is insensitive to the direction of the flow in the plane normal to the axis of the wire, the mean and fluctuating velocity measured in a turbulent flow will differ from their true values regardless of the quality of the calibration [213]. The uncertainties reported in Table A.1 account for both the uncertainty due to turbulent fluctuations and the calibration uncertainty. Across all flow conditions studied, the largest uncertainty in free-stream turbulence intensity is $\pm 3\%$ for the case of $Tu = 16\%$ studied in Chapter 7.

A.1.3 Integral Length Scale

The uncertainty in measured integral length scales was estimated by computing the integral length scales for several shorter segments of the complete hot-wire recording, and then calculating the associated uncertainty in mean integral length scale using Eq. 3.10. This procedure is similar to the bootstrap method [248], except that the shorter segments employed in this method were non-overlapping. A requirement for this method of estimating the uncertainty in the integral length scale is that each of the smaller segments are much longer than the integral time scale. For the integral length scales reported in Chapter 7, the complete hot-wire recordings had a sampling period of 300 s, and the uncertainty in the integral length scale was estimated from segments of duration 60 s to be less than $0.14c$.

A.1.4 Angle of Attack

The overall uncertainty in reported angles of attack contains contributions from the uncertainty in the angle of attack datum, and the uncertainty in the angular difference between the angle of attack and the angle of attack datum. Since a symmetric airfoil profile was used for all experiments, the zero-lift angle was used as the angle of attack datum. For the aluminium model used in Chapter 4, the zero-lift angle was determined using surface pressure measurements. For the models used in Chapters 5–7, the zero-lift angle was determined using direct force measurements. The overall uncertainty in angle of attack for the aluminium model used in Chapter 4 was estimated by comparing surface pressure measurements obtained from repeated manual re-positioning of the model at a constant angle of attack. The variations in these pressure measurements were no greater than those observed for a prescribed change in angle of attack of 0.2° [49]. Thus, the uncertainty in angle of attack for the experiments in Chapter 4 is estimated to be $\pm 0.2^\circ$. The overall

uncertainty in angle of attack for the experiments in Chapter 5 is also $\pm 0.2°$, because the angle of attack was also set manually for those experiments. The uncertainty in angle of attack for the models used in Chapters 6–7 is lower because a rotary table with an angular resolution of $0.05°$ was used to set the angle of attack. However, uncertainty in the measurement of the zero-lift angle still contributed to uncertainty in the angle of attack. The overall uncertainty in angle of attack for the experiments in Chapters 6–7 was estimated from the variations observed in lift force measurements from repeated re-positioning of the model after re-measuring the zero-lift angle. The variations in these lift force measurements were no more than those observed for a prescribed change in angle of attack of $0.06°$. Thus, the uncertainty in angle of attack for the experiments in Chapters 6–7 is estimated to be $\pm 0.06°$.

A.2 Particle Image Velocimetry

The uncertainty in PIV measurements arises from errors in timing and errors in displacement measurements. Whereas the time interval between laser pulses used for the experiments in this study was on the order of 10 µs, jitter of the timing signals sent by the field programmable gate array to the cameras and laser is on the order of 0.1ns. Therefore, the uncertainty due to PIV timing errors is considered negligible. In contrast, the uncertainty of particle displacements, which may arise from the experimental setup, the cross-correlation algorithm, or the characteristics of the flow itself [147, 164], are more significant.

One source of errors arising from the experimental set-up are errors in calibration. This may be due to errors in the grid spacing of the calibration target, optical distortion of the calibration images, or differences in the position of the calibration target and the laser sheet [147]. Errors in the calibration are usually bias errors that remain constant for a given set-up once calibration is performed. The relative uncertainty in displacement arising from errors in the grid spacing of the calibration target and the optical distortion of the calibration images are estimated to be approximately 1% for the PIV measurements in Chapters 4–6, based on the RMS residuals of the mapping function relative to the grid markers. In Chapter 7, a smaller airfoil model was used, and the corresponding decrease in spatial resolution increased the calibration uncertainty to approximately 2%. In addition to bias errors in displacement, the calibration also contributes to bias errors in the location of the origin of the mapping function's coordinate system. The absolute uncertainty in the location of the coordinate system origin relative to the lifting surface models is estimated to be approximately ± 1 mm in the x direction, ± 0.1 mm in the y direction, and ± 2 mm in the z direction for side view PIV measurements. For top-view measurements, the uncertainty in the location of the coordinate system origin is approximately ± 2 mm for all three coordinate axes. The uncertainty in the location of the coordinate system origin relative to the model is the major contributor to the uncertainty in estimates of boundary layer displacement and momentum thicknesses (δ^*,θ) and the locations of separation (x_s), transition (x_t), and reattachment (x_r).

Random errors in the particle displacement measurements arise from a multitude of

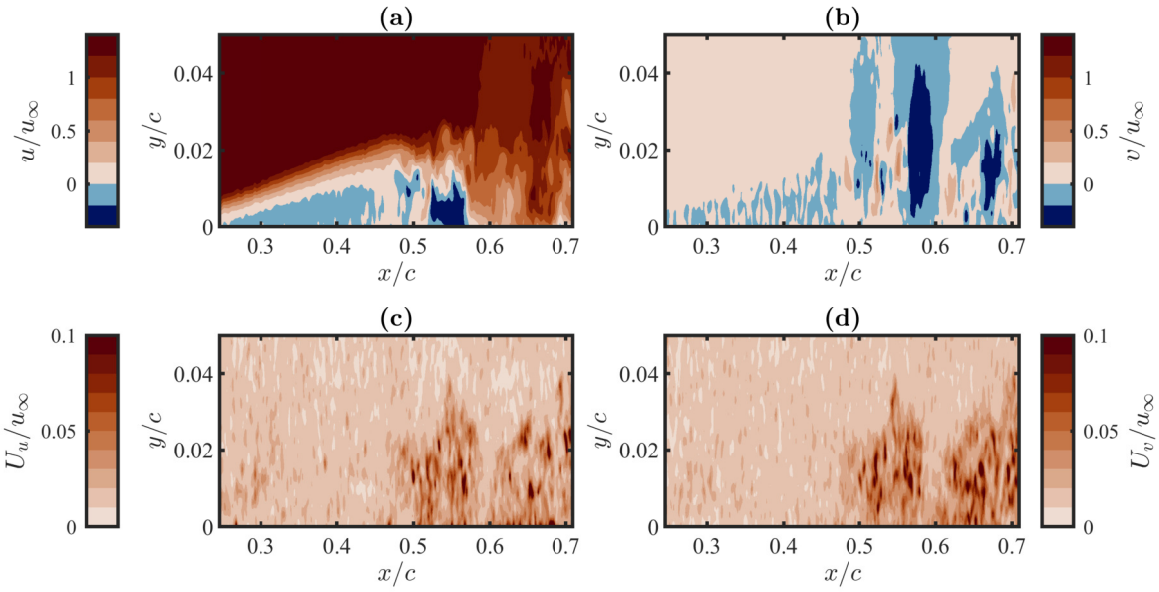


Figure A.1: Example of mean streamwise (a) and wall-normal (b) velocity fields and corresponding uncertainty due to random displacement errors in instantaneous streamwise (c) and wall-normal (d) velocity fields.

sources, including but not limited to: camera sensor noise, out-of-plane particle motion, shear in the flow, and the cross-correlation algorithm [147]. Several methods have been developed to estimate the random errors in PIV measurements through *a posteriori* analysis of particle images [164]. In this work, the correlation statistics method [149] is used. The correlation statistics method estimates the uncertainty in displacement vectors by considering the discrepancies in image intensity between pairs of particle images from each correlation window on a pixel by pixel basis. The result is an uncertainty field that provides the instantaneous uncertainty of each displacement vector component for every measured velocity vector. An example of the uncertainty field for the u and v velocity components for a representative PIV snapshot is provided in Fig. A.1. The uncertainty field can be propagated to derived quantities using the methodology presented in Section 3.5. In practice, random errors in the mean velocity fields due to random errors in measured particle displacements are relatively small because of the large sample sizes employed. More significant contributions to the random errors in mean velocity fields arise from temporal fluctuations of the velocity field, which are quantified using Eq. 3.10. However, random errors in measured particle displacements can be significant when computing instantaneous quantities.

A.2.1 Reynolds Stress

The uncertainties in RMS velocity fluctuations (Reynolds normal stresses) and Reynolds shear stresses were estimated using the expressions for the standard error in these quantities provided by Sciacchitano & Wieneke [167]. When multiplied by the critical value of the

Student's t-distribution at the prescribed confidence level (95%), these expressions become:

$$U_{u'_{\mathrm{RMS}}} = \tau_{N-1} \frac{u'_{\mathrm{RMS}}}{\sqrt{2\,(N-1)}} \tag{A.2}$$

$$U_{u'_{\mathrm{RMS}}} = \tau_{N-1} \frac{u'_{\mathrm{RMS}}}{\sqrt{2\,(N-1)}} \tag{A.3}$$

$$U_{\overline{u'v'}} = \tau_{N-1} \sqrt{\frac{u'^2_{\mathrm{RMS}} v'^2_{\mathrm{RMS}} + \overline{u'v'}^2}{N-1}} \tag{A.4}$$

The number of samples N in the above expressions should be the effective number of independent samples [167].

A.2.2 Integral Boundary Layer Parameters

The uncertainties in displacement thickness, and momentum thickness were estimated using the method of sequential perturbation. The major source of uncertainty contributing to the uncertainties in integral boundary layer parameters is the uncertainty in the location of the airfoil surface. The uncertainty in the location of the airfoil surface was estimated to be approximately equal to the vector pitch of the PIV vector fields. In the method of squential perturbation, the wall location was perturbed by shifting the location of $y = 0$ by one vector grid spacing in the wall-normal direction and re-computing the displacement thickness, and momentum thickness. The uncertainty in the shape factor was estimated by propagating the uncertainties in the displacement thickness and the momentum thickness according to Eq. 3.12, assuming that errors in the displacement thickness and momentum thickness were uncorrelated.

A.2.3 POD Modes

The uncertainty in POD eigenvalues was estimated using the formula provided by Epps & Krivitzky [220] from their perturbation analysis of POD:

$$U_{\lambda_i} = U_{\mathbf{u}} \sqrt{w} \tag{A.5}$$

where $U_{\mathbf{u}}$ is the uncertainty in velocity measurements due to random errors, and w is a weight factor that quantifies the degree of spatial correlation in the velocity measurements. In Eq. A.5, $U_{\mathbf{u}}$ was taken as the RMS of the uncertainty in velocity from correlation statistics over the entire snapshot matrix (Eq. 3.5). The uncertainty in the POD spatial modes and time coefficients was estimated using the "back of the envelope" formulae for the RMS error provided by Epps & Krivitzky [220]. When evaluated at a 95% confidence level, these formulae become:

$$U_{\mathbf{\Phi_i}} = \min\left(U_{\mathbf{u}}/\lambda_i, \tau_{N-1}\sqrt{2/\left(M\mathfrak{C}\right)}\right) \tag{A.6}$$

$$U_{\Theta_i} = \min\left(U_{\mathbf{u}}/\lambda_i, \tau_{N-1}\sqrt{2/N}\right) \tag{A.7}$$

The weight factor w is related to the size of the PIV cross-correlation window and the window overlap. In this work w was estimated from a least-squares fit of a Marcheko-Pastur distribution to the eigenvalue spectrum. Details of the Marchenko-Pastur distribution and its relationship to the weight factor can be found in [220].

A.3 Power Spectral Density

PSD estimates were obtained by averaging the PSD computed over multiple shorter segments of the complete signal, according to Welch's method (Section 3.4.1). When the data within each segment is uncorrelated, the variance of the averaged PSD can be approximated as a χ^2 distribution [153]. The number of degrees of freedom of the χ^2 distribution is approximately equal to twice the number of segments [153, 154, 249]. Therefore, the uncertainty interval for $\mathcal{P}_{u'u'}$ can be written as [154]:

$$\frac{2K\mathcal{P}_{u'u'}}{\chi^2_{2K,\text{lower}}} < \mathcal{P}_{u'u'} < \frac{2K\mathcal{P}_{u'u'}}{\chi^2_{2K,\text{upper}}} \tag{A.8}$$

where K is the number of segments, and $\chi^2_{2K,\text{upper}}$ and $\chi^2_{2K,\text{lower}}$ are the upper and lower critical values of the χ^2 distribution with $2K$ degrees of freedom at the desired confidence level, respectively. In this work a 95% confidence level is used.

A.4 Surface Pressure

The uncertainty of measured surface pressures is primarily attributed to the limited accuracy of the pressure transducers. Surface pressure measurements in Chapter 4 were measured with Setra model 239 differential pressure transducers with a manufacturer specified accuracy of $\pm 0.7\,\text{Pa}$. The uncertainty in reported surface pressure coefficients was estimated by applying the linear error propagation formula (Eq. 3.12) to the definition of the pressure coefficient:

$$C_p = \frac{\Delta P}{\frac{1}{2}\rho u_\infty^2} \tag{A.9}$$

to obtain an estimate of the uncertainty of C_p that accounts for the uncertainty in measured pressure difference (ΔP), density (ρ), and free-stream velocity (u_∞). The overall uncertainty in C_p values reported in Chapter 4 is estimated to be less than 0.8 because of the relatively low free-stream velocity. However, uncertainty in differences between C_p values measured in the same conditions is less than 0.4.

A.5 Lift and Drag Forces

The uncertainty in the forces measured using the force balance is caused primarily by the limited accuracy of the force balance and minute variations in model positioning between different trials and experimental setups. The manufacturer specified accuracy of the chord-parallel and chord-normal forces measured by the force balance is $\pm 0.1\,\mathrm{N}$. It was assumed that the angle of attack of the airfoil was sufficiently small such that the uncertainties in lift and drag forces were also $\pm 0.1\,\mathrm{N}$. However, any bias error inherent in the force balance does not affect the ability to resolve changes in forces. Unlike bias errors, random errors contribute to uncertainty in the differences between force measurements. An estimate of the random errors present in the force measurements was made from the amplitude of the noise present in force measurements when the stationary acrylic airfoil model was mounted to the load cell in quiescent conditions. The standard deviation of the noise in such conditions was $0.0741\,\mathrm{N}$ and $0.0356\,\mathrm{N}$ in the chordwise and chord-normal components of force. Thus, the uncertainty in these components of force at a 95% confidence level was obtained by multiplying the standard deviations by 1.96. The uncertainty in force measurements was propagated to the lift coefficient using Eq. 3.12. The uncertainty in the lift and drag coefficients due to random errors is estimated to be less than 0.03 and 0.02, respectively.

Table A.1: Maximum uncertainties of measured and derived quantities at a confidence level of 95%.

Quantity	Uncertainty				Method
	Chapter 4	Chapter 5	Chapter 6	Chapter 7	
c	$1\,\mathrm{mm}$	$1\,\mathrm{mm}$	$1\,\mathrm{mm}$	$0.5\,\mathrm{mm}$	Manufacturing tolerance
u_∞	$0.3\,\mathrm{m\,s^{-1}}$	$0.6\,\mathrm{m\,s^{-1}}$	$0.2\,\mathrm{m\,s^{-1}}$	$0.2\,\mathrm{m\,s^{-1}}$	Eqs. (3.11) and (3.12)
Re_c	2×10^3	2×10^3	3×10^3	4×10^3	Eqs. (3.11) and (3.12)
Tu	0.4%	0.14%	0.04%	3%	Eqs. (3.11) and (3.12)
Λ_{ux}				$0.14c$	Repeated measurements
α	0.2°	0.2°	0.06°	±0.06°	Repeated measurements
$C_{\overline{p}}$	0.4			0.2	Eqs. (3.10)–(3.12)
C_L		0.2	0.08	0.04	Eqs. (3.11) and (3.12)
$\widetilde{C_L}$		0.2	0.09		Eqs. (3.10)–(3.12)
C_D				0.03	Eqs. (3.11) and (3.12)
u [§]		$0.12u_\infty$	$0.13u_\infty$	$0.04u_\infty$	Correlation statistics [149], Eq. 3.11
$\overline{u}$	$0.02u_\infty$	$0.07u_\infty$	$0.25u_\infty$ [†]	$0.04u_\infty$	Eqs. (3.10) and (3.11)
$\widetilde{u}$			$0.5u_\infty$		Eqs. (3.10) and (3.11)
u'_{RMS}	$0.02u_\infty$			$0.03u_\infty$	Eqs. (3.10) and (3.11)
v'_{RMS}	$0.004u_\infty$			$0.005u_\infty$	Eqs. (3.10) and (3.11)
$\overline{u'v'}$		$0.02u_\infty^2$		$0.03u_\infty^2$	Eqs. (3.10) and (3.11)
$\widetilde{u'v'}$	$0.04u_\infty^2$		$0.02u_\infty^2$ [§]		Eqs. (3.10) and (3.11)
$\mathcal{P}_{v'v'}(f)$	$0.6\mathcal{P}_{v'v'}(f)$ [‡]				Appendix A.2.3

Table A.1: Maximum uncertainties of measured and derived quantities at a confidence level of 95%.

Quantity	Uncertainty				Method
	Chapter 4	Chapter 5	Chapter 6	Chapter 7	
$\mathcal{P}_{v'v'}(k)$	$0.3\mathcal{P}_{v'v'}(k)^{\ddagger}$				Appendix A.2.3
$\mathcal{P}_{v'v'}(f,k)$				$0.08\mathcal{P}_{v'v'}(f,k)$	Appendix A.2.3
$\mathcal{P}_{u'_\infty u'_\infty}$				$0.17\mathcal{P}_{u'_\infty u'_\infty}$	Appendix A.2.3
$\widetilde{\lvert\Psi_{v'}\rvert}$		$0.02u_\infty$	$0.05u_\infty$		Repeated measurements
ω_z [§]	$60u_\infty/c$	$20u_\infty/c$	$40u_\infty/c$	$40u_\infty/c$	Eqs. (3.11) and (3.12)
$\widetilde{\delta^*}$	$0.009c$				Sequential perturbation
H				2	Sequential perturbation
$\widetilde{\mathrm{Re}_{\theta_\mathrm{s}}}$		17			Sequential perturbation
$\frac{\partial\widetilde{u_\mathrm{e}}}{\partial t}$	$0.0015u_\infty^2/c$				Eqs. (3.11) and (3.12)
$u_\mathrm{e}\frac{\partial\widetilde{u_\mathrm{e}}}{\partial x}$	$0.3u_\infty^2/c$				Eqs. (3.11) and (3.12)
$\frac{\partial\widetilde{u_\infty}}{\partial t}$	$0.02u_\infty^2/c$				Eqs. (3.11) and (3.12)
$\widetilde{x_\mathrm{s}}$	$0.04c$	$0.02c$	$0.07c$		Sequential perturbation
$\widetilde{x_\mathrm{t}}$	$0.3c$	$0.07c$	0.08	$0.006c$	Sequential perturbation
$\widetilde{x_\mathrm{r}}$	$0.005c$	$0.3c$	0.02		Sequential perturbation
$\widetilde{\gamma}$	0.002				Sequential perturbation
$\widetilde{\Delta\mathcal{D}_\mathrm{transient}}$		7			Repeated measurements
$\widetilde{\Delta\mathcal{D}_\mathrm{react}}$			32		Repeated measurements
$\widetilde{\Delta\mathcal{D}_\mathrm{step}}$			13		Repeated measurements
$\lambda_i^2/\sum_{j=1}^N\lambda_j^2$				0.002	Eq. 3.12, [220]
$\mathbf{\Phi}_{i,u}$				3×10^{-4}**	Eq. 3.12, [220]
$E_\mathrm{g,P}$				0.007	Eq. 3.12, [220]
$E_\mathrm{s,P}$				$10E_\mathrm{g,t}$	Eq. 3.12, [220]
$E_\mathrm{s,F}$				0.02	Eq. 3.12, [220]
I				0.15	Sequential Perturbation
$\mathcal{P}_{E'_\mathrm{s,P}E'_\mathrm{s,P}}$				$0.2\mathcal{P}_{E'_\mathrm{s,P}E'_\mathrm{s,P}}$	Appendix A.2.3
$\rho_{\langle\lvert\mathbf{u}\rvert\rangle' u'_\infty}$				0.02	Eq. 3.12
$\rho_{E'_\mathrm{s,F}u'_\infty}$				0.02	Eq. 3.12

[§] In the vicinity of the separated shear layer. The uncertainty in instantaneous PIV measurements near the wall is substantially higher due to poor image quality caused by surface reflections.;
[†] The relatively higher maximum uncertainty is due to oscillations of the shear layer trajectory at $\mathrm{Re}_c = 8.0\times10^4$. The maximum uncertainty in $\overline{u}/u_\infty$ for the other Reynolds numbers is 0.06.;
[‡] Applies to Fig. 4.5 only because the average in Fig. 4.11 was taken over only 2 runs.
** RMS error over the field of view.